Modeling Dispersion of Radionuclides in the Turbulent Atmosphere

by

Matthew Jeffrey Krupcale

A dissertation submitted in partial fulfillment
of the requirements for the degree of
Doctor of Philosophy
(Nuclear Engineering and Radiological Sciences and Scientific Computing)
in the University of Michigan
2021

Doctoral Committee:

    Professor Emeritus John C. Lee, Chair
    Associate Research Scientist Shaun Clarke
    Professor Annalisa Manera
    Professor Kenneth G. Powell

Matthew Jeffrey Krupcale

krupcale@umich.edu

ORCID iD: 0000-0003-0551-3748

Dedication

For my parents: Denise and Jeff and Belinda and Jeff.

Acknowledgements

Thank you to John C. Lee for his commitment and encouragement to me. His insight, wisdom, and advice have proved essential over the course of the time we have worked together. I know I may have made this process more difficult and prolonged than necessary, but I am relieved we were able to make it through in the end.

Thank you also to the rest of the committee members, Dr. Shaun Clarke, Dr. Annalisa Manera, and Dr. Kenneth G. Powell, for their willingness to serve on my committee and review this work even during these turbulent, chaotic, and uncertain times.

I appreciate the NERS department and its graduate program coordinators, Ms. Peggy Jo Gramer and Dr. Garnette Roberts, for their careful attention, guidance, and regard for me. My sincerest thanks to them for helping me through the doctoral student process.

Thank you to my mentors during my time at the national laboratories: Dr. Paul W. Eslinger at Pacific Northwest National Laboratory and Dr. Matthew D. Simpson at Lawrence Livermore National Laboratory.

Finally, thank you to my friends and family who supported or took interest in me through this process. In particular, thank you to Denise and my father, Jeff, for allowing me to stay with them while I finished my defense and writing.

Table of Contents

List of Figures

List of Tables

Nomenclature

Abbreviations

AD   advection-diffusion

ATM   atmospheric transport modeling

CDF   cumulative distribution function

CFD   computational fluid dynamics

CTBT Comprehensive Nuclear-Test-Ban Treaty

CTBTO CTBT Organization

DD   drift-diffusion

DNS   direct numerical simulation

GLM   generalized Langevin model

IMS   International Monitoring System

LES   large eddy simulation

LPDM Lagrangian particle dispersion model

LRR-IP Launder, Reece, Rodi isotropization-of-production

MDC   minimum detectable concentration

NS   Navier-Stokes

PBL   planetary boundary layer

PDF   probability density function

PG   Pasquill-Gifford

RANS Reynolds-averaged Navier-Stokes

RMS   root mean square

RN   radionuclide

SDE   stochastic differential equation

SLM   simplified Langevin model

TKE   turbulent kinetic energy

Greek symbols

$\boldsymbol{\Omega}$ angular velocity vector for a rotating frame of reference

Δ volumetric strain rate or expansion, $e_{ii} = \partial U_i / \partial x_i = \nabla \cdot \mathbf{U}$

$\delta(\mathbf{Z})$ Dirac delta function, $\int_{\mathbb{R}^n} \delta(\mathbf{Z}) \mathrm{d}\mathbf{Z} = 1$

δ_{ij} Kronecker delta tensor

Γ molecular diffusivity

$\Gamma_{ij}^{\mathrm{eff}}$ effective diffusivity due to molecular and turbulent diffusion, $\Gamma \delta_{ij} + \Gamma_{ij}^{\mathrm{T}}$

Γ_{ij}^{T} turbulent diffusivity or eddy diffusivity tensor

μ dynamic viscosity

ν kinematic viscosity, μ/ρ

ν_{eff} effective viscosity due to molecular and turbulent viscosity, $\nu + \nu_{\mathrm{T}}$

ν_{T} turbulent viscosity or eddy viscosity

Φ (specific) potential, i.e. potential energy per unit mass

ρ mass density

$\sigma_{ij}(\tau)$ Lagrangian particle displacement covariance after time $\tau = t - t_0$

$\sigma_{u_i}^2$ turbulent velocity variance in direction i

τ TKE dissipation time scale, k/ε

ε TKE dissipation rate

$\xi_i(t)$ Gaussian white noise process in direction i, $\mathrm{d}W_i(t)/\mathrm{d}t$

Latin symbols

$\mathbf{U}$ total velocity

$\mathbf{u}$ turbulent velocity component

C_0 GLM diffusion coefficient

$f_{\mathbf{Z}}(\hat{\mathbf{Z}}; \mathbf{x}, t)$ 1-point, 1-time PDF of random variable $\mathbf{Z}$ parameterized on space $\mathbf{x}$ and time t

g gravitational acceleration

G_{ij} GLM drift coefficient

k TKE, $\langle u_i u_i \rangle /2$

P modified pressure, $p + \rho\Phi$

p thermodynamic pressure

$R_{ij}^{\mathrm{L}}(s)$ Lagrangian velocity autocorrelation tensor

T temperature

T_{ij}^{L} Lagrangian or integral time scale tensor

$W(\hat{\mathbf{Z}}|\hat{\mathbf{Z}}'; t)$ transition probability per unit time from state $\hat{\mathbf{Z}}'$ at time t to another state $\hat{\mathbf{Z}}$ at time $t + \Delta t$

$W_i(t)$ Wiener process in direction i

Operators

Δ difference operator

$\langle Q(\mathbf{Z}) \rangle$ mean or expected value of $Q(\mathbf{Z})$

$\mathrm{D}/\mathrm{D}t$ material or Lagrangian derivative, $\partial/\partial t + U_i \partial/\partial x_i = \partial/\partial t + \mathbf{U} \cdot \nabla$

∇ gradient operator, $\hat{\mathbf{e}}_i \partial/\partial x_i$

∇^2 Laplacian operator, $\partial^2/\partial x_i \partial x_i$

Abstract

In an effort to understand the assumptions and approximations involved in the physics on which atmospheric transport modeling (ATM) relies, we derived from first principles the Lagrangian turbulent velocity drift-diffusion model used by codes such as FLEXPART and HYSPLIT. We showed that the drift-diffusion model is a Langevin model representing the equation of motion for Lagrangian fluid particles based on the turbulent Navier-Stokes equation. That is, the incompressible turbulent Navier-Stokes equation is cast into the form of a stochastic differential equation (SDE) called the Langevin equation which describes the turbulent velocity component of the Lagrangian particle trajectory. The drift coefficient depends on the Lagrangian time scale modeled using the Lagrangian velocity autocorrelation function, while the diffusion coefficient depends additionally on the Reynolds stress or velocity variance. This makes clear that the turbulent Navier-Stokes equation is the physical basis of the drift-diffusion model used by FLEXPART and HYSPLIT and shows what assumptions and approximations are made.

In contrast to particle-based methods of the Lagrangian models, the advection-diffusion (AD) equation physically represents a mass-conservation equation in a turbulent fluid and directly models the mean Eulerian concentration field by employing an eddy diffusivity hypothesis. The AD model is the basis for Gaussian plume model codes such as MACCS2 which use the Pasquill-Gifford semi-empirical turbulence model. We parametrically compared the FLEXPART drift-diffusion model to the Gaussian puff model using synthetic meteorological data, which showed significant discrepancies between the vertical or horizontal dispersion parameters for unstable or stable atmospheres, respectively. However, by modifying the FLEXPART turbulence model to simulate the Gaussian puff model dispersion parameters, we demonstrated much better agreement between the two models. On the other hand, the FLEXPART concentration profile dispersion generally agreed well with the Lagrangian particle ensemble dispersion, validating to some extent the relationship between the Lagrangian and Eulerian turbulence parameters.

In addition to the complexities associated with physically modeling turbulence, we have demonstrated uncertainties associated with dry deposition, particle size distributions, radioactive decay chains, different meteorological data sets, virtual particle numbers, and mesoscale velocity fluctuations. We have performed studies on: local (100 km radius) and global scales, large (Fukushima) and small (DPRK) radionuclide (RN) emission sources, and particulate (volcanic ash) and gaseous species (Xe). Volcanic ash particulate transport simulations showed that it is necessary to use large numbers of particles per emission source, that the dry deposition model significantly reduces predicted atmospheric concentrations and that this is more pronounced for larger particle sizes. When we examined the radioxenon emissions from the Fukushima Daiichi nuclear accident, we found that the meteorological data set chosen has a significant impact on the simulated RN concentrations at detectors as close as Takasaki, with variations up to four orders of magnitude. Additionally, our studies on DPRK weapons tests showed that the measured RN data is often very sparse and difficult to explain and attribute to a particular source.

These studies all demonstrated the many uncertainties and difficulties associated with ATM of RNs when comparing to real data. Thus, we show that ATMs should rely as closely as possible on the underlying physics for accurately modeling RN dispersion in the turbulent atmosphere. In particular, one should use turbulence models based closely on the turbulent Navier-Stokes equation, accurate and high resolution meteorological data, and physics-based deposition and transmutation models.

Chapter 1

Background and Introduction

Fundamentally, the purpose of atmospheric transport modeling (ATM) is to estimate quantities such as the mass concentration field resulting from the simulated transport and dispersion of material in the turbulent atmosphere. The material species of interest could be chemical or radiological in nature with ATM applications ranging from accident analysis, natural disaster response, environmental regulation, and treaty verification. Our focus is on the ATM of radionuclides (RNs) for nuclear accident analysis as well as treaty verification of nuclear weapons testing or monitoring of clandestine nuclear activities. There are several approaches for ATM of RNs, primarily divided into two categories: Eulerian mass and fluid dynamics models and Lagrangian particle dispersion models (LPDMs). Each model has its own assumptions and uncertainties involved, including the systematic modeling errors of the physical model. In particular, ATMs must simulate the dispersion of species by approximating the characteristics of atmospheric turbulence.

The primary goal of this dissertation is to provide physical and mathematical justification for the computational models commonly used in ATM applications. By examining the underlying assumptions and physics of these computational models, we are able to make comparisons between various ATMs which are often used without complete understanding. This basic understanding is important in order to know the limitations and uncertainties involved in ATM for applications with real data, which is the secondary goal of this thesis. That is, we wish to emphasize the importance of understanding and acknowledging the uncertainties in ATM, especially when applied to situations which could have significant consequences. With the understanding of the physical model and its systematic uncertainties, one can seek to improve the model and reduce uncertainties by following the physics as closely as possible.

1.1 Motivation

Atmospheric transport modeling (ATM) has many applications dating back to the early and mid twentieth century [13–15]. Fundamentally, the purpose of ATM is to simulate the transport of material in the turbulent atmosphere in order to estimate quantities such as the mass concentration field of species. Applications of ATM include accident analysis such as following a nuclear meltdown [16–20] or chemical plant explosion [21], natural disasters like volcanic eruptions [22–24], environmental regulation modeling of factory emissions [25], and treaty verification [26, 27] of nuclear weapons testing or monitoring of clandestine nuclear activities. Thus, the species could be chemical or radiological in nature, undergoing potentially complex physical processes such as dry deposition, chemical reactions, and radioactive decay. It is often the case for these situations that the emission source itself is unknown, and therefore one might be interested in using measured atmospheric concentration data to estimate the source [28].

As a part of the CVT, the focus of this work has been on nuclear weapons test treaty verification and monitoring clandestine nuclear activities. In particular, if the Comprehensive Nuclear-Test-Ban Treaty (CTBT) were ratified, it would ban all explosive nuclear tests, and there would be a need to verify compliance by its signatory nations. Under the CTBT Organization (CTBTO) verification regime, a global network of detectors called the International Monitoring System (IMS) was created for this purpose. The IMS consists of four primary detection technologies: seismic [29], hydroacoustic [30], infrasound [31], and radionuclide [32]. While the former three detector networks can provide very useful information about the timing, location, and intensity of an explosion, it is this latter RN detector network which proves the nuclear nature of the explosion.

The RN detector network consists of 80 RN detectors, 40 of which have highly sensitive radioxenon measurement capabilities. These radioxenon detectors are particularly useful for CTBT verification for several reasons [33]. As a noble gas, radioxenon is chemically inert and therefore likely to seep through the surface of the Earth in underground nuclear weapons tests. Additionally, gaseous atmospheric deposition can typically be neglected whereas this is a more significant effect for particulate matter. These two attributes of noble gases make radioxenon especially useful for ATM. Finally, the radioactive decay and isotopic ratios of radioxenon can be used for discriminating civilian nuclear sources from weapons tests [5, 6]. However, while the radioxenon detectors are both necessary and useful for CTBT verification purposes [34], their placement and measured data are both relatively sparse, making verification and

source discrimination difficult [6, 35].

In addition to uncertainties associated with measured data, there are many modeling uncertainties associated with modeling turbulence. Turbulence is a challenging problem in physics [36], and we present in this thesis the physical basis and assumptions of the turbulence models employed by several ATMs. In particular, since we are interested in the global transport of RNs, we sought to use and understand some of the LPDMs most commonly used in this area [37]: FLEXPART [1, 2] and HYSPLIT [38]. After discovering the level of variability of both input and output parameters for these models, we began to focus on understanding the fundamental physics on which these models are based to see what assumptions and approximations are made and where improvements are warranted.

1.2   Significance of Thesis

The significance of this thesis is to derive from physical first principles the models commonly used in ATM applications, focusing on the FLEXPART and HYSPLIT LPDMs. While there have been many works which have discussed these models and their applications [10, 39–42], the connection to the underlying physics has not been clarified. In particular, whereas previous forms of the Langevin drift-diffusion (DD) equation are historically asserted outright as a suitable model for the turbulent fluid flow velocity [15, 43, 44], we have derived directly from the turbulent Navier-Stokes equation the Langevin DD model used by FLEXPART with a simple physical understanding of the Langevin equation of motion. Furthermore, while alternative approaches to deriving Langevin models which rely on statistical probability distribution transport equations [39, 42, 45] can obscure the underlying physics, the direct approach we use remains as close as possible to the physical equation of motion. Thus, this work attempts to make clear what underlying physics these models represent as well as what assumptions and approximations are made.

With a solid understanding of the physical model, we then present several applications to real and synthetic data with the caveat that there are many uncertainties inherent in ATM. For example, it is not uncommon to have estimated emission source uncertainties on the order of 50% or even more than 100% [22, 46]. Furthermore, relatively rapid fluctuations over several orders of magnitude in simulated and measured concentrations are not uncommon due to the sharp and chaotic nature of turbulence. Regardless of the widespread recognition that there are many uncertainties associated with ATM [47–49], researchers and organizations often employ ATM towards real situations. If not properly acknowledged, these uncertainties could have consequences on perceived dangers [50] and policy [51, 52] unwarranted by the

level of confidence in the model. This allows us to propose areas for future improvement as well as some basic recommendations.

1.3 Outline

Chapter 2 discusses the underling mathematical and physical understanding necessary for the subsequent chapters. It begins by making the distinction between the Eulerian and Lagrangian frames of reference, defining the concept of a fluid parcel or fluid particle and the material or Lagrangian derivative which follows the trajectory of a fluid particle. Then it presents and justifies the assumptions made for the mass, momentum, and energy conservation equations, as well as the equation of state, for the Earth's atmosphere. Since we are particularly concerned in this thesis with the turbulent atmosphere, we discuss several foundational concepts of random fields and processes. Finally, we derive the relationship and assumptions involved between various mathematical formulations of stochastic models and especially their relationship to the Langevin equation.

Chapter 3 begins with a derivation of the turbulent Navier-Stokes equation from the Navier-Stokes equation and the Reynolds-averaged Navier-Stokes (RANS) equation. When cast in terms of the Lagrangian derivative, this is the basis for the FLEXPART and HYSPLIT Lagrangian velocity Langevin DD model. With a simple approximation, we demonstrate that the mean velocity gradient drift coefficient can be represented in terms of the velocity autocorrelation function time scale. This model is contrasted with several alternative models which depend on other time scales.

As opposed to the Lagrangian models in chapter 3, chapter 4 derives and discusses several Eulerian approaches for ATM. First, we discuss general computational fluid dynamics (CFD) models, focusing on perhaps the simplest and most commonly used Reynolds stress turbulence closure model, the k-ε eddy viscosity model. Secondly, we discuss the advection-diffusion (AD) model with its analogous eddy diffusivity hypothesis. The AD model is the basis for the Gaussian puff or plume models commonly used in simple nuclear safety codes. We finally derive the connection between the AD model diffusion coefficients and particle dispersion parameters from chapter 3 in terms of the Lagrangian parameters.

Chapter 5 discusses the details of the FLEXPART and HYSPLIT code implementations, attempting to provide insight into the empirical models employed. First, we present the mechanics of the grid-scale, mesoscale, and microscale turbulence models used specifically by FLEXPART. Then we discuss how LPDMs such as FLEXPART determine mass concentrations

through particle averaging methods as well as their characterization and transmutation of species during transport. Finally, we discuss the backward or adjoint mode which can be used to efficiently calculate source-receptor functions.

Chapter 6 presents several practical applications of FLEXPART, HYSPLIT, and Gaussian puff models. We discuss the use of FLEXPART for source estimation with a focus on gaseous radionuclide transport applied to both treaty verification and monitoring of clandestine nuclear activities as well as nuclear accident analysis. Furthermore, we present a deposition model study with volcanic ash and studies on the grid-, meso-, and microscale turbulence models of FLEXPART.

Finally, chapter 7 provides a summary of this work, conclusions drawn, possible future directions, and recommendations of this work.

Chapter 2

Physical and Mathematical Preliminaries

As atmospheric transport modeling fundamentally seeks to represent the motion of species in the turbulent atmosphere, ATM shares many of the physical and mathematical models used in meteorology for describing and forecasting the state of the atmosphere. In particular, it relies on the laws of conservation, equations of state, and their stochastic representations for describing the spatiotemporal dynamics and thermodynamics of fluids in the turbulent atmosphere.

Since velocities in the atmospheric boundary layers are small compared to the speed of light, we may use Galilean and Newtonian classical physics [53]. In principle, one could attempt to model all turbulence scales directly as is done through direct numerical simulation (DNS), but for regional or global ATM, this is computationally impractical. Furthermore, one generally has insufficient knowledge about initial and boundary conditions. Thus, in practice, one will rely on meteorological models for resolving grid scale turbulence while employing stochastic models for resolving mesoscale and microscale turbulence. These stochastic models can take many mathematical forms, but they all fundamentally are based on the same assumption that the fields are modeled as a Markov random process—specifically, a diffusion process. The form which is employed in the ATM codes FLEXPART and HYSPLIT, for example, is a Langevin model.

2.1   Eulerian and Lagrangian Fields

Many quantities in meteorology and ATM appear as a function of both spatial position $\mathbf{x}$ and time t, and we can describe these quantities from both a Eulerian and a Lagrangian perspective. Both specifications rely on the continuum hypothesis that allows us to treat fluids as continuous media, even though they are composed of discrete molecules and atoms. The continuum hypothesis relies on the fact that the molecular mean free path λ is much smaller than the geometric and physical length scales of the fluid flow L: $\lambda \ll L \Rightarrow \mathrm{Kn} \ll 1$,

where Kn is the Knudsen number. Then one can interpret continuum field quantities at $(\mathbf{x}, t)$ as the volume-averaged quantity from the constituent molecules inside a volume ℓ^3 centered at $\mathbf{x}$ at time t, where $\lambda \ll \ell \ll L$ [39].

The Eulerian specification of the fluid field observes the spatiotemporal behavior—that is, the spatial distribution at each instant during the motion—of the field in an inertial frame of reference [39]. This relative simplicity makes Eulerian descriptions natural for a fixed observation point such as ground-based measurements or for stationary grid cells [37]. The primary flow quantity is the Eulerian velocity field $\mathbf{U}(\mathbf{x}, t)$, indexed by both spatial position $\mathbf{x}$ and time t, but quantities such as density $\rho(\mathbf{x}, t)$ and pressure $p(\mathbf{x}, t)$ are also commonly specified in this way.

In contrast, the Lagrangian perspective observes the field following a fluid parcel or fluid particle, which can be considered a more physical description and is often convenient for studying turbulent transport [37, 54]. Fluid parcels or fluid particles are infinitesimal regions of the fluid whose constituent physical particles are labeled by an identifier $\mathbf{x}_0$. Often, this identifier represents the center of mass of the fluid particle at some time t_0, but it could alternatively be a thermodynamic triple at t_0 [41, 55]. As in the continuum hypothesis, the fluid particle linear dimension is of order ℓ such that quantities may be considered constant inside the fluid particle volume [54]. The fluid particle changes shape and volume (if the fluid is compressible) as it moves with the fluid flow, but it always corresponds to the same set of particles (and mass if mass is conserved) [41, 55].

Let $\mathbf{x}(\mathbf{x}_0, t_0|t)$ and $\mathbf{U}(\mathbf{x}_0, t_0|t)$ denote the position and velocity of the Lagrangian fluid particle at time t originating from position $\mathbf{x}_0$ at the reference time $t_0 \leq t$. Then, by definition, the fluid particle position satisfies the initial condition

$$\mathbf{x}(\mathbf{x}_0, t_0|t_0) \equiv \mathbf{x}_0, \tag{2.1}$$

and the velocity of the fluid particle is defined in terms of the Eulerian velocity at the fluid particle position,

$$\mathbf{U}(\mathbf{x}_0, t_0|t) \equiv \mathbf{U}\left[\mathbf{x}\left(\mathbf{x}_0, t_0|t\right), t\right]. \tag{2.2}$$

Since the fluid particle moves with the fluid velocity, we have

$$\frac{\partial}{\partial t}\mathbf{x}(\mathbf{x}_0, t_0|t) = \mathbf{U}\left(\mathbf{x}_0, t_0|t\right) = \mathbf{U}\left[\mathbf{x}\left(\mathbf{x}_0, t_0|t\right), t\right]. \tag{2.3}$$

Thus, differentiating Eq. 2.2 with respect to t, we have

$$
\begin{aligned}
\frac{\partial}{\partial t} U_i(\mathbf{x}_0, t_0|t) &= \left[\frac{\partial}{\partial t} U_i(\mathbf{x}, t) + \frac{\partial}{\partial x_j} U_i(\mathbf{x}, t) \frac{\partial x_j}{\partial t} \right]_{\mathbf{x}=\mathbf{x}(\mathbf{x}_0, t_0|t)} \\
&= \left[\frac{\partial}{\partial t} U_i(\mathbf{x}, t) \right]_{\mathbf{x}=\mathbf{x}(\mathbf{x}_0, t_0|t)} + \frac{\partial x_j(\mathbf{x}_0, t_0|t)}{\partial t} \left[\frac{\partial}{\partial x_j} U_i(\mathbf{x}, t) \right]_{\mathbf{x}=\mathbf{x}(\mathbf{x}_0, t_0|t)} \\
&= \left[\frac{\partial}{\partial t} U_i(\mathbf{x}, t) \right]_{\mathbf{x}=\mathbf{x}(\mathbf{x}_0, t_0|t)} + U_j \left[\mathbf{x}\left(\mathbf{x}_0, t_0|t\right), t \right] \left[\frac{\partial}{\partial x_j} U_i(\mathbf{x}, t) \right]_{\mathbf{x}=\mathbf{x}(\mathbf{x}_0, t_0|t)} \\
&= \left[\frac{\mathrm{D} U_i}{\mathrm{D} t} \right]_{\mathbf{x}=\mathbf{x}(\mathbf{x}_0, t_0|t)}.
\end{aligned}
\tag{2.4}
$$

This is to say that the Lagrangian or material derivative is the rate of change following the fluid particle trajectory, where we define the Lagrangian or material derivative as

$$
\frac{\mathrm{D}}{\mathrm{D}t} \equiv \frac{\partial}{\partial t} + U_i \frac{\partial}{\partial x_i}.
\tag{2.5}
$$

More generally, one can show that the Lagrangian value of any quantity is the Eulerian value at the Lagrangian particle position at that time [41]. Consider a scalar[1] quantity $\phi(t)$ sampled from the scalar field $\varphi = \varphi(\mathbf{x}, t)$ along a particle trajectory $\mathbf{x}(t)$ in a continuum fluid flow:

$$
\phi(t) = \varphi\left[\mathbf{x}(t), t\right].
\tag{2.6}
$$

For example, this quantity might represent a physical quantity such as the fluid density ρ or velocity component U_i. Then we can calculate the total derivative of $\phi(t)$ along this trajectory $\mathbf{x}(t)$ by using the chain rule:

$$
\frac{\mathrm{d}}{\mathrm{d}t} \phi(t) = \left[\frac{\partial}{\partial t} \varphi(\mathbf{x}, t) \right]_{\mathbf{x}=\mathbf{x}(t)} + \frac{\mathrm{d} x_i(t)}{\mathrm{d}t} \left[\frac{\partial}{\partial x_i} \varphi(\mathbf{x}, t) \right]_{\mathbf{x}=\mathbf{x}(t)},
\tag{2.7}
$$

where $\dot{\mathbf{x}} = \mathrm{d}\mathbf{x}/\mathrm{d}t$ is the velocity of the control volume element. This represents the temporal change due both to a temporal change at a fixed point, represented by $\partial_t \varphi$, and the change in the control volume location within a gradient, represented by $\dot{\mathbf{x}} \cdot \nabla \varphi$. Note that the trajectory is completely arbitrary: one can choose any trajectory $\mathbf{x}(t)$ along which to measure the quantity of interest. If the trajectory along which we measure $\phi(t)$ is given by the trajectory

---

[1] φ could similarly represent a vector or tensor field.

which follows the fluid velocity,

$$\frac{d\mathbf{x}(t)}{dt} = \mathbf{U}(t) = \mathbf{U}\left[\mathbf{x}(t), t\right], \tag{2.8}$$

where $\mathbf{x}(t) \equiv \mathbf{x}(\mathbf{x}_0, t_0|t)$ is the Lagrangian particle position, and $\mathbf{U}(t) \equiv \mathbf{U}(\mathbf{x}_0, t_0|t) = \mathbf{U}\left[\mathbf{x}\left(\mathbf{x}_0, t_0|t\right), t\right]$ is the Lagrangian particle velocity, then the total derivative is given by the Lagrangian derivative:

$$\begin{aligned} \frac{d}{dt}\phi(t) &= \left[\frac{\partial}{\partial t}\varphi(\mathbf{x}, t)\right]_{\mathbf{x}=\mathbf{x}(t)} + U_i(t)\left[\frac{\partial}{\partial x_i}\varphi(\mathbf{x}, t)\right]_{\mathbf{x}=\mathbf{x}(t)} \\ &\equiv \left[\frac{D}{Dt}\varphi(\mathbf{x}, t)\right]_{\mathbf{x}=\mathbf{x}(t)}. \end{aligned} \tag{2.9}$$

Thus, the Lagrangian derivative is the correct derivative for a quantity evaluated along the Lagrangian particle trajectory, and the Lagrangian quantity value is the Eulerian value evaluated along the Lagrangian particle trajectory. This Lagrangian derivative is commonly encountered in fluid dynamics equations for conservation laws, which allows us to compactly write such equations in terms of the Lagrangian trajectory which follows the velocity of the fluid.

2.2   Conservation Laws and Equations of State

Several meteorological variables can be described in terms of conservation laws. These include conservation of mass (for species mixed in the atmosphere or the usual constituents of the air), energy, and linear momentum. One additionally requires an equation of state to describe the thermodynamic triple of pressure, temperature, and density or volume. Altogether, these conservation laws and the equation of state allow us to describe the fluid with six dependent variables: density ρ, velocity $\mathbf{U}$, pressure p, and temperature T.

2.2.1   Continuity Equation

The continuity equation is used to describe the transport of a quantity and represents a conservation law. It can be written in both a differential or integral form, but here we will use the strong, local, differential form of the continuity equation:

$$\frac{\partial \rho}{\partial t} + \frac{\partial j_i}{\partial x_i} = s, \tag{2.10}$$

where ρ is the volumetric density of the conserved quantity q (e.g. mass, energy, momentum), $\mathbf{j}$ is the flux or current density of q, and s is the internal volumetric generation rate of q. In the case of a quantity which cannot be created or destroyed, $s = 0$. Note that these equations are only considered for non-relativistic cases.

2.2.2 Conservation of Mass

For conservation of mass, $q = m$, where m is the fluid-particle mixture mass, ρ is the mass density, $\mathbf{j} = \rho \mathbf{U}$ is the mass flux density or flow rate, where $\mathbf{U}$ is the flow velocity, and (at low energies) $s = 0$, since there is no internal mass generation or loss. Thus, we write explicitly Eq. 2.10 as [55]

$$\frac{\partial \rho}{\partial t} + \frac{\partial}{\partial x_i}(\rho U_i) = 0. \tag{2.11}$$

Eq. 2.11 is also the form of the advection equation for the scalar field ρ.

An often-used approximation is in the case of an incompressible fluid, for which Eq. 2.11 becomes simply $\nabla \cdot \mathbf{U} = 0$. The derivation of this begins by expanding Eq. 2.11 using the product rule,

$$\frac{\partial \rho}{\partial t} + \rho \frac{\partial U_i}{\partial x_i} + U_i \frac{\partial \rho}{\partial x_i} = 0, \tag{2.12}$$

where $\rho = \rho(\mathbf{x}, t)$. The expanded continuity equation 2.12 can be written in terms of the material derivative as

$$\frac{\mathrm{D}\rho}{\mathrm{D}t} = -\rho \frac{\partial U_i}{\partial x_i}. \tag{2.13}$$

Thus, for an incompressible fluid, mandating a constant (nonzero) density requires that

$$\frac{\mathrm{D}\rho}{\mathrm{D}t} = -\rho \frac{\partial U_i}{\partial x_i} = 0 \tag{2.14a}$$

$$\Rightarrow \frac{\partial U_i}{\partial x_i} = 0. \tag{2.14b}$$

The latter condition is a kinematic condition that the velocity field is solenoidal or divergence-free [55].

We will frequently use this incompressibility approximation, so it is necessary to justify why and the circumstances under which this approximation may be employed. In the gaseous atmosphere with time-varying velocity $\mathbf{U}(\mathbf{x}, t)$, the variations of the density ρ will be negligibly small when [56]

1. the fluid velocity is small compared to the speed of sound:

$$U \ll c,$$

   where c is the speed of sound;

2. and, if τ and L are characteristic time and length scales, respectively, in which the fluid velocity undergoes significant changes, the time taken for sound to traverse the distance L is small compared to the time during which the flow changes perceptibly:

$$L/c \ll \tau.$$

The latter condition can be interpreted as the propagation of interactions in the fluid being instantaneous, while the former is the result of the defining relationship of the speed of sound to density and pressure changes. The first condition is nearly always satisfied in the atmosphere, which has a speed of sound $c \simeq 300 \, \mathrm{m\,s^{-1}}$ and velocities of at most $U \simeq 100 \, \mathrm{m\,s^{-1}}$ (although typically much less). The second condition is generally satisfied for turbulent motions smaller than mesoscale, so we can generally use the incompressibility approximation within the planetary boundary layer (PBL) [10, 53].

2.2.3 Conservation of Momentum

Conservation of momentum (in a non-relativistic sense) is simply described by Newton's second law on a control volume. Here we set $q = m\mathbf{U}$ to be the fluid linear momentum, with $\rho\mathbf{U}$ its momentum density, $\mathbf{j} = \rho\mathbf{U} \otimes \mathbf{U}$ is the momentum flux density, where $\mathbf{U} \otimes \mathbf{U}$ is the dyadic product of the flow velocity, $\boldsymbol{\sigma}$ is the Cauchy stress tensor describing surface forces, and $\mathbf{F}_\mathrm{b}$ incorporates the the volumetric body forces. Then Eq. 2.10 for momentum becomes

$$\frac{\partial}{\partial t}\left(\rho U_i\right) + \frac{\partial}{\partial x_j}\left(\rho U_i U_j\right) = \frac{\partial \sigma_{ij}}{\partial x_j} + F_{\mathrm{b},i}. \tag{2.15}$$

This is called the Cauchy momentum equation. In general, it is a nonlinear equation, but one can make many simplifications to make it more tractable such as assuming incompressibility, specifying the stress tensor in terms of a constitutive relation, assuming constant pressure, and assuming inviscid flow. These various assumptions lead to different forms of either the Navier-Stokes equations or the Euler equations for fluid dynamics. Ultimately, we will use the Navier-Stokes equation for an incompressible fluid in the frame of reference of the Earth's surface which is rotating with respect to the atmosphere.

2.2.3.1 Momentum Trajectory

The left-hand side of Eq. 2.15 can be expanded using the product rule as

$$\frac{\partial}{\partial t}\left(\rho U_i\right) + \frac{\partial}{\partial x_j}\left(\rho U_i U_j\right) = U_i\frac{\partial \rho}{\partial t} + \rho\frac{\partial U_i}{\partial t} + U_j\frac{\partial}{\partial x_j}\left(\rho U_i\right) + \rho U_i\frac{\partial U_j}{\partial x_j}, \tag{2.16}$$

$$= U_i\frac{\partial \rho}{\partial t} + \rho\frac{\partial U_i}{\partial t} + U_i U_j\frac{\partial \rho}{\partial x_j} + \rho U_j\frac{\partial U_i}{\partial x_j} + \rho U_i\frac{\partial U_j}{\partial x_j}. \tag{2.17}$$

Multiplying Eq. 2.12 by U_i with a change of indices yields

$$U_i\frac{\partial \rho}{\partial t} + U_i U_j\frac{\partial \rho}{\partial x_j} = -\rho U_i\frac{\partial U_j}{\partial x_j}, \tag{2.18}$$

which when combined with Eq. 2.17 results in

$$\frac{\partial}{\partial t}\left(\rho U_i\right) + \frac{\partial}{\partial x_j}\left(\rho U_i U_j\right) = \rho\frac{\partial U_i}{\partial t} + \rho U_j\frac{\partial U_i}{\partial x_j} \tag{2.19}$$

$$= \rho\frac{\mathrm{D}U_i}{\mathrm{D}t} \tag{2.20}$$

Thus, the left-hand side of the momentum conservation Eq. 2.15 follows the trajectory of the velocity material derivative. Note that this does not require that the fluid be incompressible: it is a direct result of the combination of the mass and momentum conservation equations.

2.2.3.2 Cauchy Stress Tensor

By employing a constitutive relation, we can relate the stress tensor to the fluid deformation. In particular, we consider a linear constitutive relation for a Newtonian fluid, which the air in the atmosphere behaves like to a close approximation [10, 53]. The stress tensor can be divided into an isotropic component and an anisotropic component [57],

$$\sigma_{ij} = -p\delta_{ij} + \tau_{ij}, \tag{2.21}$$

where p is the thermodynamic pressure, δ_{ij} is the Kronecker delta tensor, and $\boldsymbol{\tau}$ is the deviatoric or viscous stress tensor. The pressure is generally defined as negative one-third the trace of the stress tensor plus stress due to the divergence of the velocity, $p = \bar{p} + \zeta\nabla\cdot\mathbf{U}$, where $\bar{p} \equiv -\mathrm{tr}(\boldsymbol{\sigma})/3 = -\sigma_{ii}/3$ is the mean hydrostatic stress or the mechanical pressure, and $\zeta = \lambda + 2\mu/3$ is a proportionality constant called the bulk viscosity or second viscosity, which depends on two scalar Lamé parameters, the first parameter λ and the second parameter or

dynamic viscosity μ. The second viscosity ζ models the difference between the thermodynamic and mechanical pressures which can arise due to rapid expansion or compression when compared to the thermodynamic equilibrium relaxation time [56].

For a Newtonian fluid, the relationship between the viscous stress τ_{ij} and $\partial U_i / \partial x_j$ is linear [55]:

$$\tau_{ij} = A_{ijk\ell} \frac{\partial U_k}{\partial x_\ell}. \tag{2.22}$$

The velocity gradients $\partial U_i / \partial x_j$ can be decomposed into symmetric and antisymmetric parts:

$$\frac{\partial U_i}{\partial x_j} = e_{ij} + r_{ij},$$

where

$$e_{ij} \equiv \frac{1}{2} \left(\frac{\partial U_i}{\partial x_j} + \frac{\partial U_j}{\partial x_i} \right), \tag{2.23}$$

$$r_{ij} \equiv \frac{1}{2} \left(\frac{\partial U_i}{\partial x_j} - \frac{\partial U_j}{\partial x_i} \right) \tag{2.24}$$

are the rate-of-strain and rate-of-rotation tensors, respectively. The antisymmetric part represents fluid rotation without deformation and cannot by itself generate stress, so stresses must be generated by the strain rate tensor e_{ij}. Assuming a linearly elastic and isotropic fluid with a symmetric stress tensor, one can show that Eq. 2.22 reduces to a linear function of two coefficients [55, 57]:

$$\tau_{ij} = \lambda \Delta \delta_{ij} + 2\mu e_{ij}, \tag{2.25}$$

where $\Delta \equiv e_{ii} = \partial U_i / \partial x_i = \nabla \cdot \mathbf{U}$ is the volumetric strain rate or expansion.

Substituting Eq. 2.25 into Eq. 2.21, the Cauchy stress tensor for a Newtonian fluid is [55, 56]

$$\sigma_{ij} = - \left(p - \lambda \Delta \right) \delta_{ij} + 2\mu e_{ij} \tag{2.26a}$$

$$= - \left(p - \zeta \Delta \right) \delta_{ij} + 2\mu \left(e_{ij} - \frac{1}{3} \Delta \delta_{ij} \right), \tag{2.26b}$$

so the momentum change due to the stress tensor is [56]

$$\frac{\partial \sigma_{ij}}{\partial x_j} = - \frac{\partial p}{\partial x_i} + \frac{\partial}{\partial x_i} \left(\zeta \Delta \right) + \frac{\partial}{\partial x_j} \left[\mu \left(2 e_{ij} - \frac{2}{3} \Delta \delta_{ij} \right) \right]. \tag{2.27}$$

For many applications the Stokes assumption $\zeta = 0 \Rightarrow \lambda = -2\mu/3$ is sufficiently accurate[2]. With this assumption, the viscous stress tensor Eq. 2.25 and Cauchy stress tensor Eqs. 2.26, respectively, can be written in terms of the dynamic viscosity alone [55, 57]:

$$\tau_{ij} = -\frac{2}{3}\mu\Delta\delta_{ij} + 2\mu e_{ij}, \tag{2.28}$$

$$\sigma_{ij} = -p\delta_{ij} + 2\mu\left(e_{ij} - \frac{1}{3}\Delta\delta_{ij}\right). \tag{2.29}$$

Thus, the momentum change due to the stress tensor with the Stokes assumption is [55, 57]

$$\frac{\partial\sigma_{ij}}{\partial x_j} = -\frac{\partial p}{\partial x_i} - \frac{2}{3}\frac{\partial}{\partial x_i}\left(\mu\Delta\right) + \frac{\partial}{\partial x_j}\left(2\mu e_{ij}\right). \tag{2.30}$$

The viscosity is generally a function of pressure and temperature and thus varies spatially in the fluid. In most cases, however, the viscosity does not noticeably change in the fluid and can be regarded as constant [53, 56, 57] so that Eq. 2.30 becomes

$$
\begin{aligned}
\frac{\partial\sigma_{ij}}{\partial x_j} &= -\frac{\partial p}{\partial x_i} - \frac{2}{3}\mu\frac{\partial\Delta}{\partial x_i} + \mu\frac{\partial}{\partial x_j}\left(2e_{ij}\right) \\
&= -\frac{\partial p}{\partial x_i} - \frac{2}{3}\mu\frac{\partial\Delta}{\partial x_i} + \mu\left(\frac{\partial U_i^2}{\partial x_j\partial x_j} + \frac{\partial^2 U_j}{\partial x_i\partial x_j}\right) \\
&= -\frac{\partial p}{\partial x_i} + \mu\left(\nabla^2 U_i + \frac{1}{3}\frac{\partial\Delta}{\partial x_i}\right),
\end{aligned}
\tag{2.31}
$$

where $\nabla^2 U_i \equiv \partial^2 U_i/\partial x_j\partial x_j$.

The final simplification is to assume the fluid is incompressible: $\Delta = 0$. In this case, the viscous stress tensor Eq. 2.28 and Cauchy stress tensor Eqs. 2.29 (or Eq. 2.25 and Eqs. 2.26), respectively, simplify to

$$\tau_{ij} = 2\mu e_{ij}, \tag{2.32}$$

$$\sigma_{ij} = -p\delta_{ij} + 2\mu e_{ij}, \tag{2.33}$$

while the momentum change Eq. 2.31 (or Eqs. 2.27 or 2.30 with constant viscosity μ)

---

[2]Exceptions to this include e.g. damping of high frequency sound waves and the structure of shock waves [55].

simplifies to [55, 57]

$$\frac{\partial \sigma_{ij}}{\partial x_j} = -\frac{\partial p}{\partial x_i} + \mu \nabla^2 U_i. \tag{2.34}$$

2.2.3.3 External Body Forces

External body forces can be separated into conservative and non-conservative portions, $\mathbf{F}_{\mathrm{b}} = \mathbf{F}_{\mathrm{c}} + \mathbf{F}_{\mathrm{n}}$, such that any conservative body forces may be written in terms of the gradient of a potential field:

$$\mathbf{F}_{\mathrm{c}} = -\rho \nabla \Phi, \tag{2.35}$$

where Φ is the specific potential field—that is, the potential energy per unit mass. For constant-density flows, any conservative forces can then be absorbed into the pressure gradient, resulting in a modified pressure

$$P = p + \rho \Phi. \tag{2.36}$$

The external body forces might include any number of physical effects, but among the fundamental forces, gravity may be the most important:

$$\mathbf{F}_{\mathrm{grav}} = \rho \mathbf{g} = -\rho \nabla \Phi_{\mathrm{grav}}, \tag{2.37}$$

where [58]

$$\Phi_{\mathrm{grav}} = -\mathbf{g} \cdot \mathbf{x}, \tag{2.38}$$

with $\mathbf{g} \equiv -g\hat{\mathbf{r}}$ the gravitational acceleration vector pointing towards the Earth's polar center and $\mathbf{x}$ the polar position. If the fluid particles are charged, Lorentz forces might be significant, which also would require solving Maxwell's equations, but we will not deal with charged particle ATM.

On the other hand, the Earth's surface is a non-inertial reference frame, which generally requires fictitious forces such as the Coriolis force, centrifugal force, and Euler force. Let the frame of reference be both accelerating with linear acceleration $\mathbf{a}(t)$ and rotating with angular velocity $\mathbf{\Omega}(t)$ relative to an inertial frame. Then the fictitious forces on a fluid element are given by [55]

$$\mathbf{F}_{\mathrm{fict}} = -\rho \left[\mathbf{a} + 2\mathbf{\Omega} \times \mathbf{U} + \mathbf{\Omega} \times (\mathbf{\Omega} \times \mathbf{x}) + \frac{\mathrm{d}\mathbf{\Omega}}{\mathrm{d}t} \times \mathbf{x} \right], \tag{2.39}$$

where the force terms correspond to, respectively, the translational force, Coriolis force, centrifugal force, and Euler force of the non-inertial frame.

15

1. Translational force

$$\mathbf{F}_{\text{translational}} = -\rho \mathbf{a} \tag{2.40}$$

2. Coriolis force

$$\mathbf{F}_{\text{Coriolis}} = -2\rho \mathbf{\Omega} \times \mathbf{U} \tag{2.41}$$

3. Centrifugal force

$$\mathbf{F}_{\text{centrifugal}} = -\rho \mathbf{\Omega} \times (\mathbf{\Omega} \times \mathbf{x}) \tag{2.42}$$

4. Euler force

$$\mathbf{F}_{\text{Euler}} = -\rho \frac{d\mathbf{\Omega}}{dt} \times \mathbf{x} \tag{2.43}$$

The Coriolis and centrifugal forces are sufficient for a fluid element relative to the Earth's surface since the Earth's angular speed is nearly constant, and the relative translational motion can be neglected [58]. Furthermore, the centrifugal force can also be written in terms of a potential gradient:

$$\mathbf{F}_{\text{centrifugal}} = -\rho \mathbf{\Omega} \times (\mathbf{\Omega} \times \mathbf{x}) = -\rho \nabla \Phi_{\text{centrifugal}}, \tag{2.44}$$

with [58]

$$\Phi_{\text{centrifugal}} = -\frac{1}{2} |\mathbf{\Omega} \times \mathbf{x}|^2. \tag{2.45}$$

Thus, the centrifugal and gravitational forces may be combined into an effective gravitational potential known as the geopotential

$$\Phi_{\text{geo}} = \Phi_{\text{grav}} + \Phi_{\text{centrifugal}} = -\mathbf{g} \cdot \mathbf{x} - \frac{1}{2} |\mathbf{\Omega} \times \mathbf{x}|^2. \tag{2.46}$$

Typically, meteorological data sets provide the geopotential which thus represents the effective gravity on Earth due to true gravity and the centrifugal force, resulting in an effective gravity perpendicular to the level surfaces of the approximately oblate spheroid of the Earth. Thus, although the centrifugal force is much smaller than the gravitational force [10, 59], it is typically incorporated with the gravitational potential and does not appear explicitly in the body force terms.

On the other hand, while the centrifugal force is much larger than the Coriolis force [10, 59], the Coriolis force should not be neglected for motions over durations on the order of the Earth's period of rotation, $L/U \gtrsim \Omega^{-1}$ [59, 60]. Thus, for sufficiently large scale motions ($L \sim 1000\,\text{km}$ and $U \sim 10\,\text{m}\,\text{s}^{-1}$) or sufficiently small velocities over short ranges ($L \sim 1\,\text{km}$

16

and $U \sim 1\,\mathrm{cm\,s^{-1}}$), the Coriolis force should be considered with the geopotential or pressure gradients.

Then combining Eqs. 2.41 and 2.46 for the Coriolis, centrifugal, and gravitational forces, the force per unit volume observed in the non-inertial frame of the Earth's surface on an element is

$$F_{\mathrm{b},i} = -\rho \frac{\partial \Phi_{\mathrm{geo}}}{\partial x_i} - 2\rho \varepsilon_{ijk} \Omega_j U_k, \qquad (2.47)$$

where ε_{ijk} is the Levi-Civita tensor.

2.2.3.4 Navier-Stokes Equation

Substituting Eqs. 2.20, 2.34, and 2.47 into Eq. 2.15, we obtain the incompressible Navier-Stokes equation in the non-inertial frame of the Earth's surface:

$$\frac{\mathrm{D}U_i}{\mathrm{D}t} = \frac{1}{\rho} F_i = -\frac{1}{\rho} \frac{\partial P}{\partial x_i} + \nu \nabla^2 U_i - 2\varepsilon_{ijk} \Omega_j U_k, \qquad (2.48)$$

where $\mathbf{F} = \nabla \cdot \boldsymbol{\sigma} + \mathbf{F}_{\mathrm{b}}$ is the force per unit volume, $P = p + \rho \Phi_{\mathrm{geo}}$ is the modified pressure, and $\nu \equiv \mu/\rho$ is the kinematic viscosity. When considering small scale motions, the Coriolis force may be neglected compared to the modified pressure and viscous forces.

2.2.3.5 Pressure in an Incompressible Fluid

Typically the pressure is related to the thermodynamic properties of density and temperature through an equation of state. However, in the case of an incompressible fluid, density and pressure are unrelated, and one must use a different equation for describing pressure [39]. This equation for pressure can be derived by taking the divergence of Eq. 2.48:

$$\frac{\partial}{\partial x_i} \left(\frac{\mathrm{D}U_i}{\mathrm{D}t} \right) = \frac{1}{\rho} \nabla \cdot \mathbf{F}$$

$$\Rightarrow \frac{\partial \Delta}{\partial t} + \frac{\partial}{\partial x_i} \left(U_j \frac{\partial U_i}{\partial x_j} \right) = -\frac{1}{\rho} \nabla^2 P + \nu \nabla^2 \Delta - 2\nabla \cdot (\boldsymbol{\Omega} \times \mathbf{U})$$

$$\Rightarrow \frac{\partial \Delta}{\partial t} + U_j \frac{\partial \Delta}{\partial x_j} + \frac{\partial U_j}{\partial x_i} \frac{\partial U_i}{\partial x_j} = -\frac{1}{\rho} \nabla^2 P + \nu \nabla^2 \Delta - 2\nabla \cdot (\boldsymbol{\Omega} \times \mathbf{U})$$

$$\Rightarrow \left(\frac{\mathrm{D}}{\mathrm{D}t} - \nu \nabla^2 \right) \Delta = -\frac{1}{\rho} \nabla^2 P - \frac{\partial U_j}{\partial x_i} \frac{\partial U_i}{\partial x_j} - 2\nabla \cdot (\boldsymbol{\Omega} \times \mathbf{U}). \qquad (2.49)$$

With the initial and boundary conditions $\Delta = 0$, the solution is $\Delta = 0$ if and only if the right-hand side of Eq. 2.49 is zero. Then the modified pressure satisfies a Poisson equation

with a source term $S(\mathbf{x}, t)$ based on velocity gradients and the Coriolis force:

$$\nabla^2 P = S(\mathbf{x}, t) = -\rho \frac{\partial U_j}{\partial x_i} \frac{\partial U_i}{\partial x_j} - 2\rho \nabla \cdot (\mathbf{\Omega} \times \mathbf{U}). \tag{2.50}$$

One can then use the usual approaches for solving Poisson's equation for the pressure such as using Green's function.

2.2.4 Conservation of Energy

Conservation of energy can take many forms, depending on which form of energy one considers: kinetic, internal, total or mechanical, enthalpy, or entropy. The kinetic energy can easily be derived from the momentum conservation law, while the latter forms rely on equations of thermodynamics. In particular, multiplying Eq. 2.15 by U_i and using Eq. 2.20 yields the kinetic energy conservation equation [55]

$$U_i \frac{\mathrm{D}U_i}{\mathrm{D}t} = \frac{\mathrm{D}}{\mathrm{D}t} \left(\frac{1}{2} \mathbf{U}^2 \right) = \frac{U_i}{\rho} \frac{\partial \sigma_{ij}}{\partial x_j} + \frac{U_i F_{\mathrm{b},i}}{\rho}, \tag{2.51}$$

where $E_{\mathrm{kin}} = U_i U_i / 2 = \mathbf{U}^2 / 2$ is the kinetic energy per unit mass. This equation describes the change in kinetic energy due to work done by both surface and body forces,

$$W_{\mathrm{kin}} = \frac{U_i}{\rho} \frac{\partial \sigma_{ij}}{\partial x_j} + \frac{U_i F_{\mathrm{b},i}}{\rho}. \tag{2.52}$$

To account for heat transfer across the fluid element boundary, we use the first law of thermodynamics [55]:

$$\Delta E = Q + W_{\mathrm{int}}, \tag{2.53}$$

where E is the internal energy per unit mass, Q is the heat gain per unit mass, and W_{int} is the work per unit mass on the fluid element resulting in changes in internal energy alone. That is, W_{int} excludes work to change the kinetic energy of the fluid element. The Δ symbol used in Eq. 2.53 signifies a change in E and is distinct from the volumetric strain rate $\Delta \equiv e_{ii}$ defined in Eq. 2.25. Heat gain can come from several sources such as radiative exchange, molecular conduction, phase changes, chemical reactions, and viscous dissipation. For simplicity, we consider only molecular conduction $Q = Q_{\mathrm{cond}}$, for which the heat flux is proportional to the fluid temperature gradient [61],

$$\mathbf{q}_{\mathrm{cond}} = -k_{\mathrm{T}} \nabla T, \tag{2.54}$$

where k_{T} and T are the fluid element thermal conductivity and temperature, respectively.

Then the heat gain per unit mass of a fluid element due to molecular conduction is [55]

$$Q_{\text{cond}} = -\frac{1}{\rho}\nabla \cdot \mathbf{q}_{\text{cond}} = \frac{1}{\rho}\frac{\partial}{\partial x_i}\left(k_{\text{T}}\frac{\partial T}{\partial x_i}\right). \tag{2.55}$$

The work done on the fluid element not resulting in kinetic energy change to the fluid element is work which results in deformation of the fluid element alone [55]

$$W_{\text{int}} = \frac{\sigma_{ij}}{\rho}\frac{\partial U_i}{\partial x_j} = \frac{\sigma_{ij}e_{ij}}{\rho}. \tag{2.56}$$

Thus, substituting Eqs. 2.55 and 2.56 into Eq. 2.53, the internal energy conservation equation is given by [55]

$$\frac{\text{D}E}{\text{D}t} = Q + W_{\text{int}} = \frac{\sigma_{ij}e_{ij}}{\rho} + \frac{1}{\rho}\frac{\partial}{\partial x_i}\left(k_{\text{T}}\frac{\partial T}{\partial x_i}\right), \tag{2.57}$$

Substituting Eq. 2.26b into Eq. 2.57 then yields [55]

$$\frac{\text{D}E}{\text{D}t} = -\frac{p\Delta}{\rho} + \frac{\zeta\Delta^2}{\rho} + \dot{E}_\nu + \frac{1}{\rho}\frac{\partial}{\partial x_i}\left(k_{\text{T}}\frac{\partial T}{\partial x_i}\right), \tag{2.58}$$

where we have defined the mechanical energy dissipation rate due to viscous shear forces $\dot{E}_\nu = \text{d}E_\nu/\text{d}t$ as [55]

$$\dot{E}_\nu = 2\nu\left(e_{ij}e_{ij} - \frac{1}{3}\Delta^2\right) = 2\nu\left(e_{ij} - \frac{1}{3}\Delta\delta_{ij}\right)^2. \tag{2.59}$$

This term is the result of molecular transport of momentum leading to simple shearing motion and friction in the usual sense. The first and second terms on the right-hand side of Eq. 2.58 account for, respectively, the reversible transformation of energy due to thermodynamic pressure and the mechanical energy dissipation due to rapid expansion or compression. This second dissipation term arises due to a time lag between expansion or compression and the reestablishment of thermodynamic equilibrium of the molecules [55, 56]. As discussed in section 2.2.3.2 Eq. 2.27, the Stokes assumption for the bulk or second viscosity $\zeta = 0$ is a good approximation for cases of interest to us, allowing us to neglect the second term.

The second law of thermodynamics relates the change in entropy per unit mass δS to the heat change δQ [55]

$$T\delta S = \delta Q. \tag{2.60}$$

Then using Maxwell's thermodynamic relations, one can relate the entropy change to internal

energy, density, temperature, and pressure changes [55, 57, 58, 61]

$$T\frac{\mathrm{D}S}{\mathrm{D}t} = \frac{\mathrm{D}E}{\mathrm{D}t} + p\frac{\mathrm{D}(1/\rho)}{\mathrm{D}t} = c_{\mathrm{p}}\frac{\mathrm{D}T}{\mathrm{D}t} - \frac{\alpha T}{\rho}\frac{\mathrm{D}p}{\mathrm{D}t}, \tag{2.61}$$

where $c_{\mathrm{p}} \equiv T(\partial S/\partial T)_p$ is the specific heat capacity, and $\alpha = -\rho^{-1}(\partial\rho/\partial T)_p$ is the coefficient of thermal expansion. Combining Eq. 2.61 with the use of mass conservation Eq. 2.13, Eq. 2.58 can be written as [55, 58, 61]

$$T\frac{\mathrm{D}S}{\mathrm{D}t} = c_{\mathrm{p}}\frac{\mathrm{D}T}{\mathrm{D}t} - \frac{\alpha T}{\rho}\frac{\mathrm{D}p}{\mathrm{D}t} = \frac{\zeta\Delta^2}{\rho} + \dot{E}_\nu + \frac{1}{\rho}\frac{\partial}{\partial x_i}\left(k_{\mathrm{T}}\frac{\partial T}{\partial x_i}\right). \tag{2.62}$$

Thus, the temperature is modeled as a partial differential equation (PDE) with source terms based on the pressure, density, and velocity. Together with the mass and momentum conservation equations 2.11 and 2.15, this makes up a total of five equations for our six dependent variables. The final scalar equation then comes from the thermodynamic equation of state.

2.2.5 Equation of State

The equation of state is a thermodynamic equation which relates three thermodynamic state variables to each other. It is necessary to completely describe the fluid flow using the six dependent variables density ρ, velocity $\mathbf{U}$, pressure p, and temperature T. The most common choice of thermodynamic state variables is ρ, p, and T, and the most general equation of state for a fluid of fixed composition is written as [55, 58]

$$f(\rho, p, T) = 0, \tag{2.63}$$

where f is a function appropriate for the fluid. Common choices for a functional relationship are:

- Ideal gas law [53, 61]
$$p = \rho R T_{\mathrm{v}}, \tag{2.64}$$
  where $R = R_*/M_{\mathrm{air}} = 287.058\,\mathrm{J\,kg^{-1}\,K^{-1}}$ is the specific gas constant for dry air, and $T_{\mathrm{v}} \equiv T(1 - q + q/\epsilon)$ is the absolute virtual temperature, with water vapor mixing ratio $q = \rho_{\mathrm{v}}/\rho$ and water vapor to dry air molar mass ratio $\epsilon = M_{\mathrm{v}}/M_{\mathrm{air}} = R/R_{\mathrm{v}} = 0.62197$.

- Boussinesq fluid [62]
$$\rho = \rho_0\left[1 - \alpha\left(T - T_0\right)\right], \tag{2.65}$$

where ρ_0 and T_0 are initial values of the temperature and density, respectively, and α is the coefficient of thermal expansion.

There are more sophisticated equations of state such as the cubic Van der Waals equation and its variations, but for purposes of modeling air in the atmospheric boundary layer, the ideal gas law Eq. 2.64 is a reasonable choice [53]. In fact, even the ideal gas law for dry air without the use of the virtual temperature is a reasonable approximation in many cases [61].

2.2.6 Scalar Conservation

In addition to the physical conservation laws above, one can model a conserved passive scalar quantity denoted $\varphi = \varphi(\mathbf{x}, t)$ using the advection-diffusion equation with source term S,

$$\frac{\partial \varphi}{\partial t} + \frac{\partial}{\partial x_i} \left(U_i \varphi \right) = \frac{\partial}{\partial x_i} \left(\Gamma \frac{\partial \varphi}{\partial x_i} \right) + S. \tag{2.66}$$

Here ϕ might represent the mass concentration of a species in the atmosphere or a small temperature excess, in which case Γ is the molecular diffusivity or thermal diffusivity, respectively [10]. Since it is passive, it should have no effect on the material properties such as ρ, ν, and Γ. The source term might account for processes such as chemical reactions or volumetric material sources. For a constant-property, incompressible flow, Eq. 2.66 simplifies [10, 39] to

$$\frac{\mathrm{D}\varphi}{\mathrm{D}t} = \frac{\partial \varphi}{\partial t} + U_i \frac{\partial \varphi}{\partial x_i} = \Gamma \nabla^2 \varphi + S. \tag{2.67}$$

2.3 Random Fields and Random Processes

In principle, one could use the conservation laws in section 2.2 to describe completely the turbulent fluid flow in the atmosphere. This would require resolving all space and time scales of the turbulent motion as is done by e.g. DNS [39]. However, since the structure of turbulent fluid flows is highly complex, sharp, and irregular, this is entirely impractical for high Reynolds number flows [39, 54]. In the atmospheric surface layer, the Reynolds number is on the order of Re $\sim 10^7$, while in the mixed layer, it is even larger [53]. Thus, we must instead use a statistical description of the dependent variables in turbulent atmospheric fluids. In particular, these dependent variables can be described using probability density functions (PDFs) which vary in time and space, and we can then consider moments such as the mean and variance of these variables. In the case of Lagrangian particle dispersion models such as FLEXPART and HYSPLIT, the meteorological data supplies the mean fluid flow fields as described in Chapter 5 using sophisticated models of the conservation laws for a compressible

21

fluid. Then the turbulent components can be modeled using a stochastic model, which for FLEXPART and HYSPLIT is a Langevin model based on the incompressible Navier-Stokes equation, as described in Chapter 3.

2.3.1 Probability Distribution Functions and Expected Values

The dependent quantities described in section 2.2, i.e. $(\rho, \mathbf{U}, p, \varphi)$, can be treated as random variables. Formally [63–66], let $Z_i : \Omega_0 \to \mathbb{R}$ for $i = 1, \ldots, n$ be random variables on a probability space $(\Omega_0, \mathcal{F}_0, \mathbb{P}_{Z_i}) = (\mathbb{R}, \mathcal{B}(\mathbb{R}), \mathbb{P}_{Z_i})$ taking values in measurable space $(\mathbb{R}, \mathcal{B}(\mathbb{R}))$. These random variables each represent an individual scalar component of the set of dependent variables. Then define the n-dimensional random vector or multivariate random variable $\mathbf{Z}(\omega) = (Z_1(\omega_1), \ldots, Z_n(\omega_n)) : \Omega \to \mathbb{R}^n$ on the probability space $(\Omega, \mathcal{F}, \mathbb{P}) = (\mathbb{R}^n, \mathcal{B}(\mathbb{R}^n), \mathbb{P}_{\mathbf{Z}})$ taking values in the measurable product space $\bigotimes_{i=1}^n (\mathbb{R}, \mathcal{B}(\mathbb{R})) = (\mathbb{R}^n, \bigotimes_{i=1}^n \mathcal{B}(\mathbb{R})) = (\mathbb{R}^n, \mathcal{B}(\mathbb{R}^n))$. This random vector $\mathbf{Z}$ could represent any subset of the set of dependent variable scalar components such as $\mathbf{Z} = \mathbf{U}$ or $\mathbf{Z} = (\rho, \mathbf{U}, p, \varphi)$. Furthermore, the random variable $\mathbf{Z}$ is defined as the value of the outcome itself: $\mathbf{Z}(\omega) = \omega$, where $\omega \in \Omega = \mathbb{R}^n$.

Then the joint and marginal distributions of $\mathbf{Z}$ and Z_i are, respectively, [63]

$$\mu_{\mathbf{Z}}(A) = \mathbb{P}_{\mathbf{Z}} \left(\{ \mathbf{Z} \in A \} \right), \quad A \in \mathcal{B}(\mathbb{R}^n), \tag{2.68}$$

and, for $A_i \in \mathcal{B}(\mathbb{R})$ for $i = 1, ..., n$,

$$\mu_{Z_i}(A_i) = \mathbb{P}_{Z_i} \left(\{ Z_i \in A_i \} \right) = \mu_{\mathbf{Z}} \left(\mathbb{R}^{i-1} \times A_i \times \mathbb{R}^{n-i} \right). \tag{2.69}$$

Let $\hat{\mathbf{Z}} \in \mathbb{R}^n$ be an independent[3] variable of the measurable state space for $\mathbf{Z}$. Then the cumulative distribution function (CDF) of $\mathbf{Z}$ is defined as

$$
\begin{aligned}
F_{\mathbf{Z}}(\hat{\mathbf{Z}}) = F_{\mathbf{Z}}(\hat{Z}_1, \ldots, \hat{Z}_n) &\equiv \mu_{\mathbf{Z}} \left(\left[-\infty, \hat{Z}_1 \right] \times \cdots \times \left[-\infty, \hat{Z}_n \right] \right) \\
&= \int_{-\infty}^{\hat{Z}_1} \cdots \int_{-\infty}^{\hat{Z}_n} f_{\mathbf{Z}}(\hat{Z}_1', \ldots, \hat{Z}_n') \mathrm{d}\hat{Z}_1' \cdots \mathrm{d}\hat{Z}_n'
\end{aligned}
\tag{2.70}
$$

where

$$f_{\mathbf{Z}}(\hat{\mathbf{Z}}) = f_{\mathbf{Z}}(\hat{Z}_1, \ldots, \hat{Z}_n) = \frac{\partial^n F_{\mathbf{Z}}(\hat{Z}_1, \ldots, \hat{Z}_n)}{\partial \hat{Z}_1 \cdots \partial \hat{Z}_n} \tag{2.71}$$

is the probability density function (PDF) of $\mathbf{Z}$. If (and only if) the random variables $Z_1, \ldots, Z_n$ are independent, the joint CDF $F_{\mathbf{Z}}(\hat{\mathbf{Z}})$ and joint PDF are given by the products

---

[3]Independent here refers to a freely varying input as opposed to the dependent output.

of the marginal functions:

$$F_{\mathbf{Z}}(\hat{Z}_1, \ldots, \hat{Z}_n) = F_{Z_1}(\hat{Z}_1) \times \cdots \times F_{Z_n}(\hat{Z}_n) = \prod_{i=1}^{n} F_{Z_i}(\hat{Z}_i), \tag{2.72a}$$

$$f_{\mathbf{Z}}(\hat{Z}_1, \ldots, \hat{Z}_n) = f_{Z_1}(\hat{Z}_1) \times \cdots \times f_{Z_n}(\hat{Z}_n) = \prod_{i=1}^{n} f_{Z_i}(\hat{Z}_i), \tag{2.72b}$$

where

$$F_{Z_i}(\hat{Z}_i) = \int_{\mathbb{R}} \cdots \int_{-\infty}^{\hat{Z}_i} \cdots \int_{\mathbb{R}} f_{\mathbf{Z}}(\hat{Z}_1', \ldots, \hat{Z}_i', \ldots, \hat{Z}_n') \mathrm{d}\hat{Z}_1' \cdots \mathrm{d}\hat{Z}_i' \cdots \mathrm{d}\hat{Z}_n'$$

$$= \int_{-\infty}^{\hat{Z}_i} f_{Z_i}(\hat{Z}_i') \mathrm{d}\hat{Z}_i' \tag{2.73a}$$

$$f_{Z_i}(\hat{Z}_i) = \int_{\mathbb{R}^{n-1}} f_{\mathbf{Z}}(\hat{Z}_1', \ldots, \hat{Z}_{i-1}', \hat{Z}_i, \hat{Z}_{i+1}', \ldots, \hat{Z}_n') \mathrm{d}\hat{Z}_1' \cdots \mathrm{d}\hat{Z}_{i-1}' \mathrm{d}\hat{Z}_{i+1}' \cdots \mathrm{d}\hat{Z}_n', \tag{2.73b}$$

for $i = 1, \ldots, n$ are the marginal CDF and PDF of Z_i, respectively.

The distribution of $\mathbf{Z}$ conditioned on $B \in \mathcal{B}(\mathbb{R}^n)$ is defined as [66]

$$\mu_{\mathbf{Z}|B}\left(A\middle|B\right) = \mathbb{P}_{\mathbf{Z}|B}\left(\{\mathbf{Z} \in A\}\middle|B\right) = \frac{\mathbb{P}_{\mathbf{Z}}\left(\{\mathbf{Z} \in A \cap B\}\right)}{\mathbb{P}_{\mathbf{Z}}\left(\{\mathbf{Z} \in B\}\right)} = \frac{\mu_{\mathbf{Z}}(A \cap B)}{\mu_{\mathbf{Z}}(B)}. \tag{2.74}$$

where $\mu_{\mathbf{Z}}(B) > 0$. Then, for example, the conditional CDF and PDF, respectively, of Z_1 conditioned on $Z_2 = \hat{Z}_2$ are [45, 66]

$$F_{Z_1|Z_2}\left(\hat{Z}_1\middle|\hat{Z}_2\right) = \frac{\int_{-\infty}^{\hat{Z}_1} f_{Z_1,Z_2}(\hat{Z}_1', \hat{Z}_2)\mathrm{d}\hat{Z}_1'}{f_{Z_2}(\hat{Z}_2)} \tag{2.75a}$$

$$f_{Z_1|Z_2}\left(\hat{Z}_1\middle|\hat{Z}_2\right) = \frac{f_{Z_1,Z_2}(\hat{Z}_1, \hat{Z}_2)}{f_{Z_2}(\hat{Z}_2)} \tag{2.75b}$$

where $f_{Z_1,Z_2}(\hat{Z}_1, \hat{Z}_2)$ is the joint PDF of (Z_1, Z_2). More concretely, with $\mathbf{Z} = (\mathbf{U}, \varphi)$, the conditional PDF of φ conditioned on $\mathbf{U} = \hat{\mathbf{U}}$, Eq. 2.75b becomes

$$f_{\varphi|\mathbf{U}}\left(\hat{\varphi}\middle|\hat{\mathbf{U}}\right) = \frac{f_{\mathbf{U},\varphi}(\hat{\mathbf{U}}, \hat{\varphi})}{f_{\mathbf{U}}(\hat{\mathbf{U}})}. \tag{2.76}$$

Note that from Eq. 2.72b, for independent variables, the conditional PDF is equivalent to the marginal PDF.

Often we are interested in the mean (or expected) value of some function of the random variable $\mathbf{Z}$, $Q(\mathbf{Z})$. Formally, the expected value is given by [39, 63, 66]

$$\langle Q(\mathbf{Z}) \rangle \equiv \mathrm{E}\left[Q(\mathbf{Z})\right] \equiv \int_{\Omega} Q\left[\mathbf{Z}(\omega)\right] \mathbb{P}_{\mathbf{Z}}(\mathrm{d}\omega) = \int_{\mathbb{R}^n} Q(\hat{\mathbf{Z}}) f_{\mathbf{Z}}(\hat{\mathbf{Z}}) \mathrm{d}\hat{\mathbf{Z}}, \tag{2.77}$$

where here and throughout we use the notation $\langle \cdot \rangle$ to denote the mean or expected value. For example, $Q(\mathbf{Z}) = \mathbf{Z}$ corresponds to the mean of $\mathbf{Z}$, and when $\mathbf{Z} = \mathbf{U}$, we have the mean velocity:

$$\langle \mathbf{U} \rangle = \int \hat{\mathbf{U}} f_{\mathbf{U}}(\hat{\mathbf{U}}) \mathrm{d}\hat{\mathbf{U}}. \tag{2.78}$$

Similarly, defining the velocity fluctuation about the mean as $\mathbf{u} \equiv \mathbf{U} - \langle \mathbf{U} \rangle$ and letting $Q(\mathbf{U}) = \left(U_i - \langle U_i \rangle\right)\left(U_j - \langle U_j \rangle\right) = u_i u_j$, we obtain the velocity covariance function[4]

$$\mathrm{cov}\left(U_i, U_j\right) \equiv \langle u_i u_j \rangle = \int \left(\hat{U}_i - \langle U_i \rangle\right)\left(\hat{U}_i - \langle U_j \rangle\right) f_{\mathbf{U}}(\hat{\mathbf{U}}) \mathrm{d}\hat{\mathbf{U}}. \tag{2.80}$$

One can analogously calculate a conditional expected value such as $\left\langle Q(Z_1, Z_2) | Z_2 = \hat{Z}_2 \right\rangle = \left\langle Q | \hat{Z}_2 \right\rangle$ using the appropriate conditional PDF, i.e. $f_{Z_1|Z_2}(\hat{Z}_1|\hat{Z}_2)$.

2.3.2 Fine-grained PDF

One way of forming the PDF is through the use of the fine-grained PDF [45, 67], which is defined as

$$f'_{\mathbf{Z}}(\hat{\mathbf{Z}}) = \delta(\mathbf{Z} - \hat{\mathbf{Z}}) = \prod_{i=1}^{n} \delta(Z_i - \hat{Z}_i), \tag{2.81}$$

where $\delta(\mathbf{Z})$ is the Dirac delta function defined through the identity $\int_{\mathbb{R}^n} \delta(\mathbf{Z}) \mathrm{d}\mathbf{Z} = 1$. The fine-grained PDF has the property that it is zero at all values of $\hat{\mathbf{Z}}$ except for $\hat{\mathbf{Z}} = \mathbf{Z}$. That is, it describes one possible realization of the random variable $\mathbf{Z}$. Since the fine-grained PDF is a Dirac delta function, it has all of the properties of the Dirac delta function. By definition, the fine-grained PDF is already normalized, and the PDF of $\mathbf{Z}$ is given by the expected value

---

[4]Note that the covariance is independent of a constant (i.e. deterministic) shift: given constants $z_i, z_j \in \mathbb{R}^n$,

$$\begin{aligned} \mathrm{cov}\left(Z_i + z_i, Z_j + z_j\right) &\equiv \langle \left[Z_i + z_i - \langle Z_i + z_i \rangle\right]\left[Z_j + z_j - \langle Z_j + z_j \rangle\right] \rangle \\ &= \langle \left[Z_i - \langle Z_i \rangle\right]\left[Z_j - \langle Z_j \rangle\right] \rangle \\ &\equiv \mathrm{cov}\left(Z_i, Z_j\right). \end{aligned} \tag{2.79}$$

Then for $\mathbf{Z} = \mathbf{U}$ and $\mathbf{z} = -\langle \mathbf{U} \rangle$, it immediately follows from Eq. 2.79 that $\mathrm{cov}(U_i, U_j) \equiv \langle u_i u_j \rangle = \mathrm{cov}(u_i, u_j)$.

of the fine-grained PDF [39, 45]:

$$
\begin{aligned}
\left\langle f'_{\mathbf{Z}}(\hat{\mathbf{Z}}) \right\rangle &= \left\langle \delta(\mathbf{Z} - \hat{\mathbf{Z}}) \right\rangle \\
&= \int_{\mathbb{R}^n} \delta(\hat{\mathbf{Z}}' - \hat{\mathbf{Z}}) f_{\mathbf{Z}}(\hat{\mathbf{Z}}') \mathrm{d}\hat{\mathbf{Z}}' \\
&= f_{\mathbf{Z}}(\hat{\mathbf{Z}}),
\end{aligned}
\tag{2.82}
$$

where we have used $Q(\mathbf{Z}) = f'_{\mathbf{Z}}(\hat{\mathbf{Z}}) = \delta(\mathbf{Z} - \hat{\mathbf{Z}})$ in Eq. 2.77, replacing the integration variable $\hat{\mathbf{Z}}$ with $\hat{\mathbf{Z}}'$, and we have used the Dirac delta shifting property in the final step. Additionally, we have the property that for any random variable ξ which may or may not depend on $\mathbf{Z}$, [39, 45]

$$
\begin{aligned}
\left\langle \xi f'_{\mathbf{Z}}(\hat{\mathbf{Z}}) \right\rangle &= \left\langle \xi \delta(\mathbf{Z} - \hat{\mathbf{Z}}) \right\rangle \\
&= \int \int \hat{\xi} \delta(\hat{\mathbf{Z}}' - \hat{\mathbf{Z}}) f_{\mathbf{Z},\xi}(\hat{\mathbf{Z}}', \hat{\xi}) \mathrm{d}\hat{\mathbf{Z}}' \mathrm{d}\hat{\xi} \\
&= \int \hat{\xi} f_{\mathbf{Z},\xi}(\hat{\mathbf{Z}}, \hat{\xi}) \mathrm{d}\hat{\xi} \\
&= f_{\mathbf{Z}}(\hat{\mathbf{Z}}) \int \hat{\xi} f_{\xi|\mathbf{Z}} \left(\hat{\xi} \,\middle|\, \hat{\mathbf{Z}} \right) \mathrm{d}\hat{\xi} \\
&= \left\langle \xi | \mathbf{Z} = \hat{\mathbf{Z}} \right\rangle f_{\mathbf{Z}}(\hat{\mathbf{Z}}) \\
&= \left\langle \xi | \hat{\mathbf{Z}} \right\rangle f_{\mathbf{Z}}(\hat{\mathbf{Z}}).
\end{aligned}
\tag{2.83}
$$

If ξ is independent of $\mathbf{Z}$, then $\left\langle \xi | \hat{\mathbf{Z}} \right\rangle = \langle \xi \rangle$, while if $\xi = \xi(\mathbf{Z})$, then $\left\langle \xi | \hat{\mathbf{Z}} \right\rangle = \xi(\hat{\mathbf{Z}})$. These properties make the fine-grained PDF useful for deriving PDF transport equations [39, 45] as we will show in chapter 3. Alternative methods are discussed in section 2.4.

2.3.3 Eulerian and Lagrangian PDFs

In the Eulerian field description, dependent quantities are functions of both space and time. Thus, the distributions of random dependent variables such as velocity are also functions of space and time. Taking the Eulerian velocity $\mathbf{U} = \mathbf{U}(\mathbf{x}, t)$ for example, the fine-grained Eulerian velocity PDF is [45]

$$
f'_{\mathbf{U}}(\hat{\mathbf{U}}; \mathbf{x}, t) = \delta \left[\mathbf{U}(\mathbf{x}, t) - \hat{\mathbf{U}} \right] = \prod_{i=1}^{3} \delta \left[U_i(\mathbf{x}, t) - \hat{U}_i \right],
\tag{2.84}
$$

and the Eulerian velocity PDF is $f_{\mathbf{U}}(\hat{\mathbf{U}}; \mathbf{x}, t) = \left\langle f'_{\mathbf{U}}(\hat{\mathbf{U}}; \mathbf{x}, t) \right\rangle$. The notation used here treats the space and time variables $(\mathbf{x}, t)$ after the semicolon as parameters of the distribution as opposed to independent distribution density variables before the semicolon and with hats. Thus, the Eulerian velocity in turbulent media is treated as a random variable which is parameterized by space and time.

Similarly, when using the Lagrangian description, the dependent quantities are a function of the Lagrangian particle parameters $(\mathbf{x}_0, t_0)$ and the time t. That is, for the Lagrangian particle position $\mathbf{x}(t) \equiv \mathbf{x}(\mathbf{x}_0, t_0|t)$ and velocity $\mathbf{U}(t) \equiv \mathbf{U}(\mathbf{x}_0, t_0|t) = \mathbf{U}\left[\mathbf{x}\left(\mathbf{x}_0, t_0|t\right), t\right]$, we have the fine-grained Lagrangian joint PDF [45]

$$f'_{\mathbf{U}, \mathbf{x}}\left(\hat{\mathbf{U}}, \hat{\mathbf{x}}; t \,\middle|\, \mathbf{x}_0, t_0\right) = \delta\left[\mathbf{U}(t) - \hat{\mathbf{U}}\right] \delta\left[\mathbf{x}(t) - \hat{\mathbf{x}}\right]$$
$$= \prod_{i=1}^{3} \delta\left[U_i(t) - \hat{U}_i\right] \prod_{i=1}^{3} \delta\left[x_i(t) - \hat{x}_i\right], \tag{2.85}$$

and the Lagrangian joint PDF is $f_{\mathbf{U}, \mathbf{x}}(\hat{\mathbf{U}}, \hat{\mathbf{x}}; t|\mathbf{x}_0, t_0) = \left\langle f'_{\mathbf{U}, \mathbf{x}}(\hat{\mathbf{U}}, \hat{\mathbf{x}}; t|\mathbf{x}_0, t_0) \right\rangle$. This Lagrangian joint PDF is a function of the time t and is conditional on the Lagrangian particle initial position $\mathbf{x}_0$ at time t_0. In variable density, compressible flows, the joint PDF of $\mathbf{Z} = (\mathbf{U}, \mathbf{x}, \boldsymbol{\varphi})$ may additionally be conditioned on some initial scalar conditions $\boldsymbol{\varphi}(\mathbf{x}_0, t_0|t_0) = \boldsymbol{\varphi}_0$, but for the incompressible flows of interest to us, we have the relation [45]

$$f_{\mathbf{U}}(\hat{\mathbf{U}}; \hat{\mathbf{x}}, t) = \int f_{\mathbf{U}, \mathbf{x}}\left(\hat{\mathbf{U}}, \hat{\mathbf{x}}; t \,\middle|\, \mathbf{x}_0, t_0\right) \mathrm{d}\mathbf{x}_0 \tag{2.86}$$

between the Eulerian and Lagrangian PDFs. Furthermore, there is a correspondence [39] between the Lagrangian velocity PDF conditioned on $\mathbf{x}(t) = \hat{\mathbf{x}}$

$$f_{\mathbf{U}|\mathbf{x}}\left(\hat{\mathbf{U}} \,\middle|\, \hat{\mathbf{x}}; t|\mathbf{x}_0, t_0\right) = \frac{f_{\mathbf{U}, \mathbf{x}}\left(\hat{\mathbf{U}}, \hat{\mathbf{x}}; t \,\middle|\, \mathbf{x}_0, t_0\right)}{f_{\mathbf{x}}\left(\hat{\mathbf{x}}; t \,\middle|\, \mathbf{x}_0, t_0\right)} \tag{2.87}$$

and the Eulerian velocity PDF $f_{\mathbf{U}}(\hat{\mathbf{U}}; \hat{\mathbf{x}}, t)$ when the Lagrangian position marginal PDF

$$f_{\mathbf{x}}\left(\hat{\mathbf{x}}; t \,\middle|\, \mathbf{x}_0, t_0\right) = \int f_{\mathbf{U}, \mathbf{x}}\left(\hat{\mathbf{U}}, \hat{\mathbf{x}}; t \,\middle|\, \mathbf{x}_0, t_0\right) \mathrm{d}\hat{\mathbf{U}} \tag{2.88}$$

is uniform and constant, i.e.

$$f_{\mathbf{x}}\left(\hat{\mathbf{x}}; t \,\middle|\, \mathbf{x}_0, t_0\right) = \frac{1}{V}, \tag{2.89}$$

where V is fluid volume. Since there is no correspondence to $f_{\mathbf{x}}$ in the Eulerian description,

$f_{\mathbf{x}}$ must be uniform and constant [39], so there is a correspondence between the Lagrangian velocity conditional PDF $f_{\mathbf{U}|\mathbf{x}}$ and the Eulerian velocity PDF $f_{\mathbf{U}}$—that is,

$$f_{\mathbf{U}}(\hat{\mathbf{U}}; \hat{\mathbf{x}}, t) = f_{\mathbf{U}|\mathbf{x}}\left(\hat{\mathbf{U}}\,\middle|\,\hat{\mathbf{x}}; t|\mathbf{x}_0, t_0\right) = V f_{\mathbf{U},\mathbf{x}}\left(\hat{\mathbf{U}}, \hat{\mathbf{x}}; t\,\middle|\,\mathbf{x}_0, t_0\right). \tag{2.90}$$

This allows us to use either the Eulerian or Lagrangian PDF transport equations and their moments interchangeably.

2.3.4 Random Fields and Processes

The dependent random conserved quantities are all random processes depending on a time parameter t. More specifically, since they also depend on space $\mathbf{x}$, they are random fields. We will consider them as one-point, one-time random fields, meaning that they are fully characterized by a distribution $f_{\mathbf{Z}}(\hat{\mathbf{Z}}; \mathbf{x}, t)$ at a single point in time and space $(\mathbf{x}, t)$. In contrast, letting $\{(\mathbf{x}_i, t_i)\}_{i=1,\dots,N}$ be a set of N distinct positions and times, the N-point, N-time CDF and PDF of random variable $\mathbf{Z}$ are given by [39, 45]

$$F_{\mathbf{Z}_1,\dots,\mathbf{Z}_N}(\hat{\mathbf{Z}}_1, \dots, \hat{\mathbf{Z}}_N; \mathbf{x}_1, t_1, \dots, \mathbf{x}_N, t_N) \equiv \mathbb{P}_{\mathbf{Z}_1,\dots,\mathbf{Z}_N}\left[\mathbf{Z}(\mathbf{x}_1, t_1) \leq \hat{\mathbf{Z}}_1, \dots, \mathbf{Z}(\mathbf{x}_N, t_N) \leq \hat{\mathbf{Z}}_N\right], \tag{2.91a}$$

$$f_{\mathbf{Z}_1,\dots,\mathbf{Z}_N}(\hat{\mathbf{Z}}_1, \dots, \hat{\mathbf{Z}}_N; \mathbf{x}_1, t_1, \dots, \mathbf{x}_N, t_N) = \frac{\partial^N F_{\mathbf{Z}_1,\dots,\mathbf{Z}_N}(\hat{\mathbf{Z}}_1, \dots, \hat{\mathbf{Z}}_N; \mathbf{x}_1, t_1, \dots, \mathbf{x}_N, t_N)}{\partial \hat{\mathbf{Z}}_1 \dots \partial \hat{\mathbf{Z}}_N}. \tag{2.91b}$$

The one-point, one-time PDF can be recovered from the N-point, N-time PDF by integrating over the other $N-1$ variables:

$$f_{\mathbf{Z}}(\hat{\mathbf{Z}}; \mathbf{x}, t) = \int_{\mathbb{R}^{n(N-1)}} f_{\mathbf{Z},\mathbf{Z}_2,\dots,\mathbf{Z}_N}(\hat{\mathbf{Z}}, \hat{\mathbf{Z}}_2, \dots, \hat{\mathbf{Z}}_N; \mathbf{x}, t, \mathbf{x}_2, t_2, \dots, \mathbf{x}_N, t_N) \mathrm{d}\hat{\mathbf{Z}}_2 \cdots \mathrm{d}\hat{\mathbf{Z}}_N. \tag{2.92}$$

However, the opposite is not true: there is not sufficient information in the one-point, one-time PDF to derive the N-point, N-time PDF.

It is impossible to completely describe the random turbulence field using the one-point, one-time PDF, nor is it possible to determine the N-point, N-time PDF at all positions and times [39, 45]. Thus, one cannot completely characterize the random turbulence field. By approximating the random turbulence field using the one-point, one-time PDF, we lose the information about the frequency or length scales of fluctuations [45], which must be supplied separately. The models we will discuss will supply this information separately, and so we will

only use the one-point, one-time PDF.

There are several ways to categorize and classify turbulence fields from a statistical viewpoint. A process is strictly *statistically stationary* or *statistically homogeneous* if the distribution is invariant under time or space translations, respectively. Given the N-point, N-time PDF, the random field is *statistically stationary* if for all $\Delta t, t_1, \ldots, t_N \in \mathbb{R}$

$$
\begin{aligned}
f_{\mathbf{z}_1,\ldots,\mathbf{z}_N}(\hat{\mathbf{Z}}_1, \ldots, \hat{\mathbf{Z}}_N; \mathbf{x}_1, t_1 + \Delta t, \ldots, \mathbf{x}_N, t_N + \Delta t) = \\
f_{\mathbf{z}_1,\ldots,\mathbf{z}_N}(\hat{\mathbf{Z}}_1, \ldots, \hat{\mathbf{Z}}_N; \mathbf{x}_1, t_1, \ldots, \mathbf{x}_N, t_N).
\end{aligned}
\tag{2.93}
$$

Thus, such probabilities depend only on the time differences $t_i - t_j$, and the one-time PDF is independent of time [45, 68]. Similarly, the random field is *statistically homogeneous* if for all $\Delta \mathbf{x}, \mathbf{x}_1, \ldots, \mathbf{x}_N \in \mathbb{R}^3$

$$
\begin{aligned}
f_{\mathbf{z}_1,\ldots,\mathbf{z}_N}(\hat{\mathbf{Z}}_1, \ldots, \hat{\mathbf{Z}}_N; \mathbf{x}_1 + \Delta \mathbf{x}, t_1, \ldots, \mathbf{x}_N + \Delta \mathbf{x}, t_N) = \\
f_{\mathbf{z}_1,\ldots,\mathbf{z}_N}(\hat{\mathbf{Z}}_1, \ldots, \hat{\mathbf{Z}}_N; \mathbf{x}_1, t_1, \ldots, \mathbf{x}_N, t_N),
\end{aligned}
\tag{2.94}
$$

with such probabilities depending only on position differences $\mathbf{x}_i - \mathbf{x}_j$, and the one-point PDF being independent of space $\mathbf{x}$ altogether [45]. If the conditional probability of future states of a random process conditioned on the past and present values depends only on the present state, the process has the *Markov property* and is said to be *Markovian* or a *Markov process*. In particular, letting $t_1 \leq \cdots \leq t_i \leq t_{i+1} \leq \cdots \leq t_N$, then $\mathbf{Z}(t)$ is a Markov process if [68]

$$
\begin{aligned}
f_{\mathbf{z}_{i+1},\ldots,\mathbf{z}_N|\mathbf{z}_1,\ldots,\mathbf{z}_i}\left(\hat{\mathbf{Z}}_{i+1}, \ldots, \hat{\mathbf{Z}}_N; t_{i+1}, \ldots, t_N \middle| \hat{\mathbf{Z}}_1, \ldots, \hat{\mathbf{Z}}_i; t_1, \ldots, t_i\right) = \\
f_{\mathbf{z}_{i+1},\ldots,\mathbf{z}_N|\mathbf{z}_i}\left(\hat{\mathbf{Z}}_{i+1}, \ldots, \hat{\mathbf{Z}}_N; t_{i+1}, \ldots, t_N \middle| \hat{\mathbf{Z}}_i; t_i\right).
\end{aligned}
\tag{2.95}
$$

As a consequence of the Markov property and the definition of conditional probability, one can thus construct arbitrary joint probability functions using a sequential chain of conditional probabilities [68, 69]:

$$
\begin{aligned}
f_{\mathbf{z}_1,\ldots,\mathbf{z}_i}(\hat{\mathbf{Z}}_1, \ldots, \hat{\mathbf{Z}}_i; t_1, \ldots, t_i) = f_{\mathbf{Z}|\mathbf{Z}}\left(\hat{\mathbf{Z}}_i; t_i \middle| \hat{\mathbf{Z}}_{i-1}; t_{i-1}\right) \\
f_{\mathbf{Z}|\mathbf{Z}}\left(\hat{\mathbf{Z}}_{i-1}; t_{i-1} \middle| \hat{\mathbf{Z}}_{i-2}; t_{i-2}\right) \cdots f_{\mathbf{Z}|\mathbf{Z}}\left(\hat{\mathbf{Z}}_2; t_2 \middle| \hat{\mathbf{Z}}_1; t_1\right) f_{\mathbf{Z}}(\hat{\mathbf{Z}}_1; t_1),
\end{aligned}
\tag{2.96}
$$

for $1 \leq i \leq N$. Thus, the N-time joint PDF for a Markov process depends only on the conditional PDF $f_{\mathbf{Z}|\mathbf{Z}}(\hat{\mathbf{Z}}_i; t_i | \hat{\mathbf{Z}}_{i-1}; t_{i-1})$ and the one-time PDF $f_{\mathbf{Z}}(\hat{\mathbf{Z}}; t)$. Finally, a random field is said to be *statistically isotropic* if its distribution is invariant under rotations or reflections.

If the velocity field $\mathbf{U}(\mathbf{x}, t)$ is statistically homogeneous and described using a one-point PDF, $\langle \mathbf{U}(\mathbf{x}, t) \rangle$ is spatially uniform and one can choose an inertial frame for which $\langle \mathbf{U}(\mathbf{x}, t) \rangle = 0$. In contrast, sometimes the notion of *homogeneous turbulence* is used to describe the less-restrictive condition that the fluctuating velocity $\mathbf{u}(\mathbf{x}, t) \equiv \mathbf{U}(\mathbf{x}, t) - \langle \mathbf{U}(\mathbf{x}, t) \rangle$ is statistically homogeneous. In this case, the mean velocity gradient $\partial \langle U_i \rangle / \partial x_j$ may be nonzero but uniform [39]. Many flows of interest are statistically stationary and homogeneous in one or two dimensions [45]. While turbulence is generally anisotropic, many simplifications result from considering isotropic turbulence models, and isotropic turbulence has been studied much more extensively [39].

2.3.5 Reynolds Decomposition and Averaging

As might be apparent from the discussions in sections 2.3.1 and 2.3.4, the mean or expected value $\langle \mathbf{Z}(\mathbf{x}, t) \rangle$ of a random field $\mathbf{Z}(\mathbf{x}, t)$ is important for studying turbulence models. Additionally, one is often interested in examining the fluctuation about the mean alone:

$$\mathbf{Z}'(\mathbf{x}, t) \equiv \mathbf{Z}(\mathbf{x}, t) - \langle \mathbf{Z}(\mathbf{x}, t) \rangle. \tag{2.97}$$

Rearranging Eq. 2.97, it is common to separate a random field $\mathbf{Z}(\mathbf{x}, t)$ into a mean component $\langle \mathbf{Z}(\mathbf{x}, t) \rangle$ and turbulent or fluctuating component $\mathbf{Z}'(\mathbf{x}, t)$ as

$$\mathbf{Z}(\mathbf{x}, t) \equiv \langle \mathbf{Z}(\mathbf{x}, t) \rangle + \mathbf{Z}'(\mathbf{x}, t). \tag{2.98}$$

This process is sometimes called a Reynolds decomposition, and it allows one to derive conservation laws or equations of balance for both the mean and turbulent components individually as we will do in chapter 3. In the case of the velocity, we have chosen to use the notation

$$\mathbf{U}(\mathbf{x}, t) \equiv \langle \mathbf{U}(\mathbf{x}, t) \rangle + \mathbf{u}(\mathbf{x}, t), \tag{2.99}$$

where $\mathbf{u}(\mathbf{x}, t)$ is the turbulent component so that we can avoid using the prime symbol repeatedly or in combination with exponents.

Section 2.3.1 defined the $\langle \cdot \rangle$ operator as the expected value in terms of the PDF according to Eq. 2.77. This is correct from a purely theoretical viewpoint, but it is not possible to actually measure the PDF, so one often approximates the expected value using alternative averages. Common choices are [45]:

- Ensemble average for flows that can be repeated with several realizations

$$\langle Q\left[\mathbf{Z}(\mathbf{x},t)\right]\rangle_N \equiv \frac{1}{N}\sum_{i=1}^{N} Q\left[\mathbf{Z}^{(i)}(\mathbf{x},t)\right]. \tag{2.100}$$

- Time average for statistically stationary fields

$$\langle Q\left[\mathbf{Z}(\mathbf{x},t)\right]\rangle_{t_k} \equiv \frac{1}{\Delta t_k}\int_{t_k}^{t_k+\Delta t_k} Q\left[\mathbf{Z}(\mathbf{x},t')\right]\mathrm{d}t'. \tag{2.101}$$

- Spatial average for statistically homogeneous fields

$$\langle Q\left[\mathbf{Z}(\mathbf{x},t)\right]\rangle_{V_k} \equiv \frac{1}{V_k}\int_{V_k} Q\left[\mathbf{Z}(\mathbf{x}',t)\right]\mathrm{d}\mathbf{x}'. \tag{2.102}$$

One can define similar spatial averages for fields statistically homogeneous in one or two dimensions.

Equations 2.100 through 2.102 are themselves random variables since $Q(\mathbf{Z})$ is a random variable. One can then estimate the true expected value as

$$\langle Q\left[\mathbf{Z}(\mathbf{x},t)\right]\rangle = \mathrm{E}\left\{\langle Q\left[\mathbf{Z}(\mathbf{x},t)\right]\rangle_N\right\},$$

or similarly using any of the averaging methods. By the central limit theorem, as the number of realizations $N \to \infty$, the estimated mean will approach the true expected value with a statistical error $\varepsilon_N = O(N^{-1/2})$. This is the error expected from a purely Monte Carlo method, but depending on factors such as the averaging kernel or the Lagrangian particle distribution, the actual error convergence rate could be faster or slower than this [39, 70–72].

2.4   Stochastic Balance and Langevin Equations

In section 2.3 we discussed the general description of random fields and processes through the use of distributions and their expected values. While the PDF $f_{\mathbf{Z}}(\hat{\mathbf{Z}};t)$ provides a description for the random variable $\mathbf{Z}(t)$, we need to have a physical and mathematical model for the evolution of the PDF and the stochastic state. We will derive several different forms of mathematical models under the assumption that $\mathbf{Z}(t)$ is a Markov process, which is to say that the state transitions $\hat{\mathbf{Z}}' \to \hat{\mathbf{Z}}$ depend only on the current state $\hat{\mathbf{Z}}'$, and the system is said to be memoryless. The forms we will discuss are the general Master equation and its Kramers–Moyal expansion, the Fokker-Planck equation, and the Langevin equation.

Under some simple assumptions, all of these forms can be treated as equivalent methods for describing the evolution of the stochastic state $\mathbf{Z}(t)$.

2.4.1 Master Equation

Perhaps the most general description of a Markov process for a memoryless system in equilibrium is the Master equation. The Master equation is a general balance equation for the probability density $f_{\mathbf{Z}}(\hat{\mathbf{Z}}; t)$ for system state $\hat{\mathbf{Z}}$ at time t, where $\mathbf{Z}(t)$ is a Markov process. It is the differential form of the Chapman–Kolmogorov equation which describes the gain and loss processes for the system state in terms of a transition probability rate $W(\hat{\mathbf{Z}}|\hat{\mathbf{Z}}'; t)$ and which models the temporal evolution of the PDF $f_{\mathbf{Z}}$. Using a Taylor series expansion called the Kramers–Moyal expansion, the Master equation can be cast into the form of a partial differential equation with series coefficients given by moments of the transition rate.

2.4.1.1 Chapman–Kolmogorov Equation

The Chapman–Kolmogorov equation starts with the three-time joint PDF written in terms of the conditional probabilities according to Eq. 2.96

$$f_{\mathbf{Z},\mathbf{Z},\mathbf{Z}}(\hat{\mathbf{Z}}_1, \hat{\mathbf{Z}}_2, \hat{\mathbf{Z}}_3; t_1, t_2, t_3) = f_{\mathbf{Z}|\mathbf{Z}}\left(\hat{\mathbf{Z}}_3; t_3 \middle| \hat{\mathbf{Z}}_2; t_2\right) f_{\mathbf{Z}|\mathbf{Z}}\left(\hat{\mathbf{Z}}_2; t_2 \middle| \hat{\mathbf{Z}}_1; t_1\right) f_{\mathbf{Z}}(\hat{\mathbf{Z}}_1; t_1), \quad (2.103)$$

where $t_1 \leq t_2 \leq t_3$. Integrating Eq. 2.103 over $\hat{\mathbf{Z}}_2$ yields the marginal distribution $f_{\mathbf{Z},\mathbf{Z}}(\hat{\mathbf{Z}}_1, \hat{\mathbf{Z}}_3; t_1, t_3)$, and dividing by $f_{\mathbf{Z}}(\hat{\mathbf{Z}}_1; t_1)$ yields the conditional distribution [69]

$$f_{\mathbf{Z}|\mathbf{Z}}\left(\hat{\mathbf{Z}}_3; t_3 \middle| \hat{\mathbf{Z}}_1; t_1\right) = \int f_{\mathbf{Z}|\mathbf{Z}}\left(\hat{\mathbf{Z}}_3; t_3 \middle| \hat{\mathbf{Z}}_2; t_2\right) f_{\mathbf{Z}|\mathbf{Z}}\left(\hat{\mathbf{Z}}_2; t_2 \middle| \hat{\mathbf{Z}}_1; t_1\right) d\hat{\mathbf{Z}}_2. \quad (2.104)$$

This is called the *Chapman–Kolmogorov equation* which relates all conditional probabilities $f_{\mathbf{Z}|\mathbf{Z}}\left(\hat{\mathbf{Z}}_i; t_i \middle| \hat{\mathbf{Z}}_j; t_j\right)$, and it is satisfied by all Markov processes.

2.4.1.2 Master Equation

The Master equation is derived from the Chapman–Kolmogorov Eq. 2.104 in the limit of vanishing time differences between state transitions. That is, it is an integro-differential equation for the time evolution of state probabilities. This makes the Master equation easier to work with and more relevant to physical systems [69]. van Kampen [69] derives it starting with a (temporally) homogeneous Markov process, for which transition probabilities depend only on the time difference, while Gardiner [68] uses a somewhat different approach which divides the transitions into continuous and discontinuous components.

Let

$$W\left(\hat{\mathbf{Z}}\middle|\hat{\mathbf{Z}}';t\right) \equiv \lim_{\Delta t \to 0} \frac{1}{\Delta t} f_{\mathbf{Z}|\mathbf{Z}}\left(\hat{\mathbf{Z}};t+\Delta t\middle|\hat{\mathbf{Z}}';t\right) \tag{2.105}$$

be the transition probability per unit time from state $\hat{\mathbf{Z}}'$ at time t to another state $\hat{\mathbf{Z}}$ at time $t + \Delta t$. Then the *Master equation* is [68, 69]

$$\frac{\partial f_{\mathbf{Z}|\mathbf{Z}}\left(\hat{\mathbf{Z}};t\middle|\hat{\mathbf{Z}}_0;t_0\right)}{\partial t} = \int \left[W\left(\hat{\mathbf{Z}}\middle|\hat{\mathbf{Z}}';t\right) f_{\mathbf{Z}|\mathbf{Z}}\left(\hat{\mathbf{Z}}';t\middle|\hat{\mathbf{Z}}_0;t_0\right) \right.$$
$$\left. - W\left(\hat{\mathbf{Z}}'\middle|\hat{\mathbf{Z}};t\right) f_{\mathbf{Z}|\mathbf{Z}}\left(\hat{\mathbf{Z}};t\middle|\hat{\mathbf{Z}}_0;t_0\right) \right] d\hat{\mathbf{Z}}', \tag{2.106}$$

with initial condition

$$\lim_{t \to t_0^+} f_{\mathbf{Z}|\mathbf{Z}}\left(\hat{\mathbf{Z}};t\middle|\hat{\mathbf{Z}}_0;t_0\right) = \delta(\hat{\mathbf{Z}} - \hat{\mathbf{Z}}_0). \tag{2.107}$$

The Master equation 2.106 is sometimes instead written for the state PDF

$$f_{\mathbf{Z}}(\hat{\mathbf{Z}};t) = \int f_{\mathbf{Z}|\mathbf{Z}}\left(\hat{\mathbf{Z}};t\middle|\hat{\mathbf{Z}}_0;t_0\right) f_{\mathbf{Z}}(\hat{\mathbf{Z}}_0;t_0) d\hat{\mathbf{Z}}_0 \tag{2.108}$$

as [69, 73]

$$\frac{\partial f_{\mathbf{Z}}(\hat{\mathbf{Z}};t)}{\partial t} = \int \left[W\left(\hat{\mathbf{Z}}\middle|\hat{\mathbf{Z}}';t\right) f_{\mathbf{Z}}(\hat{\mathbf{Z}}';t) - W\left(\hat{\mathbf{Z}}'\middle|\hat{\mathbf{Z}};t\right) f_{\mathbf{Z}}(\hat{\mathbf{Z}};t) \right] d\hat{\mathbf{Z}}', \tag{2.109}$$

which has the simple interpretation that the state PDF $f_{\mathbf{Z}}(\hat{\mathbf{Z}};t)$ gains from all states transitioning to state $\hat{\mathbf{Z}}$ and loses due to transitions to any state away from $\hat{\mathbf{Z}}$.

2.4.1.3 Kramers–Moyal Expansion

By performing a Taylor series expansion, we can turn the integro-differential Master equation into a partial differential equation for the PDF $f_{\mathbf{Z}}$ with coefficients depending on moments of the transition rate $W(\hat{\mathbf{Z}}|\hat{\mathbf{Z}}';t)$. For notational simplicity, we will present a derivation in the one-dimensional, homogeneous case. First substitute $\hat{Z}'$ by defining $\hat{Y} = \hat{Z} - \hat{Z}'$ in the first term and $\hat{Y} = \hat{Z}' - \hat{Z}$ in the second term of Eq. 2.109. Then define $w(\hat{Y}, \hat{Z}) \equiv W(\hat{Y} + \hat{Z}|\hat{Z}) \Rightarrow W(\hat{Z}|\hat{Z}') = w(\hat{Z} - \hat{Z}', \hat{Z}')$ such that the first and second terms of the integral

in Eq. 2.109 become, respectively,

$$
\int_{-\infty}^{\infty} W\left(\hat{Z}\middle|\hat{Z}'\right) f_Z(\hat{Z}';t) \mathrm{d}\hat{Z}' = -\int_{\hat{Z}+\infty}^{\hat{Z}-\infty} w(\hat{Y}, \hat{Z}-\hat{Y}) f_Z(\hat{Z}-\hat{Y};t) \mathrm{d}\hat{Y}
$$
$$
= -\int_{\infty}^{-\infty} w(\hat{Y}, \hat{Z}-\hat{Y}) f_Z(\hat{Z}-\hat{Y};t) \mathrm{d}\hat{Y}
$$
$$
= \int_{-\infty}^{\infty} w(\hat{Y}, \hat{Z}-\hat{Y}) f_Z(\hat{Z}-\hat{Y};t) \mathrm{d}\hat{Y}, \qquad (2.110a)
$$
$$
\int_{-\infty}^{\infty} W\left(\hat{Z}'|\hat{Z}\right) f_Z(\hat{Z};t) \mathrm{d}\hat{Z}' = \int_{-\infty-\hat{Z}}^{\infty-\hat{Z}} w(\hat{Y}, \hat{Z}) f_Z(\hat{Z};t) \mathrm{d}\hat{Y}
$$
$$
= \int_{-\infty}^{\infty} w(\hat{Y}, \hat{Z}) f_Z(\hat{Z};t) \mathrm{d}\hat{Y}, \qquad (2.110b)
$$

where we have used the infinite integration interval to absorb the sign change associated with the change of variables. Thus, Eq. 2.109 becomes [68]

$$
\frac{\partial f_Z(\hat{Z};t)}{\partial t} = \int \left[w(\hat{Y}, \hat{Z}-\hat{Y}) f_Z(\hat{Z}-\hat{Y};t) - w(\hat{Y}, \hat{Z}) f_Z(\hat{Z};t) \right] \mathrm{d}\hat{Y}. \qquad (2.111)
$$

Now we make a basic assumption that $w(\hat{Y}, \hat{Z})$ is a sharply peaked function of $\hat{Y}$ but varies slowly with $\hat{Z}$ [69]. Furthermore, we assume $f_Z(\hat{Z};t)$ varies slowly with $\hat{Z}$. Then we may expand $g(\hat{Z}-\hat{Y}) = w(\hat{Y}, \hat{Z}-\hat{Y}) f_Z(\hat{Z}-\hat{Y};t)$ in the first integral using a power series about $\hat{Z}-\hat{Y} = \hat{Z} \Rightarrow \hat{Y} = 0$,

$$
g(\hat{Z}-\hat{Y}) = \sum_{n=0}^{\infty} \frac{1}{n!} g^{(n)}(\hat{Z})(\hat{Z}-\hat{Y}-\hat{Z})^n
$$
$$
= \sum_{n=0}^{\infty} \frac{(-\hat{Y})^n}{n!} g^{(n)}(\hat{Z})
$$
$$
= \sum_{n=0}^{\infty} \frac{(-\hat{Y})^n}{n!} \frac{\partial^n}{\partial \hat{Z}^n} \left[w(\hat{Y}, \hat{Z}) f_Z(\hat{Z};t) \right]. \qquad (2.112)
$$

Substituting Eq. 2.112 into Eq. 2.111 yields [68]

$$
\begin{aligned}
\frac{\partial f_Z(\hat{Z};t)}{\partial t} &= \int \sum_{n=0}^{\infty} \frac{(-\hat{Y})^n}{n!} \frac{\partial^n}{\partial \hat{Z}^n} \left[w(\hat{Y},\hat{Z}) f_Z(\hat{Z};t) \right] \mathrm{d}\hat{Y} - \int w(\hat{Y},\hat{Z}) f_Z(\hat{Z};t) \mathrm{d}\hat{Y} \\
&= \int \sum_{n=1}^{\infty} \frac{(-Y)^n}{n!} \frac{\partial^n}{\partial \hat{Z}^n} \left[w(\hat{Y},\hat{Z}) f_Z(\hat{Z};t) \right] \mathrm{d}\hat{Y} \\
&= \sum_{n=1}^{\infty} \frac{(-1)^n}{n!} \frac{\partial^n}{\partial \hat{Z}^n} \left[\alpha^{(n)}(\hat{Z}) f_Z(\hat{Z};t) \right],
\end{aligned}
\tag{2.113}
$$

where we define the nth moment of W as

$$
\alpha^{(n)}(\hat{Z}) = \int (\hat{Z}' - \hat{Z})^n W\left(\hat{Z}' \,\middle|\, \hat{Z} \right) \mathrm{d}\hat{Z}' = \int \hat{Y}^n w(\hat{Y},\hat{Z}) \mathrm{d}\hat{Y}.
\tag{2.114}
$$

Equations 2.113 and 2.114 generalize to an inhomogeneous process in multiple dimensions by using the multivariate Taylor series expansion [74]:

$$
\frac{\partial f_{\mathbf{Z}}(\hat{\mathbf{Z}};t)}{\partial t} = \sum_{n=1}^{\infty} \frac{(-1)^n}{n!} \sum_{j_1,\ldots,j_n} \frac{\partial^n}{\partial \hat{Z}_{j_1} \cdots \partial \hat{Z}_{j_n}} \left[\alpha_{j_1,\ldots,j_n}^{(n)}(\hat{\mathbf{Z}},t) f_{\mathbf{Z}}(\hat{\mathbf{Z}};t) \right],
\tag{2.115}
$$

where the nth moment of W is

$$
\alpha_{j_1,\ldots,j_n}^{(n)}(\hat{\mathbf{Z}},t) = \int (\hat{Z}'_{j_1} - \hat{Z}_{j_1}) \cdots (\hat{Z}'_{j_n} - \hat{Z}_{j_n}) W\left(\hat{\mathbf{Z}}' \,\middle|\, \hat{\mathbf{Z}};t \right) \mathrm{d}\hat{\mathbf{Z}}'.
\tag{2.116}
$$

2.4.2 Fokker-Planck Equation

By truncating the Kramers–Moyal expansion of the Master equation after the first two terms, one obtains the *Fokker-Planck equation* or the forward Kolmogorov equation:

$$
\frac{\partial f_{\mathbf{Z}}(\hat{\mathbf{Z}};t)}{\partial t} = -\frac{\partial}{\partial \hat{Z}_i} \left[A_i(\hat{\mathbf{Z}},t) f_{\mathbf{Z}}(\hat{\mathbf{Z}};t) \right] + \frac{1}{2} \frac{\partial^2}{\partial \hat{Z}_i \partial \hat{Z}_j} \left[B_{ij}(\hat{\mathbf{Z}},t) f_{\mathbf{Z}}(\hat{\mathbf{Z}};t) \right],
\tag{2.117}
$$

where

$$
\mathbf{A}(\hat{\mathbf{Z}},t) = \alpha^{(1)}(\hat{\mathbf{Z}},t) = \int (\hat{\mathbf{Z}}' - \hat{\mathbf{Z}}) W\left(\hat{\mathbf{Z}}' \,\middle|\, \hat{\mathbf{Z}};t \right) \mathrm{d}\hat{\mathbf{Z}}',
\tag{2.118a}
$$

$$
B(\hat{\mathbf{Z}};t) = \alpha^{(2)}(\hat{\mathbf{Z}},t) = \int (\hat{\mathbf{Z}}' - \hat{\mathbf{Z}})(\hat{\mathbf{Z}}' - \hat{\mathbf{Z}})^{\mathrm{T}} W\left(\hat{\mathbf{Z}}' \,\middle|\, \hat{\mathbf{Z}};t \right) \mathrm{d}\hat{\mathbf{Z}}'.
\tag{2.118b}
$$

are the drift vector and diffusion matrix, respectively [68, 75], with the state vector $\mathbf{Z}$ in Eq. 2.118b treated as a column vector. The process corresponding to the PDF modeled by

34

the Fokker-Planck equation is mathematically defined as a *diffusion process* and is uniquely determined by the coefficients A and B. From Eq. 2.118b, it is apparent that the diffusion matrix B is positive semidefinite and symmetric [68, 75]. The diffusion process is continuous, meaning that the probability that the final state $\hat{\mathbf{Z}}$ is finitely different from the initial state $\hat{\mathbf{Z}}'$ approaches zero faster than the time increment Δt: for any $\varepsilon > 0$, we have [68]

$$\lim_{\Delta t \to 0} \frac{1}{\Delta t} \int_{|\hat{\mathbf{Z}}-\hat{\mathbf{z}}'|>\varepsilon} f_{\mathbf{Z}|\mathbf{Z}}\left(\hat{\mathbf{Z}}; t+\Delta t \middle| \hat{\mathbf{Z}}'; t\right) \mathrm{d}\hat{\mathbf{Z}} = \int_{|\hat{\mathbf{Z}}-\hat{\mathbf{z}}'|>\varepsilon} W\left(\hat{\mathbf{Z}} \middle| \hat{\mathbf{Z}}'; t\right) \mathrm{d}\hat{\mathbf{Z}} = 0 \qquad (2.119)$$

uniformly in $\hat{\mathbf{Z}}'$, t, and Δt. Thus, for a continuous Markov process, $W(\hat{\mathbf{Z}}|\hat{\mathbf{Z}}'; t) = 0$ for $|\hat{\mathbf{Z}}-\hat{\mathbf{Z}}'| > \varepsilon$.

2.4.3 Langevin Equation

In contrast to the PDF-based models of sections 2.4.1 and 2.4.2, the Langevin equation is a stochastic (ordinary) differential equation (SDE) which models the stochastic process evolution directly. The historical origins [40, 68] of the Langevin equation can be traced back to the work of Robert Brown on Brownian motion in the early 19th century, Einstein [13] on molecular diffusion, and Langevin [14] on random forces on particles suspended in a fluid. Langevin's original derivation essentially started with a macroscopic equation of motion for particles with a linear drag force and added an a stochastic forcing term to represent the turbulent motion. Given spherical particles of mass m and radius r in a fluid of dynamic viscosity μ, Langevin wrote an equation of motion for the Brownian particle velocity $u(t)$ as [68, 69]

$$\frac{\mathrm{d}u(t)}{\mathrm{d}t} = -\frac{6\pi\mu r}{m}u(t) + f, \qquad (2.120)$$

where f is the fluctuating force per unit mass. The viscous drag forces which is linear in velocity $u(t)$ represents drift, while the fluctuating force term representing incessant fluid molecule collisions with the Brownian particle accounts for diffusion. The latter was characterized famously by Einstein and independently by Langevin as related to the mean squared spatial deviation $\sigma_x^2 = 2\Gamma t$, where $\Gamma = k_{\mathrm{B}}T/(6\pi\mu r)$ is the molecular diffusion coefficient with the Boltzmann constant k_{B} and temperature T. This is referred to as Einstein's relation from kinetic theory. Taylor [43] first applied this model to turbulent diffusion, and Uhlenbeck and Ornstein [15] studied the case of a stationary Brownian motion process with constant coefficients.

As the Langevin equation follows the trajectory of a particle—Brownian or turbulent fluid— the Langevin equation is a Lagrangian equation. Langevin's approach of starting with a

deterministic macroscopic equation of motion and adding a stochastic forcing term with the appropriate mean squared fluctuations is perhaps the simplest way of deriving a Langevin equation. However, there was not a solid mathematical foundation for it until Itô formalized the concepts of stochastic calculus and ordinary differential equations. In the remainder of this subsection, we outline these mathematical foundations and show that the Langevin equation can be derived from the PDF-based models from sections 2.4.1 and 2.4.2 and vice versa. Then from the uniqueness of the solutions to PDF models and SDEs [75], these two approaches can be considered equivalent formulations for a Markov process. In particular, the Fokker-Planck equation and the Langevin equation are equivalent representations of a diffusion process which can be used to model Brownian motion.

2.4.3.1 Wiener Process

A Wiener process is a homogeneous m-dimensional Markov process $\mathbf{W}(t)$ defined for $t \in [0, \infty)$, whose components $W_i(t)$ for $1 \leq i \leq m$ are all independent, with the following properties [68, 75]:

- Initial condition

$$\mathbf{W}(0) = \mathbf{W}_0 = 0. \tag{2.121}$$

- Independent increments: the random variables $\Delta\mathbf{W}_k \equiv \mathbf{W}(t_k) - \mathbf{W}(t_{k-1})$ for $1 \leq k \leq N$ are independent of each other and $\mathbf{W}(t_0)$, where $t_0 = 0 < t_1 < \cdots < t_N$.

- Gaussian increments: $\Delta\mathbf{W}_k \sim \mathcal{N}\left(\langle\mathbf{W}_0\rangle, \Delta t_k I_m\right) = \mathcal{N}\left(0, \Delta t_k I_m\right)$, where $\Delta t_k \equiv t_k - t_{k-1}$ and I_m is the m-dimensional identity matrix. That is,

$$\langle\Delta\mathbf{W}_i\rangle = \langle\mathbf{W}_0\rangle = 0, \tag{2.122a}$$

$$\langle\Delta\mathbf{W}_{k,i}\Delta\mathbf{W}_{k,j}\rangle = \langle[W_i(t_k) - W_i(t_{k-1})][W_j(t_k) - W_j(t_{k-1})]\rangle = \Delta t_k \delta_{ij}. \tag{2.122b}$$

This latter equation leads one to often informally write $dW_i(t)dW_j(t) \equiv \delta_{ij}dt$.

- Continuous paths: $\mathbf{W}(t)$ is continuous in t.

The Wiener process $\mathbf{W}(t)$ mathematically models the Brownian motion of a free particle in the absence of friction [75]. It is a diffusion process and thus has continuous paths, but the paths are not differentiable [68, 75]. Then while $\mathbf{W}(t)$ provides a good model for the experimentally observed irregular motion of Brownian particles, if $\mathbf{W}(t)$ represents the position of the Brownian particle, the particle does not possess a velocity at any instant.

Thus, it is more rigorous to use the Wiener process to represent the particle velocity as opposed to its position directly.

2.4.3.2 Stochastic Differential Equations and the Langevin Equation

Formally [68, 75], we define an Itô *stochastic differential equation* as an equation of the form

$$dZ_i(t) = a_i(\mathbf{Z}, t)dt + b_{ij}(\mathbf{Z}, t)dW_j(t), \tag{2.123a}$$

$$Z_i(t_0) = Z_{0,i}, \tag{2.123b}$$

for $1 \leq i \leq n$, and where $\mathbf{W}(t)$ is an m-dimensional Wiener process. Equations 2.123a and 2.123b together should be interpreted as a symbolic way of writing the Itô stochastic integrals

$$Z_i(t) = Z_i(t_0) + \int_{t_0}^t a_i\left[\mathbf{Z}(t'), t'\right] dt' + \int_{t_0}^t b_{ij}\left[\mathbf{Z}(t'), t'\right] dW_j(t'). \tag{2.124}$$

Informally, Eq. 2.123a is often written—especially in physics and engineering literature—in the form of a more classical differential equation called a *Langevin equation*

$$\frac{dZ_i(t)}{dt} = a_i(\mathbf{Z}, t) + b_{ij}(\mathbf{Z}, t)\xi_j(t), \tag{2.125}$$

where $\xi_i(t)$ is a Gaussian white noise process defined by $dW_i(t) \equiv W_i(t+dt) - W_i(t) = \xi_i(t)dt$ or

$$W_i(t) = \int_0^t \xi_i(t')dt', \tag{2.126a}$$

$$\xi_i(t) = \frac{dW_i(t)}{dt}. \tag{2.126b}$$

This latter relation is to say that informally[5] white noise is the derivative of the Wiener process. Gaussian white noise is understood as a stationary Gaussian process with:

- Zero mean

$$\langle \xi_i(t) \rangle = 0. \tag{2.127}$$

- Dirac delta covariance

$$\langle \xi_i(t)\xi_j(t') \rangle = \delta(t - t')\delta_{ij}. \tag{2.128}$$

---

[5]As noted in section 2.4.3.1, the Wiener process is not differentiable, so technically the Langevin equation is not mathematically rigorous, but one can interpret the integral equations 2.126a and 2.124 with $dW_i(t) = \xi_i(t)dt$ consistently.

It is common for one to assume that the white noise process is Gaussian while satisfying Eq. 2.128, but this follows directly from the continuity of the Wiener process [68].

2.4.3.3   Master Equation Derivation

We can derive the Langevin equation for the given Master Eq. 2.109 by calculating the first and second moments of W, called the drift vector and diffusion matrix, respectively. Taking the first moment of Eq. 2.109, where the mean of $\mathbf{Z}(t)$ is $\langle \mathbf{Z}(t) \rangle \equiv \int \hat{\mathbf{Z}} f_{\mathbf{Z}}(\hat{\mathbf{Z}}; t) \mathrm{d}\hat{\mathbf{Z}}$, we have

$$
\begin{aligned}
\frac{\partial}{\partial t} \int \hat{\mathbf{Z}} f_{\mathbf{Z}}(\hat{\mathbf{Z}}; t) \mathrm{d}\hat{\mathbf{Z}} &= \int \int \hat{\mathbf{Z}} \left[W\left(\hat{\mathbf{Z}} \middle| \hat{\mathbf{Z}}'; t\right) f_{\mathbf{Z}}(\hat{\mathbf{Z}}'; t) - W\left(\hat{\mathbf{Z}}' \middle| \hat{\mathbf{Z}}; t\right) f_{\mathbf{Z}}(\hat{\mathbf{Z}}; t) \right] \mathrm{d}\hat{\mathbf{Z}}' \mathrm{d}\hat{\mathbf{Z}} \\
\Rightarrow \frac{\mathrm{d}}{\mathrm{d}t} \langle \mathbf{Z}(t) \rangle &= \int \int \hat{\mathbf{Z}} W\left(\hat{\mathbf{Z}} \middle| \hat{\mathbf{Z}}'; t\right) f_{\mathbf{Z}}(\hat{\mathbf{Z}}'; t) \mathrm{d}\hat{\mathbf{Z}}' \mathrm{d}\hat{\mathbf{Z}} \\
&\quad - \int \int \hat{\mathbf{Z}} W\left(\hat{\mathbf{Z}}' \middle| \hat{\mathbf{Z}}; t\right) f_{\mathbf{Z}}(\hat{\mathbf{Z}}; t) \mathrm{d}\hat{\mathbf{Z}}' \mathrm{d}\hat{\mathbf{Z}}.
\end{aligned}
\tag{2.129}
$$

The drift vector Eq. 2.118a has a mean value

$$
\begin{aligned}
\langle \mathbf{A}(\mathbf{Z}, t) \rangle &\equiv \int \mathbf{A}(\hat{\mathbf{Z}}, t) f_{\mathbf{Z}}(\hat{\mathbf{Z}}'; t) \mathrm{d}\hat{\mathbf{Z}} \\
&= \int \int (\hat{\mathbf{Z}}' - \hat{\mathbf{Z}}) W\left(\hat{\mathbf{Z}}' \middle| \hat{\mathbf{Z}}; t\right) f_{\mathbf{Z}}(\hat{\mathbf{Z}}; t) \mathrm{d}\hat{\mathbf{Z}}' \mathrm{d}\hat{\mathbf{Z}} \\
&= \int \int \hat{\mathbf{Z}}' W\left(\hat{\mathbf{Z}}' \middle| \hat{\mathbf{Z}}; t\right) f_{\mathbf{Z}}(\hat{\mathbf{Z}}; t) \mathrm{d}\hat{\mathbf{Z}}' \mathrm{d}\hat{\mathbf{Z}} \\
&\quad - \int \int \hat{\mathbf{Z}} W\left(\hat{\mathbf{Z}}' \middle| \hat{\mathbf{Z}}; t\right) f_{\mathbf{Z}}(\hat{\mathbf{Z}}; t) \mathrm{d}\hat{\mathbf{Z}}' \mathrm{d}\hat{\mathbf{Z}} \\
&= \int \int \hat{\mathbf{Z}} W\left(\hat{\mathbf{Z}} \middle| \hat{\mathbf{Z}}'; t\right) f_{\mathbf{Z}}(\hat{\mathbf{Z}}'; t) \mathrm{d}\hat{\mathbf{Z}}' \mathrm{d}\hat{\mathbf{Z}} \\
&\quad - \int \int \hat{\mathbf{Z}} W\left(\hat{\mathbf{Z}}' \middle| \hat{\mathbf{Z}}; t\right) f_{\mathbf{Z}}(\hat{\mathbf{Z}}; t) \mathrm{d}\hat{\mathbf{Z}}' \mathrm{d}\hat{\mathbf{Z}},
\end{aligned}
\tag{2.130}
$$

where in the final step we have swapped the dummy variables of integration in the first integrals using Fubini's theorem so we can write Eq. 2.129 as [73]

$$
\frac{\mathrm{d}}{\mathrm{d}t} \langle \mathbf{Z}(t) \rangle = \langle \mathbf{A}(\mathbf{Z}, t) \rangle.
\tag{2.131}
$$

In the case of a linear system, $\mathbf{A}(\mathbf{Z}, t)$ is defined to be linear in its state,

$$
\mathbf{A}(\mathbf{Z}, t) \equiv \mathbf{A}_0 - \Lambda \mathbf{Z},
\tag{2.132}
$$

and Eq. 2.131 simply becomes [73]

$$\frac{\mathrm{d}}{\mathrm{d}t} \langle \mathbf{Z}(t) \rangle + \Lambda \langle \mathbf{Z}(t) \rangle = \mathbf{A}_0. \tag{2.133}$$

Given the steady-state equilibrium value $\mathbf{Z}_0 \equiv \langle \mathbf{Z}(t) \rangle$, the steady-state drift for a linear system is given by $\mathbf{A}(\mathbf{Z}_0, t) = 0 \Rightarrow \mathbf{A}_0 = \Lambda \mathbf{Z}_0$. Defining the fluctuation about the equilibrium mean as $\boldsymbol{\zeta}(t) = \mathbf{Z}(t) - \mathbf{Z}_0$, Eq. 2.133 can be written in terms of the mean fluctuation as [73]

$$\frac{\mathrm{d}}{\mathrm{d}t} \langle \boldsymbol{\zeta}(t) \rangle + \Lambda \langle \boldsymbol{\zeta}(t) \rangle = 0, \tag{2.134}$$

which with the initial value $\langle \boldsymbol{\zeta}(t_0) \rangle$ has the solution $\langle \boldsymbol{\zeta}(t) \rangle = \langle \boldsymbol{\zeta}(t_0) \rangle \exp\left[-\Lambda(t - t_0) \right]$. For a nonlinear system, Eq. 2.131 is not closed, so Eq. 2.134 is only approximate and is obtained from Eq. 2.131 by expanding about an equilibrium state $\mathbf{Z}_0$ given by $\mathbf{A}(\mathbf{Z}_0, t) = 0$ and ignoring higher order terms in $\boldsymbol{\zeta}(t)$ by linearization. In this case, $\Lambda = -\partial \mathbf{A}(\mathbf{Z}, t) / \partial \mathbf{Z}$.

In addition to the first moment equation 2.134, one can further show [76] directly from higher moments of the Master equation that for a linear system, $\boldsymbol{\zeta}(t) = \mathbf{Z}(t) - \mathbf{Z}_0$ satisfies the Langevin equation [73, 76]

$$\left(\frac{\mathrm{d}}{\mathrm{d}t} + \Lambda \right) \boldsymbol{\zeta}(t) = \mathbf{S}(t), \tag{2.135}$$

with has the following properties [73, 76]:

1. $\langle \mathbf{S}(t) \rangle = 0$,

2. $\langle \mathbf{S}(t) \boldsymbol{\zeta}^{\mathrm{T}}(t') \rangle = 0$ for $t > t'$ (causality),

3. $\langle \mathbf{S}(t) \mathbf{S}^{\mathrm{T}}(t') \rangle = \langle B \left[\mathbf{Z}(t), t \right] \rangle \delta(t - t')$ (white noise),

where the diffusion matrix B is defined in Eq. 2.118b. For linear systems $\langle B\left(\mathbf{Z}, t \right) \rangle$ is linear in $\mathbf{Z}$ so that $\langle B\left[\mathbf{Z}(t), t \right] \rangle = B\left[\langle \mathbf{Z}(t) \rangle, t \right]$ [73]. Equation 2.135 generalizes in the nonlinear case to the Langevin equation [76]

$$\frac{\mathrm{d}\mathbf{Z}(t)}{\mathrm{d}t} = \mathbf{a}(\mathbf{Z}, t) + \mathbf{S}(t). \tag{2.136}$$

2.4.3.4 Itô's Lemma

Itô's lemma is one of the most important results of Itô calculus. It represents a change of variables formula for a stochastic process according to a twice-differentiable function $g(\mathbf{Z}, t)$,

and it can be used to show the connection between the Langevin and Fokker-Planck equations. We present a simple proof for this in 1D, but this generalizes readily to arbitrary dimensions [75]. Since g is twice differentiable, we can expand it as a Taylor series:

$$dg = \frac{\partial g}{\partial t}dt + \frac{\partial g}{\partial Z}dZ + \frac{1}{2}\frac{\partial^2 g}{\partial Z^2}(dZ)^2 + O\left[(dt)^2\right] + O\left[(dZ)^3\right]. \tag{2.137}$$

Now assuming that $Z(t)$ is an Itô diffusion process satisfying the stochastic differential equation

$$dZ(t) = a(Z,t)dt + b(Z,t)dW(t), \tag{2.138}$$

where $dW(t)$ is a Wiener process with variance $\langle W(t)W(t)\rangle = t$, Eq. 2.137 for $g\left[Z(t),t\right]$ becomes

$$\begin{aligned}dg &= \frac{\partial g}{\partial t}dt + \frac{\partial g}{\partial Z}\left[a(Z,t)dt + b(Z,t)dW(t)\right] \\ &+ \frac{1}{2}\frac{\partial^2 g}{\partial Z^2}\left[a^2(Z,t)(dt)^2 + 2a(Z,t)b(Z,t)dtdW(t) + b^2(Z,t)(dW(t))^2\right] \\ &+ O\left[(dt)^2\right] + O\left[(dZ)^3\right].\end{aligned} \tag{2.139}$$

In the limit $dt \to 0$, the terms $(dt)^2$ and $dtdW(t) = (dt)^{3/2}$ tend to zero faster than $(dW(t))^2 = dt$, so Eq. 2.139 becomes

$$dg = \left[\frac{\partial g}{\partial t} + a(Z,t)\frac{\partial g}{\partial Z} + \frac{1}{2}b^2(Z,t)\frac{\partial^2 g}{\partial Z^2}\right]dt + b(Z,t)\frac{\partial g}{\partial Z}dW(t). \tag{2.140}$$

Equation 2.140 is referred to as *Itô's lemma* and is the stochastic counterpart of the chain rule of classical calculus for Itô calculus. Taking the mean of both sides of 2.140 results in

$$\begin{aligned}\frac{d}{dt}\langle g(Z,t)\rangle &= \left\langle \frac{\partial g}{\partial t}\right\rangle + \left\langle a(Z,t)\frac{\partial g}{\partial Z}\right\rangle + \frac{1}{2}\left\langle b^2(Z,t)\frac{\partial^2 g}{\partial Z^2}\right\rangle \\ \Rightarrow \frac{d}{dt}\int g(\hat{Z},t)f_Z(\hat{Z};t)d\hat{Z} &= \int f_Z(\hat{Z};t)\left[\frac{\partial g}{\partial t}\right. \\ &\left. + a(\hat{Z},t)\frac{\partial g}{\partial \hat{Z}} + \frac{1}{2}b^2(\hat{Z},t)\frac{\partial^2 g}{\partial \hat{Z}^2}\right]d\hat{Z}\end{aligned} \tag{2.141}$$

since $\langle dW(t)\rangle = 0$. Moving the $\partial_t g$ term to the left-hand side of Eq. 2.141 and using the product rule to expand the $\partial_t(gf_Z)$ term yields

$$\frac{d}{dt}\int g(\hat{Z},t)f_Z(\hat{Z};t)d\hat{Z} - \int \frac{\partial g}{\partial t}f_Z(\hat{Z};t)d\hat{Z} = \int g(\hat{Z},t)\frac{\partial f_Z}{\partial t}d\hat{Z}. \tag{2.142}$$

Substituting Eq. 2.142 into Eq. 2.141, integrating by parts the Z-derivatives, and discarding surface terms since $f_Z(\hat{Z}, t)$ vanishes at the boundary, Eq. 2.141 becomes

$$\int g(\hat{Z}, t) \frac{\partial f_Z}{\partial t} \mathrm{d}\hat{Z} =$$
$$\int g(\hat{Z}, t) \left\{ -\frac{\partial}{\partial \hat{Z}} \left[a(\hat{Z}, t) f_Z(\hat{Z}; t) \right] + \frac{1}{2} \frac{\partial^2}{\partial \hat{Z}^2} \left[b^2(\hat{Z}, t) f_Z(\hat{Z}; t) \right] \right\} \mathrm{d}\hat{Z}. \qquad (2.143)$$

Since g is arbitrary, we can factor it out of Eq. 2.143, producing the Fokker-Planck equation

$$\frac{\partial f_Z(\hat{Z}; t)}{\partial t} = -\frac{\partial}{\partial \hat{Z}} \left[a(\hat{Z}, t) f_Z(\hat{Z}; t) \right] + \frac{1}{2} \frac{\partial^2}{\partial \hat{Z}^2} \left[b^2(\hat{Z}, t) f_Z(\hat{Z}; t) \right]. \qquad (2.144)$$

This derivation readily generalizes to arbitrary dimensions, for which the SDE in Eq. 2.123a results in the Fokker-Planck equation 2.117 where

$$A_i(\mathbf{Z}, t) = a_i(\mathbf{Z}, t) \qquad (2.145\mathrm{a})$$
$$B_{ij}(\mathbf{Z}, t) = b_{ik}(\mathbf{Z}, t) b_{jk}(\mathbf{Z}, t) \qquad (2.145\mathrm{b})$$

are the drift and diffusion coefficients, respectively. In matrix notation, Eq. 2.145b can be written as $B = bb^{\mathrm{T}}$. Thus, from the uniqueness of solutions to the SDE and the Fokker-Planck equation, the diffusion process can be equivalently modeled using either the SDE Eq. 2.123a (or its Langevin equation form Eq. 2.125) or the Fokker-Planck Eq. 2.117 provided that the drift and diffusion coefficients satisfy Eqs. 2.145a and 2.145b.

2.4.3.5 Kramers–Moyal Coefficients

A final method for showing the connection between the Master equation and the Langevin equation is to calculate the Kramers–Moyal expansion coefficients for a given SDE. As in section 2.4.3.4, we will prove this for the simple 1D SDE in Eq. 2.138, but the proof generalizes to multiple dimensions. Equation 2.138 can be cast into the integral form

$$Z(t + \Delta t) - Z(t) = \int_t^{t+\Delta t} \left\{ a\left[Z(t'), t' \right] \mathrm{d}t' + b\left[Z(t'), t' \right] \mathrm{d}W(t') \right\}, \qquad (2.146)$$

where $Z = Z(t)$ is the initial value. Expanding a and b as the Taylor series

$$a\left[Z(t'), t'\right] = a(X, t') + \frac{\partial a}{\partial Z}(Z, t')\left[Z(t') - Z\right] + \cdots, \tag{2.147a}$$

$$b\left[Z(t'), t'\right] = b(X, t') + \frac{\partial b}{\partial Z}(Z, t')\left[Z(t') - Z\right] + \cdots, \tag{2.147b}$$

and substituting Eqs. 2.147a and 2.147b into Eq. 2.146 yields

$$
\begin{aligned}
Z(t + \Delta t) - Z = & \int_t^{t+\Delta t} \left\{ a(X, t') + \frac{\partial a}{\partial Z}(Z, t')\left[Z(t') - Z\right] + \cdots \right\} \mathrm{d}t' \\
& + \int_t^{t+\Delta t} \left\{ b(X, t') + \frac{\partial b}{\partial Z}(Z, t')\left[Z(t') - Z\right] + \cdots \right\} \mathrm{d}W(t').
\end{aligned}
\tag{2.148}
$$

One can recursively substitute $Z(t') - Z$ into the integrands of Eq. 2.148 so that the integrand depends only on a and b and their derivatives:

$$
\begin{aligned}
Z(t + \Delta t) - Z = & \int_t^{t+\Delta t} a(X, t')\mathrm{d}t' + \int_t^{t+\Delta t} b(X, t')\mathrm{d}W(t') \\
& + \int_t^{t+\Delta t} \frac{\partial a}{\partial Z} \left[\int_t^{t'} a(X, t'')\mathrm{d}t'' + \int_t^{t'} b(X, t'')\mathrm{d}W(t'') \right] \mathrm{d}t' \\
& + \int_t^{t+\Delta t} \frac{\partial b}{\partial Z} \left[\int_t^{t'} a(X, t'')\mathrm{d}t'' + \int_t^{t'} b(X, t'')\mathrm{d}W(t'') \right] \mathrm{d}W(t') + \cdots
\end{aligned}
\tag{2.149}
$$

Then we can take moments of Eq. 2.149 to calculate the Kramers–Moyal coefficients according to

$$\alpha^{(n)}(Z, t) = \lim_{\Delta t \to 0} \frac{1}{\Delta t} \left\langle [Z(t + \Delta t) - Z]^n \right\rangle_{Z(t)=Z}. \tag{2.150}$$

Equations 2.114 and 2.150 have the equivalent interpretation of measuring the expected rate of $(Z' - Z)^n$ when transitioning from $Z = Z(t)$ to $Z' = Z(t + \Delta t)$. Substituting Eq. 2.149 into 2.150 and using the Itô integral, one finds [74]

$$
\begin{aligned}
\alpha^{(1)}(Z, t) &= a(Z, t) \\
\alpha^{(2)}(Z, t) &= b^2(Z, t) \\
\alpha^{(n)}(Z, t) &= 0, \quad n \geq 3.
\end{aligned}
$$

Thus, as in section 2.4.3.4, Eq. 2.138 corresponds directly to the Fokker-Planck equation 2.144 for the diffusion process $Z(t)$.

Chapter 3

Lagrangian Velocity Langevin Models

The turbulent velocity formulation for the DD model of the FLEXPART and HYSPLIT codes follows from the Langevin velocity formulation by Legg and Raupach [44], where the fluid motion is represented in terms of a drift term proportional to the velocity, a stochastic source term, and a Reynolds stress term. Although the Langevin equation is frequently used in various system analysis [14, 73], use of the formulation for the turbulent fluid motion has not been clarified. Our study of the DD model began with a simple inquiry about the physical basis of the Langevin model contrasted with the first principle representation of the fluid motion, in particular, the Navier-Stokes equation of motion. This led us to study the turbulent Navier-Stokes (NS) equation resulting from the difference between the regular NS equation and Reynolds-averaged Navier-Stokes (RANS) equation. Our derivation of the FLEXPART model requires representation of the drift term in the Langevin formulation with the turbulent NS equation. In the original Langevin formulation [44], the drift term is represented in terms of the autocorrelation function of the turbulent fluid velocity, and our derivation of the drift term with the turbulent NS equation requires a somewhat approximate, although physical, representation of the Lagrangian time scale by mean velocity gradient through the turbulent autocorrelation function.

Our derivation and justification of the FLEXPART DD model should be contrasted with several different Langevin formulations for the turbulent fluid motion [39, 77] which rely mostly on representing the Lagrangian time scale via Reynolds stress dissipation time, often with a mean velocity gradient term unaccounted for. We begin with the derivation of the DD model from the turbulent NS equation in section 3.1, with a clear introduction of the DD model in section 3.1.1 followed by comparison between the turbulent NS equation and the DD equation in section 3.1.2.2 and the Lagrangian time scale formulation to follow in sections 3.1.3 and 3.1.4. Section 3.2.2 compares and contrasts the FLEXPART DD model with alternative Langevin models in which the Lagrangian time scale depends on the turbulent

kinetic energy dissipation rate.

3.1 Drift-diffusion Turbulent Flow Model

We derive from first principles the stochastic drift-diffusion models used in FLEXPART and HYSPLIT, with section 3.1.1 presenting the FLEXPART and HYSPLIT model in the form of a Langevin equation. The turbulent component Navier-Stokes equation is then used in Lagrangian form to derive a Langevin model for the turbulent velocity following a Lagrangian fluid particle in section 3.1.2. This can be directly compared with the Langevin model used by FLEXPART and HYSPLIT. In sections 3.1.3 and 3.1.4 we present a justification for the Lagrangian time scale model proposed. Finally, we make comparisons and contrast with the models presented by Pope [39, 77] and others in sections 3.2.1 through 3.2.3, where we clarify in section 3.2.4 that our model for the Lagrangian time scale is the correct model for FLEXPART and HYSPLIT.

3.1.1 FLEXPART and HYSPLIT Langevin Drift-diffusion Model

Both the FLEXPART and HYSPLIT codes are Lagrangian particle dispersion models (LPDMs) widely used for ATM in the turbulent atmosphere. They are based on a Langevin model for the turbulent component of the fluid particle velocity, $\mathbf{u}(t) = \mathbf{U}(t) - \langle \mathbf{U}(t) \rangle$, where $\mathbf{U}(t)$ is the total fluid particle velocity, and $\langle \cdot \rangle$ denotes the ensemble average of stochastic process realizations. We discuss the theory behind the linear Langevin model in more detail in section 3.1.3. The mean velocity itself is treated as a simulation input coming from the meteorological data model. The FLEXPART model, excluding the density correction [78], is given by Stohl et al. [1, 2] as

$$\frac{\mathrm{d}u_i(t)}{\mathrm{d}t} = -\frac{u_i(t)}{T_{ii}^{\mathrm{L}}} + \frac{\partial \sigma_{u_i}^2}{\partial x_i} + \left(\frac{2\sigma_{u_i}^2}{T_{ii}^{\mathrm{L}}}\right)^{1/2} \xi_i(t), \tag{3.1}$$

where T_{ii}^{L} is the Lagrangian time scale, $\sigma_{u_i}^2 = \langle u_i^2(t) \rangle$ is the fluctuating velocity variance, and $\xi_i(t)$ is a Gaussian white noise process, with no Einstein summation implied. As discussed in section 2.4.3.2, Gaussian white noise is a stationary stochastic process with a Gaussian probability density function with mean $\langle \xi_i(t) \rangle = 0$ and covariance $\langle \xi_i(t)\xi_j(t') \rangle = \delta(t - t')\delta_{ij}$.

The Lagrangian time scale describes the autocorrelation time scale of the turbulent velocity, while the velocity variance is the magnitude of fluctuations, as discussed in detail in section 3.1.3. The second term on the right-hand side of Eq. 3.1 is the drift correction proposed by Legg and Raupach [44] based on the RANS equation, but we will derive it directly using the

turbulent Navier-Stokes equation in section 3.1.2.2. Equation 3.1 is thus the model presented in [44] and is used by HYSPLIT. FLEXPART includes a density correction [78] term which accounts for spatial variations in the fluid density, but we will not carry the term in our derivation for notational convenience.

3.1.2 Navier-Stokes Equation in Turbulent Flows

We begin with the derivation of the Langevin model used by both FLEXPART and HYS-PLIT for the turbulent velocity component, including the drift correction, based on first principles. Fundamentally, the drift-diffusion model is based on the Navier-Stokes momentum conservation equation in turbulent fluids cast into the form of a stochastic drift-diffusion equation for particle trajectories. In particular, they are based on the turbulent Navier-Stokes equation which is the result of subtracting the mean component from the Navier-Stokes equation. Thus, we reproduce here the equations for mass and momentum conservation in incompressible flows—the continuity and Navier-Stokes Eqs. 2.14a and 2.48—respectively, from chapter 2:

$$\frac{\mathrm{D}\rho}{\mathrm{D}t} = \frac{\partial \rho}{\partial t} + u_i \frac{\partial \rho}{\partial x_i} = -\rho \frac{\partial u_i}{\partial x_i} = 0, \tag{3.2a}$$

$$\frac{\mathrm{D}U_i}{\mathrm{D}t} = \frac{\partial U_i}{\partial t} + \frac{\partial}{\partial x_j}\left(U_i U_j\right) = \frac{1}{\rho} F_i \tag{3.2b}$$

where

$$\frac{1}{\rho} F_i = -\frac{1}{\rho}\frac{\partial P}{\partial x_i} + \nu \nabla^2 U_i - 2\varepsilon_{ijk}\Omega_j U_k, \tag{3.3}$$

is the force per unit mass, $P = p + \rho \Phi_{\text{geo}}$ is the modified pressure, $\nu = \mu/\rho$ is the kinematic viscosity, and $\mathrm{D}/\mathrm{D}t \equiv \partial/\partial t + U_i \partial/\partial x_i$ is the material or Lagrangian derivative. In Eq. 3.2b we have used the incompressibility condition 3.2a and the product rule to write $U_j \partial U_i/\partial x_j = \partial(U_i U_j)/\partial x_j$.

3.1.2.1 Reynolds Decomposition and the Reynolds-averaged Navier-Stokes Equation

Using a Reynolds decomposition, we expand $U_i = \langle U_i \rangle + u_i$ and $F_i = \langle F_i \rangle + f_i$ into mean and turbulent components and substitute them into Eq. 3.2b:

$$\frac{\partial}{\partial t} \left(\langle U_i \rangle + u_i \right) + \frac{\partial}{\partial x_j} \left[\left(\langle U_i \rangle + u_i \right) \left(\langle U_j \rangle + u_j \right) \right] = \frac{1}{\rho} \langle F_i \rangle + \frac{1}{\rho} f_i \qquad (3.4\text{a})$$

$$\Rightarrow \frac{\partial \langle U_i \rangle}{\partial t} + \frac{\partial u_i}{\partial t} + \frac{\partial}{\partial x_j} \langle U_i \rangle \langle U_j \rangle + \frac{\partial}{\partial x_j} u_i u_j$$

$$+ \frac{\partial}{\partial x_j} \langle U_i \rangle u_j + \frac{\partial}{\partial x_j} u_i \langle U_j \rangle = \frac{1}{\rho} \langle F_i \rangle + \frac{1}{\rho} f_i, \qquad (3.4\text{b})$$

where

$$\frac{1}{\rho} \langle F_i \rangle = -\frac{1}{\rho} \frac{\partial \langle P \rangle}{\partial x_i} + \nu \nabla^2 \langle U_i \rangle - 2\varepsilon_{ijk} \Omega_j \langle U_k \rangle, \qquad (3.5\text{a})$$

$$\frac{1}{\rho} f_i = -\frac{1}{\rho} \frac{\partial p'}{\partial x_i} + \nu \nabla^2 u_i - 2\varepsilon_{ijk} \Omega_j u_k. \qquad (3.5\text{b})$$

Assuming the geopotential is deterministic, here we have used the Reynolds decomposition $P = \langle P \rangle + P'$, where $\langle P \rangle = \langle p \rangle + \rho \Phi_{\text{geo}}$ and $P' = p'$ is the fluctuating thermodynamic pressure. Often the fluctuating Coriolis force $-2\varepsilon_{ijk} \Omega_j u_k$ is neglected when compared to the fluctuating pressure gradient and fluctuating viscous stress forces. Taking the ensemble-average of both sides of Eq. 3.2b and Eq. 3.4b, we obtain

$$\frac{\partial}{\partial t} \langle U_i \rangle + \frac{\partial}{\partial x_j} \langle U_i U_j \rangle = \frac{1}{\rho} \langle F_i \rangle \qquad (3.6\text{a})$$

$$\Rightarrow \frac{\partial \langle U_i \rangle}{\partial t} + \frac{\partial}{\partial x_j} \langle U_i \rangle \langle U_j \rangle + \frac{\partial}{\partial x_j} \langle u_i u_j \rangle = \frac{1}{\rho} \langle F_i \rangle. \qquad (3.6\text{b})$$

The quantity $\langle u_i u_j \rangle$ is referred to as the *Reynolds stress* and is analogous to the viscous shear stress. Specifically, while the viscous stress is a result of the molecular shearing motion and friction forces, the Reynolds stress is a shear force resulting from the fluctuating velocity field. Using the ensemble-averaged incompressible continuity equation, $\partial \langle U_i \rangle / \partial x_i = 0$, and so $\partial \langle U_i \rangle \langle U_j \rangle / \partial x_j = \langle U_j \rangle \partial \langle U_i \rangle / \partial x_j$, and Eq. 3.6b yields the *Reynolds-averaged Navier-Stokes (RANS) equation*,

$$\frac{\partial \langle U_i \rangle}{\partial t} + \langle U_j \rangle \frac{\partial}{\partial x_j} \langle U_i \rangle + \frac{\partial}{\partial x_j} \langle u_i u_j \rangle = \frac{1}{\rho} \langle F_i \rangle. \qquad (3.7)$$

Equation 3.7 can be written in terms of the mean substantial derivative

$$\frac{\overline{D}}{\overline{D}t} \equiv \frac{\partial}{\partial t} + \langle U_i \rangle \frac{\partial}{\partial x_i} \tag{3.8}$$

representing the rate of change along a trajectory following the mean local velocity $\langle \mathbf{U} \rangle$ as

$$\frac{\overline{D} \langle U_i \rangle}{\overline{D}t} = -\frac{\partial}{\partial x_j} \langle u_i u_j \rangle + \frac{1}{\rho} \langle F_i \rangle. \tag{3.9}$$

3.1.2.2 Turbulent Component Navier-Stokes Equation

Using the results of section 3.1.2.1, we may derive an equation for the turbulent velocity component, which is the basis for the FLEXPART and HYSPLIT drift-diffusion model. Subtracting Eq. 3.6a from Eq. 3.2b (or equivalently Eq. 3.6b from Eq. 3.4b), we obtain

$$\frac{\partial u_i}{\partial t} + \frac{\partial}{\partial x_j} u_i \langle U_j \rangle + \frac{\partial}{\partial x_j} u_i u_j + \frac{\partial}{\partial x_j} \langle U_i \rangle u_j - \frac{\partial}{\partial x_j} \langle u_i u_j \rangle = \frac{1}{\rho} f_i. \tag{3.10}$$

The three middle terms on the left-hand side can be expanded using the product rule, which when combined with incompressibility condition $\partial U_i / \partial x_i = 0 \Rightarrow \partial \langle U_i \rangle / \partial x_i = \partial u_i / \partial x_i = 0$ effectively means that the j-velocity components can be pulled outside the derivative such that Eq. 3.10 can also be written as

$$\frac{\partial u_i}{\partial t} + \langle U_j \rangle \frac{\partial u_i}{\partial x_j} + u_j \frac{\partial u_i}{\partial x_j} + u_j \frac{\partial \langle U_i \rangle}{\partial x_j} - \frac{\partial}{\partial x_j} \langle u_i u_j \rangle = \frac{1}{\rho} f_i. \tag{3.11}$$

Combining the second and third terms on the left-hand side of Eq. 3.11, $\langle U_j \rangle \partial u_i / \partial x_j + u_j \partial u_i / \partial x_j = U_j \partial u_i / \partial x_j$, we obtain the turbulent component Navier-Stokes equation in terms of the Lagrangian derivative,

$$\frac{D u_i}{Dt} = -u_j \frac{\partial \langle U_i \rangle}{\partial x_j} + \frac{\partial}{\partial x_j} \langle u_i u_j \rangle + \frac{1}{\rho} f_i. \tag{3.12}$$

The material derivative is the correct definition of the derivative to use for deriving the Langevin equation because it describes the rate of change when following the Lagrangian fluid particle as discussed in section 2.1. Note that in contrast to the RANS equations 3.7 or 3.9, the Reynolds stress gradient has the opposite sign in the turbulent Navier-Stokes equation 3.12.

The Langevin model used by FLEXPART and HYSPLIT is a model for the turbulent velocity

component, which can be derived directly from Eq. 3.12. To do this we use the results in sections 2.1 and 2.4.3 to construct a Lagrangian velocity Langevin model. In particular:

1. Let $\mathbf{x}(t) \equiv \mathbf{x}(\mathbf{x}_0, t_0|t)$ denote the position at time t of the fluid particle that is located at $\mathbf{x}_0$ at the specified fixed reference time t_0.

2. Let $\mathbf{U}(t) \equiv \mathbf{U}(\mathbf{x}_0, t_0|t) = \mathbf{U}\left[\mathbf{x}\left(\mathbf{x}_0, t_0|t\right), t\right]$ denote the Lagrangian velocity of the fluid particle, which sets the trajectory according to Eq. 2.8:

$$\frac{\mathrm{d}\mathbf{x}(t)}{\mathrm{d}t} = \mathbf{U}(t). \tag{3.13}$$

3. Write the Eulerian velocity in terms of the Lagrangian velocity: $\mathbf{U}(\mathbf{x}_0, t) \equiv \mathbf{U}(t) \equiv \mathbf{U}\left[\mathbf{x}(\mathbf{x}_0, t_0|t), t\right]$.

4. Write the Lagrangian time derivative of the Eulerian velocity in terms of the time derivative of the Lagrangian velocity using Eqs. 2.4 or 2.9:

$$\frac{\mathrm{d}\mathbf{U}(t)}{\mathrm{d}t} = \frac{\mathrm{D}}{\mathrm{D}t}\mathbf{U}\left[\mathbf{x}(t), t\right]. \tag{3.14}$$

5. Consider only the diagonal terms of Eq. 3.12, such that the equations become uncoupled.

6. Model the stochastic forcing term f_i/ρ in terms of a Gaussian white noise process.

Steps one through four can equally be applied to the Lagrangian and Eulerian turbulent velocity components, replacing $\mathbf{U}$ with the turbulent component $\mathbf{u}$ and replacing $\mathbf{x}$ with the turbulent position $\mathbf{x}'$. In step four, however, the Lagrangian derivative should still be evaluated as described in section 2.1 along the particle position $\mathbf{x}(t) = \langle \mathbf{x}(t) \rangle + \mathbf{x}'(t)$ whose trajectory satisfies

$$\frac{\mathrm{d}\mathbf{x}(t)}{\mathrm{d}t} = \frac{\mathrm{d}\langle \mathbf{x}(t) \rangle}{\mathrm{d}t} + \frac{\mathrm{d}\mathbf{x}'(t)}{\mathrm{d}t} = \langle \mathbf{U}(t) \rangle + \mathbf{u}(t), \tag{3.15}$$

where $\mathrm{d}\langle \mathbf{x}(t) \rangle / \mathrm{d}t = \langle \mathbf{U}(t) \rangle$ is the mean velocity along the particle trajectory. In FLEXPART and HYSPLIT, the mean trajectory is determined by interpolating the meteorological data to the particle position as described in section 5.1. Once the particle trajectory is determined, one can calculate mass concentration fields as described in section 5.4. Step five is necessary since the FLEXPART model Eq. 3.1 treats each direction independently and thus neglects any coupling between the different directions. That is, it neglects the terms $u_j \partial \langle U_i \rangle / \partial x_j$ and $\partial \langle u_i u_j \rangle / \partial x_j$ for $i \neq j$ when compared to those for $i = j$ such that the cross product

terms disappear in the uncoupled 1D FLEXPART Langevin model equations. Step six is consistent with the original Langevin formulation of modeling the stochastic force in the equation of motion as a Gaussian white noise process as discussed in section 2.4.3.

Carrying out these steps, we obtain the Langevin model for the turbulent velocity component as

$$\frac{\mathrm{d}u_i(t)}{\mathrm{d}t} = -u_i(t)\frac{\partial \langle U_i(t)\rangle}{\partial x_i} + \frac{\partial}{\partial x_i}\langle u_i(t)u_i(t)\rangle + \lambda_i\xi_i(t), \tag{3.16}$$

where we are not using Einstein summation, and Eulerian quantities such as $\partial \langle U_i\rangle /\partial x_i$ are to be evaluated at the particle position $\mathbf{x} = \mathbf{x}(t)$. The first term on the right-hand side can be understood as the drift due to a mean velocity gradient along the particle's trajectory. The second term is an additional drift due to the Reynolds stress or turbulent velocity variance, which is the drift correction [44] that we have now derived directly from the turbulent Navier-Stokes equation. Comparing Eqs. 3.1 and 3.16 allows us to propose

$$\frac{\partial \langle U_i(t)\rangle}{\partial x_i} \simeq \frac{1}{T_{ii}^{\mathrm{L}}} \tag{3.17}$$

and the diffusion parameter $\lambda_i = \left(2\sigma_{u_i}^2/T_{ii}^{\mathrm{L}}\right)^{1/2}$. Thus, with the approximation Eq. 3.17 we derived the FLEXPART and HYSPLIT Langevin drift-diffusion model Eq. 3.1 directly using the turbulent Navier-Stokes equation. When compared to the original Langevin Eq. 2.120, our turbulent velocity drift-diffusion model Eq. 3.1 now includes the Reynolds stress or velocity variance term $\langle u_i(t)u_i(t)\rangle$ as well as the ansatz Eq. 3.17 for representing the drift coefficient.

3.1.3 Turbulent Velocity Drift-diffusion Equation

The stochastic velocity drift-diffusion model is a Langevin model which models the trajectory of species in turbulent fluid flows [44]. Like the Navier-Stokes equation, it is a force balance equation [40], but it is written in the form of an equation of motion which includes a retarding drift acceleration and a random acceleration representing diffusion [44]. Specifically, the Langevin equation for the turbulent velocity in stationary, homogeneous turbulence is [40, 44]

$$\frac{\mathrm{d}u_i(t)}{\mathrm{d}t} = -\alpha_i u_i(t) + \lambda_i\xi_i(t), \tag{3.18}$$

where the terms on the right are the drift and diffusion terms, respectively, α_i is the drift coefficient, λ_i is the diffusion parameter, and $\xi_i(t)$ is a Gaussian white noise process. The drift coefficient can be represented through the velocity autocorrelation function, while Akcasu

[73] takes a different approach to obtain α directly from a balance equation equivalent to the master equation for a Markovian process, as shown in section 2.4.3.3. Similarly, Langevin [14] represented α directly in terms of physical drag parameters in the equation of motion for particles undergoing Brownian motion. We show these alternative approaches for producing Langevin equations in section 2.4.3. In our case, we emphasize that the Langevin model in Eq. 3.18 represents the turbulent fluid motion obeying the turbulent Navier-Stokes equation, and the drift coefficient has to be determined from the Navier-Stokes equation.

To show that our approximation in Eq. 3.17 has a physical justification based on the turbulent fluid motion, we begin by examining the properties of the solution to Eq. 3.18. Equation 3.18 is a linear stochastic ODE with constant coefficients, so its solution with initial condition $u_i(t_0)$ at time t_0 can be analytically written as [40, 44]

$$u_i(t) = u_i(t_0)e^{-\alpha_i(t-t_0)} + \lambda_i \int_{t_0}^{t} e^{\alpha_i(t'-t)}\xi_i(t')\mathrm{d}t', \tag{3.19}$$

with mean $\langle u_i(t) \rangle = \langle u_i(t_0) \rangle = 0$, as expected for the turbulent velocity component. Using Eq. 3.19 and the Gaussian white noise ensemble-averaged integral

$$
\begin{aligned}
\int_{t_0}^{t}\int_{t_0}^{t} e^{\alpha_i(t'-t)}e^{\alpha_i(t''-t)}\left\langle \xi_i(t')\xi_i(t'') \right\rangle \mathrm{d}t'\mathrm{d}t'' &= \int_{t_0}^{t}\int_{t_0}^{t} e^{\alpha_i(t'-t)}e^{\alpha_i(t''-t)}\delta(t'-t'')\mathrm{d}t'\mathrm{d}t'' \\
&= \int_{t_0}^{t} e^{2\alpha_i(t'-t)}\mathrm{d}t' \\
&= \frac{1}{2\alpha_i}\left[1 - e^{-2\alpha_i(t-t_0)}\right],
\end{aligned}
\tag{3.20}
$$

the velocity variance and covariance are, respectively, [40, 44]

$$\langle u_i(t)u_i(t) \rangle = \langle u_i(t_0)u_i(t_0) \rangle e^{-2\alpha_i(t-t_0)} + \frac{\lambda_i^2}{2\alpha_i}\left[1 - e^{-2\alpha_i(t-t_0)}\right], \tag{3.21a}$$

$$\langle u_i(t_0)u_i(t) \rangle = \langle u_i(t_0)u_i(t_0) \rangle e^{-\alpha_i(t-t_0)}. \tag{3.21b}$$

The diffusion term coefficient can be related to both the Reynolds stress $\langle u_i u_i \rangle$ and the drift parameter α_i. If $u_i(t)$ is a stationary random process with constant mean $\langle u_i(t) \rangle = 0$ and

constant variance $\sigma_{u_i}^2 = \langle u_i(t)u_i(t) \rangle = \langle u_i(t_0)u_i(t_0) \rangle$, then Eq. 3.21a requires for all t [40, 44]

$$\sigma_{u_i}^2 = \sigma_{u_i}^2 e^{-2\alpha_i(t-t_0)} + \frac{\lambda_i^2}{2\alpha_i} \left[1 - e^{-2\alpha_i(t-t_0)} \right]$$

$$\Rightarrow \sigma_{u_i}^2 \left[1 - e^{-2\alpha_i(t-t_0)} \right] = \frac{\lambda_i^2}{2\alpha_i} \left[1 - e^{-2\alpha_i(t-t_0)} \right]$$

$$\Rightarrow \lambda_i^2 = 2\alpha_i \sigma_{u_i}^2.$$

Thus, the velocity variance $\sigma_{u_i}^2$ and drift coefficient α_i are sufficient to determine the particle velocities and trajectories using Eq. 3.18 with some initial velocity distribution $u_i(t_0)$.

The drift coefficient can be written in terms of the Lagrangian time scale T_{ii}^{L} related to the Lagrangian velocity autocorrelation function $R_{ii}^{\mathrm{L}}(t)$. We define the Lagrangian time scale as the turbulent velocity correlation time [39, 40, 54]

$$T_{ii}^{\mathrm{L}} \equiv \int_{t_0}^{\infty} R_{ii}^{\mathrm{L}}(t - t_0)\mathrm{d}t, \tag{3.22}$$

where

$$R_{ii}^{\mathrm{L}}(t - t_0) \equiv \frac{\langle u_i(t_0)u_i(t) \rangle}{\sigma_{u_i}^2} \tag{3.23}$$

is the Lagrangian velocity autocorrelation function. The Lagrangian time scales provide time or frequency scale information required by the models based on the one-time PDF as discussed in section 2.3.4. They are implemented in FLEXPART and HYSPLIT via the empirical correlations such as in Hanna [79]. The particular parameterization of the Lagrangian time scale is determined by the measured autocorrelation under given atmospheric conditions as discussed in section 5.3.2. Substituting Eq. 3.21b in Eqs. 3.23 and 3.22 requires that the drift coefficient be the inverse Lagrangian time scale [40, 44]:

$$\alpha_i = \frac{1}{T_{ii}^{\mathrm{L}}}. \tag{3.24}$$

One often defines a single Lagrangian time scale $T_{\mathrm{L}} = \int_{t_0}^{\infty} R_{\mathrm{L}}(t - t_0)\mathrm{d}t$, where T_{L} can be approximated by either the maximum or mean value of T_{ii}^{L} for $i \in \{1, 2, 3\}$ [54]. The autocorrelation function and its relationship to the Lagrangian time scale can be visualized as shown in Fig. 3.1, where the the area under the unit rectangle of time length T_{L} is equivalent to the total area under the curve. We use this relationship in section 3.1.4 to determine particle displacement functions. We note that $R_{\mathrm{L}}(t)$ physically represents a measure of the propagation of turbulent velocity over time t.
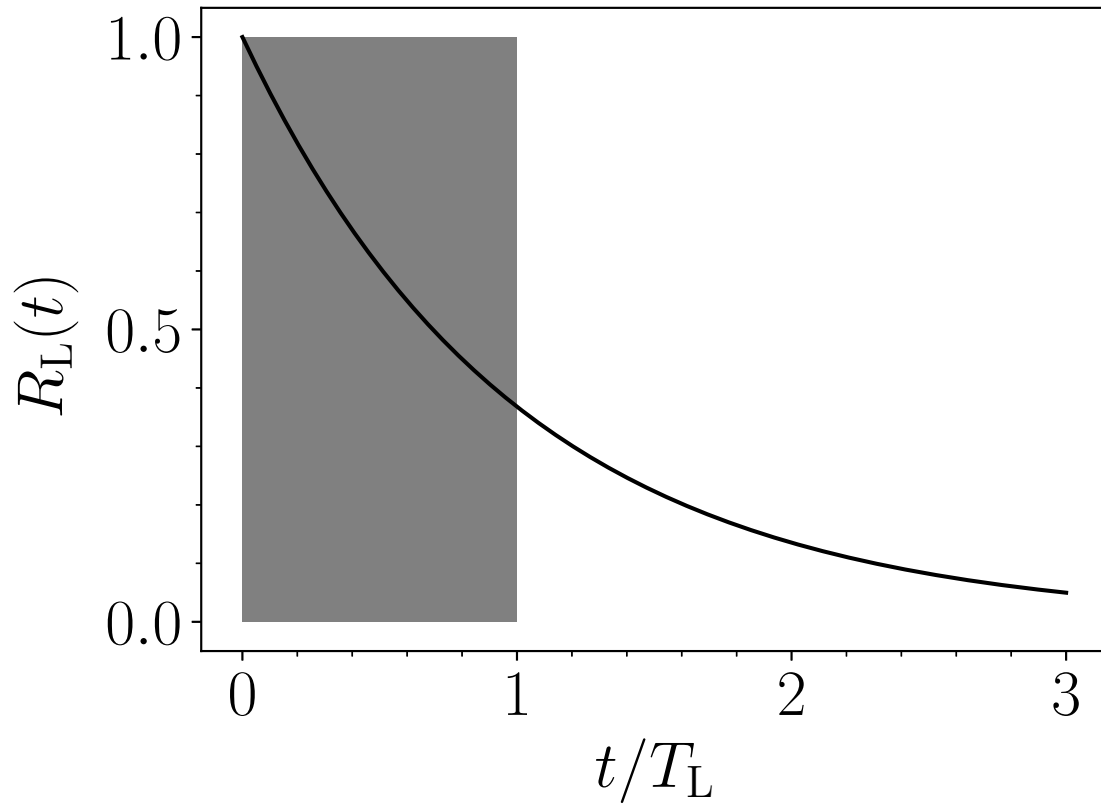
Figure 3.1: Lagrangian velocity autocorrelation function and its relationship to the Lagrangian time scale. The shaded area of the unit rectangle of time length T_{L} is equivalent to the total area under the autocorrelation function.

3.1.4 Turbulent Particle Dispersion Parameters for a Point Source

The Langevin model also allows us to calculate particle positions by integrating the particle velocity trajectories according to Eq. 3.13. Then the Lagrangian particle displacement covariance at time τ for a point source release at time t_0 in stationary, homogeneous turbulence is obtained as [54]

$$\sigma_{ij}(\tau) = \langle [x_i(\tau) - \langle x_i(\tau) \rangle] [x_j(\tau) - \langle x_j(\tau) \rangle] \rangle \tag{3.25a}$$

$$= \int_{t_0}^{t_0+\tau} \int_{t_0}^{t_0+\tau} \langle u_i(t_1) u_j(t_2) \rangle \, \mathrm{d}t_1 \mathrm{d}t_2, \tag{3.25b}$$

where $\tau = t - t_0$ is the time displacement. Since the turbulence is stationary and homogeneous, the fluctuating velocity is stationary, and it can be written in terms of the Lagrangian velocity autocorrelation depending only on the time difference using Eq. 3.23:

$$\langle u_i(t_1) u_j(t_2) \rangle = \left[\sigma_{u_i}^2 \sigma_{u_j}^2 \right]^{1/2} R_{ij}^{\mathrm{L}}(t_2 - t_1). \tag{3.26}$$

Defining the variable transform $\varphi(t_1, t_2) = [s(t_1, t_2), t(t_1, t_2)] = [t_2 - t_1, (t_1 + t_2)/2]$, the Jacobian determinant magnitude is

$$|\det J_\varphi(t_1, t_2)| = \left| \det \begin{bmatrix} \frac{\partial s}{\partial t_1} & \frac{\partial s}{\partial t_2} \\ \frac{\partial t}{\partial t_1} & \frac{\partial t}{\partial t_2} \end{bmatrix} \right| = \left| \det \begin{bmatrix} -1 & 1 \\ \frac{1}{2} & \frac{1}{2} \end{bmatrix} \right| = 1. \tag{3.27}$$

The region of integration $A = \{(t_1, t_2) : t_0 \leq t_1 \leq t_0 + \tau \wedge t_0 \leq t_2 \leq t_0 + \tau\}$ corresponds to the region

$$
\begin{aligned}
\varphi(A) &= \{ \varphi(t_1, t_2) : t_0 \leq t_1 \leq t_0 + \tau \wedge t_0 \leq t_2 \leq t_0 + \tau \} \\
&= \{ (t_2 - t_1, (t_1 + t_2)/2) : t_0 \leq t_1 \leq t_0 + \tau \wedge t_0 \leq t_2 \leq t_0 + \tau \} \\
&= \left\{ (s, t) : 0 \leq |s| \leq \tau \wedge t_0 + \frac{|s|}{2} \leq t \leq t_0 + \tau - \frac{|s|}{2} \right\}.
\end{aligned}
\tag{3.28}
$$

Then using the change of variables formula $\int_A f\left[\varphi(t_1, t_2)\right] |\det J_\varphi(t_1, t_2)| \, \mathrm{d}t_1 \mathrm{d}t_2 = \int_{\varphi(A)} f(s, t) \mathrm{d}t \mathrm{d}s$ for Eq. 3.25b with Eq. 3.26 substituted yields

$$\sigma_{ij}(\tau) = \left[\sigma_{u_i}^2 \sigma_{u_j}^2 \right]^{1/2} \int_{-\tau}^{\tau} \int_{t_0+\frac{|s|}{2}}^{t_0+\tau-\frac{|s|}{2}} R_{ij}^{\mathrm{L}}(s) \mathrm{d}t \mathrm{d}s. \tag{3.29}$$

Since Eq. 3.26 is symmetric, i.e. $R_{ij}^{\mathrm{L}}(-s) = R_{ji}^{\mathrm{L}}(s)$, we can integrate the right-hand side of Eq. 3.29 over the positive values of s [54]:

$$\sigma_{ij}(\tau) = \left[\sigma_{u_i}^2 \sigma_{u_j}^2\right]^{1/2} \int_0^\tau \int_{t_0+\frac{s}{2}}^{t_0+\tau-\frac{s}{2}} \left[R_{ij}^{\mathrm{L}}(s) + R_{ji}^{\mathrm{L}}(s)\right] \mathrm{d}t \mathrm{d}s \qquad (3.30a)$$

$$= \left[\sigma_{u_i}^2 \sigma_{u_j}^2\right]^{1/2} \int_0^\tau (\tau - s) \left[R_{ij}^{\mathrm{L}}(s) + R_{ji}^{\mathrm{L}}(s)\right] \mathrm{d}s, \qquad (3.30b)$$

where we have explicitly integrating with respect to t in the final step. Using Eq. 3.21b in 3.23, we can explicitly calculate the particle displacement variances in Eq. 3.30b for $i = j$ with $\sigma_{ii}(\tau) \equiv \sigma_i^2(\tau)$ and $T_{ii}^{\mathrm{L}} \equiv T_i^{\mathrm{L}}$:

$$\sigma_i^2(\tau) = 2\sigma_{u_i}^2 \int_0^\tau (\tau - s) e^{-s/T_i^{\mathrm{L}}} \mathrm{d}s$$

$$= 2\sigma_{u_i}^2 \left(\left[-\tau T_i^{\mathrm{L}} e^{-s/T_i^{\mathrm{L}}}\right]_0^\tau + \left[s T_i^{\mathrm{L}} e^{-s/T_i^{\mathrm{L}}}\right]_0^\tau - \int_0^\tau e^{-s/T_i^{\mathrm{L}}} \mathrm{d}s\right)$$

$$= 2\sigma_{u_i}^2 T_i^{\mathrm{L}} \left(\tau - \tau e^{-\tau/T_i^{\mathrm{L}}} + \tau e^{-\tau/T_i^{\mathrm{L}}} + T_i^{\mathrm{L}} \left[e^{-s/T_i^{\mathrm{L}}}\right]_0^\tau\right)$$

$$= 2\sigma_{u_i}^2 T_i^{\mathrm{L}} \left[\tau - T_i^{\mathrm{L}} \left(1 - e^{-\tau/T_i^{\mathrm{L}}}\right)\right]. \qquad (3.31)$$

Rearranging Eq. 3.31, and letting $\Delta U_i(\tau) = u_i(\tau) = U_i(\tau) - \langle U_i(\tau)\rangle$, $\Delta x_i(\tau) = x_i'(\tau) = x_i(\tau) - \langle x_i(\tau)\rangle$, and $\tau \simeq T_i^{\mathrm{L}}$, we obtain

$$\frac{\langle \Delta U_i^2(T_i^{\mathrm{L}})\rangle^{1/2}}{\langle \Delta x_i^2(T_i^{\mathrm{L}})\rangle^{1/2}} = \sqrt{\frac{\sigma_{u_i}^2}{\sigma_i^2(T_i^{\mathrm{L}})}} = \frac{e^{1/2}}{\sqrt{2}} \frac{1}{T_i^{\mathrm{L}}} \approx \frac{1.17}{T_i^{\mathrm{L}}}. \qquad (3.32)$$

We can interpret this result by treating the ratio of the root mean square (RMS) velocity fluctuation to the RMS particle displacement on the left-hand side, as a mean velocity gradient along the particle trajectory. This is justified by the fact that the variance is not affected by a constant shift according to Eq. 2.79, so $\sigma_{u_i}^2 = \sigma_{U_i}^2$, so that

$$\sqrt{\frac{\sigma_{u_i}^2}{\sigma_i^2(T_i^{\mathrm{L}})}} = \sqrt{\frac{\sigma_{U_i}^2}{\sigma_{x_i}^2(T_{\mathrm{L}})}} \simeq \frac{\partial \langle U_i(t)\rangle}{\partial x_i}. \qquad (3.33)$$

This latter equivalence approximation in Eq. 3.33 is somewhat subtle. The first and second terms are written in terms of a RMS velocity and position, which represent the Lagrangian particle displacement along its trajectory. The final term written in terms of the mean velocity

gradient along this trajectory relies on the fact that the mean turbulent velocity change is zero by definition. Equation 3.32 then indicates that the velocity gradient is approximately constant over the Lagrangian time scale, where the constant is *approximately* the inverse Lagrangian time scale:

$$\frac{\partial \langle U(t) \rangle}{\partial x} \simeq \frac{1}{T_{\mathrm{L}}}. \tag{3.34}$$

This leads to Eq. 3.17 proposed in section 3.1.2.2. Another way of seeing this is to integrate the particle trajectories over some averaging time scale. When observing particle trajectories over a time period similar to the Lagrangian time scale, the ratio of the time-averaged mean velocity to the time-averaged mean particle displacement is also on the order of the inverse Lagrangian time scale. Although the Langevin Eq. 3.1 or 3.18 does not represent spatial dependence of turbulent velocity $\mathbf{u}$ explicitly, we represent the dependence implicitly via the autocorrelation function $R_{ii}^{\mathrm{L}}(t)$ integrated over time in Eq. 3.31, with the understanding that $R_{ii}^{\mathrm{L}}(t)$ represents a measure or extent of the velocity propagation over time t. The autocorrelation function $R_{ii}^{\mathrm{L}}(t)$ can then be used to determine the Lagrangian time scale T_{ii}^{L} by Eq. 3.22, with the parameterization depending on atmospheric conditions as discussed in section 5.3.2.

3.2   Alternate Langevin Models

In sections 3.1.1 and 3.1.2, we presented and derived directly from the turbulent Navier-Stokes Eq. 3.12 the turbulent velocity DD model Eq. 3.1 used by FLEXPART and HYSPLIT. Furthermore, we clarified in sections 3.1.3 and 3.1.4 how FLEXPART uses the velocity autocorrelation function to represent velocity propagation with the Lagrangian time scale. We present in sections 3.2.1 through 3.2.3 some alternative Langevin models commonly encountered in the literature and argue that these models are either not physically suitable or representative of specifically the FLEXPART model of the turbulent Navier-Stokes equation. This is not necessarily to say that these alternate models are unsuitable under some circumstances or that they are less accurate models than FLEXPART. Rather, this is to emphasize specifically that the derivation presented in section 3.1 is the correct model representation for FLEXPART.

3.2.1   Normalized Turbulent Velocity Langevin Drift-diffusion

For long integration time steps, FLEXPART uses the turbulent velocity DD model of the form in Eq. 3.1 [1, 2]. Alternatively, one can form a Langevin model for the normalized turbulent velocity u_i/σ_{u_i} which is used (with the addition of a density correction term) by

FLEXPART for short integration time steps [1, 2]:

$$\frac{\mathrm{d}}{\mathrm{d}t}\left(\frac{u_i(t)}{\sigma_{u_i}(t)}\right) = -\frac{u_i(t)}{\sigma_{u_i}(t)T_{ii}^{\mathrm{L}}} + \frac{\partial \sigma_{u_i}}{\partial x_i} + \left(\frac{2}{T_{ii}^{\mathrm{L}}}\right)^{1/2}\xi_i(t). \tag{3.35}$$

Equation 3.35 for stationary, inhomogeneous turbulence was originally proposed by Wilson [80] but was rigorously derived by Thomson [81] and shown to fulfill the well-mixed criterion [82]. However, Minier [42] showed that Eq. 3.35:

1. depends on whether or not the coordinate reference system is aligned with the principal axes of $\langle u_i u_j \rangle$ or not for even homogeneous anisotropic turbulence

2. results in spurious drifts for general inhomogeneous flows

Furthermore, generalizations of the normalized turbulent velocity Langevin model Eq. 3.35 were shown by Minier [42] to not produce the correct Reynolds-stress equations. Thus, normalized turbulent velocity Langevin DD models are inconsistent with the turbulent Navier-Stokes equation and are therefore unsuitable for inhomogeneous turbulent flows. In contrast, the turbulent velocity Langevin DD model presented in section 3.1 is consistent with the turbulent Navier-Stokes equation and has the proper drift correction necessary for inhomogeneous turbulent flows.

3.2.2 Generalized Langevin Model (GLM)

Pope [39] suggests an alternate Langevin model for the turbulent velocity component, which he refers to as the generalized Langevin model (GLM):

$$\frac{\mathrm{d}u_i}{\mathrm{d}t} = -u_j\frac{\partial \langle U_i \rangle}{\partial x_j} + \frac{\partial}{\partial x_j}\langle u_i u_j \rangle + G_{ij}u_j + (C_0\varepsilon)^{1/2}\xi_i(t), \tag{3.36}$$

where

$$\varepsilon(\mathbf{x}, t) \equiv 2\nu \left\langle e'_{ij}e'_{ij}\right\rangle \tag{3.37}$$

is the turbulent kinetic energy dissipation rate with fluctuating rate of strain tensor—the difference of Eqs. 2.23 and 4.2—given by

$$e'_{ij} \equiv e_{ij} - \langle e_{ij} \rangle = \frac{1}{2}\left(\frac{\partial u_i}{\partial x_j} + \frac{\partial u_j}{\partial x_i}\right). \tag{3.38}$$

Equation 3.37 is analogous to the mechanical energy dissipation rate $\dot{E}_\nu$ in Eq. 2.59 but for the turbulent velocity in an incompressible flow. $G_{ij}(\mathbf{x}, t)$ and $C_0(\mathbf{x}, t)$ are coefficients for the particular model, with G_{ij} having dimensions of inverse time and C_0 being non-dimensional. In general, G_{ij} and C_0 might depend on the local Reynolds stresses $\langle u_k u_\ell \rangle$, velocity gradients $\partial \langle U_m \rangle / \partial x_n$, and dissipation rate ε [39, 83]. Comparing Eqs. 3.36 and 3.12, we note that this models the pressure fluctuation and viscous forcing terms collectively as

$$\frac{1}{\rho} f_i = G_{ij} u_j + (C_0 \varepsilon)^{1/2} \xi_i(t). \tag{3.39}$$

In contrast, we simply model the stochastic force in terms of the Gaussian white noise alone: $f_i/\rho = \lambda_i \xi_i(t)$, where $\lambda_i = \left(2\sigma_{u_i}^2 / T_{ii}^{\mathrm{L}} \right)^{1/2}$.

Furthermore, in contrast to the simple physical model we propose in Eq. 3.34 in which the mean velocity gradient is modeled using the Lagrangian time scale, Pope uses a second-order closure model for the Reynolds stress in order to derive various models for G_{ij} and C_0. Pope [39] presents several models based on the probability density function (PDF) for the turbulent velocity. These are derived from the fine-grained PDF $f'_{\mathbf{u}}(\hat{\mathbf{u}}; \mathbf{x}, t) \equiv \delta \left[\mathbf{u}(\mathbf{x}, t) - \hat{\mathbf{u}} \right]$ and written in terms of the Dirac delta function to produce a PDF transport equation, and the physics is incorporated through the expected value of the Lagrangian derivative of the turbulent velocity. This PDF transport equation is in the form of a Fokker-Planck equation, with force term modeled as in Eq. 3.39, which can then be transformed into an equivalent Langevin equation like Eq. 3.36 using the results of sections 2.4.3.4 or 2.4.3.5 and Eqs. 2.145. This PDF model can be used to derive a second-order closure model based on the modeled Reynolds stress equation, and the comparison with the Reynolds stress equation places constraints on the values of G_{ij} and C_0. In the PDF approach, the Langevin equation derived from the Navier-Stokes equation depends on how the Lagrangian time scale and force terms are modeled.

Instead of using a PDF-based approach to determine G_{ij} and C_0, we can derive the second-order closure model for the Reynolds stress equations directly from Eqs. 3.12 and 3.36. In section 3.2.2.1 we derive the exact Reynolds stress transport model directly from Eq. 3.12, while in section 3.2.2.2 we derive the Reynolds stress transport model corresponding to the GLM Eq. 3.36. The method for deriving the Reynolds stress models uses the product rule with the addition of two symmetric variants of the equation. Then by comparing the exact and GLM Reynolds stress transport equations, one is then able to constrain G_{ij} and C_0 in the GLM in order to be consistent with the second-order Reynolds stress model.

3.2.2.1 Exact Reynolds Stress Transport Model

First multiply the left-hand side of Eq. 3.12 by u_j, yielding $u_j \mathrm{D} u_i / \mathrm{D} t$. Then interchanging the indices i and j, adding the two terms and using the product rule, we find

$$
\begin{aligned}
u_j \frac{\mathrm{D} u_i}{\mathrm{D} t} + u_i \frac{\mathrm{D} u_j}{\mathrm{D} t} &= u_j \frac{\partial u_i}{\partial t} + u_i \frac{\partial u_j}{\partial t} + u_j U_k \frac{\partial u_i}{\partial x_k} + u_i U_k \frac{\partial u_j}{\partial x_k} \\
&= \frac{\partial u_i u_j}{\partial t} + U_k \frac{\partial u_i u_j}{\partial x_k} \\
&= \frac{\mathrm{D} u_i u_j}{\mathrm{D} t}.
\end{aligned}
\tag{3.40}
$$

Ensemble-averaging Eq. 3.40 yields, for an incompressible fluid,

$$
\begin{aligned}
\left\langle \frac{\mathrm{D} u_i u_j}{\mathrm{D} t} \right\rangle &= \frac{\partial \langle u_i u_j \rangle}{\partial t} + \left\langle U_k \frac{\partial u_i u_j}{\partial x_k} \right\rangle \\
&= \frac{\partial \langle u_i u_j \rangle}{\partial t} + \langle U_k \rangle \frac{\partial \langle u_i u_j \rangle}{\partial x_k} + \left\langle u_k \frac{\partial u_i u_j}{\partial x_k} \right\rangle \\
&= \frac{\overline{\mathrm{D}} \langle u_i u_j \rangle}{\overline{\mathrm{D}} t} + \frac{\partial \langle u_i u_j u_k \rangle}{\partial x_k}.
\end{aligned}
\tag{3.41}
$$

Applying the same procedure to the right-hand side of Eq. 3.12 one term at a time, we obtain the terms [39]:

- Production tensor

$$
\begin{aligned}
\mathcal{P}_{ij} &= -\left\langle u_j u_k \frac{\partial \langle U_i \rangle}{\partial x_k} + u_i u_k \frac{\partial \langle U_j \rangle}{\partial x_k} \right\rangle \\
&\equiv -\langle u_j u_k \rangle \frac{\partial \langle U_i \rangle}{\partial x_k} - \langle u_i u_k \rangle \frac{\partial \langle U_j \rangle}{\partial x_k}.
\end{aligned}
\tag{3.42}
$$

- Velocity-pressure-gradient tensor

$$
\begin{aligned}
\Pi_{ij} &\equiv \left\langle -\frac{1}{\rho} u_j f_i^{(p)} - \frac{1}{\rho} u_i f_j^{(p)} \right\rangle \\
&\equiv -\frac{1}{\rho} \left\langle u_j \frac{\partial p'}{\partial x_i} + u_i \frac{\partial p'}{\partial x_j} \right\rangle \\
&= -\frac{1}{\rho} \left\langle \frac{\partial u_j p'}{\partial x_i} - p' \frac{\partial u_j}{\partial x_i} + \frac{\partial u_i p'}{\partial x_j} - p' \frac{\partial u_i}{\partial x_j} \right\rangle \\
&= \left\langle \frac{p'}{\rho} \left(\frac{\partial u_i}{\partial x_j} + \frac{\partial u_j}{\partial x_i} \right) \right\rangle - \frac{\partial}{\partial x_k} \left(\frac{1}{\rho} \langle u_i p' \rangle \delta_{jk} + \frac{1}{\rho} \langle u_j p' \rangle \delta_{ik} \right) \\
&= \mathcal{R}_{ij} - \frac{\partial}{\partial x_k} T_{kij}^{(p)},
\end{aligned}
$$

(3.43)

(3.44)

where

$$
\begin{aligned}
\mathcal{R}_{ij} &\equiv \left\langle \frac{p'}{\rho} \left(\frac{\partial u_i}{\partial x_j} + \frac{\partial u_j}{\partial x_i} \right) \right\rangle \\
&= 2 \left\langle \frac{p' e'_{ij}}{\rho} \right\rangle
\end{aligned}
$$

(3.45)

is the pressure-rate-of-strain tensor, and

$$
T_{kij}^{(p)} \equiv \frac{1}{\rho} \langle u_i p' \rangle \delta_{jk} + \frac{1}{\rho} \langle u_j p' \rangle \delta_{ik}
$$

(3.46)

is the Reynolds stress flux due to pressure fluctuations.

- Viscous dissipation tensor

$$
\begin{aligned}
\left\langle -\frac{1}{\rho} u_j f_i^{(\nu)} - \frac{1}{\rho} u_i f_j^{(\nu)} \right\rangle &= \nu \left\langle u_j \nabla^2 u_i + u_i \nabla^2 u_j \right\rangle \\
&= \nu \left\langle u_j \frac{\partial^2 u_i}{\partial x_k \partial x_k} + u_i \frac{\partial^2 u_j}{\partial x_k \partial x_k} \right\rangle \\
&= \nu \left\langle \frac{\partial}{\partial x_k} \left(u_j \frac{\partial u_i}{\partial x_k} \right) - \frac{\partial u_j}{\partial x_k} \frac{\partial u_i}{\partial x_k} + \frac{\partial}{\partial x_k} \left(u_i \frac{\partial u_j}{\partial x_k} \right) - \frac{\partial u_i}{\partial x_k} \frac{\partial u_j}{\partial x_k} \right\rangle \\
&= -2\nu \left\langle \frac{\partial u_i}{\partial x_k} \frac{\partial u_j}{\partial x_k} \right\rangle \\
&\quad + \nu \left\langle \frac{\partial}{\partial x_k} \left(\frac{\partial u_j u_i}{\partial x_k} - u_i \frac{\partial u_j}{\partial x_k} \right) + \frac{\partial}{\partial x_k} \left(\frac{\partial u_i u_j}{\partial x_k} - u_j \frac{\partial u_i}{\partial x_k} \right) \right\rangle \\
&= -\varepsilon_{ij} + \nu \left\langle 2\nabla^2 u_i u_j - \frac{\partial}{\partial x_k} \left(u_i \frac{\partial u_j}{\partial x_k} + u_j \frac{\partial u_i}{\partial x_k} \right) \right\rangle \\
&= -\varepsilon_{ij} + \nu \nabla^2 \langle u_i u_j \rangle,
\end{aligned}
$$

(3.47)

where

$$\varepsilon_{ij} \equiv 2\nu \left\langle \frac{\partial u_i}{\partial x_k} \frac{\partial u_j}{\partial x_k} \right\rangle \tag{3.48}$$

is the dissipation tensor.

- Coriolis tensor

$$\left\langle \frac{1}{\rho} u_j f_{\text{Coriolis},i} + \frac{1}{\rho} u_i f_{\text{Coriolis},j} \right\rangle = -2\varepsilon_{i\ell k}\Omega_\ell \left\langle u_j u_k \right\rangle - 2\varepsilon_{j\ell k}\Omega_\ell \left\langle u_i u_k \right\rangle. \tag{3.49}$$

Typically, the Coriolis tensor can be neglected compared to the production, velocity-pressure-gradient, and viscous dissipation tensors [53].

Combining all the terms in Eqs. 3.41, 3.42, 3.43, and 3.47 results in the (exact) Reynolds stress transport equation [39]

$$\frac{\overline{D} \left\langle u_i u_j \right\rangle}{\overline{D}t} = \mathcal{P}_{ij} + \Pi_{ij} - \varepsilon_{ij} + \nu \nabla^2 \left\langle u_i u_j \right\rangle - \frac{\partial \left\langle u_i u_j u_k \right\rangle}{\partial x_k} \tag{3.50a}$$

$$= \mathcal{P}_{ij} + \mathcal{R}_{ij} - \varepsilon_{ij} - \frac{\partial T_{kij}}{\partial x_k}, \tag{3.50b}$$

where

$$T_{kij} \equiv T_{kij}^{(u)} + T_{kij}^{(p)} + T_{kij}^{(\nu)}, \tag{3.51a}$$

$$T_{kij}^{(u)} \equiv \left\langle u_i u_j u_k \right\rangle, \tag{3.51b}$$

$$T_{kij}^{(p)} \equiv \frac{1}{\rho} \left\langle u_i p' \right\rangle \delta_{jk} + \frac{1}{\rho} \left\langle u_j p' \right\rangle \delta_{ik}, \tag{3.51c}$$

$$T_{kij}^{(\nu)} \equiv -\nu \frac{\partial \left\langle u_i u_j \right\rangle}{\partial x_k}, \tag{3.51d}$$

are the total Reynolds stress fluxes, and Reynolds stress fluxes due to fluctuating velocity Eq. 3.51b, pressure Eq. 3.51c, and viscosity Eq. 3.51d.

3.2.2.2   GLM Reynolds Stress Transport Model

Using the reverse of the procedure described in section 3.1.2.2 for deriving the Langevin Eq. 3.16 from the turbulent Navier-Stokes Eq. 3.12, starting from step four, Eq. 3.36 corresponds to the Eulerian equation

$$\frac{Du_i}{Dt} = -u_j \frac{\partial \left\langle U_i \right\rangle}{\partial x_j} + \frac{\partial}{\partial x_j} \left\langle u_i u_j \right\rangle + G_{ij} u_j + (C_0 \varepsilon)^{1/2} \xi_i(t). \tag{3.52}$$

Then using the same procedure as in section 3.2.2.1, the model terms in Eq. 3.52 result in the Reynolds stress transport model terms:

- Modeled linear drift tensor

$$\langle G_{ik}u_ju_k + G_{jk}u_iu_k \rangle = G_{ik}\langle u_ju_k \rangle + G_{jk}\langle u_iu_k \rangle. \tag{3.53}$$

- Modeled diffusion tensor

$$\left\langle (C_0\varepsilon)^{1/2} u_j\xi_i(t) + (C_0\varepsilon)^{1/2} u_i\xi_j(t) \right\rangle = (C_0\varepsilon)^{1/2} \langle u_j\xi_i(t) \rangle + (C_0\varepsilon)^{1/2} \langle u_i\xi_j(t) \rangle. \tag{3.54}$$

The term $\langle u_j\xi_i(t) \rangle$ can be calculated by using the integral form of Eq. 3.52,

$$u_i(t) = u_i(t_0) + \int_{t_0}^{t} \left[-u_j \frac{\partial \langle U_i \rangle}{\partial x_j} + \frac{\partial}{\partial x_j} \langle u_iu_j \rangle + G_{ij}u_j \right] \mathrm{d}t' + \int_{t_0}^{t} (C_0\varepsilon)^{1/2} \xi_i(t') \mathrm{d}t'. \tag{3.55}$$

Thus

$$
\begin{aligned}
\langle u_j\xi_i(t) \rangle &= \langle u_j(t_0)\xi_i(t) \rangle + \int_{t_0}^{t} \left[-\langle u_k(t')\xi_i(t) \rangle \frac{\partial \langle U_j \rangle}{\partial x_k} + G_{jk}\langle u_k(t')\xi_i(t) \rangle \right] \mathrm{d}t' \\
&\quad + (C_0\varepsilon)^{1/2} \int_{t_0}^{t} \langle \xi_i(t)\xi_j(t') \rangle \, \mathrm{d}t' \\
&= (C_0\varepsilon)^{1/2} \int_{t_0}^{t} \delta(t - t')\delta_{ij}\mathrm{d}t' \\
&= \frac{1}{2} (C_0\varepsilon)^{1/2} \delta_{ij}.
\end{aligned}
\tag{3.56}
$$

Note that in the second step the terms with $\langle u_j(t')\xi_i(t) \rangle = 0$ for $t' \neq t$ since the white noise is uncorrelated with the turbulent velocity process itself. In the final step, the Dirac delta integral is halved since t is on the boundary of the integration domain. Substituting Eq. 3.56 into Eq. 3.54 yields the modeled diffusion tensor

$$(C_0\varepsilon)^{1/2} \langle u_j\xi_i(t) \rangle + (C_0\varepsilon)^{1/2} \langle u_i\xi_j(t) \rangle = C_0\varepsilon\delta_{ij}. \tag{3.57}$$

Another way to calculate the modeled diffusion tensor is to use the correspondence between the Langevin and Fokker-Planck diffusion coefficients $b_{ij} = (C_0\varepsilon)^{1/2} \delta_{ij}$ and $B_{ij} = b_{ik}b_{jk} = C_0\varepsilon\delta_{ij}$, respectively, from section 2.4.3.4 and Eq. 2.145b. Then the Reynolds stress transport equation modeled diffusion term is given by the Fokker-Planck

diffusion term in Eq. 2.117 multiplied by $\hat{u}_i \hat{u}_j$ and integrated over the velocity space:

$$
\begin{aligned}
\int \frac{\hat{u}_i \hat{u}_j}{2} \frac{\partial^2}{\partial \hat{u}_k \partial \hat{u}_\ell} \left[B_{k\ell}\left(\hat{\mathbf{u}}, \mathbf{x}, t\right) f_{\mathbf{u}}\left(\hat{\mathbf{u}}; \mathbf{x}, t\right) \right] \mathrm{d}\hat{\mathbf{u}} &= \frac{1}{2} \int \left[B_{k\ell}\left(\hat{\mathbf{u}}, \mathbf{x}, t\right) f_{\mathbf{u}}\left(\hat{\mathbf{u}}; \mathbf{x}, t\right) \right] \frac{\partial^2 \hat{u}_i \hat{u}_j}{\partial \hat{u}_k \partial \hat{u}_\ell} \mathrm{d}\hat{\mathbf{u}} \\
&= \frac{1}{2} \int \left[B_{k\ell}\left(\hat{\mathbf{u}}, \mathbf{x}, t\right) f_{\mathbf{u}}\left(\hat{\mathbf{u}}; \mathbf{x}, t\right) \right] \delta_{ik}\delta_{j\ell} \mathrm{d}\hat{\mathbf{u}} \\
&+ \frac{1}{2} \int \left[B_{k\ell}\left(\hat{\mathbf{u}}, \mathbf{x}, t\right) f_{\mathbf{u}}\left(\hat{\mathbf{u}}; \mathbf{x}, t\right) \right] \delta_{jk}\delta_{i\ell} \mathrm{d}\hat{\mathbf{u}} \\
&= \frac{1}{2} \int \left[B_{ij}\left(\hat{\mathbf{u}}, \mathbf{x}, t\right) f_{\mathbf{u}}\left(\hat{\mathbf{u}}; \mathbf{x}, t\right) \right] \mathrm{d}\hat{\mathbf{u}} \\
&+ \frac{1}{2} \int \left[B_{ji}\left(\hat{\mathbf{u}}, \mathbf{x}, t\right) f_{\mathbf{u}}\left(\hat{\mathbf{u}}; \mathbf{x}, t\right) \right] \mathrm{d}\hat{\mathbf{u}} \\
&= \frac{1}{2} \left[\langle B_{ij}\left(\mathbf{u}, \mathbf{x}, t\right) \rangle + \langle B_{ji}\left(\mathbf{u}, \mathbf{x}, t\right) \rangle \right] \\
&= \frac{1}{2} \left(C_0 \varepsilon \delta_{ij} + C_0 \varepsilon \delta_{ji} \right) \\
&= C_0 \varepsilon \delta_{ij}.
\end{aligned}
$$

Note that we have used the product rule twice in the first step with the surface terms vanishing due to the distribution vanishing at the boundary.

Combining the modeled linear drift and diffusion terms with the production term results in the Reynolds stress transport model [39]

$$
\frac{\overline{\mathrm{D}} \langle u_i u_j \rangle}{\overline{\mathrm{D}t}} = \mathcal{P}_{ij} + G_{ik} \langle u_j u_k \rangle + G_{jk} \langle u_i u_k \rangle + C_0 \varepsilon \delta_{ij} - \frac{\partial \langle u_i u_j u_k \rangle}{\partial x_k}. \tag{3.58}
$$

Comparing the exact Reynolds stress transport model Eqs. 3.50 and the GLM Reynolds stress transport Eq. 3.58, the two models are consistent when

$$
G_{ik} \langle u_j u_k \rangle + G_{jk} \langle u_i u_k \rangle + C_0 \varepsilon \delta_{ij} = \Pi_{ij} - \varepsilon_{ij} + \nu \nabla^2 \langle u_i u_j \rangle \tag{3.59a}
$$

$$
= \mathcal{R}_{ij} - \varepsilon_{ij} - \frac{\partial}{\partial x_k} T_{kij}^{(p)} - \frac{\partial}{\partial x_k} T_{kij}^{(\nu)}. \tag{3.59b}
$$

3.2.3 Simplified, LRR-IP, and Haworth–Pope Models

Here we present several alternate models which are based on the results of section 3.2.2.2 and Eqs. 3.59 to compare with the model we propose in Eq. 3.34. When pressure and viscous transport are neglected, Eq. 3.59b simplifies to [39]

$$
G_{ik} \langle u_j u_k \rangle + G_{jk} \langle u_i u_k \rangle + C_0 \varepsilon \delta_{ij} \approx \mathcal{R}_{ij} - \varepsilon_{ij}, \tag{3.60}
$$

and the coefficients G_{ij} and C_0 correspond to the pressure rate of strain tensor and viscous dissipation. If the dissipation is isotropic, such as in high Reynolds number flows, the dissipation tensor can be written as [39]

$$\varepsilon_{ij} = \frac{2}{3}\varepsilon\delta_{ij}, \tag{3.61}$$

and Eq. 3.60 reduces to [39]

$$G_{ik}\langle u_j u_k\rangle + G_{jk}\langle u_i u_k\rangle + \left(\frac{2}{3} + C_0\right)\varepsilon\delta_{ij} \approx \mathcal{R}_{ij}. \tag{3.62}$$

Finally, for $\mathcal{R}_{ij}$ to be redistributive, one requires that $\mathcal{R}_{ii} = 0$, and Eq. 3.62 becomes the simple constraint [39]

$$\mathcal{R}_{ii} = \mathcal{R}_{ij}\delta_{ij} = 0$$

$$\Rightarrow G_{ik}\langle u_j u_k\rangle\delta_{ij} + G_{jk}\langle u_i u_k\rangle\delta_{ij} + \left(\frac{2}{3} + C_0\right)\varepsilon\delta_{ij}\delta_{ij} \approx 0$$

$$\Rightarrow 2G_{ij}\langle u_i u_j\rangle + 3\left(\frac{2}{3} + C_0\right)\varepsilon = 0$$

$$\Rightarrow \left(1 + \frac{3}{2}C_0\right)\varepsilon + G_{ij}\langle u_i u_j\rangle = 0. \tag{3.63}$$

For the simplified Langevin model (SLM) [77, 84], the drift coefficient G_{ij} is isotropic:

$$G_{ij} = -\frac{\delta_{ij}}{T_{\mathrm{L}}}, \tag{3.64}$$

where T_{L} is the Lagrangian time scale. Substituting Eq. 3.64 into Eq. 3.63, the Lagrangian time scale is [39]

$$\left(1 + \frac{3}{2}C_0\right)\varepsilon - \frac{\delta_{ij}}{T_{\mathrm{L}}}\langle u_i u_j\rangle = 0$$

$$\Rightarrow \left(1 + \frac{3}{2}C_0\right)\varepsilon - \frac{2k}{T_{\mathrm{L}}} = 0$$

$$\Rightarrow T_{\mathrm{L}} = 2\left(\frac{1}{2} + \frac{3}{4}C_0\right)^{-1}\tau, \tag{3.65}$$

where C_0 is a non-negative constant, and

$$k \equiv \frac{1}{2} \langle \mathbf{u} \cdot \mathbf{u} \rangle = \frac{1}{2} \langle u_i u_i \rangle \tag{3.66}$$

$$\tau \equiv \frac{k}{\varepsilon} \tag{3.67}$$

are the turbulent kinetic energy (TKE) and TKE dissipation time scale, respectively. Similarly, substituting Eq. 3.65 into Eq. 3.64, the linear drift coefficient for the SLM is

$$G_{ij} = -\frac{\delta_{ij}}{T_{\mathrm{L}}} = -\left(\frac{1}{2} + \frac{3}{4} C_0 \right) \frac{\delta_{ij}}{\tau}. \tag{3.68}$$

The SLM corresponds to Rotta's linear return to isotropy turbulence model [85] with

$$C_{\mathrm{R}} = 1 + \frac{3}{2} C_0. \tag{3.69}$$

A model incorporating both slow (from Rotta's model) and rapid pressure fluctuations is the isotropization of production LRR-IP model [86], for which

$$G_{ij} = -\frac{1}{2} C_{\mathrm{R}} \frac{\delta_{ij}}{\tau} + C_2 \frac{\partial \langle U_i \rangle}{\partial x_j}, \tag{3.70}$$

where

$$C_{\mathrm{R}} = 1 + \frac{3}{2} C_0 + C_2 \frac{\langle u_i u_j \rangle}{\varepsilon} \frac{\partial \langle U_i \rangle}{\partial x_j}. \tag{3.71}$$

The most general form of G_{ij} depending linearly on the Reynolds stresses $\langle u_i u_j \rangle$, mean velocity gradients $\partial \langle U_k \rangle / \partial x_\ell$, and dissipation rate τ is perhaps that of Haworth and Pope [77, 83]:

$$G_{ij} = \frac{\alpha_1 \delta_{ij} + \alpha_2 b_{ij} + \alpha_3 b_{ij}^2}{\tau} + H_{ijk\ell} \frac{\partial \langle U_k \rangle}{\partial x_\ell}, \tag{3.72}$$

where

$$b_{ij} = \frac{\langle u_i u_j \rangle}{2k} - \frac{1}{3} \delta_{ij} \tag{3.73}$$

is the normalized Reynolds stress anisotropy tensor, and H is the fourth-order tensor

$$\begin{aligned} H_{ijk\ell} = {} & \beta_1 \delta_{ij} \delta_{k\ell} + \beta_2 \delta_{ik} \delta_{j\ell} + \beta_3 \delta_{i\ell} \delta_{jk} \\ & + \gamma_1 \delta_{ij} b_{k\ell} + \gamma_2 \delta_{ik} b_{j\ell} + \gamma_3 \delta_{i\ell} b_{jk} \\ & + \gamma_4 b_{ij} \delta_{k\ell} + \gamma_5 b_{ik} \delta_{j\ell} + \gamma_6 b_{i\ell} \delta_{jk}. \end{aligned} \tag{3.74}$$

Constraints are placed on the coefficients through Eqs. 3.59, so the 12 coefficients (α, β, γ) can depend on scalar invariants of the normalized Reynolds stress anisotropy tensor b_{ij} and the normalized rate of strain and rotation tensors $\tau \langle e_{ij} \rangle$ and $\tau \langle r_{ij} \rangle$, such as $b' = |b_{ii}|$ and $P/\varepsilon = -2\tau b_{ij} \langle e_{ij} \rangle$ [77]. It is implicitly *assumed* here that G_{ij} is inversely proportional to the Lagrangian time scale T_{ij}^{L}, so the Lagrangian time scale would depend on Reynolds stresses $\langle u_i u_j \rangle$, mean velocity gradients $\partial \langle U_k \rangle / \partial x_\ell$, and dissipation rate τ.

3.2.4   Contrast with Proposed Drift-diffusion Langevin Model

Thus, there are two key differences between our drift-diffusion Langevin model proposed in sections 3.1.2.2 and 3.1.3 and alternate models suggested by Pope and others in sections 3.2.2 and 3.2.3:

1. Our stochastic force term is modeled using only a Gaussian white noise process alone, rather than also including a drift term linearly proportional to the turbulent velocity $G_{ij} u_j$.

2. In our model, the Lagrangian time scale T_{L} depends only on the time scale of the mean velocity gradient, whereas in the second-order closure models presented by Pope and others, the Lagrangian time scale is derived in terms of the dissipation time scale $\tau = k/\varepsilon$.

With these two differences, we obtain the correct form of the Langevin model used in FLEXPART and HYSPLIT directly from the turbulent Navier-Stokes equation with a model for the Lagrangian time scale written in terms of the mean velocity gradient alone. Our Lagrangian time scale model characterizes the velocity autocorrelation in the FLEXPART and HYSPLIT models rather than the Reynolds stress models represented by Pope and others. Using the alternate models, on the other hand, results in an additional mean velocity gradient drift term, $u_j \partial \langle U_i \rangle / \partial x_j$, appearing in the Langevin model, which is not present in the FLEXPART or HYSPLIT models.

Chapter 4

Eulerian Physical Models

In chapter 3 we discussed Lagrangian models in the form of Langevin equations for the turbulent fluid flow velocity field **u** which are based on the turbulent Navier-Stokes Eq. 3.12 following a Lagrangian particle trajectory. As mentioned briefly in sections 2.3, 3.1.1 and 3.1.2.2, FLEXPART and HYSPLIT determine the mean fluid fields from the meteorological data input on fixed Eulerian grids, which is described in more detail in section 5.1. One can instead determine the mean fluid fields in the Eulerian frame of reference by solving the mean conservation laws, as is done by computational fluid dynamics (CFD) models or advection-diffusion (AD) models. CFD codes have the ability to perform turbulent flow simulation to produce several realizations of the fields which can be used to represent the random variation in the field solutions, or they can employ algebraic or transport turbulence models for the mean fields [39]. This latter method we discuss briefly in section 4.1 with a focus on the k-ε model. Advection-diffusion models instead directly solve for the mean mass concentration field of a species in a turbulent fluid as discussed in section 4.2.

4.1 Computational Fluid Dynamics (CFD) Models

There are many different proprietary and open source (e.g. OpenFOAM) CFD codes available for solving the conservation laws discussed in section 2.2 in turbulent fluids. The simplest and most common models are based on the RANS Eqs. 3.7 or 3.9, where one must employ a turbulence closure model for the Reynolds stress $\langle u_i u_j \rangle$. Turbulence models include first-order eddy viscosity models such as the k-ε and k-ω models or second-order Reynolds stress models which use Eqs. 3.50. Some CFD codes also support more sophisticated models such as large eddy simulation (LES) and direct numerical simulation (DNS) in which the largest or all turbulence scales, respectively, are directly resolved and thus do not require a turbulence model. As indicated suggested in chapter 2, however, these are computationally impractical for the global scale ATMs of interest. Thus, we will focus here only on perhaps the simplest

and most common turbulence model, the RANS eddy viscosity k-ε model.

4.1.1 RANS Eddy Viscosity

In order to solve Eq. 3.7, one must employ a turbulence model for the Reynolds stress term. One of the simplest models is a linear turbulent viscosity model [39]

$$\langle u_i u_j \rangle = \frac{2}{3} k \delta_{ij} - 2\nu_{\mathrm{T}} \langle e_{ij} \rangle , \qquad (4.1)$$

where k is the TKE from Eq. 3.66, $\nu_{\mathrm{T}}(\mathbf{x}, t)$ is the *turbulent viscosity* or *eddy viscosity*, and

$$\langle e_{ij} \rangle = \frac{1}{2} \left(\frac{\partial \langle U_i \rangle}{\partial x_j} + \frac{\partial \langle U_j \rangle}{\partial x_i} \right) \qquad (4.2)$$

is the mean rate of strain tensor based on Eq. 2.23. Thus, the turbulent viscosity model assumes that the Reynolds stress anisotropy is proportional to the mean velocity gradients $\partial \langle U_i \rangle / \partial x_j$. This hypothesis can be traced to the classical theory of Boussinesq [87]. There are more general linear turbulent viscosity models which also account for anisotropy in the turbulent length scales, but Eq. 4.1 is useful in many cases as an approximation with isotropic turbulence length scales [54]. Additionally, there are nonlinear viscosity models which can be beneficial for calculating secondary flows [39].

Substituting the hypothesis Eq. 4.1 into Eq. 3.9, we obtain a RANS equation with diffusion terms in the mean velocity and a modified source [39]:

$$\frac{\overline{\mathrm{D}} \langle U_i \rangle}{\overline{\mathrm{D}} t} = \frac{\partial}{\partial x_j} \left[\nu_{\mathrm{T}} \left(\frac{\partial \langle U_i \rangle}{\partial x_j} + \frac{\partial \langle U_j \rangle}{\partial x_i} \right) \right] - \frac{2}{3} \frac{\partial k}{\partial x_i} + \frac{1}{\rho} \langle F_i \rangle \qquad (4.3\mathrm{a})$$

$$= \frac{\partial}{\partial x_j} \left[\nu_{\mathrm{eff}} \left(\frac{\partial \langle U_i \rangle}{\partial x_j} + \frac{\partial \langle U_j \rangle}{\partial x_i} \right) \right] + \frac{1}{\rho} \langle F_i' \rangle \qquad (4.3\mathrm{b})$$

where

$$\nu_{\mathrm{eff}}(\mathbf{x}, t) = \nu + \nu_{\mathrm{T}}(\mathbf{x}, t) \qquad (4.4)$$

is the effective viscosity due to both molecular and turbulent viscosity, and

$$\frac{1}{\rho} \langle F_i' \rangle = \frac{1}{\rho} \langle F_i \rangle - \frac{2}{3} \frac{\partial k}{\partial x_i} - \nu \nabla^2 \langle U_i \rangle \qquad (4.5)$$

is the modified mean force per unit mass.

4.1.2 k-ε Model

As implied by the name, the k-ε model is a two-equation model for the TKE k and the dissipation rate ε [39]. These two quantities can be used to calculate turbulence dissipation time scale $\tau = k/\varepsilon$, a length scale $L = k^{3/2}/\varepsilon$, and a viscosity scale

$$\nu_{\mathrm{T}} = C_\mu \frac{k^2}{\varepsilon}, \tag{4.6}$$

where $C_\mu = 0.09$ [39]. The TKE equation is given by half the trace of the Reynolds stress transport Eq. 3.50b [39]:

$$\frac{1}{2} \frac{\overline{\mathrm{D}} \langle u_i u_j \rangle}{\overline{\mathrm{D}} t} \delta_{ij} = \frac{1}{2} \mathcal{P}_{ij} \delta_{ij} + \frac{1}{2} \mathcal{R}_{ij} \delta_{ij} - \frac{1}{2} \varepsilon_{ij} \delta_{ij} - \frac{1}{2} \frac{\partial T_{kij}}{\partial x_k} \delta_{ij}$$

$$\Rightarrow \frac{\overline{\mathrm{D}} k}{\overline{\mathrm{D}} t} = \mathcal{P} - \varepsilon - \nabla \cdot \mathbf{T}, \tag{4.7}$$

where

$$\mathcal{P} = \frac{1}{2} \mathcal{P}_{ij} \delta_{ij} = - \langle u_i u_j \rangle \frac{\partial \langle U_i \rangle}{\partial x_j} = - \langle u_i u_j \rangle \langle e_{ij} \rangle, \tag{4.8a}$$

$$T_i \equiv \frac{1}{2} \langle u_i u_j u_j \rangle + \frac{1}{\rho} \langle u_i p' \rangle - 2\nu \langle u_j e'_{ij} \rangle, \tag{4.8b}$$

are the TKE production and TKE flux, respectively, $\varepsilon = \varepsilon_{ij} \delta_{ij}/2$ from Eq. 3.61, and $\mathcal{R}_{ij} \delta_{ij} = \mathcal{R}_{ii} = 0$ for redistributive $\mathcal{R}_{ij}$ as in section 3.2.3. Since the TKE flux Eq. 4.8b depends on unknown quantities, it is modeled with a gradient-diffusion hypothesis [39]

$$T_i = - \frac{\nu_{\mathrm{T}}}{\sigma_{\mathrm{k}}} \frac{\partial k}{\partial x_i}, \tag{4.9}$$

where $\sigma_k = 1.0$ is the turbulent Prandtl number for kinetic energy. Substituting the TKE flux hypothesis Eq. 4.9 into Eq. 4.7 then yields the k model

$$\frac{\overline{\mathrm{D}} k}{\overline{\mathrm{D}} t} = \frac{\partial}{\partial x_i} \left(\frac{\nu_{\mathrm{T}}}{\sigma_k} \frac{\partial k}{\partial x_i} \right) + \mathcal{P} - \varepsilon. \tag{4.10}$$

In contrast to the k model Eq. 4.10 which is based on the exact TKE transport Eq. 4.7, the ε model is entirely empirical [39]:

$$\frac{\overline{\mathrm{D}} \varepsilon}{\overline{\mathrm{D}} t} = \frac{\partial}{\partial x_i} \left(\frac{\nu_{\mathrm{T}}}{\sigma_\varepsilon} \frac{\partial \varepsilon}{\partial x_i} \right) + C_{\varepsilon,1} \frac{\mathcal{P} \varepsilon}{k} - C_{\varepsilon,2} \frac{\varepsilon^2}{k}, \tag{4.11}$$

where $C_{\varepsilon,1} = 1.44$, $C_{\varepsilon,2} = 1.92$ and $\sigma_\varepsilon = 1.3$. Equations 4.3, 4.6, 4.10, and 4.11 together with a model for the mean pressure $\langle P \rangle$ then provide a complete set of equations for the mean fields in the k-ε model.

4.1.3 Turbulent Fields and Particle Dispersion

The RANS eddy viscosity models provide a solution for the mean fields in the turbulent flow, which is sufficient to determine mean particle trajectory. However, since we are interested in calculating particle dispersion, we need the turbulent velocity $\mathbf{u}$ as is determined by the models in chapter 3. Thus, we must also employ a stochastic turbulence model which depends only on the modeled mean field quantities such as k, ε, $\langle U_i \rangle$, and $\partial \langle U_i \rangle / \partial x_j$. One could use a simple purely stochastic Langevin model such as [88]

$$\frac{\mathrm{d}u_i}{\mathrm{d}t} = \sigma \zeta_i(t), \tag{4.12}$$

where $\zeta_i(t) = \xi_i(t)$ or $\zeta_i(t) = d_i(t)\xi(t)$ are Gaussian white noise processes. A simple model like this would not be consistent with the turbulent Navier-Stokes equation as we demonstrated in chapter 3, however. Thus, one should really use one of the Langevin models presented in chapter 3 in conjunction with the mean fields obtained from the RANS turbulence model. As indicated in section 3.1.2.2, after determining the particle trajectory according to Eq. 3.15, one can calculate mass concentration fields as described in section 5.4.

4.2 Advection-diffusion (AD) Model

Ultimately we are interested in obtaining the concentration of a species undergoing turbulent dispersion in the atmosphere. An alternative approach to those described in chapter 3 and section 4.1.3 is one which more directly models the mass concentration of a material in a turbulent fluid through the mass continuity Eq. 2.66, where the conserved scalar is the mass concentration. Using a semi-empirical hypothesis similar to that of the turbulent viscosity hypothesis Eq. 4.1 for the RANS Eqs. 4.3 discussed in section 4.1, we obtain an advection-diffusion model for turbulent diffusion. The AD model can be solved numerically as is done by codes such as Polair3D [89, 90]. Alternately, with simple velocity fields and boundary conditions, the AD model can be analytically solved for stationary, homogeneous turbulence [10, 54]. In particular, the AD model in a uniform velocity field is the basis for the Gaussian puff and plume models commonly used in codes such as MACCS2 [91] and HotSpot [92].

4.2.1 Advection-diffusion Equation

The advection-diffusion equation is used to model the mass concentration of a species $C(\mathbf{x}, t)$ in a turbulent atmosphere and can be derived using the mass conservation advection-diffusion Eq. 2.66

$$\frac{\partial C}{\partial t} + \frac{\partial}{\partial x_i}(U_i C) = \frac{\partial}{\partial x_i}\left(\Gamma \frac{\partial C}{\partial x_i}\right) + S, \tag{4.13}$$

where $S(\mathbf{x}, t)$ is the mass source, and Γ is the fluid molecular diffusivity. Substituting the Reynolds decompositions $U_i = \langle U_i \rangle + u_i$, $C = \langle C \rangle + C'$, and $S = \langle S \rangle + S'$ into Eq. 4.13 yields

$$\frac{\partial}{\partial t}(\langle C \rangle + C') + \frac{\partial}{\partial x_i}[(\langle U_i \rangle + u_i)(\langle C \rangle + C')] = \frac{\partial}{\partial x_i}\left[\Gamma \frac{\partial}{\partial x_i}(\langle C \rangle + C')\right] + \langle S \rangle + S'. \tag{4.14a}$$

$$\Rightarrow \frac{\partial \langle C \rangle}{\partial t} + \frac{\partial C'}{\partial t} + \frac{\partial}{\partial x_i}\langle U_i \rangle \langle C \rangle + \frac{\partial}{\partial x_i}u_i C'$$

$$+ \frac{\partial}{\partial x_i}\langle U_i \rangle C' + \frac{\partial}{\partial x_i}u_i \langle C \rangle = \frac{\partial}{\partial x_i}\left(\Gamma \frac{\partial \langle C \rangle}{\partial x_i}\right) + \frac{\partial}{\partial x_i}\left(\Gamma \frac{\partial C'}{\partial x_i}\right)$$

$$+ \langle S \rangle + S', \tag{4.14b}$$

where we have expanded the terms in the second step. Then taking the ensemble average of both sides of Eq. 4.14b, using the product rule with $\partial \langle U_i \rangle / \partial x_i = 0$ for an incompressible fluid, we obtain the Reynolds-averaged advection-diffusion equation

$$\frac{\partial \langle C \rangle}{\partial t} + \langle U_i \rangle \frac{\partial \langle C \rangle}{\partial x_i} + \frac{\partial}{\partial x_i}\langle u_i C' \rangle = \frac{\partial}{\partial x_i}\left(\Gamma \frac{\partial \langle C \rangle}{\partial x_i}\right) + \langle S \rangle. \tag{4.15}$$

Equations 3.7 and 4.15 have an interesting symmetry which reflects the attempt to model the behavior of massive particles in turbulent media, albeit in somewhat different ways.

Similar to the turbulent viscosity model of Eq. 4.1 employed in section 4.1.1, we must employ a turbulence model for the scalar flux $\langle \mathbf{u}C' \rangle$. Namely, we use the gradient-diffusion hypothesis, which states that the transport is proportional to the mean scalar gradient [10, 39, 54]:

$$\langle u_i C' \rangle = -\Gamma_{ij}^{\mathrm{T}} \frac{\partial \langle C \rangle}{\partial x_j}, \tag{4.16}$$

where $\Gamma_{ij}^{\mathrm{T}}(\mathbf{x}, t)$ is the *turbulent diffusivity* or *eddy diffusivity* tensor. This first-order closure approximation is often called gradient transport theory or K-theory [53]. In simple cases with isotropic turbulent diffusivity, one can simply use the scalar turbulent diffusivity Γ_{T}

with $\Gamma^{\mathrm{T}}_{ij} = \Gamma_{\mathrm{T}}\delta_{ij}$, but it is more common to use the general anisotropic diffusivity tensor than in the case of the eddy viscosity discussed in section 4.1.1. Substituting the turbulent diffusivity hypothesis of Eq. 4.16 into Eq. 4.15, we arrive at the advection-diffusion equation for turbulent diffusion:

$$\frac{\overline{\mathrm{D}}\langle C \rangle}{\overline{\mathrm{D}}t} = \frac{\partial}{\partial x_i}\left(\Gamma^{\mathrm{eff}}_{ij}\frac{\partial \langle C \rangle}{\partial x_j}\right) + \langle S \rangle, \tag{4.17}$$

where

$$\Gamma^{\mathrm{eff}}_{ij}(\mathbf{x}, t) = \Gamma\delta_{ij} + \Gamma^{\mathrm{T}}_{ij}(\mathbf{x}, t) \tag{4.18}$$

is the effective mass diffusivity due to both molecular diffusion and turbulent diffusion.

As in the case of the RANS eddy viscosity model discussed in section 4.1, solving Eq. 4.17 requires a turbulence closure model for the eddy diffusivity Γ^{T}_{ij}. In the k-ε model discussed in section 4.1.2, this took the simple form in Eq. 4.6 for the eddy viscosity ν_{T}. There are several choices of parameterizations and models available for the eddy diffusivity Γ_{T} in the atmospheric boundary layer [53]. AD codes such as Polair3D employ parameterizations based on the local mean flow, while Gaussian puff model codes typically use semi-empirical parameterizations based on atmospheric stability as discussed in section 4.3.

4.2.2   Symmetry of the RANS and AD Equations with Turbulence Models

Comparing Eqs. 4.3a and 4.17 suggests a nice symmetry between the models for the mean velocity and mass concentration fields. For high Reynolds number flows such as the atmospheric surface and mixed layers, the molecular viscosity ν and diffusivity Γ are negligible compared to the turbulent viscosity ν_{T} and diffusivity Γ_{T}, respectively [39]. Furthermore, in most simple turbulent flows, the turbulent Prandtl number $\sigma_{\mathrm{T}} = \nu_{\mathrm{T}}/\Gamma_{\mathrm{T}}$ is found to be of order unity [39]. Thus, in such flows we can define $K \simeq \nu_{\mathrm{T}} \simeq \Gamma_{\mathrm{T}}$ to be the turbulent diffusion coefficient, and Eqs. 4.3a and 4.17 become

$$\frac{\overline{\mathrm{D}}\langle U_j \rangle}{\overline{\mathrm{D}}t} = \frac{\partial \langle U_j \rangle}{\partial t} + \langle U_i \rangle \frac{\partial \langle U_j \rangle}{\partial x_i} = \frac{\partial}{\partial x_i}\left[K\left(\frac{\partial \langle U_i \rangle}{\partial x_j} + \frac{\partial \langle U_j \rangle}{\partial x_i}\right)\right] + \frac{1}{\rho}\langle F'_j \rangle, \tag{4.19}$$

$$\frac{\overline{\mathrm{D}}\langle C \rangle}{\overline{\mathrm{D}}t} = \frac{\partial \langle C \rangle}{\partial t} + \langle U_i \rangle \frac{\partial \langle C \rangle}{\partial x_i} = \frac{\partial}{\partial x_i}\left(K\frac{\partial \langle C \rangle}{\partial x_i}\right) + \langle S \rangle, \tag{4.20}$$

respectively. Both of these equations have a drift component as well as a diffusion component with the same diffusion coefficient used to model both the velocity and the mass concentration fields. This is not entirely unexpected of course since they are both based on the ensemble-averaged general continuity Eq. 2.10 with a turbulent gradient hypothesis closure model. However, it highlights the fact that the two approaches fundamentally represent the same

underlying physics albeit in different ways.

4.3 Gaussian Plume and Puff Models

The general anisotropic advection-diffusion equation from Eq. 4.20 with $\langle C \rangle \to C$ and $\langle \mathbf{U} \rangle \to \mathbf{U}$ for notational simplicity and source $S(\mathbf{x}, t)$ becomes

$$\frac{\partial C}{\partial t} + U_i \frac{\partial C}{\partial x_i} - \frac{\partial}{\partial x_i} \left(K_{ij} \frac{\partial C}{\partial x_j} \right) = S(\mathbf{x}, t). \tag{4.21}$$

The solution to this equation for a puff source $S(\mathbf{x}, t) = S_0 \delta(\mathbf{x} - z_0 \hat{\mathbf{z}}) \delta(t)$ with uniform, time-invariant velocity $\mathbf{U} = U \hat{\mathbf{x}}$ and reflecting boundary conditions is [10]

$$C(\mathbf{x}, t) = \frac{S_0}{(2\pi)^{3/2} \sigma_x \sigma_y \sigma_z} \exp \left(-\frac{(x - ut)^2}{2\sigma_x^2} - \frac{y^2}{2\sigma_y^2} \right)$$
$$\times \left[\exp \left(-\frac{(z - z_0)^2}{2\sigma_z^2} \right) + \exp \left(-\frac{(z + z_0)^2}{2\sigma_z^2} \right) \right]. \tag{4.22}$$

This equation represents the mean concentration of a scalar quantity transported by a fluid particle in turbulent fluid flow and is related to the particle displacement probability density function. In particular, the particle displacement covariance functions are defined in terms of the diffusion coefficients for time scales $t \gg T_{\mathrm{L}}$ as

$$\sigma_{ij}(t) \equiv 2 K_{ij} t, \tag{4.23}$$

from which it immediately follows that

$$K_{ij} = \frac{1}{2} \frac{\mathrm{d}\sigma_{ij}(t)}{\mathrm{d}t}. \tag{4.24}$$

By examining the dispersion parameter limiting behaviors in time, we can gain insight into the physical significance of the particle dispersion characteristics. For $\tau \ll T_i^{\mathrm{L}}$, with $\lim_{s \to 0} R_{ii}^{\mathrm{L}}(s) = \lim_{T_i^{\mathrm{L}} \to \infty} R_{ii}^{\mathrm{L}}(s) = 1$, Eq. 3.30b for $i = j$ becomes [39, 54]

$$\sigma_i^2(\tau) \approx 2\sigma_{u_i}^2 \int_0^\tau (\tau - s) \left[\lim_{T_i^{\mathrm{L}} \to \infty} R_{ii}^{\mathrm{L}}(s) \right] \mathrm{d}s$$
$$= 2\sigma_{u_i}^2 \lim_{\tau \to 0} \left[\tau s - \frac{s^2}{2} \right]_0^\tau$$
$$= \sigma_{u_i}^2 \tau^2, \quad \tau \ll T_i^{\mathrm{L}}. \tag{4.25}$$

Thus, for times scales less than T_i^{L}, the velocities become well correlated, so the root mean squared displacements increase linearly with time in proportion to the turbulent velocity standard deviation. Said differently, for short time scales, the particle displacements travel reversibly in a straight line with the turbulent velocity. If we also assume that the integral $\int_0^\infty s R_{ii}^{\mathrm{L}}(s)\mathrm{d}s$ is finite, then for $\tau \gg T_i^{\mathrm{L}}$ Eq. 3.30b becomes [39, 54]

$$
\begin{aligned}
\sigma_i^2(\tau) &\approx 2\sigma_{u_i}^2 \int_0^\infty (\tau - s)\, R_{ii}^{\mathrm{L}}(s)\mathrm{d}s \\
&= 2\sigma_{u_i}^2 \left[\tau \int_0^\infty R_{ii}^{\mathrm{L}}(s)\mathrm{d}s - \int_0^\infty s R_{ii}^{\mathrm{L}}(s)\mathrm{d}s \right] \\
&= 2\sigma_{u_i}^2 T_i^{\mathrm{L}} \tau, \quad \tau \gg T_i^{\mathrm{L}},
\end{aligned} \tag{4.26}
$$

where the finite term $\int_0^\infty s R_{ii}^{\mathrm{L}}(s)\mathrm{d}s$ is neglected compared to the term τT_i^{L} for $\tau \gg T_i^{\mathrm{L}}$. Then for long time scales compared to T_i^{L}, the velocities are uncorrelated, and the particle displacements increase in proportion to the square-root of time. This is indicative of an irreversible, dissipative process such as diffusion and will be useful for calculating the diffusion coefficient. In particular, substituting 4.26 into Eq. 4.24, we obtain for $i = j$ with $\sigma_{ii}(t) \equiv \sigma_i^2(t)$ the diffusion coefficient based on the Lagrangian particle dispersion parameters [39, 40, 54]

$$
K_{ii} = \sigma_{u_i}^2 T_i^{\mathrm{L}}. \tag{4.27}
$$

Equations 4.23 and 4.27 can be written for each of the three directions x, y, and z. Additionally, the dispersion factors σ_x, σ_y, and σ_z are commonly written in terms of downwind plume distance x and depend on atmospheric variables, with now two ways to determine them for the drift-diffusion model:

1. Determine plume concentrations profiles as a function of time and performing a Gaussian curve fit with Eq. 4.22 for the dispersion parameters $\sigma_i(x)$;

2. Evaluate the Lagrangian particle velocity statistics $\sigma_{u_i}^2$ and T_i^{L}, and use the definition Eq. 4.23 and $\sigma_{ii}(t) \equiv \sigma_i^2(t)$ with Eq. 4.27 to yield

$$
\sigma_i(t) = \sqrt{2\sigma_{u_i}^2 T_i^{\mathrm{L}} t}, \tag{4.28}
$$

where $t = x/U$ is the plume downwind travel time.

We employ both of these methods in the FLEXPART benchmark study of the Gaussian puff

73

model presented in chapter 6. In contrast to the two above methods for determining the dispersion parameters $\sigma_i(x)$, Gaussian puff models have classically relied on the Pasquill-Gifford (PG) semi-empirical curves [93, 94]. These curves are parameterized most simply as the power law

$$\sigma_i(x) = a_i x^{b_i}, \tag{4.29}$$

with a_i and b_i depending on Pasquill atmospheric stability classes A through F discussed in section A.5. Section 6.3.3.3 then presents a comparison of the dispersion parameters of the classical PG semi-empirical curves to those determined in FLEXPART by applying the above two methods.

Chapter 5

Lagrangian Velocity Model Code Description

As discussed in chapters 2 and 3, Lagrangian velocity models like the drift-diffusion models FLEXPART and HYSPLIT rely on both meteorological data for mean fluid flow fields and empirical models for the turbulence characterization [37]. The meteorological data is constructed using physical models for the conservation laws described in section 2.2 on a relatively coarse global or regional grid. Using this meteorological data as input, both mesoscale and microscale turbulence models empirically specify the turbulent velocity components. The remaining fluid flow dependent variables density ρ, pressure p, and temperature T are treated as grid-resolved mean quantities obeying the equation of state Eq. 2.63. That is, turbulent fluctuations of these thermodynamic state variables are not considered by FLEXPART or HYSPLIT.

In addition to the fluid flow models, FLEXPART and HYSPLIT employ several other models associated with the Lagrangian particle dispersion. Since one is interested in the transport of materials in the atmosphere, one must characterize the behavior of the species according to how it interacts with the surrounding fluid flow and other species in the transport model. If the species is of a chemical or radionuclide, chemical reactions and radioactive decay transmutation might be significant factors affecting atmospheric concentration. Similarly, if the species is a particulate or aerosol as opposed to a well-mixed gas, wet and dry deposition may result in significant reductions in atmospheric concentration.

There are additionally several parameters and modes of measuring the simulated species concentration in FLEXPART. Species concentration can be measured with user-specified averaging time and sampling periods on fixed Eulerian grids or using a parabolic averaging kernel at selected ground-based detector locations. Alternatively, one can specify the output units in mass mixing ratio if desired. Finally, FLEXPART and HYSPLIT are capable of operating in an adjoint or backwards mode whereby particle trajectories are integrated in

reverse. This may be more computationally efficient when there are many more source parameters than detector parameters as might be the case for optimal source estimation or inversion [37].

5.1 Meteorological Data

Meteorological data provides the mean fluid flow fields for FLEXPART and HYSPLIT. Sophisticated physical models for the conservation laws described in section 2.2 are used to determine meteorological conditions on a relatively coarsely discretized Eulerian grid. If the time period of interest is in the future, one must use a forecast model; if the time period is in the past, however, one can perform a reanalysis which combines both the physical model and a data assimilation model incorporating data measurements. For global and regional meteorological data sets, the horizontal coordinates are typically specified in latitude ϕ and longitude λ geographic coordinates, while the vertical coordinates are specified in pressure $\langle p \rangle$ or hybrid [95] η levels. These pressure or hybrid levels provide a correspondence between geopotential height z_{geo} and the pressure $\langle p \rangle$. In combination with a fixed radius of the Earth $R_{\oplus}$, one can determine the physical coordinates $\mathbf{x}$ of the meteorological data fields. The meteorological variables are then linearly interpolated in time and space to the Lagrangian particle coordinates to drive the mean Lagrangian trajectory and determine mean fields at the Lagrangian particle time and position. FLEXPART and HYSPLIT require 3D meteorological fields such as velocity $\langle \mathbf{U} \rangle$, temperature $\langle T \rangle$, humidity, and pressure $\langle p \rangle$. Additionally, they require 2D fields defined at particular heights or surfaces such as the planetary boundary layer height h_{PBL}, surface pressure p_{s}, precipitation, cloud cover, $10\,\text{m}$ velocity and $2\,\text{m}$ temperature.

5.2 Mesoscale Turbulent Velocity

FLEXPART divides the turbulent velocity into mesoscale $\mathbf{u}_{\text{meso}}$ and microscale $\mathbf{u}$ turbulent components such that the total velocity is given by

$$\mathbf{U} = \langle \mathbf{U} \rangle + \mathbf{u}_{\text{meso}} + \mathbf{u}, \tag{5.1}$$

where $\langle \mathbf{U} \rangle$ is the mean grid-scale velocity from the meteorological data. These mesoscale velocity fluctuations represent the intermediate turbulence scales not resolved by the grid-scale meteorological data or the microscale turbulent velocity parameterizations discussed in section 5.3.

Similarly to the microscale turbulent velocity discussed in chapter 3, FLEXPART uses

a Langevin equation to model the mesoscale turbulent velocity. However, the mesoscale velocity variance $\sigma^2_{u_i,\text{meso}}$ is determined using the grid-scale velocity variance $\sigma^2_{U_i,\text{grid}}$ with the assumption that this provides some information of the subgrid variance [1, 2]. This grid-scale standard deviation $\sigma_{U_i,\text{grid}}$ is then scaled by a fixed parameter called `turbmesoscale` which defaults to $f_{\text{meso}} = 0.16$. The autocorrelation time $T_{\text{L,meso}}$ is taken as half the time interval between meteorological data fields Δt_{grid} on the assumption that linear interpolation between the grid points can recover half the subgrid variability [1, 2]. Thus, the mesoscale velocity in each spatial direction is modeled using to the Langevin model

$$\frac{\mathrm{d}u_{i,\text{meso}}}{\mathrm{d}t} = -\frac{u_{i,\text{meso}}}{T_{\text{L,meso}}} + \left(\frac{2\sigma^2_{u_i,\text{meso}}}{T_{\text{L,meso}}}\right)^{1/2} \xi_i(t), \tag{5.2}$$

where $T_{\text{L,meso}} = \Delta t_{\text{grid}}/2$ is the estimated mesoscale velocity Lagrangian autocorrelation time scale, $\sigma_{u_i,\text{meso}} = f_{\text{meso}}\sigma_{U_i,\text{grid}}$ is the estimated mesoscale velocity standard deviation, $\sigma_{U_i,\text{grid}}$ is the estimated standard deviation of the grid-scale velocity determined using the velocities of the eight nearest meteorological data points to the Lagrangian particle, and $\xi_i(t)$ is a Gaussian white noise process. No Einstein summation is implied in Eq. 5.2.

5.3   Microscale Turbulent Velocity

As shown in 3.1.3, the microscale turbulent velocity is characterized by the velocity variances $\sigma^2_{u_i}$ and the Lagrangian time scale T^{L}_i. Within the atmospheric boundary layer in FLEXPART, these quantities are parameterized differently depending on the atmospheric stability, which itself depends on the Monin-Obukhov length L defined by Eq. A.1 discussed in appendix A. HYSPLIT, however, uses a fixed, user-specified value for the Lagrangian time scale and a parameterization for the velocity variances. Above the atmospheric planetary boundary layer ($z > h_{\text{PBL}}$), FLEXPART uses a constant vertical diffusivity $\Gamma_z = 0.1\,\text{m}^2\,\text{s}^{-1}$ in the stratosphere and a horizontal diffusivity of $\Gamma_\parallel = \Gamma_\perp = 50\,\text{m}^2\,\text{s}^{-1}$ in the troposphere [1, 2]. The diffusivity can then be converted to a velocity deviation according to

$$\sigma_{u_i} = \sqrt{\frac{\Gamma_i}{\mathrm{d}t}}. \tag{5.3}$$

5.3.1   Estimation of Monin-Obukhov Length

FLEXPART calculates the Monin-Obukhov length using an iterative procedure called the profile method [96] in which the following three equations are solved iteratively until they

converge [1, 2]:

$$U_\star = \frac{\kappa \Delta U}{\ln \frac{z_l}{10\,\mathrm{m}} - \varphi_\mathrm{M}\left(\frac{z_l}{L}\right) + \varphi_\mathrm{M}\left(\frac{10\,\mathrm{m}}{L}\right)}, \tag{5.4a}$$

$$\Theta_\star = \frac{\kappa \Delta \Theta}{0.74\left[\ln \frac{z_l}{2\,\mathrm{m}} - \varphi_\mathrm{H}\left(\frac{z_l}{L}\right) + \varphi_\mathrm{H}\left(\frac{2\,\mathrm{m}}{L}\right)\right]}, \tag{5.4b}$$

$$L = \frac{\langle T \rangle U_\star^2}{\kappa g \Theta_\star}, \tag{5.4c}$$

where z_l is the height of the second model level, ΔU is the difference between wind speed at the second model level and at a height of $10\,\mathrm{m}$, $\Delta \Theta$ is the difference between potential temperature at the second model level and at a height of $2\,\mathrm{m}$, $\Theta_\star$ is the temperature scale, and $\langle T \rangle$ is the average surface layer temperature (taken at the first model level). This profile method uses the $10\,\mathrm{m}$ wind and $2\,\mathrm{m}$ temperature data, but if the surface shear stresses in the east/west and north/south directions are available in the meteorological data, then the friction velocity is calculated simply as

$$U_\star = \sqrt{\frac{\tau_0}{\rho}}, \tag{5.5}$$

where $\tau_0 = \sqrt{\tau_1^2 + \tau_2^2}$, and τ_1 and τ_2 are the surface shear stresses in the east/west and north/south directions, respectively.

Comparing Eq. A.1 to Eq. 5.4c, we can see that the two formulas are equal if

$$-\frac{\rho c_\mathrm{p} T_0 U_\star^3}{\kappa g \langle q_z \rangle} = \frac{\langle T \rangle U_\star^2}{\kappa g \Theta_\star}$$
$$\Rightarrow \langle q_z \rangle = -\rho c_\mathrm{p} U_\star \Theta_\star,$$

and $\langle T \rangle = T_0$. In FLEXPART, the heat flux is computed by

$$\langle u_z \theta_\mathrm{v}' \rangle = -\rho c_\mathrm{p} U_\star \Theta_\star,$$

so indeed the two formulas for the Monin-Obukhov length are equal.

5.3.2   Parameterization of Turbulence

Once the Monin-Obukhov length and other boundary layer parameters have been determined using the meteorological data, the standard deviations in the velocity components σ_{U_i} and the Lagrangian time scales T_{ii}^L are determined from the formulation for the autocorrelation

Table 5.1: FLEXPART atmospheric stability classification [1, 2].

Condition	Stability class
$h_{\mathrm{PBL}} < |L|$	neutral
$L < 0$	unstable
$L \geq 0 \wedge h_{\mathrm{PBL}} \geq |L|$	stable

$R_{ii}^{\mathrm{L}}(t)$ and according to a parameterization proposed by Hanna [79], as defined and discussed in chapter 3. That is, as opposed to the alternate formulations presented in section 3.2 in which the Lagrangian time scale T_{ij}^{L} is represented by G_{ij} and depends on dissipation rate $\tau = k/\varepsilon$, FLEXPART empirically models T_{ii}^{L} via the autocorrelation $R_{ii}^{\mathrm{L}}(t)$. In particular, the velocity standard deviations and Lagrangian time scales depend on planetary boundary layer height h_{PBL}, Monin-Obukhov length L, friction velocity $U_{\star}$, convective velocity scale $W_{\star}$, surface roughness length z_0, and Coriolis parameter $f = 2\Omega \sin\phi$. The variables h_{PBL}, L, and z_0 can be considered boundary condition parameters in the set of conservation equations, which control the atmospheric surface layer thickness and stability. FLEXPART categorizes the turbulence into three stability classes according to the rules shown in Table 5.1.

The empirical form of the velocity deviations and Lagrangian time scales is then determined based on the stability classes according to the parameterizations of Hanna [79]. The velocity deviations and Lagrangian time scales are divided into three components: $\parallel$, $\perp$, and z for the components parallel and perpendicular to the horizontal wind components and the vertical wind component, respectively. The lower bounds of the horizontal and vertical Lagrangian time scales are set to $10\,\mathrm{s}$ and $30\,\mathrm{s}$, respectively, to avoid excessive computation time for particles close to the surface [1, 2].

5.3.2.1 Neutral Atmosphere Representation

For the neutral atmosphere, the perpendicular and vertical velocity deviation components are equal, and the Lagrangian time scales in all directions are equal. The velocity deviations are exponential in particle height, while the Lagrangian time scales take the form of a rational fraction of linear polynomials.

$$\frac{\sigma_{u_{\parallel}}}{U_{\star}} = 2.0 \exp\left(-\frac{3fz}{U_{\star}}\right), \quad \frac{\sigma_{u_{\perp}}}{U_{\star}} = \frac{\sigma_w}{U_{\star}} = 1.3 \exp\left(-\frac{2fz}{U_{\star}}\right) \tag{5.6}$$

$$T_{\parallel}^{\mathrm{L}} = T_{\perp}^{\mathrm{L}} = T_z^{\mathrm{L}} = \frac{0.5z/\sigma_w}{1 + 15fz/U_{\star}} \tag{5.7}$$

5.3.2.2 Unstable Atmosphere Representation

In the unstable atmosphere, the parallel and perpendicular velocity deviation components and Lagrangian time scales are equal, while the vertical components are different. The parallel and perpendicular velocity deviations depend only on the planetary boundary layer height h_{PBL}, Monin-Obukhov length L, and friction velocity $U_\star$, while the vertical velocity deviation depends also on the convective velocity scale $W_\star$ according to a complex power-law expression. Similarly, the parallel and perpendicular Lagrangian time scales depend only on h_{PBL} and $\sigma_{u_\parallel} = \sigma_{u_\perp}$, while the vertical Lagrangian time scale has a more complex piecewise form depending on the particle height z in comparison to h_{PBL} and the surface roughness z_0.

$$\frac{\sigma_{u_\parallel}}{U_\star} = \frac{\sigma_{u_\perp}}{U_\star} = \left(12 + \frac{h_{\mathrm{PBL}}}{2\,|L|}\right)^{1/3}$$

$$\sigma_w = \left[1.2W_\star^2\left(1 - 0.9\frac{z}{h_{\mathrm{PBL}}}\right)\left(\frac{z}{h_{\mathrm{PBL}}}\right)^{2/3} + \left(1.8 - 1.4\frac{z}{h_{\mathrm{PBL}}}\right)U_\star^2\right]^{1/2} \tag{5.8}$$

$$T_\parallel^{\mathrm{L}} = T_\perp^{\mathrm{L}} = 0.15\frac{h_{\mathrm{PBL}}}{\sigma_{u_\parallel}}$$

$$T_z^{\mathrm{L}} = \begin{cases} 0.1\frac{z}{\sigma_w}\left[0.55 - 0.38\left(\frac{z-z_0}{L}\right)\right]^{-1} & \frac{z}{h_{\mathrm{PBL}}} < 0.1 \wedge z - z_0 > -L \\ 0.59\frac{z}{\sigma_w} & \frac{z}{h_{\mathrm{PBL}}} < 0.1 \wedge z - z_0 < -L \\ 0.15\frac{h_{\mathrm{PBL}}}{\sigma_w}\left[1 - \exp\left(-\frac{5z}{h_{\mathrm{PBL}}}\right)\right] & \frac{z}{h_{\mathrm{PBL}}} > 0.1 \end{cases} \tag{5.9}$$

5.3.2.3 Stable Atmosphere Representation

For the stable atmosphere, the perpendicular and vertical velocity deviation components are equal, and the Lagrangian time scales in all directions are slightly different. The velocity deviation components are linear in the particle height, while the Lagrangian time scales follow a square-root power law with coefficients depending on the vertical deviation in the respective components.

$$\frac{\sigma_{u_\parallel}}{U_\star} = 2.0\left(1 - \frac{z}{h_{\mathrm{PBL}}}\right), \quad \frac{\sigma_{u_\perp}}{U_\star} = \frac{\sigma_w}{U_\star} = 1.3\left(1 - \frac{z}{h_{\mathrm{PBL}}}\right) \tag{5.10}$$

$$T_{ii}^{\mathrm{L}} = \alpha_i\frac{h_{\mathrm{PBL}}}{\sigma_{u_i}}\left(\frac{z}{h_{\mathrm{PBL}}}\right)^{1/2}, \tag{5.11}$$

for $i = \{\parallel, \perp, z\}$, where $\alpha_\parallel = 0.15$, $\alpha_\perp = 0.07$, and $\alpha_z = 0.1$.

5.4   Particle Averaging

We wish to determine the spatiotemporal behavior of the mass-concentration $C_j(\mathbf{x}, t)$ for species j in the simulation. In FLEXPART, this can be done using either a uniform or parabolic averaging kernel for determining concentrations on a fixed Eulerian grid or a fixed ground-based detector location, respectively. Although we use the term mass here, the mass might represent the number of nuclides N_j or radioactivity $A_j = \lambda_j N_j$, where λ_j is the decay constant, in the case of radionuclides. These masses are assigned to the Lagrangian particle during emission and follow the trajectory determined according to the Langevin velocity model.

Let there be n_j Lagrangian particles of species j within the simulation domain carrying mass $m_{ij}(t) \equiv m_j\left[\mathbf{x}_i(t), t\right]$ at Lagrangian particle position $\mathbf{x}_i(t)$ at time t for $0 \leq i < n_j$. Both the uniform and parabolic kernel averaging methods in FLEXPART use a time averaging over a period Δt_{avg} which is sampled every Δt_{s} such that there are $n_{\mathrm{s}} = \Delta t_{\mathrm{avg}}/\Delta t_{\mathrm{s}}$ time samples per averaging interval. Then the mean concentration of species j at time $t_k = t_0 + k\Delta t_{\mathrm{avg}}$ may be calculated using samples at sample time $t_{k\ell} = t_k + \ell\Delta t_{\mathrm{s}}$ as [1, 2]

$$C_j(\mathbf{x}, t_k) = \langle C_j(\mathbf{x}, t)\rangle_{t_k} = \frac{1}{n_{\mathrm{s}}} \sum_{\ell=0}^{n_{\mathrm{s}}-1} \langle C_{\mathrm{s},j}(\mathbf{x}, t_{k\ell})\rangle, \tag{5.12}$$

where [1, 2, 39, 97]

$$\langle C_{\mathrm{s},j}(\mathbf{x}, t)\rangle_{\mathbf{h}} = \frac{1}{V} \sum_{i=0}^{n_j-1} W_j\left[\mathbf{x}, \mathbf{x}_i(t), \mathbf{h}\right] m_{ij}(t) \tag{5.13}$$

is the estimated mass concentration at time t in volume V due to each particle, and $W_j\left[\mathbf{x}, \mathbf{x}_i(t), \mathbf{h}\right]$ is the kernel estimator weight function with bandwidth $\mathbf{h} = \mathbf{h}\left[\mathbf{x}_i(t), t\right]$ determining the virtual size or smoothing length of the Lagrangian particles [97, 98]. The weight function should be normalized such that [99]

$$\int \frac{1}{V} W_j\left[\mathbf{x}, \mathbf{x}_i(t), \mathbf{h}\right] \mathrm{d}\mathbf{x} = 1 \tag{5.14}$$

and

$$\frac{1}{V} \lim_{h\to 0} W_j\left[\mathbf{x}, \mathbf{x}_i(t), \mathbf{h}\right] = \delta\left[\mathbf{x} - \mathbf{x}_i(t)\right]. \tag{5.15}$$

This weight function can take various forms such as orthogonal function expansions, interpolating splines, or polynomials [98, 100]. Sometimes it is written in the form of the

Nadaraya–Watson estimator weight [39, 100, 101]

$$W_j\left[\mathbf{x}, \mathbf{x}_i(t), \mathbf{h}\right] = \frac{K_{\mathbf{h}}\left[\mathbf{x}, \mathbf{x}_i(t)\right]}{\sum_{k=0}^{n_j-1} K_{\mathbf{h}}\left[\mathbf{x}, \mathbf{x}_k(t)\right]} \tag{5.16}$$

with kernel estimator function $K_{\mathbf{h}}\left[\mathbf{x}, \mathbf{x}_i(t)\right]$, from from which it is apparent that the weights sum to unity: $\sum_{i=0}^{n_j-1} W_j\left[\mathbf{x}, \mathbf{x}_i(t), \mathbf{h}\right] = 1$.

5.4.1 Grid Averaging: Uniform Kernel

When using the uniform kernel averaging, the concentration output grid is divided into uniformly sized latitude-longitude regions with corners at $(\lambda_{\mathrm{g},i}, \phi_{\mathrm{g},j}) = (\lambda_{\mathrm{g},0} + i\Delta\lambda_{\mathrm{g}}, \phi_{\mathrm{g},0} + j\Delta\phi_{\mathrm{g}})$ for $0 \leq i < n_{\mathrm{g},x}$, $0 \leq j < n_{\mathrm{g},y}$ and user-specified heights $z_{\mathrm{g},k}$ for $0 \leq k < n_{\mathrm{g},z}$. These grid cell regions with center $\mathbf{x}_{ijk}$ correspond to a volume $V = V_{\mathrm{g},ijk} = A_{\mathrm{g},ij}\Delta z_{\mathrm{g},k}$, with area $A_{\mathrm{g},ij}$ determined by the spherical segment area

$$\begin{aligned}
A_{\mathrm{g},ij} &= R_{\oplus}^2 \int_{\lambda_{\mathrm{g},i}}^{\lambda_{\mathrm{g},i+1}} \mathrm{d}\lambda \left| \int_{\theta_{\mathrm{g},j}}^{\theta_{\mathrm{g},j+1}} \sin\theta \mathrm{d}\theta \right| \\
&= R_{\oplus}^2 \left| \cos\theta_{\mathrm{g},j} - \cos\theta_{\mathrm{g},j+1} \right| \Delta\lambda_{\mathrm{g}} \\
&= R_{\oplus}^2 \left| \sin\phi_{\mathrm{g},j} - \sin\phi_{\mathrm{g},j+1} \right| \Delta\lambda_{\mathrm{g}},
\end{aligned} \tag{5.17}$$

where $\theta_j = \pi/2 - \phi_j$ is the polar angle, and $R_{\oplus} = 6.371 \times 10^6 \,\mathrm{m}$ is the Earth's radius. Given a Lagrangian particle at position $\mathbf{x}_\ell(t)$ at time t, FLEXPART determines the uniform bandwidth based on the nearest output grid cell: $\mathbf{h} = \mathbf{h}_{ijk} = \mathbf{h}\left[\mathbf{x}_\ell(t)\right] = (\Delta\lambda_{\mathrm{g}}, \Delta\phi_{\mathrm{g}}, \Delta z_{\mathrm{g},k})$. The uniform kernel assigns mass from each particle to its nearest four grid cells in the $\lambda\phi$-plane at the height level of the particle according to the fraction of the kernel's area falling within the cells [1, 2, 102]. Then the weight function for this particle is given by

$$W_j\left[\mathbf{x}, \mathbf{x}_\ell(t), \mathbf{h}\right] = b_1\left(\frac{\Delta\lambda\left[\mathbf{x}, \mathbf{x}_\ell(t)\right]}{\Delta\lambda_{\mathrm{g}}}\right) b_1\left(\frac{\Delta\phi\left[\mathbf{x}, \mathbf{x}_\ell(t)\right]}{\Delta\phi_{\mathrm{g}}}\right) b_0\left(\frac{z - z_\ell(t)}{\Delta z_{\mathrm{g},k}}\right), \tag{5.18}$$

where $\Delta\lambda\left[\mathbf{x}, \mathbf{x}_\ell(t)\right] = \lambda(\mathbf{x}) - \lambda\left[\mathbf{x}_\ell(t)\right]$ and $\Delta\phi\left[\mathbf{x}, \mathbf{x}_\ell(t)\right] = \phi(\mathbf{x}) - \phi\left[\mathbf{x}_\ell(t)\right]$ are the longitude and latitude differences, respectively, between the points $\mathbf{x}$ and $\mathbf{x}_\ell(t)$. Here we have defined

the zeroth- and first-order basis spline or B-spline functions $b_0(\xi)$ and $b_1(\xi)$, respectively, as[1]

$$b_0(\xi) = \begin{cases} 1, & |\xi| \leq 1/2 \\ 0, & \text{otherwise} \end{cases} \tag{5.19a}$$

$$b_1(\xi) = \begin{cases} 1 - |\xi|, & |\xi| \leq 1 \\ 0, & \text{otherwise} \end{cases}. \tag{5.19b}$$

5.4.2 Detector Averaging: Parabolic Kernel

FLEXPART additionally has the ability to use a parabolic kernel for measuring the concentration of a ground-based detector. This may be more accurate than the uniform grid kernel, but it is more computationally demanding since it is of higher order. In this case, the weight function bandwidth $\mathbf{h} = \mathbf{h}\left[\mathbf{x}_\ell(t), t\right] = (h_{x_\ell}(\tau_\ell), h_{y_\ell}(\tau_\ell), h_{z_\ell}(\tau_\ell))$ depends on the Lagrangian particle's age $\tau_\ell = t - t_{\ell,0}$, where

$$h_{x_\ell}(\tau_\ell) = \min\left\{ \left(0.29\,\text{m} + 2.222 \times 10^{-3}\,\text{m}\,\text{s}^{-1/2}\sqrt{\tau_\ell}\right) \Delta\lambda_\text{m} + 1.2 \times 10^{-5}\,\text{m}\,\text{s}^{-1}\tau_\ell, \right.$$
$$\left. h_{x_\ell,\text{max}} \right\}, \tag{5.20a}$$

$$h_{y_\ell}(\tau_\ell) = \min\left\{ \left(0.18\,\text{m} + 1.389 \times 10^{-3}\,\text{m}\,\text{s}^{-1/2}\sqrt{\tau_\ell}\right) \Delta\phi_\text{m} + 7.5 \times 10^{-6}\,\text{m}\,\text{s}^{-1}\tau_\ell, \right.$$
$$\left. h_{y_\ell,\text{max}} \right\} \tag{5.20b}$$

$$h_{z_\ell}(\tau_\ell) = \min\left\{ 50\,\text{m} + 0.3\,\text{m}\,\text{s}^{-1/2}\sqrt{\tau_\ell}, h_{z_\ell,\text{max}} \right\}, \tag{5.20c}$$

where $\Delta\lambda_\text{m}$ and $\Delta\phi_\text{m}$ are the meteorological data grid cell spans in the $\lambda\phi$-plane, and the weight function is [103]

$$W_j\left[\mathbf{x}, \mathbf{x}_\ell(t), \mathbf{h}\right] = \begin{cases} \frac{\alpha V}{h_{x_\ell} h_{y_\ell} h_{z_\ell}}\left(1 - \xi^2\right) & |\xi| \leq 1, \\ 0, & \text{otherwise} \end{cases}, \tag{5.21}$$

with $\xi^2 = \xi_i \xi_i$, where $\xi_i = \left[x_i - x_{i,\ell}(t)\right]/h_{\mathbf{x}_{i,\ell}}$ for $i \in \{x, y, z\}$, and $\alpha = 15/8\pi = 0.596831$. The averaging volume is given by the meteorological data grid cell area at the detector location $A_{\text{m},i} = \Delta x_{\text{m},i}\Delta y_{\text{m},i}$ and half the vertical component bandwidth: $V = A_{\text{m},i}h_{z_i}/2$, where $\Delta x_{\text{m},i} = R_\oplus \cos\phi_{\text{d},i}\Delta\lambda_\text{m}$ and $\Delta y_{\text{m},i} = R_\oplus\Delta\phi_\text{m}$ are the meteorological data grid cell spans in the horizontal plane at detector location $(\lambda_{\text{d},i}, \phi_{\text{d},i})$. The volume vertical bandwidth component is halved due to the reflection of particles at the surface.

---

[1]In general, the m-order B-spline is given by $m - 1$ repeated convolutions with the zero-order B-spline: $b_m(\xi) = (b_0 * b_{m-1})(\xi) = \int_{-\infty}^{\infty} b_0(\xi - \xi')b_{m-1}(\xi')\text{d}\xi'$.

5.5   Species Characterization and Mass Transfer

LPDMs such as FLEXPART and HYSPLIT are well-suited for modeling complex physical processes that the species being transported undergoes due to the Lagrangian particle description. This might include processes such as chemical interactions for chemical species, radioactive decay for radioisotope species, and particulate aerosol processes for particulate species. Such processes have the effect of either transferring mass from one species to another as in radiological or chemical transmutation or removing the species from the atmosphere as in deposition. In general, all of these processes could be coupled as in, e.g. a radioactive aerosol in chemical form. For chemical species, one might require reaction rates, while here we will only focus on the radioactive decay and dry deposition processes.

5.5.1   Dry Deposition

Both FLEXPART and HYSPLIT provide models for dry deposition of gases and particulates. Since it is impractical to explicitly model all of the microphysical processes by which species are removed from the atmosphere and deposited on solid surfaces [10], one instead characterizes the deposition using a parameter called the deposition velocity $\mathbf{U}_{\mathrm{dep}}$. This parameter is the proportionality constant defining the dry deposition mass flux $\mathbf{j}_{\mathrm{dep}}$ according to

$$\mathbf{j}_{\mathrm{dep}}(\mathbf{x}, t) = -\mathbf{U}_{\mathrm{dep}}(\mathbf{x}, t)C(\mathbf{x}, t), \tag{5.22}$$

where $C(\mathbf{x}, t)$ is the species concentration in the atmosphere. By convention, $\mathbf{U}_{\mathrm{dep}}$ is defined positive in the downward direction. Given the deposition velocity at some position for a given species, one can calculate a deposition time scale within a layer of thickness Δz_{p} near the Earth's surface [38]:

$$\lambda_{\mathrm{dep}} = U_{\mathrm{dep}}\Delta z_{\mathrm{p}}^{-1}. \tag{5.23}$$

This time scale determines the mass removal according to an exponential decay process [38, 104]

$$\frac{\mathrm{d}C(\mathbf{x}, t)}{\mathrm{d}t} = -\lambda_{\mathrm{dep}}C(\mathbf{x}, t). \tag{5.24}$$

That is, the atmospheric concentration after dry deposition within the layer Δz_{p} during a time step Δt is given by [1, 2, 38]

$$C(\mathbf{x}, t + \Delta t) = C(\mathbf{x}, t) \exp\left(-\lambda_{\mathrm{dep}}\Delta t\right). \tag{5.25}$$

Alternatively, one could use a probabilistic model in which each particle within the layer Δz_{p} deposits all of its mass during time period Δt with probability $\mathbb{P}_{\mathcal{U}(0,1)}\left[\xi < U_{\mathrm{dep}}\Delta z_{\mathrm{p}}^{-1}\Delta t\right]$, where $\xi \sim \mathcal{U}(0,1)$ [38]. In FLEXPART, $\Delta z_{\mathrm{p}} = 2h_{\mathrm{ref}}$ is the height below which particles may be deposited, where $h_{\mathrm{ref}} = 15\,\mathrm{m}$ by default is the reference height at which the deposition velocity is calculated, $U_{\mathrm{dep}} = U_{\mathrm{dep}}(h_{\mathrm{ref}})$.

FLEXPART and HYSPLIT allow the user to specify explicitly the deposition velocity parameter for a given species, or they can use the resistance method [1, 2, 10] to estimate it using alternative parameters for the species. Specifically, the resistance method [10, 105] for gases requires the diffusivity Γ, effective Henry's constant H, and specific reactivity parameter f_0 [1, 2, 38]. For particulates, the resistance method requires the particle density ρ_{p} and mean diameter $\langle d_{\mathrm{p}} \rangle$ since the deposition velocity depends on the gravitational settling velocity [2, 10]

$$U_{\mathrm{dep,grav}} = \frac{g\rho_{\mathrm{p}} \langle d_{\mathrm{p}} \rangle^2 C_{\mathrm{cun}}}{18\mu}, \tag{5.26}$$

where g is the gravitational acceleration μ is the air dynamic viscosity, C_{cun} is the Cunningham slip correction factor, and $\rho \ll \rho_{\mathrm{p}}$. FLEXPART additionally requires $\sigma_{d_{\mathrm{p}}}$, a measure of particle diameter variation in a log-normal distribution [1, 2]. Since the gravitational settling velocity has a strong (i.e. quadratic) dependence on particle diameter, it is therefore essential that one has an accurate representation of the particle density and size distribution when modeling particulate dry deposition.

5.5.2 Radioactive Decay

In the simplest case in which one is only interested in a single species undergoing radioactive decay without inter-species mass transfer, FLEXPART has a built-in linear loss model for species radioactive decay similar to the linear loss due to deposition. However, for modeling multiple species with inter-species mass transfer, a more sophisticated model must be used. Generally, the number of radionuclides for a given location satisfies the radionuclide transmutation or Bateman equation [106]

$$\frac{\partial N_j(\mathbf{x}, t)}{\partial t} = -\lambda_j N_j(\mathbf{x}, t) + \sum_{i \neq j} \beta_{ji} \lambda_i N_i(\mathbf{x}, t) + S_j(\mathbf{x}, t), \quad j \in J, \tag{5.27a}$$

with initial condition

$$N_j(\mathbf{x}, t_0) = N_{0,j}(\mathbf{x}) = \lambda_j^{-1} A_j(\mathbf{x}, t_0) = \lambda_j A_{0,j}(\mathbf{x}), \quad j \in J, \tag{5.27b}$$

where $\lambda_j = \ln 2 / T_{1/2,j}$ is the decay rate constant for a radionuclide with half-life $T_{1/2,j}$, β_{ji} is the branching ratio or fractional yield of nuclide j from decay of nuclide i, $S_j(\mathbf{x}, t)$ is a radionuclide source, and J is the set of radionuclides to model in the system. Equation 5.27a is a simplification of the depletion equation [107–109] used in nuclear reactor physics codes such as SCALE/ORIGEN [106], where we have neglected any transmutation due to neutron scalar flux $\phi(\mathbf{x}, E, t)$. The angle- and energy-integrated neutron flux in the atmosphere is on the order of $\phi \sim 10^{-3}\,\mathrm{cm}^{-2}\,\mathrm{s}^{-1}$ [110–112], and typical effective microscopic cross sections for e.g. neutron-induced fission $(\mathrm{n,f})$ or radiative capture (n,γ) reactions are on the order of $\sigma_{(\mathrm{n},x)} \sim 1\,\mathrm{b}$. Thus, the effective radionuclide transmutation rates are at most on the order of $\sigma_{(\mathrm{n},x)}\phi \sim 10^{-27}\,\mathrm{s}^{-1}$, and we can neglect these mechanisms in the atmosphere in comparison to radioactive decay alone provided $\sigma_{(\mathrm{n},x)}\phi \ll \lambda_j \Rightarrow T_{1/2,j} \ll \ln 2/\sigma_{(\mathrm{n},x)}\phi \sim 10^{27}\,\mathrm{s} \sim 10^{19}\,\mathrm{yr}$, which is true for most radionuclides.

When the species all have the same atmospheric transport characteristics one can completely decouple the ATM calculation from the radioactive decay calculation. This is the case when dealing with noble gases such as radioxenon and gaseous iodine. Iodine can form many chemical compounds, but gaseous iodine I_2 is often the dominant form of iodine in the radioactive decay chain $I \rightarrow {}^{\mathrm{m}}\mathrm{Xe} \rightarrow \mathrm{Xe}$. Thus, one can use a unit mass emission source to determine the ATM dilution factor $c(\mathbf{x}, t)$ according to Eq. 5.12 and scale the dilution factor by the radioactive decay. That is, the radionuclide (number) concentration for species or isotope j is given by

$$C_j(\mathbf{x}, t) = c(\mathbf{x}, t) N_j(\mathbf{x}, t), \tag{5.28a}$$

where $N_j(\mathbf{x}, t)$ is the number of radionuclides of isotope j at position $\mathbf{x}$ and time t. Alternatively, the radioactivity concentration is given by

$$C_j(\mathbf{x}, t) = c(\mathbf{x}, t) A_j(\mathbf{x}, t), \tag{5.28b}$$

where $A_j(\mathbf{x}, t) = \lambda_j N_j(\mathbf{x}, t)$ is the radioactivity of isotope j at position $\mathbf{x}$ and time t. When averaging Eqs. 5.28a or 5.28b over the same time periods as in Eq. 5.12, $c(\mathbf{x}, t_k)$ can be treated as constant over the time period $[t_k, t_{k+1})$. Then the mean radionuclide number or activity concentrations during this period are, respectively,

$$C_j(\mathbf{x}, t_k) = c(\mathbf{x}, t_k) \left\langle N_j(\mathbf{x}, t) \right\rangle_{t_k}, \tag{5.29a}$$

$$C_j(\mathbf{x}, t_k) = c(\mathbf{x}, t_k) \left\langle A_j(\mathbf{x}, t) \right\rangle_{t_k}. \tag{5.29b}$$

For multiple emission source time periods or locations, one can then simply add the contribu-
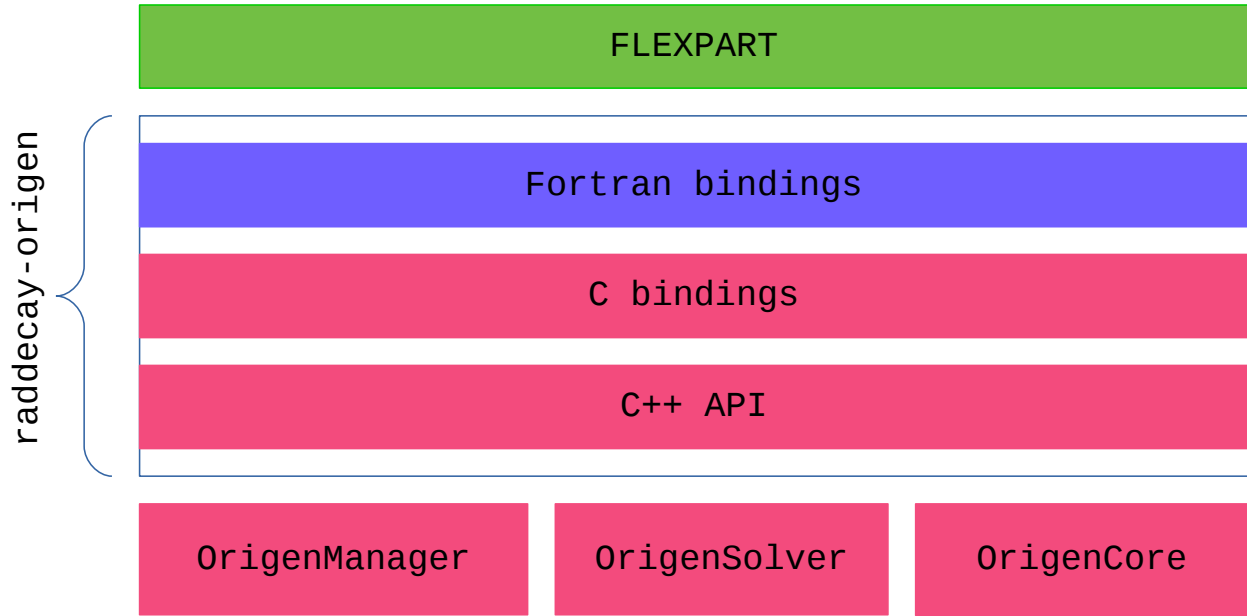
Figure 5.1: Structural diagram of FLEXPART bindings to ORIGEN depletion solver library.

tions from each source.

On the other hand, when there are complicated interactions between the radionuclide and chemical transmutation and the atmospheric transport, the radionuclide transmutation should be computed directly in the ATM. In this case, species transmutation and mass transfer are handled during the transport calculation, so Eq. 5.12 directly represents the radionuclide concentration. If the species also has chemical or gaseous dry deposition, the methods discussed in section 5.5.1 also apply. We have implemented a simple coupling between FLEXPART and the ORIGEN depletion solver to handle such cases and for comparison to our method relying on post-processing of the ATM dilution simulation results using Eqs. 5.27a and 5.28b. Figure 5.1 shows the structure of the bindings between FLEXPART and the ORIGEN libraries.

5.6 Adjoint Mode

In addition to the standard forward mode of operation, FLEXPART and HYSPLIT can be operated in a backward or adjoint [107, 108] mode. The measured adjoint ATM concentration profile represents the sensitivity of a receptor or to a spatiotemporal source region. That is, the adjoint concentration profile represents the spatiotemporal source contributions to a given receptor measurement. The Langevin stochastic velocity model is self-adjoint except for reversal of the time. Thus, the velocity is also reversed, and the Lagrangian particle trajectory

is backward relative to the standard trajectory, with particles originating at receptor locations. The advantage of an adjoint approach is that when there are far more source parameters than receptor parameters (i.e. measurements), as is often the case in source inversion/estimation problems, it can be computationally more efficient to use the adjoint method for constructing the source-receptor relationship [37]. However, this requires care to ensure that the well-mixed condition [82] is satisfied, and not all processes processes (such as deposition) can be easily represented through an adjoint formulation.

FLEXPART uses the concept of a backward residence time $T_\mathrm{r}^*(\mathbf{x}', t'|\mathbf{x}, t)$ which represents the amount of time spent within a gridded spatiotemporal region $(\mathbf{x}', t')$ by Lagrangian particles originating from a particular receptor location and time $(\mathbf{x}, t)$ [1, 2, 113, 114]. The spatiotemporal mass concentration field for species j in the receptor volume is determined by folding the residence time with the mass emission source density rate $S_j(\mathbf{x}, t)$ [103, 113]

$$C_j(\mathbf{x}, t_k) = \frac{1}{V(t_k - t_0)} \int_{t_0}^{t_k} \int_V T_\mathrm{r}^*(\mathbf{x}', t'|\mathbf{x}, t_k) S_j(\mathbf{x}', t') \mathrm{d}\mathbf{x}' \mathrm{d}t', \qquad (5.30)$$

where V is the simulation volume. In the simplest case of a constant source in a single grid cell and time period, this reduces to a simple multiplication.

Chapter 6

Applications of ATM

We presented the derivation of and physical basis for the Lagrangian particle dispersion models FLEXPART and HYSPLIT in chapter 3. Similarly, we derived in chapter 4 several different Eulerian models based on the Reynolds-averaged Navier-Stokes equation or the advection-diffusion equation with eddy viscosity or eddy diffusivity hypothesis. AD models with constant velocity field in stationary, homogeneous turbulence lead to the Gaussian puff and plume models such as the one discussed in section 4.3. Chapter 5 then discussed several aspects of the FLEXPART and HYSPLIT empirical models for transport, species transmutation, and particle averaging.

In this chapter we apply these models to several ATM simulations using both real and synthetic data sets. Section 6.1 presents several studies associated with source estimation or inversion for radionuclides, first looking at a large radioxenon source from the Fukushima Daiichi nuclear accident and then looking at emissions detected surrounding the DPRK. In section 6.2 we show a study on the atmospheric concentration of particulate matter undergoing dry deposition using FLEXPART or HYSPLIT. Finally, section 6.3 presents several studies on the different turbulence model scales involved in ATM.

6.1   Source Estimation
6.1.1   Fukushima Daiichi Gaseous Radioxenon and Iodine

In the aftermath of a radiological disaster, it is desirable to predict and estimate the amount of radionuclides released into the atmosphere and environment. We obtained [115] an estimate for radioxenon activity released into the atmosphere during the Fukushima Daiichi nuclear accident by minimizing the discrepancy between the measured radioactivity at several IMS detectors and that simulated with FLEXPART.

Table 6.1: Total Fukushima Daiichi radionuclide half lives and ORIGIN2 estimated inventories [3]. Inventories were estimated at the time of reactor shutdown (approximately 2011-03-11 05:46 UTC) and include Units 1-3 cores and Units 1-4 spent fuel pools.

Nuclide	$T_{1/2}$	ORIGEN2 inventory (PBq)
^{131m}Xe	11.934 d	6.70×10^1
^{133}Xe	5.2475 d	1.21×10^4
^{133m}Xe	2.198 d	3.58×10^2
^{135}Xe	9.14 h	4.28×10^3
^{135m}Xe	15.29 min	2.67×10^3
^{131}I	8.0252 d	6.02×10^3
^{133}I	20.83 h	1.26×10^4
^{135}I	6.58 h	1.20×10^4

6.1.1.1 Radiological Data

ORIGEN2 calculations [3] of Fukushima Daiichi radionuclide inventories were used as a starting point for estimating the radiological source emissions. The radionuclides of interest are shown in Table 6.1. Radionuclide concentration measurements from 11 US stations as well as two Japan stations in the IMS were used for comparison. Five of these stations included radioxenon measurement capabilities for detecting ^{131m}Xe, ^{133}Xe, ^{133m}Xe, and ^{135}Xe: USX74 in Ashland KS, USX75 in Charlottesville VA, USX77 on Wake Island, USX79 in Oahu HI, and JPX38 in Takasaki, Japan. The radioxenon stations have averaging periods of approximately 12 hours, while the particulate stations are typically averaged over 24 approximately hours. Insufficient data for USX75 was available during the simulation time, however, and is thus excluded from the comparison. Additionally, ^{133m}Xe and ^{135}Xe were not compared since ^{133m}Xe measurements were found to be unreliable due to difficulty discriminating with ^{133}Xe, while ^{135}Xe measurements exhibited a background concentration not significantly affected by the Fukushima events.

6.1.1.2 FLEXPART Configuration

We used FLEXPART to simulate the release of radioactive particles over an 8-day period from 2011-03-12 to 2011-03-20 UTC from a point source at the approximate center of units 1-4 and a height of 25 m. Particle deposition was disabled to represent the radioxenon and iodine gases, and the simulation was driven using hourly meteorological data from the
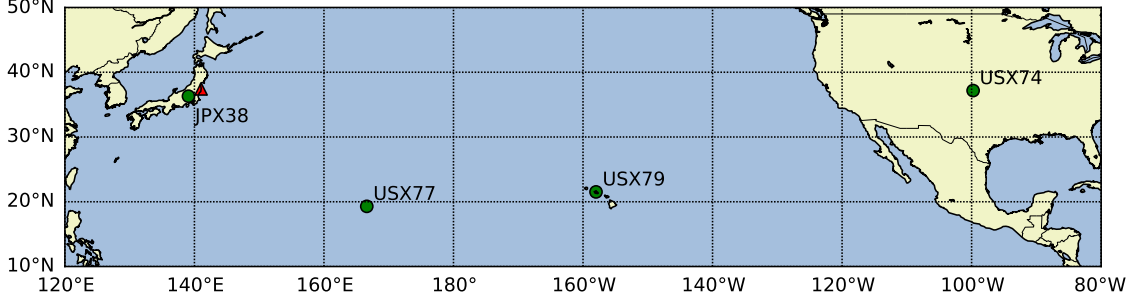
Figure 6.1: Fukushima Daiichi accident simulation release origin (*red triangle*) and IMS radioxenon detectors (*green circles*).

National Center for Environmental Prediction (NCEP) Climate Forecast System Reanalysis (CFSRv2) [116] on a 0.5°×0.5° horizontal spatial grid with 37 vertical atmospheric pressure levels. Simulated receptor measurements averaged over 3-hour periods were taken at all of the US IMS detectors as well as JPX38 for comparison to actual IMS radioxenon measurements. Figure 6.1 shows the release origin at the Fukushima Daiichi site as well as the nearest IMS RN stations of interest.

6.1.1.3   Radioactive Decay Post-processing

The radioactive decay chains for the gaseous radioxenon and iodine isotopes of interest are shown in Fig. 6.2. In order to account for radioxenon production due to iodine decay, the decay chains are each broken into two-step decay chains:

$$I \xrightarrow{\lambda_{\mathrm{I}}} {}^{\mathrm{m}}\mathrm{Xe} \xrightarrow{\lambda_{\mathrm{X}^*}} \mathrm{Xe}, \tag{6.1}$$

where X^* and X, respectively, represent the metastable and non-metastable xenon isotopes. Then the depletion Eqs. 5.27 for each decay chain take the form

$$\dot{\mathbf{N}}(\mathbf{x}, t) = \Lambda \mathbf{N}(\mathbf{x}, t), \tag{6.2}$$

where $\mathbf{N}(\mathbf{x}, t) = \begin{bmatrix} N_{\mathrm{I}}(\mathbf{x}, t) & N_{\mathrm{X}^*}(\mathbf{x}, t) & N_{\mathrm{X}}(\mathbf{x}, t) \end{bmatrix}^{\mathrm{T}}$ is the gaseous iodine and radioxenon amount, and

$$\Lambda = \begin{bmatrix} -\lambda_{\mathrm{I}} & 0 & 0 \\ \beta_{\mathrm{I} \to \mathrm{X}^*} \lambda_{\mathrm{I}} & -\lambda_{\mathrm{X}^*} & 0 \\ 0 & \beta_{\mathrm{X}^* \to \mathrm{X}} \lambda_{\mathrm{X}^*} & -\lambda_{\mathrm{X}} \end{bmatrix}, \tag{6.3}$$

$^{135}_{56}\text{Ba}$

100%

$^{133}_{55}\text{Cs}$ $^{135}_{55}\text{Cs}$

100%   100%

$^{131}_{54}\text{Xe}$ $^{133}_{54}\text{Xe}$ $^{135}_{54}\text{Xe}$ 0.6%

99.61%   100%   98.92%   100%   98.1%   99.4%

$^{131}_{53}\text{I}$ 0.39% $^{131m}_{54}\text{Xe}$ $^{133}_{53}\text{I}$ 1.08% $^{133m}_{54}\text{Xe}$ $^{135}_{53}\text{I}$ 1.9% $^{135m}_{54}\text{Xe}$
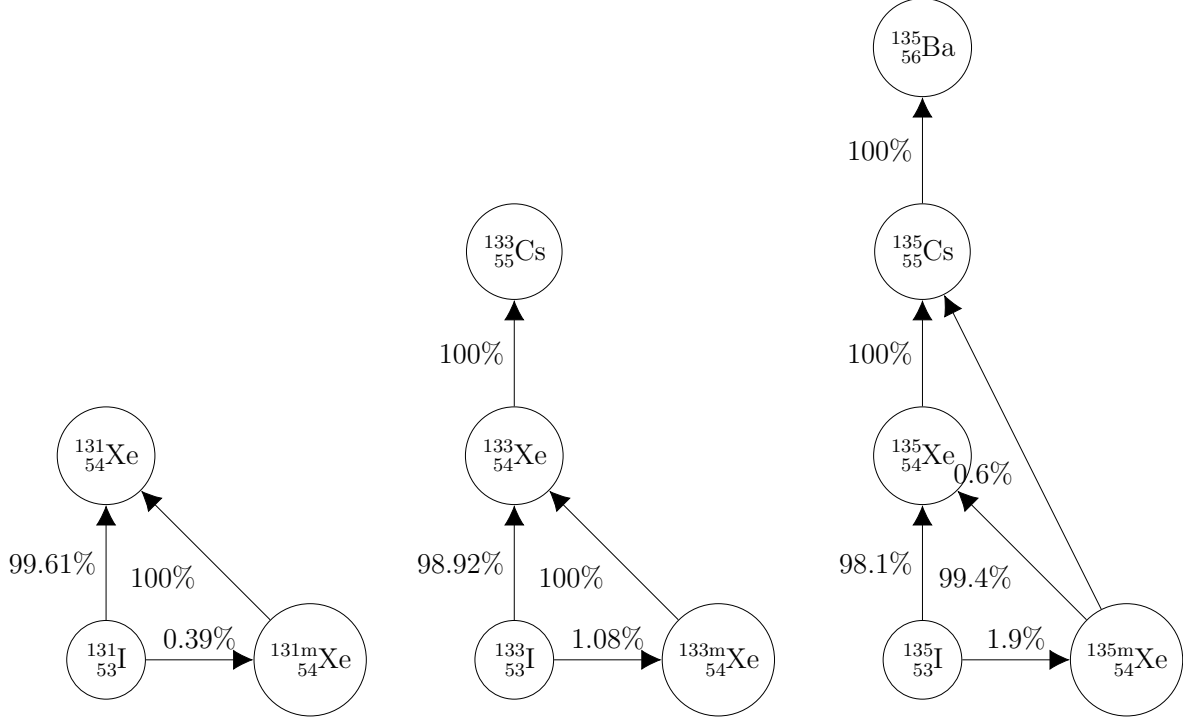
Figure 6.2: Iodine and xenon radionuclide decay chains

is the radionuclide transmutation matrix with branching ratios $\beta_{ji} = \beta_{i\to j}$. Equation 6.2 is solved analytically with the solution

$$\mathbf{N}(\mathbf{x}, t) = \exp\left[\Lambda(t - t_0)\right] \mathbf{N}(\mathbf{x}, t_0) \tag{6.4}$$

written in terms of the matrix exponential $\exp\left[\Lambda(t - t_0)\right]$ and initial condition Eq. 5.27b.

Since the gaseous iodine and radioxenon have the same atmospheric transport behavior, the detector radionuclide concentrations are given by averaging Eq. 6.4 according to Eq. 5.29b for each decay chain and each emission source period. In particular, the activity concentration $C_j(\mathbf{x}_i, t_k)$ of radionuclide j at a given detector location $\mathbf{x}_i$ and time t_k is given by the product of the atmospheric dilution $c_\ell(\mathbf{x}_i, t_k)$ due to a unit source emitted uniformly from t_ℓ to $t_\ell + \Delta t_\ell$ and the radioactivity of radionuclide j:

$$C_j(\mathbf{x}_i, t_k) = \sum_{\ell \in L} c_\ell(\mathbf{x}_i, t_k) \left\langle A_{j\ell}(\mathbf{x}_i, t) \right\rangle_{t_k}, \tag{6.5}$$

where L is the set of emission sources and the radioactivity of isotope j due to source ℓ is

$$A_{j\ell}(\mathbf{x}, t) = \lambda_j N_{j\ell}(\mathbf{x}, t) = \lambda_j \left\{ \exp\left[\Lambda(t - t_0)\right] \mathbf{N}_\ell(\mathbf{x}, t_0) \right\}_j, \tag{6.6}$$

with no implied Einstein summation. Similarly, we can calculate the averaged emitted radioactivity for radionuclide j due to emission source ℓ at $\mathbf{x}_\ell$ and the total radioactivity S_j due to all sources:

$$S_{j\ell} = \langle A_{j\ell}(\mathbf{x}_\ell, t)\rangle_{t_\ell}, \tag{6.7a}$$

$$S_j = \sum_{\ell \in L} S_{j\ell}. \tag{6.7b}$$

6.1.1.4 Source Estimation

We estimated the source intensities of $^{131\mathrm{m}}$Xe and ^{133}Xe by iteratively varying the emission magnitude for each isotope and attempting to minimize a metric based on the difference between the measured and the simulated isotope concentration at each IMS detector averaged over either a 7- or 14-day period from the first simulated measurement. The iodine emissions were held fixed at 10% of the inventory, roughly consistent with the literature [19]. Several different metrics were tested, all of which can be written in the form

$$\mathcal{L}(S) = \frac{1}{\sum_{i=1}^{D} w_i} \sum_{i=1}^{D} \frac{w_i}{N_i} \sum_{j=1}^{N_i} f(C_{ij}, \overline{C}_{ij}), \tag{6.8}$$

where w_i and N_i are the weights and number of measurements for each detector i, respectively, and $f(C_{ij}, \overline{C}_{ij})$ is a function of the simulated and measured concentrations C_{ij} and $\overline{C}_{ij}$, respectively, with $C_{ij} = C_{ij}(S)$ a function of the emission intensities S. The weights w_i examined were

1. unweighted N_i

2. geographic inverse squared distance N_i/r_i^2

while the functions $f(C_{ij}, \overline{C}_{ij})$ examined were

(a) absolute difference $\left(C_{ij} - \overline{C}_{ij}\right)^2$

(b) relative difference $\left(C_{ij}/\overline{C}_{ij} - 1\right)^2$

(c) difference relative to mean $4\left(C_{ij} - \overline{C}_{ij}\right)^2 / \left(C_{ij} + \overline{C}_{ij}\right)^2$.

6.1.1.5 Results and Analysis

A simple, uniform-time radionuclide release of 100% of the radioxenon inventory was used as the base source estimate. By varying the radioxenon source magnitude logarithmically from 0.01% to 100% of the radionuclide inventory from Table 6.1 and comparing the metrics for each source, we determined the optimal radioxenon source to be approximately 100% of the radioxenon inventory. After determining the optimal emission scaling factor for radioxenon in the case of a uniform emission, the 8-day emission period was divided into two separate 4-day periods of uniform emission, with each 4-day period having a different source emission intensity. Four separate weights were tested: 25%-75%, 50%-50%, 75%-25% and 87.5%-12.5% for the first and second periods, respectively. Performing the same sort of iteration over these cases resulted in an optimal time-dependent source which favored more of the release occurring in the first time period.

The unweighted and geographic distance weighted absolute concentration difference metrics yielded the same optimal estimate since they both emphasized the nearest detector, JPX38, due to the large absolute concentrations at the nearest detector. Using a 14-day comparison period also yielded smaller metrics on average than did a 7-day period. Ultimately, the unweighted concentration difference relative to the mean value of the measured and simulated concentration, metric 1(c), was used for optimal source estimation, corresponding to $w_i = N_i$ and $f(C_{i,j}, \overline{C}_{i,j}) = 4\left(C_{ij} - \overline{C}_{ij}\right)^2 / \left(C_{ij} + \overline{C}_{ij}\right)^2$ in Eq. 6.8. This metric is is relatively independent of the absolute magnitude of the concentrations and is symmetric in that simulated values which are greater than or less than the measurements by a given factor will impact the metric equally. Its value ranges from 0 at best to 4 at worst.

Simulated and measured IMS detector concentrations for ^{131m}Xe and ^{133}Xe are shown in Fig. 6.3, and the corresponding metrics for the different detectors, radionuclides and time periods for which there was sufficiently reliable data are given in Table 6.2. All three US IMS stations show a relatively good agreement between the measured and simulated concentrations around the time of the initial peak, followed by a significant dip and resurgence. The Oahu HI station USX79 shows a time offset of about 6 hours between the measured and simulated dip time, while the Wake Island station USX77 has an offset of about 12 hours. The Ashland KS station modeled concentrations show an initial set of two peaks which are not observed in the IMS data. Additionally, the simulated concentrations at USX77 and JPX38 show a gap of approximately 12 hours and 4 days, respectively, around the time of the dip not observed in the IMS data. When comparing the metrics for the base case and optimized
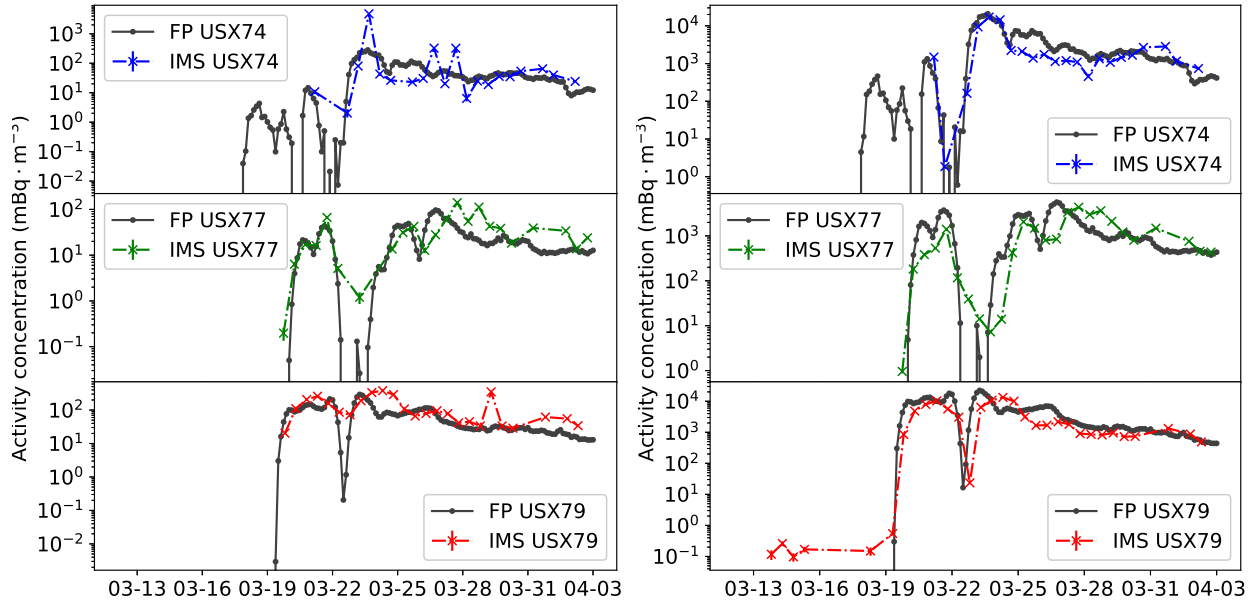
Figure 6.3: US IMS ^{131m}Xe (*left*) and ^{133}Xe (*right*) concentrations assuming 100% radioxenon inventory emissions and 10% iodine emissions with a time-dependent source emitting 87.5% over the first 4 days and 12.5% over the final 4 days. The solid grey lines are FLEXPART (FP) predictions, and the dashed lines are IMS detector measurements.

case, the time-dependent optimization benefited both the first and second 7-day periods of the comparison window for stations USX77 and USX79, while for detectors JPX38 and USX74, there was a small improvement in the second 7-day period metric. The worst overall agreement was observed at JPX38, while the best agreement was observed at the US detectors for ^{133}Xe in the second 7-day period. Using a metric such as 1(a) which more heavily weights larger concentrations would improve the agreement at JPX38 at the cost of worsening the agreement at the US stations.

After obtaining the optimal source estimate, using Eq. 6.7a and summing over all emission sources, we calculated the total emissions for ^{133}Xe to be 8×10^3 PBq. Values found in the literature for the estimated emissions of ^{133}Xe during the Fukushima Daiichi accident vary from 4.1×10^2 PBq [19] to 1.53×10^4 PBq [16]. Most previous estimates, however, are on the order of 10^4 PBq, so our estimate is roughly in line with what has been found in the literature. An estimated 60 PBq of ^{131m}Xe were also emitted. Using metric 1(a) results in an optimally estimated emission of 100 PBq and 0.5 PBq for ^{133}Xe and ^{131m}Xe, respectively, which could be viewed as a lower-bound estimate.

Table 6.2: Iteration summary for metric 1(c) in Eq. 6.8 for the optimized, time-dependent source plotted in Fig. 6.3.

| Detector | Time (days) | Radionuclide | | Average |
		^{131m}Xe	^{133}Xe	
JPX38	0-7	2.92	3.85	3.69
	7-14	3.49	1.48	3.28
	0-14	3.41	3.56	3.47
USX74	0-7	1.50	1.04	1.25
	7-14	0.891	0.542	0.709
	0-14	1.09	0.714	0.894
USX77	0-7	0.956	1.56	1.29
	7-14	0.650	0.373	0.512
	0-14	0.810	1.06	0.942
USX79	0-7	0.583	1.74	1.27
	7-14	0.514	0.349	0.432
	0-14	0.552	1.23	0.930
Average	0-7	1.08	2.14	1.74
	7-14	1.63	0.485	1.15
	0-14	1.41	1.48	1.44

6.1.2 Fukushima Daiichi Kalman Filter Estimation

After performing a simple, heuristic-based optimization of the radioxenon and iodine emissions from the Fukushima Daiichi nuclear accident as described in section 6.1.1, we sought to perform a more systematic source estimation using a Kalman filter algorithm. The Kalman filter algorithm is an optimal algorithm in that it is a minimum variance estimation method, and it is equivalent to a maximum likelihood estimation (MLE) or Bayesian maximum *a posteriori* (MAP) estimation method with Gaussian errors [117–119]. As in section 6.1.1, we used FLEXPART to simulate the emissions over the 8-day period from 2011-03-12 to 2011-03-20 UTC from a point source at the approximate center of units 1-4 and a height of 25 m. We used the same CFSRv2 meteorological data, but the 8-day emission period was divided into 16 independent 12-hour uniform sources, and simulated receptor concentrations were averaged over 12-hour periods, consistent with the IMS data.

6.1.2.1 Kalman Filter Description

The discrete-time Kalman filter is the optimal linear filter for estimating the state of linear dynamical systems [118]. In discrete-time form, the linear dynamical system is characterized by a linear dynamical model for the state $\mathbf{x}_k \in \mathbb{R}^N$ at step k and a linear observation model

for the measurements $\mathbf{z}_k \in \mathbb{R}^M$, respectively [118]:

$$\mathbf{x}_k = F_{k-1}\mathbf{x}_{k-1} + B_{k-1}\mathbf{u}_{k-1} + \mathbf{w}_{k-1}, \tag{6.9a}$$

$$\mathbf{z}_k = H_k\mathbf{x}_k + \mathbf{v}_k, \tag{6.9b}$$

where $F_k \in \mathbb{R}^{N \times N}$ is the state transition model, B_k is the control-input model for a control vector $\mathbf{u}_k$, $H_k \in \mathbb{R}^{M \times N}$ is the observation model matrix, and $\mathbf{w}_k \sim \mathcal{N}(0, Q_k)$ and $\mathbf{v}_k \sim \mathcal{N}(0, R_k)$ are uncorrelated Gaussian white noise processes with covariances $Q_k \in \mathbb{R}^{N \times N}$ and $R_k \in \mathbb{R}^{M \times M}$, respectively. Thus, Q_k is the model or process covariance, while R_k is the measurement or observation covariance. The purpose of the Kalman filter is to optimally estimate the true state $\mathbf{x}_k$ with the estimate $\hat{\mathbf{x}}_{k|m}$ based on noisy measurements $\{\mathbf{z}_k\}_{k=1,\ldots m}$ and the model dynamics by minimizing the state covariance matrix $P_{k|m}$:

$$\hat{\mathbf{x}}_{k|m} \equiv \langle \mathbf{x}_k | \mathbf{z}_1, \ldots, \mathbf{z}_m \rangle, \tag{6.10a}$$

$$P_{k|m} \equiv \left\langle \left[\mathbf{x}_k - \hat{\mathbf{x}}_{k|m}\right]\left[\mathbf{x}_k - \hat{\mathbf{x}}_{k|m}\right]^{\mathrm{T}} \middle| \mathbf{z}_1, \ldots, \mathbf{z}_m \right\rangle. \tag{6.10b}$$

As is apparent from Eqs. 6.9, the state $\mathbf{x}_k$ at step k depends only on the state $\mathbf{x}_{k-1}$ from the previous step. Then the Kalman filter is a recursive algorithm, and it is closely related to the hidden Markov model [120]. Typically, the Kalman filter algorithm is written in two steps: a prediction step using the dynamical model Eq. 6.9a and an update step incorporating the observation Eq. 6.9b. In particular, the Kalman filter predicts the *a priori* state estimate $\hat{\mathbf{x}}_{k|k-1}$ at step k using the *a posteriori* state $\hat{\mathbf{x}}_{k-1|k-1}$ from step $k-1$, and the *a posteriori* state estimate $\hat{\mathbf{x}}_{k|k}$ updates the *a priori* estimate $\hat{\mathbf{x}}_{k|k-1}$ by incorporating the observation $\mathbf{z}_k$ at step k. By taking the ensemble average of Eq. 6.9a, one can show that for $k \geq 1$ the *a priori* state estimate $\hat{\mathbf{x}}_{k|k-1}$ and covariance $P_{k|k-1}$, respectively, from the prediction step are given by [118]:

$$\hat{\mathbf{x}}_{k|k-1} = F_{k-1}\hat{\mathbf{x}}_{k-1|k-1} + B_{k-1}\mathbf{u}_{k-1}, \tag{6.11a}$$

$$P_{k|k-1} = F_{k-1}P_{k-1|k-1}F_{k-1}^{\mathrm{T}} + Q_{k-1}. \tag{6.11b}$$

Then the update step incorporates the measurement $\mathbf{z}_k$ using the observation Eq. 6.9b with the predicted *a priori* state estimate $\hat{\mathbf{x}}_{k|k-1}$ to calculate the *a posteriori* state estimate $\hat{\mathbf{x}}_{k|k}$

and covariance $P_{k|k}$ as [118]

$$K_k = P_{k|k-1}H_k^{\mathrm{T}}(H_k P_{k|k-1}H_k^{\mathrm{T}} + R_k)^{-1}, \qquad (6.12\mathrm{a})$$

$$\hat{\mathbf{x}}_{k|k} = \hat{\mathbf{x}}_{k|k-1} + K_k(\mathbf{z}_k - H_k\hat{\mathbf{x}}_{k|k-1}), \qquad (6.12\mathrm{b})$$

$$P_{k|k} = (I_N - K_k H_k)\,P_{k|k-1}, \qquad (6.12\mathrm{c})$$

where $K_k \in \mathbb{R}^{N \times M}$ is the Kalman filter gain matrix, $\mathbf{y}_k = \mathbf{z}_k - H_k\hat{\mathbf{x}}_{k|k-1}$ is the innovation or residual, and $S_k = H_k P_{k|k-1}H_k^{\mathrm{T}} + R_k$ is the system or innovation covariance.

6.1.2.2   Results and Analysis

For our observation model, measurements $\mathbf{z}_k$ consist of the radioxenon isotope concentrations profiles at the IMS detectors, while the state $\mathbf{x}_k$ we seek to estimate is the radionuclide emission source magnitude. In our dynamical model, the state transition matrix is the identity matrix $F_k = I_N$, and the control vector $\mathbf{u}_k$ is zero. That is, we assume that the estimated emission source $\hat{\mathbf{x}}_{k|k}$ depends only on the measurements and not a dynamical model or control system. The measurements vector consists of measurements for the set of radioxenon isotopes we wish to optimize against at each detector location and time. Similarly, the state vector consists of the set of radionuclides which are emitted from the set of source locations and times which contribute to the measured radioxenon isotopes. Thus, the observation or source-receptor matrix H_k accounts for both radionuclide transmutation and atmospheric dilution from the FLEXPART model, with each row yielding the radionuclide source contribution to a given receptor concentration measurement. Then for $N_{\mathrm{src},t} = 16$ uniform time emission sources and $N_{\mathrm{src,iso}} = 8$ emitted radioxenon and gaseous iodine isotopes of mass numbers 131, 133, and 135, we have $N = N_{\mathrm{src},t}N_{\mathrm{src,iso}} = 128$ source terms to optimize against $M = 244$ radioxenon detector measurements.

Using the ORIGEN2 inventory from Table 6.1, the initial estimate for $\hat{\mathbf{x}}_{0|0}$ was constructed such that the radionuclide inventories were allocated uniformly to each time period. Similarly, the initial error estimate $P_{0|0}$ was constructed with the assumption that there is 25% uncertainty in the initial state, which is also used for estimating the model uncertainty Q_k. Table 6.3 shows the optimally estimated emissions for each radionuclide, while Fig. 6.4 shows the optimal ^{133}Xe concentration profiles at the JPX38, USX74, USX77, and USX79 IMS detector stations. In particular, we estimate the ^{133}Xe emissions at $7.0(1) \times 10^3$ PBq, which is relatively consistent with the results of section 6.1.1. Furthermore, as in section 6.1.1, the ^{133}Xe estimated and measured concentration profiles at the IMS detectors are similar in their trend but often with different magnitudes or peak and trough timing. That is, the peak and

Table 6.3: Total estimated radionuclide emissions at Fukushima Daiichi from 16 12-hour uniform emission sources from 2011-03-12 to 2011-03-20 UTC.

Nuclide	S_j (PBq)
^{131m}Xe	$3.07(3) \times 10^2$
^{133}Xe	$7.0(1) \times 10^3$
^{133m}Xe	$4.74(1) \times 10^3$
^{135}Xe	$9(2) \times 10^1$
^{135m}Xe	$1.1(4) \times 10^{-1}$
^{131}I	$8.1(4) \times 10^3$
^{133}I	$1.66(2) \times 10^4$
^{135}I	$9(2) \times 10^1$

trough concentrations often differ by one or two orders of magnitude.

6.1.3   DPRK Weapons Tests

We have simulated several of the DPRK nuclear weapons tests and made comparisons to local IMS radioxenon data. Here we present an analysis of the most recent and largest DPRK nuclear weapon test performed on September 3, 2017. We used FLEXPART to simulate a 24-hour delayed, 72-hour radioxenon emission from the DPRK test site using both ERA-Interim and CFSRv2 meteorological data. This delay is intended to account for a delayed leakage from the underground test site, while the 72-hour emission is intended to capture a sufficiently broad release duration, since the exact timing is unknown. The simulated concentration measurements were then compared to IMS measurements in order to estimate the emission intensity. Unfortunately, there was only a single IMS measurement above the minimum detectable concentration (MDC) of ^{133}Xe $\sim 3\,\mathrm{mBq\,m^{-3}}$ from USX75 at Charlottesville, VA on September 30.

6.1.3.1   Results and Analysis

The ^{133}Xe measurement at USX75 was used to scale the emission intensity for each mete-orological data simulation using a simple linear least-squares estimation. This resulted in an optimally estimated ^{133}Xe emissions of 20 PBq and 70 PBq when using the CFSRv2 and ERA-Interim data sets, respectively. Figures 6.5 and 6.6 show the ^{133}Xe plume concentration profile when scaled by this emission intensity for the CFSRv2 and ERA-Interim data sets, respectively. Comparing the two figures, it is apparent that the plume is more diffuse when using the ERA-Interim data set than when using the CFSRv2 data set since there is a larger region with relatively high concentration (shown in red) in Fig. 6.6 at each time step. This

99

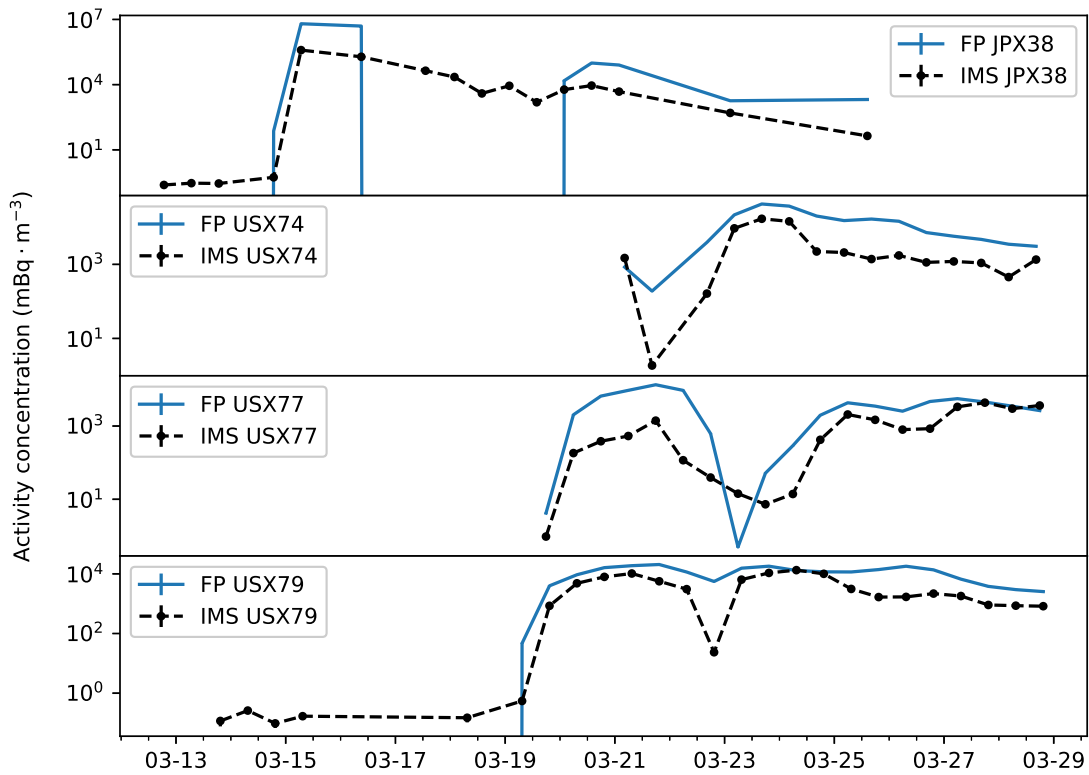Figure 6.4: IMS detector ^{133}Xe concentrations. The solid blue lines are FLEXPART (FP) predictions, and the dashed black lines are IMS detector measurements.
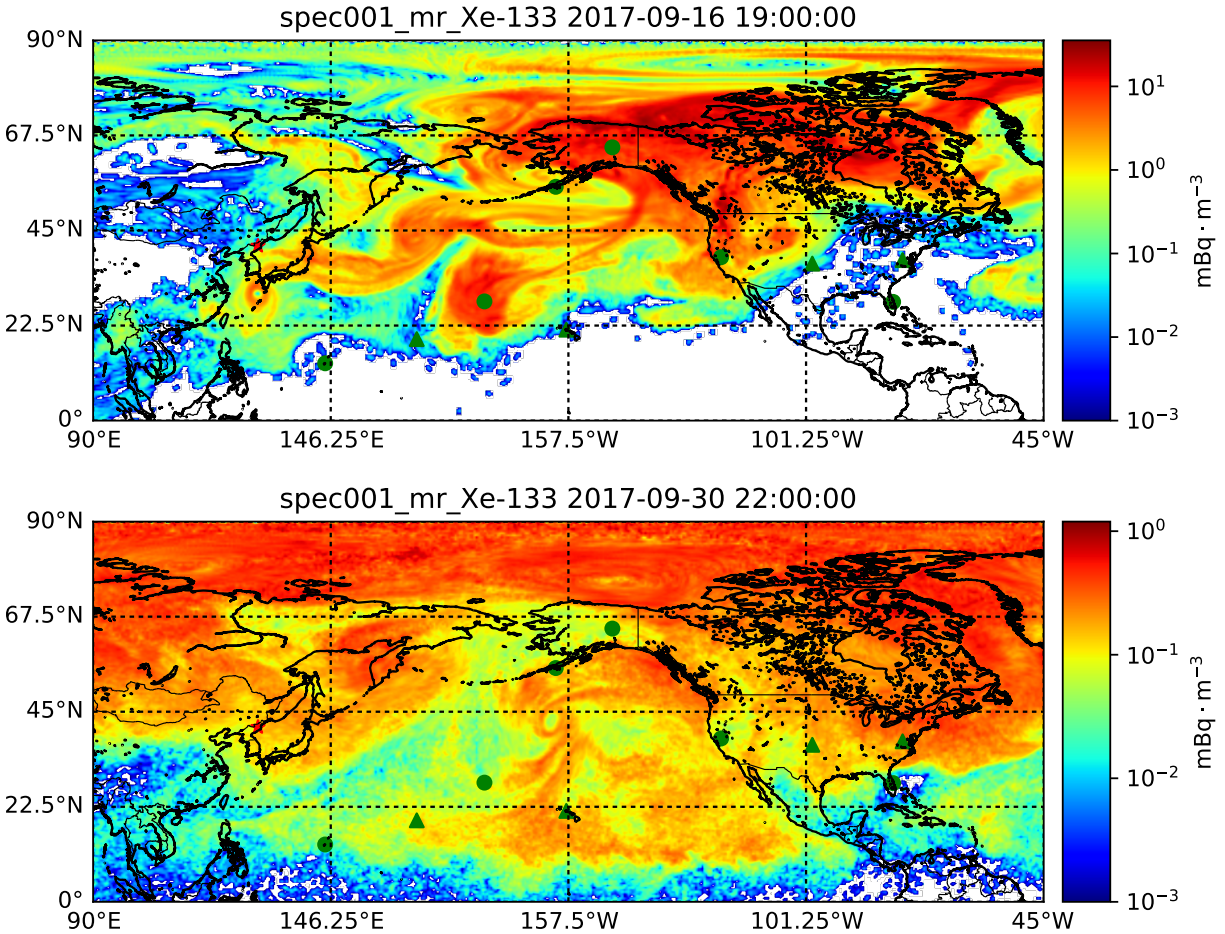
Figure 6.5: FLEXPART simulated optimal ^{133}Xe plume concentration profile at 2017-09-16 19:00 UTC (*top*) and 2017-09-30 22:00 UTC (*bottom*) using the CFSRv2 meteorological data set. The DPRK test site is shown by the red star, while the green circles and green triangles show the US IMS particulate and radioxenon stations, respectively.

explains why a larger emission is predicted by the ERA-Interim data set: the more diffuse plume requires a larger intensity emission to explain the measurement at USX75.

6.1.4 May 2010 DPRK Radionuclide ATM Analysis

In May 2010 there were several unusual measurements of radioxenon and particulate radionuclides from four RN detectors near the Korean peninsula [4, 7]:

- Radioxenon: Korea Institute of Nuclear Safety (KINS) SAUNA station at Geojin, ROK and JPX38 at Takasaki, Japan

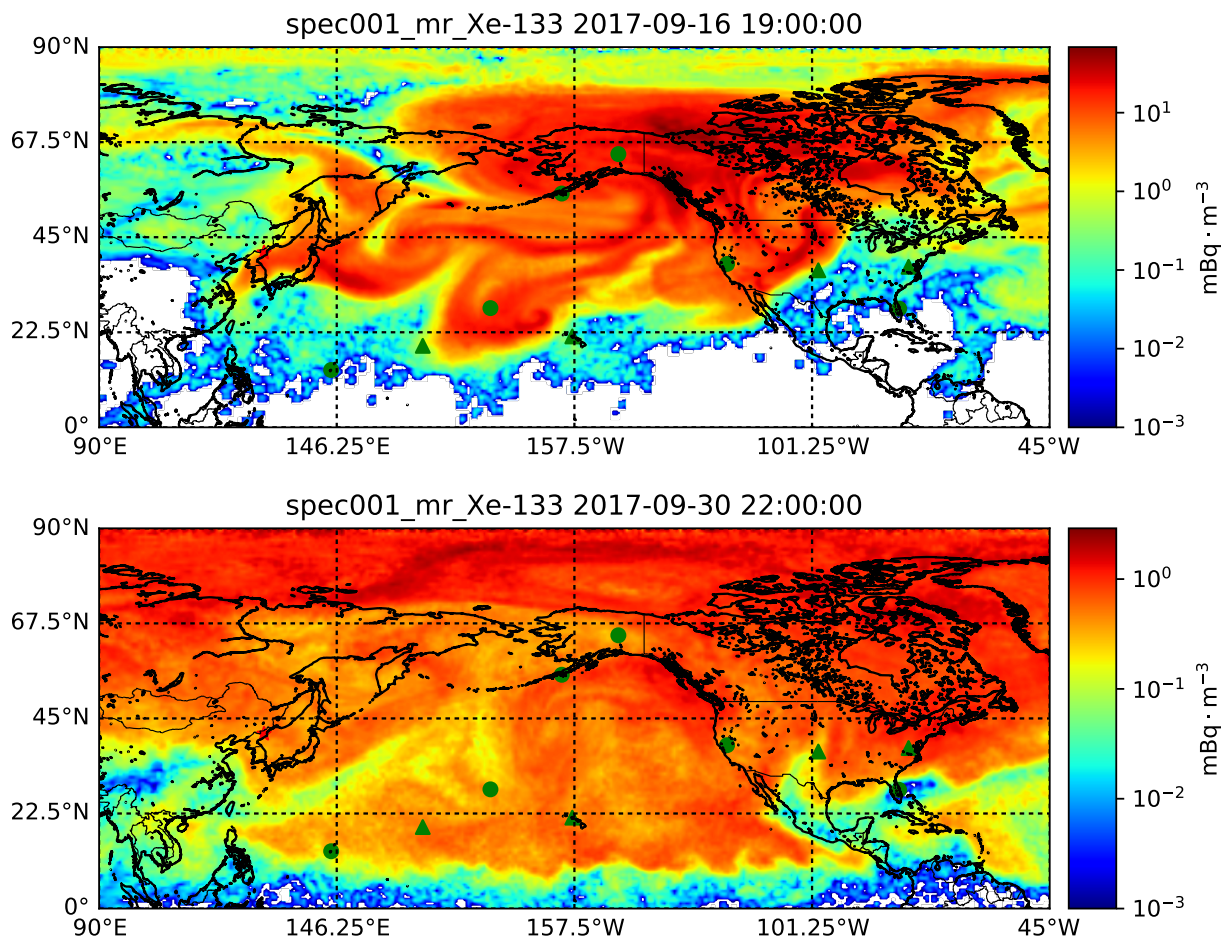- Particulate: JPP37 at Okinawa, Japan and RUP58 at Ussuriysk, RU

Figure 6.6: FLEXPART simulated optimal ^{133}Xe plume concentration profile at 2017-09-16 19:00 UTC (*top*) and 2017-09-30 22:00 UTC (*bottom*) using the ERA-Interim meteorological data set. The DPRK test site is shown by the red star, while the green circles and green triangles show the US IMS particulate and radioxenon stations, respectively.

Station	Time (UTC)	^{131m}Xe	^{133m}Xe	^{133}Xe	^{135}Xe
Geojin	13 May 23:00	< 0.2	< 0.2	2.45 ± 0.2	10.01 ± 0.6
JPX38	15 May 18:46	< 0.02	< 0.06	< 0.10	< 0.61
JPX38	16 May 06:46	0.04 ± 0.03	< 0.09	0.16 ± 0.07	< 0.57
JPX38	16 May 18:46	0.05 ± 0.03	< 0.08	0.23 ± 0.06	< 0.47
JPX38	17 May 06:46	0.16 ± 0.07	< 0.09	1.49 ± 0.11	< 0.20
JPX38	17 May 18:46	< 0.04	< 0.05	0.52 ± 0.07	< 0.06
JPX38	18 May 06:46	< 0.11	0.10 ± 0.06	0.79 ± 0.09	< 0.58
JPX38	18 May 18:46	0.06 ± 0.03	< 0.02	< 0.10	0.42 ± 0.23
JPX38	19 May 06:46	< 0.07	< 0.05	0.18 ± 0.06	< 0.52

Table 6.4: Radioxenon concentrations in mBq m^{-3} at Geojin, ROK and Takasaki, Japan which were unusual in their concentration (highlighted in red) for normal civilian activities [4].

These radioxenon measurements and isotopic ratios are summarized in Tables 6.4 and 6.5.

De Geer and Wright used these measurements to make the following observations and claims:

- The ^{140}La/^{140}Ba isotopic ratio detected at Okinawa was used to estimate an emission time origin.

- The most likely candidate origin for the measurements at Okinawa and Geojin was North Korea based on ATM.

- Isotopic ratios were consistent with a nuclear explosion or a nuclear reactor near start-up.

- There may have been a low-yield, decoupled nuclear test by North Korea on 11 May 2010.

However, there were several problems with these claims:

- The Seismic evidence does not support an explosive test at this time and location [121, 122]

- Some isotopes were not detected.

Station	Time (UTC)	$\frac{^{133m}\text{Xe}}{^{133}\text{Xe}}$	$\frac{^{133m}\text{Xe}}{^{131m}\text{Xe}}$	$\frac{^{133}\text{Xe}}{^{131m}\text{Xe}}$	$\frac{^{135}\text{Xe}}{^{131m}\text{Xe}}$	$\frac{^{135}\text{Xe}}{^{133}\text{Xe}}$
Geojin	13 May 23:00	< 0.08		> 12	> 50	4.1 ± 0.4
JPX38	15 May 18:46					
JPX38	16 May 06:46	< 0.56	< 2.25	4.0 ± 3.5	< 14	< 3.6
JPX38	16 May 18:46	< 0.35	< 1.60	4.6 ± 3.0	< 9.4	< 2.0
JPX38	17 May 06:46	< 0.06	< 0.56	9.3 ± 4.1	< 1.25	< 0.13
JPX38	17 May 18:46	< 0.10		> 13		< 0.12
JPX38	18 May 06:46	0.13 ± 0.08	> 0.91	> 7.2		< 0.73
JPX38	18 May 18:46		< 0.33	< 1.7	7.0 ± 5.2	> 4.20
JPX38	19 May 06:46	< 0.28		> 2.6		< 2.89

Table 6.5: Radioxenon isotopic ratios at Geojin, ROK and Takasaki, Japan which were unusual (highlighted in red) for normal civilian activities [5, 6].

- We cannot be certain nuclides came from a nuclear explosion or from the North Korea Test Site (NKTS) based on ATM

This latter point is based on the fact that the ATM results presented by De Geer and Wright were relatively simplistic and did not appreciate all of the uncertainties involved in ATM. Thus, we have analyzed this event by two methods: forward simulation of atmospheric emissions and backward/adjoint detector sensitivity calculations. Consistent with Wright, we analyzed three potential emission sites, shown in Fig. 6.7:

- Bolshoi Kamen, RU: Russian naval base near Vladivostok

- Uljin, ROK: nuclear power reactor

- NKTS, DPRK: weapons test site

6.1.4.1 Forward Simulation Results and Analysis

For the forward simulations, we used three potential emission sites at various times in a 48-hour window predicted by De Geer's $^{140}\text{La}/^{140}\text{Ba}$ ratio detected at Okinawa. Emissions consisted of a unit source release divided into several radionuclides from the iodine and xenon decay chains for mass numbers 131, 133, and 135. Radioactive decay was coupled to the transport process using ORIGEN with FLEXPART as described in section 5.5.2. For
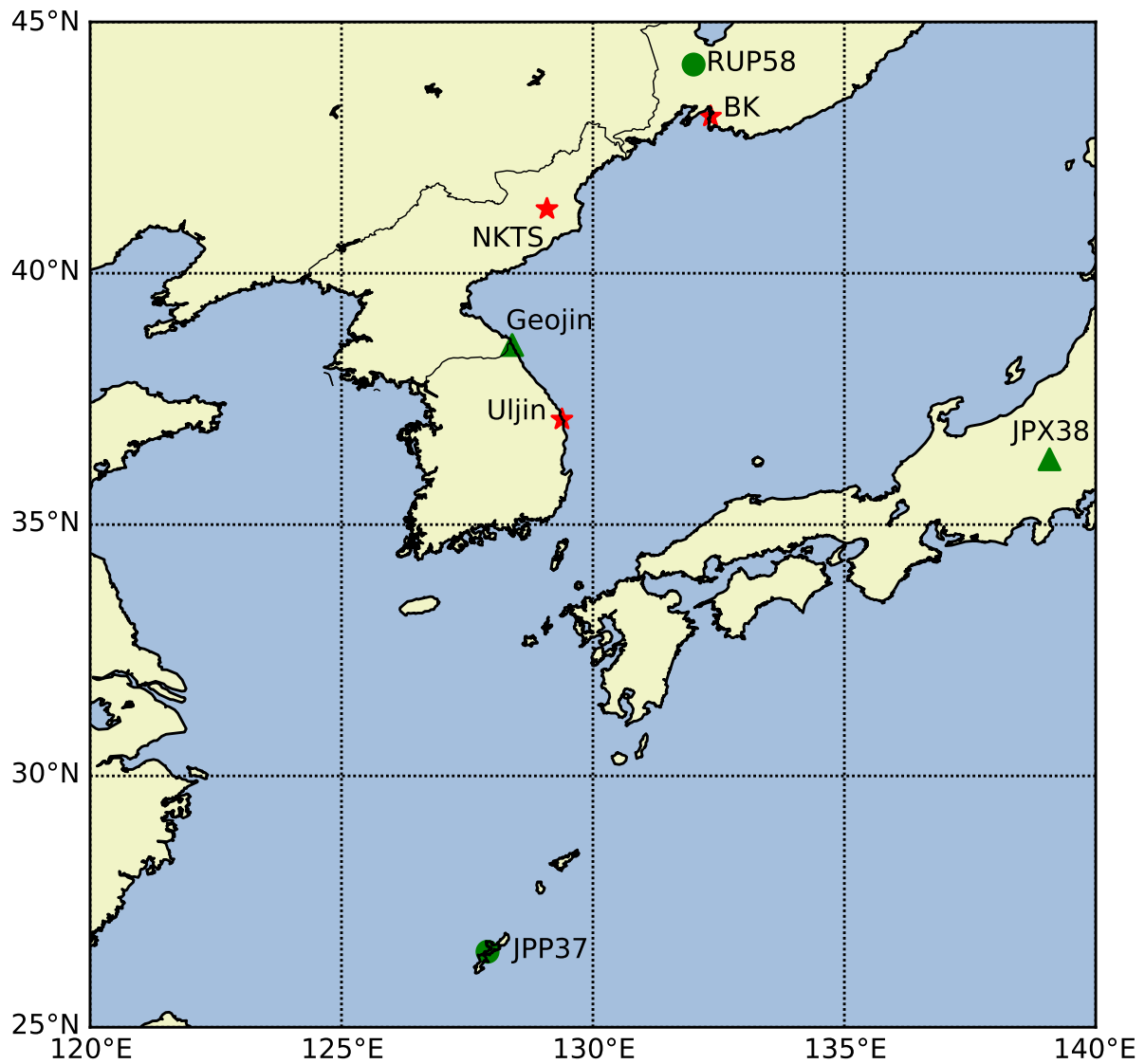
Figure 6.7: Potential emission sites (*red stars*) as well as RN particulate (*green circles*) and radioxenon detectors (*green triangles*) for the DPRK 2010 RN ATM simulations.

Emission time (UTC)	Emission site	Met data	^{131m}Xe	^{133m}Xe	^{133}Xe	^{135}Xe
10 May 12:00	BK, RU	CFSR	1.51e10	8.05e10	2.71e12	9.63e11
		ERAI	5.87e11	3.14e12	1.06e14	3.75e13
11 May 06:00	NKTS, DPRK	CFSR	2.00e10	1.07e11	3.59e12	1.27e12
		ERAI	6.97e13	3.72e14	1.25e16	4.45e15
	Uljin, ROK	CFSR	4.60e11	2.46e12	8.27e13	2.94e13
		ERAI	4.33e12	2.31e13	7.78e14	2.77e14
12 May 18:00	NKTS, DPRK	CFSR	5.60e09	2.99e10	1.01e12	3.57e11
		ERAI	8.63e10	4.61e11	1.55e13	5.51e12
	Uljin, ROK	CFSR	3.23e10	1.72e11	5.80e12	2.06e12
		ERAI	6.45e11	3.44e12	1.16e14	4.11e13

Table 6.6: Emission levels estimated by source optimization against IMS data for each of the emission sites, times, and meteorological data sets. Values highlighted in red are relatively high for the emission source type, while those in blue are relatively low for the type of emission source. Emission times were selected as potentially significant based on Wright's analysis [7].

Site	Type	^{131m}Xe	^{133m}Xe	^{133}Xe	^{135}Xe	Total
Bolshoi Kamen, RU	Naval reactor					1e8-1e9
Uljin, ROK	Power reactor	1e9	1e8	1e10	1e10	1e10-1e11
NKTS, DPRK	Nuclear weapon test					1e12-1e15

Table 6.7: Typical radioxenon emission levels for the different types of sites [8].

each emission site and time, we used either CFSR or ERA-Interim meteorological data and measured the simulated concentrations at Takasaki and Geojin, primarily focusing on ^{133}Xe when comparing to the IMS data. The unit source release was scaled using a simple linear-least squares optimization against the IMS data in order to estimate actual radionuclide emissions in becquerel. These emissions, shown in Table 6.6, were compared to typical emission levels for various source types as shown in Table 6.7.

From these results we can see that the NKTS has emission intensities which are of the right order of magnitude in two of our simulations, while the other simulations indicate unreasonable emission magnitudes. However, we cannot conclusively say that this validates De Geer's claim that the origin of the radionuclide signatures is from the NKTS because we have not fully explored the emission parameter space. In particular, the emission intensities are highly dependent on both the meteorological data and the emission site and time. Figures
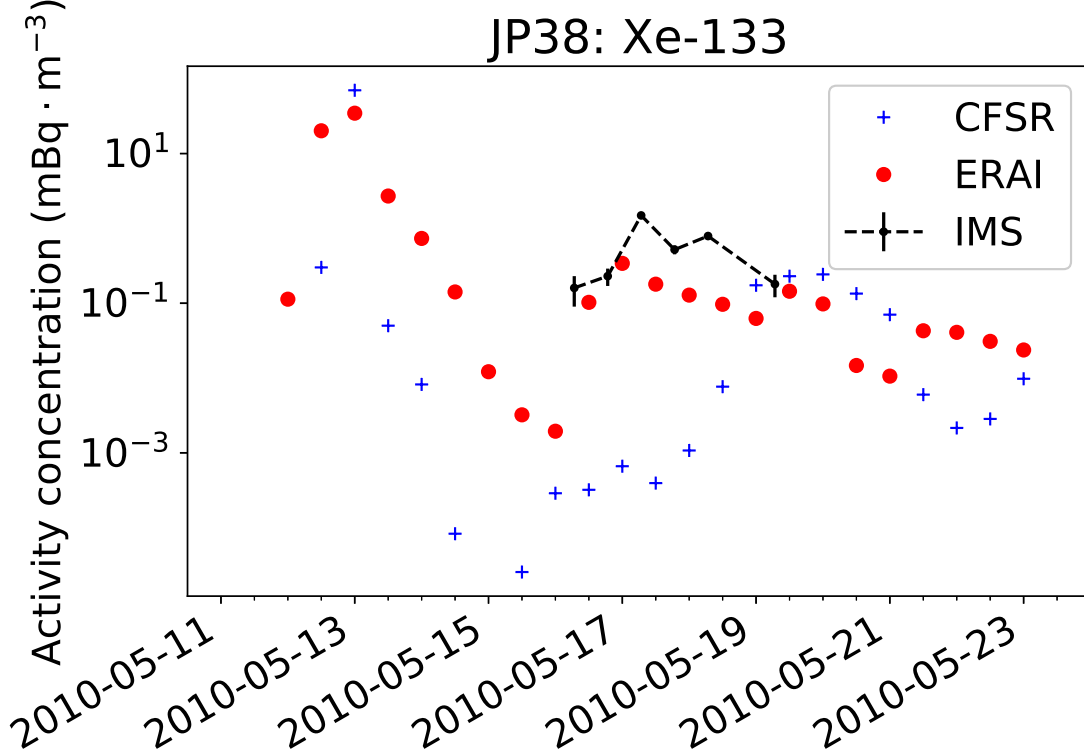
Figure 6.8: ^{133}Xe concentrations at Takasaki, Japan JPX38 IMS station due to an emission source from Bolshoi Kamen at 2010-05-10 12:00 UTC. The dashed lines are IMS detector measurements, while the colored markers are optimally estimated FLEXPART concentrations for each meteorological data set.

6.8 and 6.9, respectively, show the optimal temporal concentration profiles of ^{133}Xe at JPX38 due the emission source from Bolshoi Kamen at 2010-05-10 12:00 UTC and from NKTS at 2010-05-12 18:00 UTC. We observe that the Bolshoi Kamen emission results in a large peak concentration before the measured data, and the CFSR simulation predicts a peak ~ 2 days late. While the NKTS emission yields a temporal trend more similar to the IMS data, the peak concentration is still underestimated by about an order of magnitude.

6.1.4.2 Backward/Adjoint Detector Sensitivity Analysis

As shown in Tables 6.4 and 6.5, the measurement at Geojin in particular was significant. Thus, we used this measurement in adjoint simulations to try to estimate spatiotemporal sensitivities for potential emission sites and times. The $2°\times2°$ regional averages around our

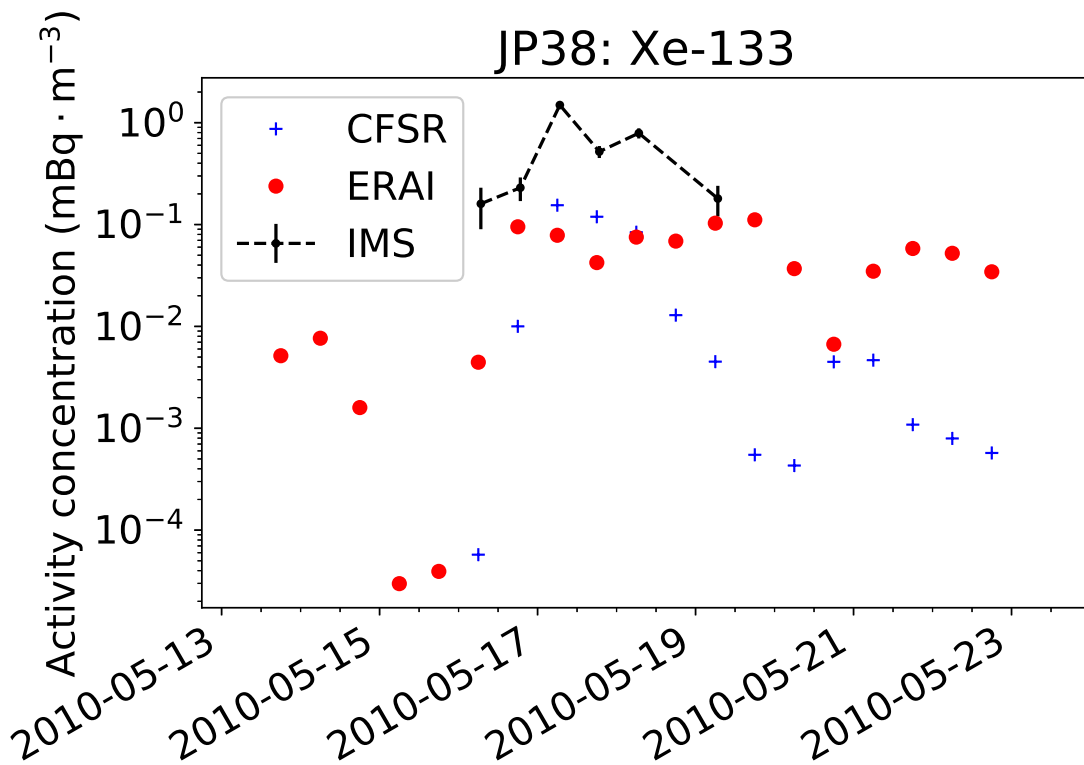Figure 6.9: ^{133}Xe concentrations at Takasaki, Japan JPX38 IMS station due to an emission source from NKTS at 2010-05-12 18:00 UTC. The dashed lines are IMS detector measurements, while the colored markers are optimally estimated FLEXPART concentrations for each meteorological data set.

Emission time (UTC)	Met data	Location		
		BK, RU	NKTS	Uljin, ROK
2010-05-10 00:00	CFSR	8.3e-3	4.5e-2	2.5e-4
	ERAI	5.7e-3	1.0e-3	3.6e-5
2010-05-11 06:00	CFSR	4.6e-7	4.7e-3	2.7e-4
	ERAI	9.5e-7	0	0
2010-05-12 00:00	CFSR	0	4.6e-3	4.4e-3
	ERAI	4.5e-5	5.0e-5	0

Table 6.8: 2°×2° spatial average of regional contribution (in seconds) from 0 to 5 meters AGL to the Geojin detector measurement. Emission times were selected at the beginning, middle, and end of the 48-hour window predicted by De Geer.

postulated emission sites of these sensitivities for three different potential emission times are shown in Table 6.8.

The largest sensitivity does appear to be to the NKTS with an emission time of midnight on 10 May. However, the data also demonstrates that there are several emission sites and times to which the Geojin detector has similar sensitivity. In particular, the values highlighted in red show that Bolshoi Kamen, NKTS, and Uljin are nearly equally likely contributors do the Geojin measurement for various emission times and meteorological data sets.

6.1.4.3 Conclusions

Both the forward and adjoint analysis of the data presented by De Geer show that the NKTS is a potential emission site for the radioxenon measurements at Geojin and Takasaki. However, neither of these methods can conclusively (individually or together) determine that the release site must be the NKTS because there is ambiguity in the emission site, time, and meteorological conditions. That is, there are a few emission times and locations which show similar sensitivity to the measured data at Geojin in the adjoint simulations. Furthermore, the optimally estimated Xe-133 concentration profiles resulting from different meteorological data sets and emission times and locations have sufficient variability to prevent conclusive attribution to a particular emission site. This uncertainty in the simulation parameters is sufficient to question the degree to which one can confidently conclude that the source is even likely to have been the NKTS.

6.2 Dry Deposition
6.2.1 Iceland 2010 Volcanic Ash: FLEXPART vs. HYSPLIT

In 2010 there was a volcanic eruption of Eyjafjallajökull in Iceland which created a large ash cloud. We used this eruption to test the dry deposition model of FLEXPART and HYSPLIT and make comparisons of the two ATM codes. Specifically, we used the optimally estimated emission source and ash particle size distribution parameters from a prior study of this event by Stohl et al. [22] in order to compare the two models. Additionally, we compared the FLEXPART and HYSPLIT simulated air concentrations with aircraft measurement data. Figure 6.10 shows the predicted (simulated) and observed (aircraft measured) ash concentrations. We can see that we are underpredicting ash concentrations relative to the aircraft data, which could be due to excessive simulated deposition, poorly represented particle size distribution, or inaccurate aircraft sensor data. We also observe that there are relatively large differences between the two ATMs.

In addition to the atmospheric ash concentration, we examined the relative error associated with using different numbers of Lagrangian particles in the emission source. As shown in Fig. 6.11, we observe the expected Monte Carlo statistical error $\varepsilon_N = O(N^{-1/2})$ for N particles discussed in section 2.3.5. Thus, in order to minimize statistical errors below a relative error of e.g. 1% at all times, this simulation required 10^4 particles per release location and time, resulting in 6×10^7 particles altogether. It is not uncommon for ATM simulations to require 10^5 to 10^8 particles for sufficiently small statistical error.

6.3 Grid, Mesoscale, and Microscale Uncertainties
6.3.1 Grid Meteorological Data Uncertainties: Fukushima Daiichi WRF Data Ensemble

In collaboration with Dr. Matthew Simpson from Lawrence Livermore National Laboratory (LLNL), we revisited the Fukushima Daiichi nuclear accident gaseous emissions studied in section 6.1.1. This time, however, we intended to see what the affects of different meteorological data sets with higher resolution than the CFSRv2 were on the simulated ^{133}Xe IMS detector concentrations. In particular, we used the WRF code to generate an ensemble of six different meteorological data sets based on the GFS, CFSRv2, and ECMWF ERA-Interim datasets with various PBL physics models. These WRF meteorological data sets were then used to drive the FLEXPART model, and each simulation was optimized using the IMS data to determine the optimal ^{133}Xe emissions and concentration time profile for each detector.
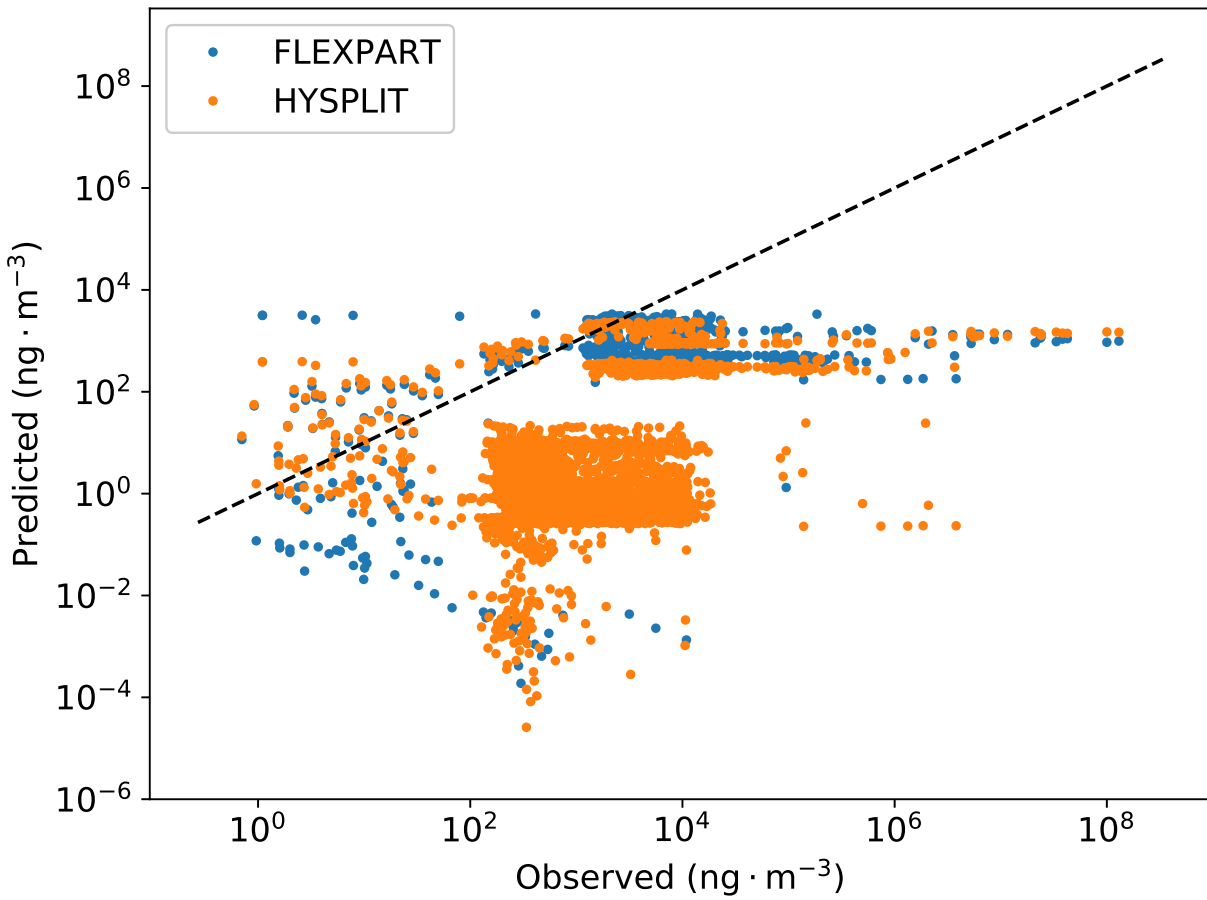
Figure 6.10: ^{133}Xe concentrations at Takasaki, Japan JPX38 IMS station using an interpolated grid averaging uniform kernel. The dashed lines are IMS detector measurements, while the colored markers are optimally estimated FLEXPART concentrations for each WRF meteorological data set.

Figure 6.11: ^{133}Xe concentrations at Takasaki, Japan JPX38 IMS station using an interpolated grid averaging uniform kernel. The dashed lines are IMS detector measurements, while the colored markers are optimally estimated FLEXPART concentrations for each WRF meteorological data set.
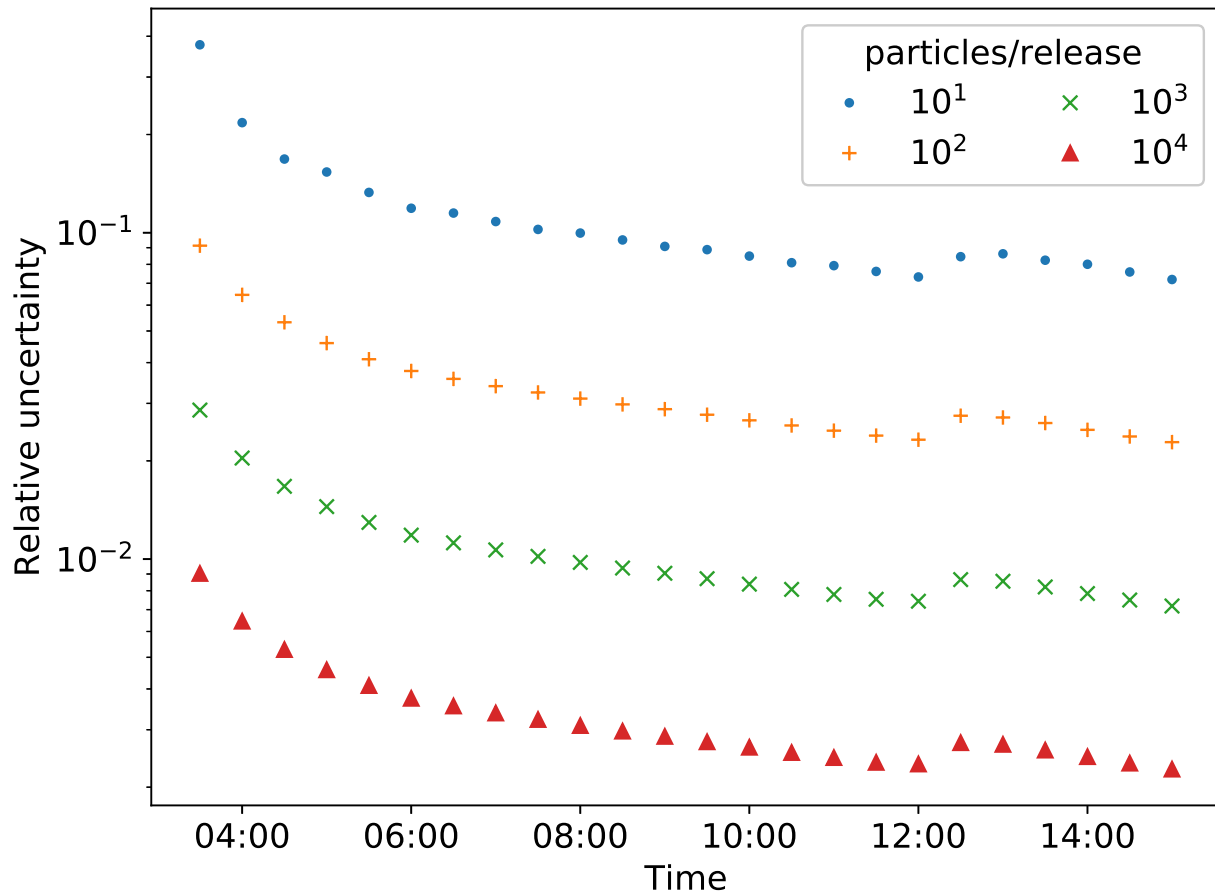
Figure 6.12: ^{133}Xe concentrations at Takasaki, Japan JPX38 IMS station using an interpolated grid averaging uniform kernel. The dashed lines are IMS detector measurements, while the colored markers are optimally estimated FLEXPART concentrations for each WRF meteorological data set.
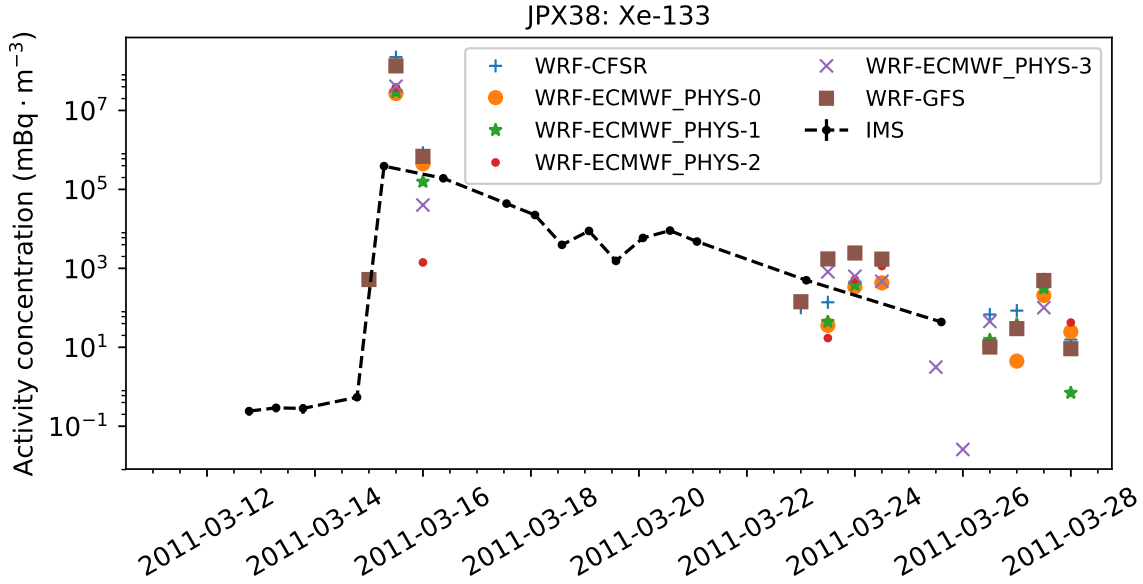
Figures 6.12 through 6.15 show the measured IMS and FLEXPART estimated ^{133}Xe concentrations at the detectors JPX38, USX74, USX77, and USX79 for each of the WRF meteorological data sets. For each of the WRF data sets, a similar temporal trend is observed in the ^{133}Xe concentration at each detector in comparison to the IMS data. However, between the different WRF data sets, very large ensemble fluctuations are observed for any given time and detector. In particular, at the JPX38 detector closest to the Fukushima emission source, fluctuations up to 4 orders of magnitude are observed. For the US IMS stations, fluctuations of one to two orders of magnitude are commonly observed between the different data sets.

Note that the FLEXPART concentration profiles in Fig. 6.12 are determined using the grid averaging discussed in section 5.4.1, whereas those in Figs. 6.13 through 6.15 are determined using the receptor parabolic averaging kernel discussed in section 5.4.2. Comparing Figs. 6.12 and 6.16, we see that the FLEXPART concentration profiles at JPX38 when using the detector averaging parabolic kernel are significantly higher towards the beginning and end of the simulation period. In the middle of the simulation period—roughly from March 16 to 23—there was no radioxenon detected at JPX38 when using the interpolated grid averaging uniform kernel, while when using the detector averaging kernel, the simulated concentrations were substantially below the IMS measurements. In contrast, comparing Figs. 6.15 and 6.17, the detector averaging parabolic kernel yielded better agreement between the FLEXPART
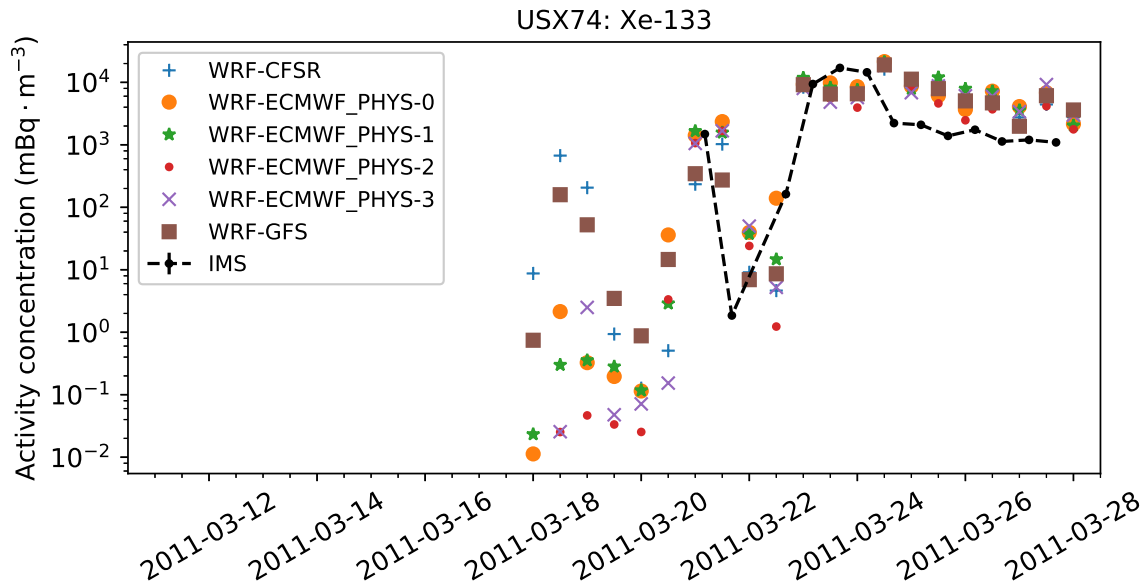
113

Figure 6.13: ^{133}Xe concentrations at Ashland, KS USX74 IMS station using a detector averaging parabolic kernel. The dashed lines are IMS detector measurements, while the colored markers are optimally estimated FLEXPART concentrations for each WRF meteorological data set.

Figure 6.14: ^{133}Xe concentrations at Wake Island USX77 IMS station using a detector averaging parabolic kernel. The dashed lines are IMS detector measurements, while the colored markers are optimally estimated FLEXPART concentrations for each WRF meteorological data set.

Figure 6.15: ^{133}Xe concentrations at Oahu, HI IMS station using a detector averaging parabolic kernel. The dashed lines are IMS detector measurements, while the colored markers are optimally estimated FLEXPART concentrations for each WRF meteorological data set.
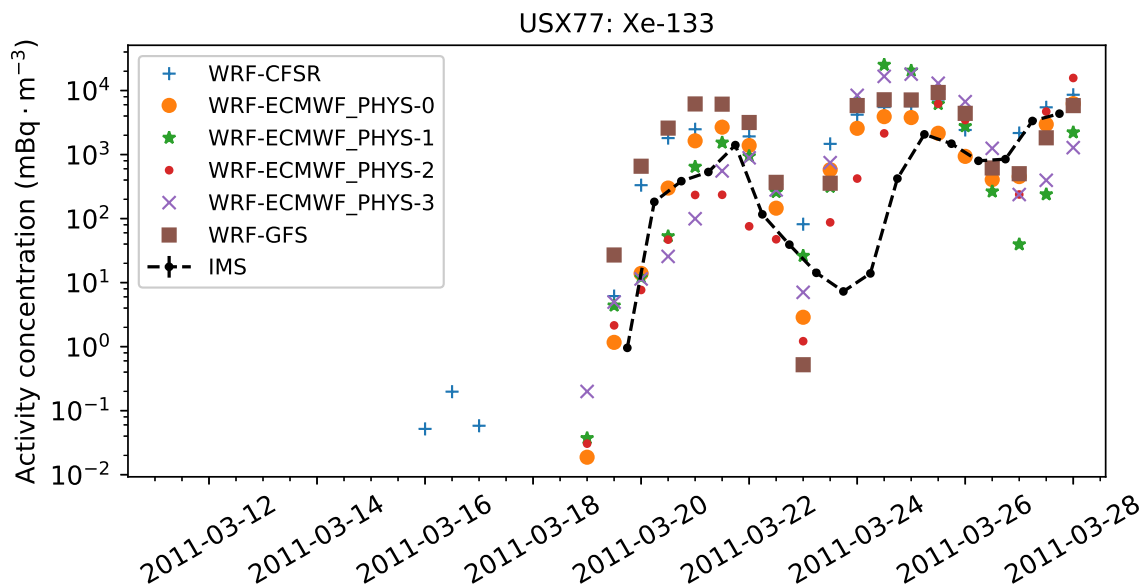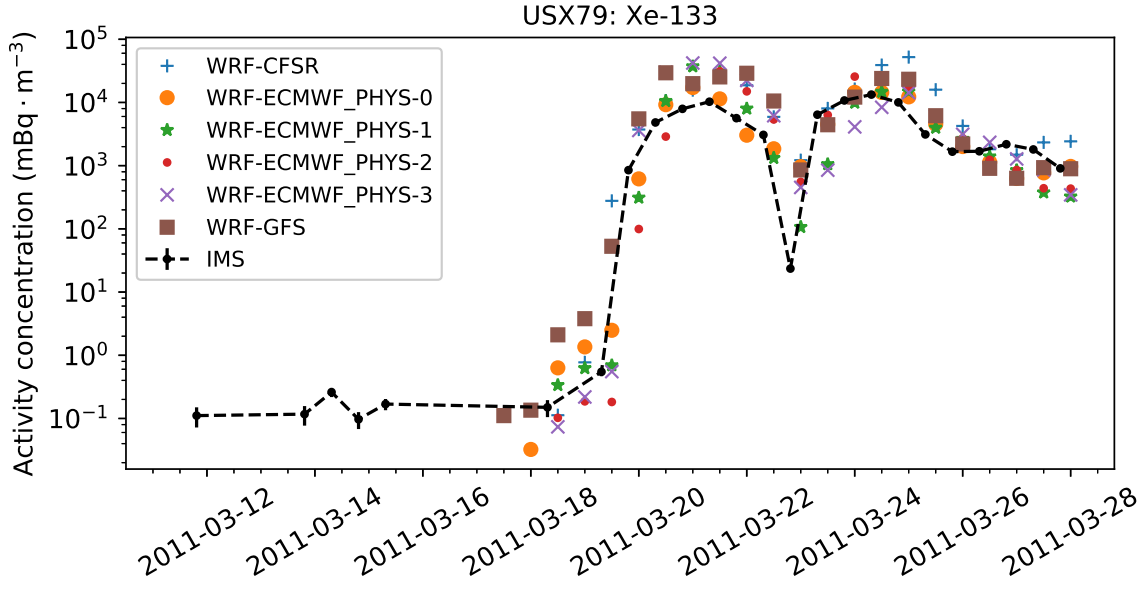
simulated concentration and the IMS measurements than did the grid averaging uniform kernel. This suggests that perhaps the detector averaging parabolic kernel bandwidth Eqs. 5.20 are unsuitable for nearby emission sources.

6.3.2 Mesoscale Turbulence Fluctuations

In order to understand the mesoscale turbulence model discussed in section 5.2, we simulated in FLEXPART the emission of 100 particles from the DPRK test site over a period of 24 hours. We then compared the trajectory of the mean $\langle \mathbf{U} \rangle$, mesoscale $\mathbf{u}_{\mathrm{meso}}$, and turbulent $\mathbf{u}$ velocity components in all three directions as is shown in Fig. 6.18. As expected, the turbulent velocity components have an ensemble average of nearly zero. The mean and turbulent components in all three directions are at times of similar magnitude, while the mesoscale turbulent velocity tends to be of smaller magnitude, especially in the vertical direction.

6.3.3 Microscale Turbulence Parametric Study: Gaussian Puff Model

In order to compare the different dispersion models used for ATM, we used a Gaussian puff model benchmark study in which we simulated the emission of a puff source in FLEXPART under several meteorological conditions. The meteorological data FLEXPART uses not only drive the mean particle trajectory but also dictate the atmospheric stability and turbulence

115
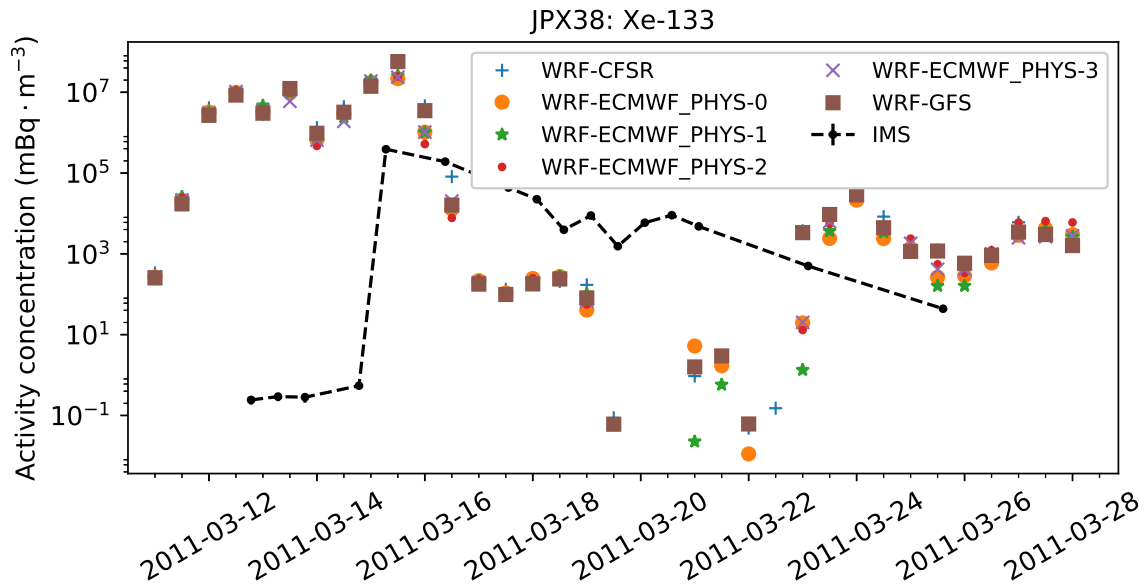
Figure 6.16: ^{133}Xe concentrations at Takasaki, Japan JPX38 IMS station using a detector averaging parabolic kernel. The dashed lines are IMS detector measurements, while the colored markers are optimally estimated FLEXPART concentrations for each WRF meteorological data set.

Figure 6.17: ^{133}Xe concentrations at Oahu, HI IMS station using an interpolated grid averaging uniform kernel. The dashed lines are IMS detector measurements, while the colored markers are optimally estimated FLEXPART concentrations for each WRF meteorological data set.
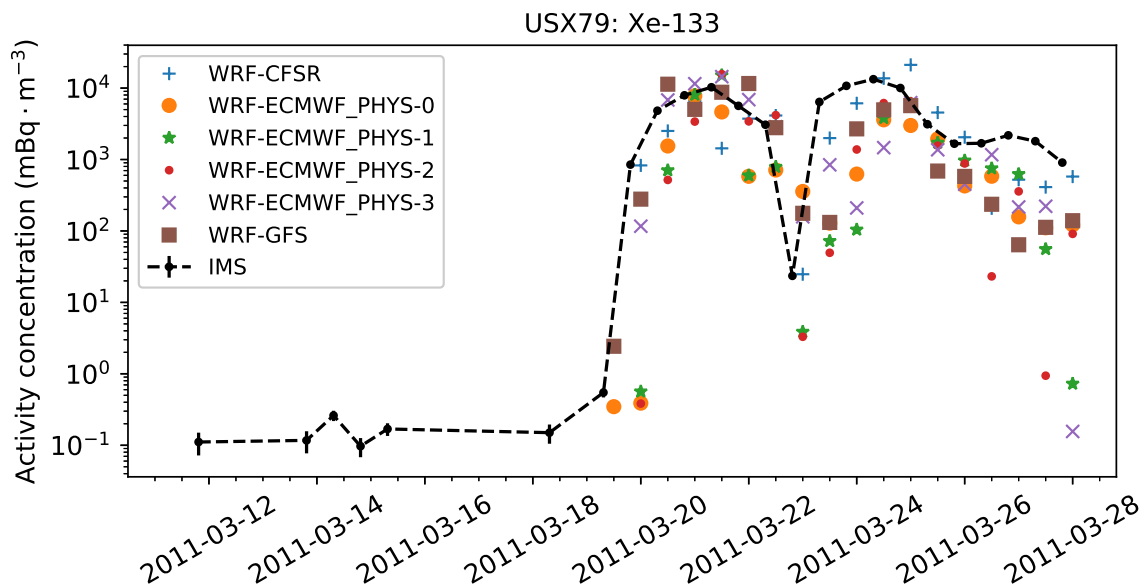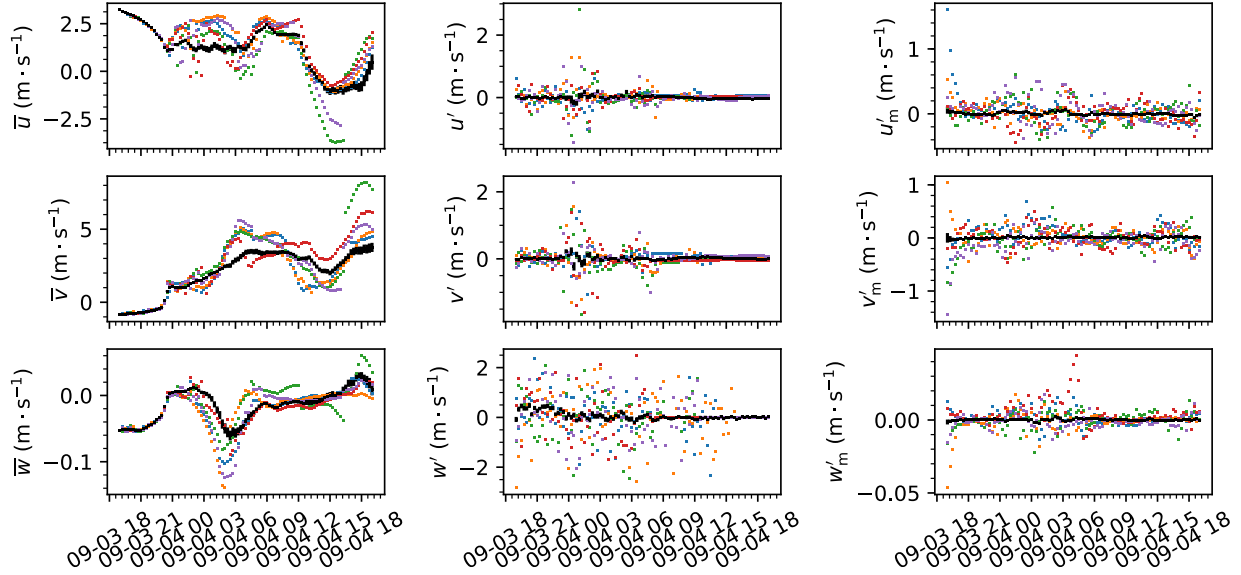
Figure 6.18: FLEXPART DPRK test site emission particle trajectory over 24 hours. Five individual particle trajectories are shown in *color*, while the ensemble average and standard deviation over all 100 particles is shown in *black*. From left to right, the columns show the mean, turbulent, and mesoscale turbulent components. From top to bottom, the rows show the velocity components in the x, y, and z directions.

parameterization as described in section 5.3.2. We then compared the resulting Gaussian plume dispersion parameters obtained in FLEXPART simulation to those predicted by the PG semi-empirical model, as described in section 4.3. This allowed us to compare the empirical turbulence models of the two dispersion models as well as the characterization of the dispersion parameters using the Lagrangian parameters $\sigma_{u_i}^2$ and T_i^{L}.

6.3.3.1   Meteorological Data

To simulate the assumptions made by the semi-empirical Gaussian puff model in FLEXPART, we constructed synthetic meteorological data to drive the FLEXPART model. This synthetic data are constant in time, horizontally homogeneous, and with vertically varying horizontal velocity $U(z)$, temperature $T(z)$, and pressure $p(z)$ [10]:

$$U(z) = U(h_{\mathrm{r}}) \left(\frac{z}{h_{\mathrm{r}}}\right)^{\gamma}, \tag{6.13}$$

$$T(z) = T_0 + \frac{\partial T}{\partial z} z, \tag{6.14}$$

$$p(z) = p_0 \exp\left(-\frac{z}{H}\right), \tag{6.15}$$

117

where $h_r = 10\,\mathrm{m}$ is the reference height, $U(h_r)$ is the horizontal velocity at the reference height, γ is the parameter for velocity power law, $T_0 = 288\,\mathrm{K}$ is the standard atmosphere surface temperature, $\partial T/\partial z$ is the (constant) vertical temperature gradient, $p_0 = 101.325\,\mathrm{kPa}$ is the standard atmosphere surface pressure, and $H = 7400\,\mathrm{m}$ is the pressure scale height. The temperature gradient determined the Pasquill atmospheric stability class A through F based on Table A.2, while we categorized stability using the Monin-Obukhov length with the FLEXPART iterative scheme. The vertical pressure gradient used was that of a hydrostatic atmosphere.

Four parameters were varied over a reasonable range to cover the sample space: $U(10\,\mathrm{m})$, γ, $\partial T/\partial z$, and planetary boundary layer height h_{PBL}. In total, approximately 75 simulations were run with the parameters covering the ranges $0.5\,\mathrm{m}\cdot\mathrm{s}^{-1} \leq U(10\,\mathrm{m}) \leq 8\,\mathrm{m}\cdot\mathrm{s}^{-1}$, $0 \leq \gamma \leq 1$, $-2 \times 10^{-2}\,\mathrm{K}\cdot\mathrm{m}^{-1} \leq \partial T/\partial z \leq 2 \times 10^{-2}\,\mathrm{K}\cdot\mathrm{m}^{-1}$, and $200\,\mathrm{m} \leq h_{\mathrm{PBL}} \leq 2000\,\mathrm{m}$ to produce simulations of all Pasquill and FLEXPART stability classes and variations within each class. This variation was performed first using a heuristic approach and then using a more systematic maximin distance Latin-hypercube design (LHD) space-filling algorithm [123]. In the LHD method, this 4D space was divided into 10^4 equally sized hypercubes from which the points were sampled using the LHD algorithm. The design was optimized by maximizing the minimum Euclidean distance between points in the space over 10^3 LHDs. Ten of the simulations (corresponding to the 10 hypercube intervals in each dimension) were derived using the maximin LHD algorithm.

6.3.3.2 Emission and Concentration Configuration

Once the meteorological data was constructed, the concentration profile and Lagrangian particle trajectories of a unit puff (60 s duration) point source consisting of 10^5 particles released at $z_0 = 25\,\mathrm{m}$ were determined as a function of time. The concentration grid spanned $(100\,\mathrm{km} \times 100\,\mathrm{km} \times 1\,\mathrm{km})$ with cells measuring $(50\,\mathrm{m} \times 50\,\mathrm{m} \times 50\,\mathrm{m})$ in the x-, y-, and z-directions, respectively. This covers a large enough range of dispersion for the Gaussian puff model and should have sufficient spatial resolution for concentration profile curve-fitting. The FLEXPART turbulence parameterization is only valid within the planetary boundary layer, and particles which attempt to exceed the planetary boundary layer height will be reflected downwards [1]. Thus, if h_{PBL} is different from the concentration grid height, the curve-fitting will not work as well since the concentration profile will either not reflect the full profile or will contain zeros above the planetary boundary layer. So we focus on the dispersion parameter comparison in the simulations yielding the best comparison for which $h_{\mathrm{PBL}} = 1.0\,\mathrm{km}$.

6.3.3.3 FLEXPART Benchmark Results

The three methods for calculating the dispersion factors via Eqs. 4.22, 4.28, and 4.29 were compared in each simulation using the FLEXPART results and the Pasquill-Gifford (PG) curves. Figures 6.19 through 6.20 show the comparison of the FLEXPART and PG dispersion factors for two of the sampled parameter sets, representing some of the simulations showing the best agreement between FLEXPART and the PG curves. The FLEXPART concentration profile and particle trajectory ensemble dispersion factors agree quite well, while there is still some discrepancy between the FLEXPART results and the PG curves. Additionally, the class A (unstable) FLEXPART simulations generally agree better with the PG curves in σ_y than σ_z, while the reverse is true for class F (stable) simulations. This also demonstrates that in contrast to the PG semi-empirical model, the FLEXPART turbulence parameterization typically predicts less dispersion in both horizontal and vertical directions, especially in the case of highly unstable atmosphere.

In the case of the unstable atmosphere, there is a deviation between the first curve-fit of the horizontal dispersion parameter as well as the curve-fit of the vertical dispersion parameter for distances approaching 100 km from the Lagrangian parameter and PG curves. The former discrepancy may be due to the concentration profile only spanning a few concentration grid cells since it has not undergone much dispersion for these shorter distances. The latter discrepancy can be attributed to the fact that for these larger distances, the concentration profile may no longer appear to be Gaussian in this highly unstable atmosphere, as is evident from both the large error bars and large predicted vertical dispersion of the PG model in this case.

After using the default FLEXPART turbulence model for $\sigma_{u_i}^2$ and T_i^{L} in section 5.3.2, we then modified the FLEXPART model to equate Eqs. 4.28 and 4.29 for a given PG stability class. This is a simple way of directly incorporating the PG semi-empirical turbulence model into the FLEXPART turbulence parameterization and may be a more consistent way of comparing the two dispersion models. As shown in Fig. 6.21, we get much better agreement between the dispersion parameters in this synthetic model, which validates the relationship between the Lagrangian parameters and the diffusion coefficient from Eq. 4.27.

Figure 6.19: Dispersion factors vs downwind distance computed using PG curves (*red*), FLEXPART concentration (*black*), and FLEXPART trajectory ensemble (*blue*) for PG class A (unstable) with $h_{\mathrm{PBL}} = 1000\,\mathrm{m}$.

Figure 6.20: Dispersion factors vs downwind distance computed using PG curves (*red*), FLEXPART concentration (*black*), and FLEXPART trajectory ensemble (*blue*) for PG class F (stable) with $h_{\mathrm{PBL}} = 1000\,\mathrm{m}$.
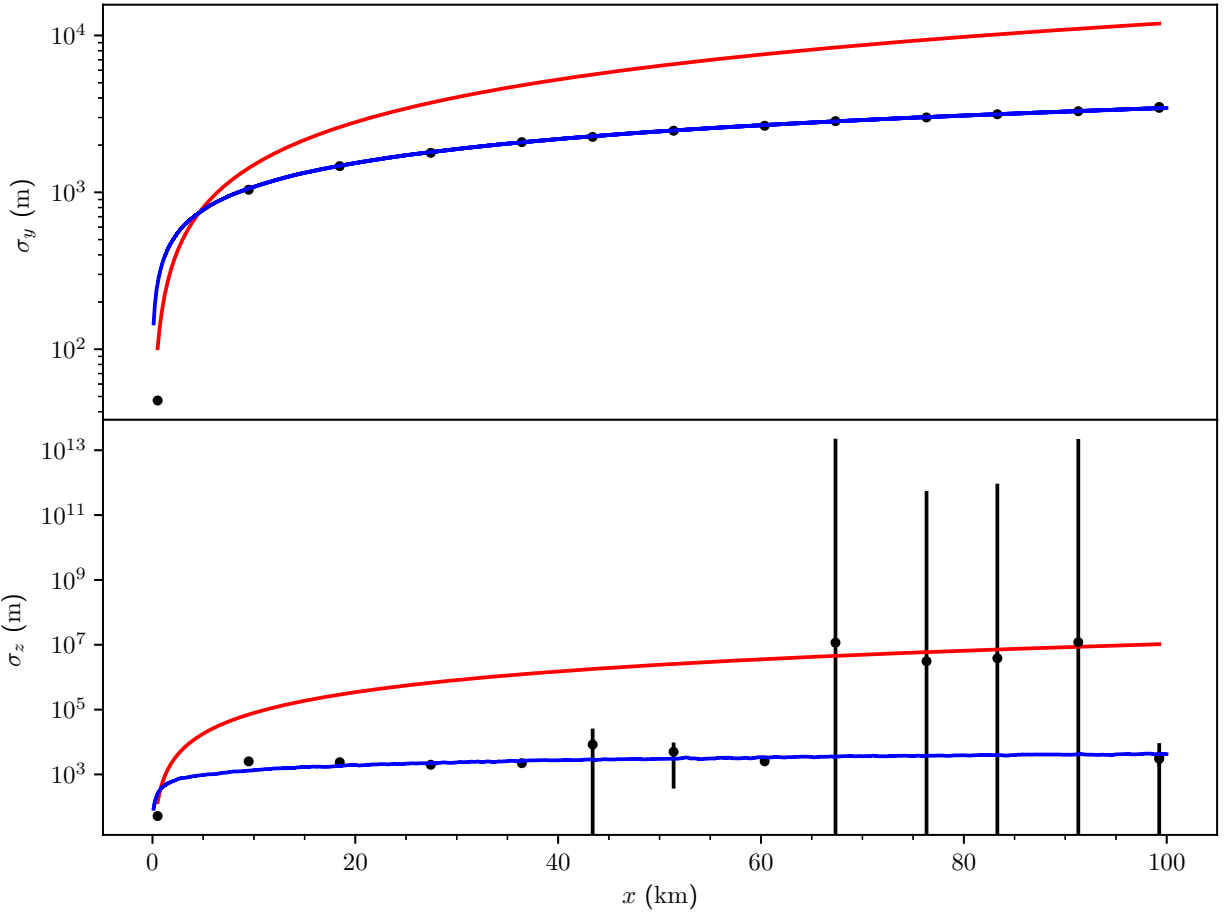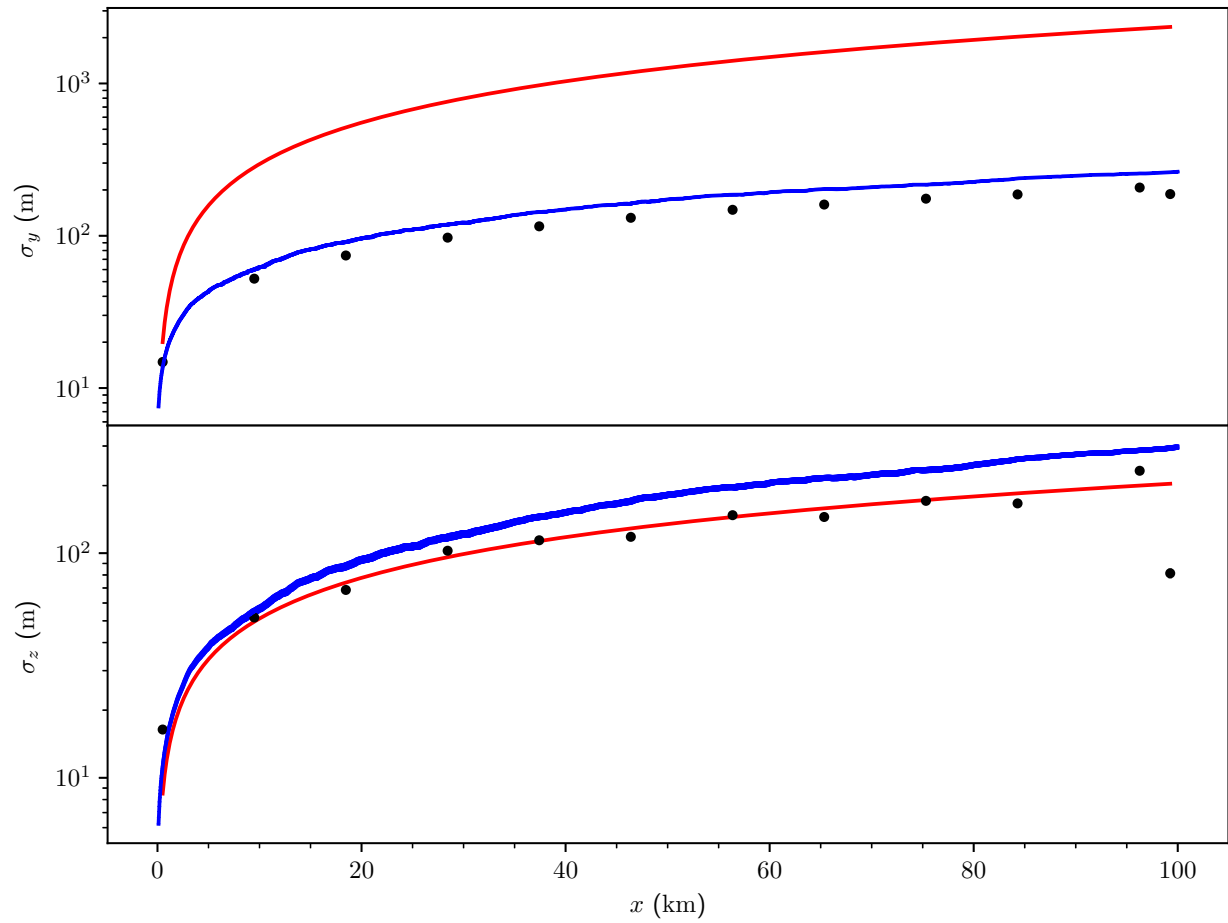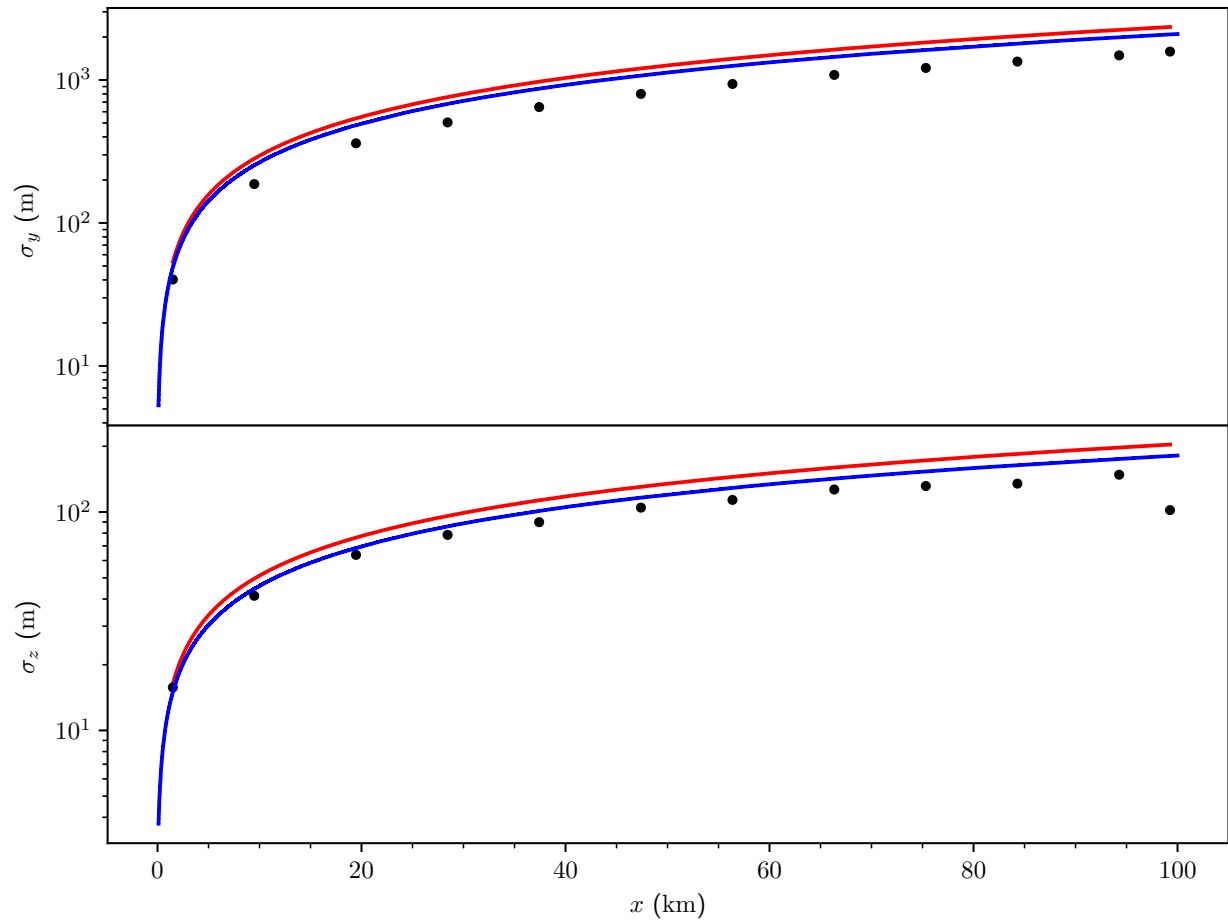
Figure 6.21: Dispersion factors vs downwind distance computed using PG curves (*red*), modified FLEXPART concentration (*black*), and modified FLEXPART trajectory ensemble (*blue*) for PG class F (stable) with $h_{\mathrm{PBL}} = 1000\,\mathrm{m}$.

Chapter 7

Conclusions

7.1 Summary and Conclusions

In chapter 1 we provided some motivation for the uses of ATM and discussed why it is essential to understand the complexities, assumptions, and uncertainties associated with ATM. This requires an understanding of the fundamental physics of the atmosphere and the mathematical representations of turbulent fluid flows. We derived and discussed the basic physical conservation laws and stochastic equations of balance necessary to understand the representations of turbulence in the Earth's atmosphere in chapter 2.

We have shown how the FLEXPART and HYSPLIT drift-diffusion model representing turbulent fluid motion can be derived from first principles based on the turbulent Navier-Stokes equation in section 3.1. In our model, we represent the drift coefficient using a physical approximation of the Lagrangian time scale T_i^{L} by the mean velocity gradient $\partial \langle U_i \rangle / \partial x_i$ as justified through the turbulent Lagrangian velocity autocorrelation function $R_{ii}^{\mathrm{L}}(t)$. The autocorrelation function, integrated over time, implicitly represents the velocity propagation and spatial displacement of the fluid particles. Through this approach, we obtained the correct model for FLEXPART and HYSPLIT, albeit with a slight numerical approximation. In contrast to other alternate Langevin models proposed by Pope and others, we indicate that the model we propose correctly represents the drift-diffusion Langevin equation implemented in FLEXPART and HYSPLIT. In the alternate models, the Lagrangian time scale depends additionally on the Reynolds stress dissipation rate. These models would also result in an additional mean velocity gradient term in the Langevin model which does not appear in the FLEXPART or HYSPLIT models as clarified in section 3.2.4.

We have presented and derived the Eulerian CFD and AD turbulence models, the latter of which is the basis of the Gaussian puff and plume models in chapter 4. The connection between the Lagrangian models discussed in chapter 3 is also made through the use of the particle dispersion parameters of the Gaussian puff model. In chapter 5, we discussed

in detail the empirical models that FLEXPART and HYSPLIT use for species transport, characterization, transmutation, and particle averaging. The FLEXPART and HYSPLIT transport models in particular use the mean fluid flow fields from the meteorological data input to drive the mean particle trajectory as well as to determine the meso- and microscale turbulence parameterization for the turbulent velocity models.

Finally, in chapter 6 we presented many studies using the FLEXPART, HYSPLIT, and Gaussian puff models to showcase the complexities and uncertainties associated with ATM. Having clarified that the FLEXPART and HYSPLIT Lagrangian velocity drift-diffusion models represent the turbulent Navier-Stokes equation, one can see that it is of paramount importance to properly model the drift and diffusion coefficients. In particular, the Lagrangian time scale T_i^{L} parameters and velocity variances $\sigma_{u_i}^2$ determine the Lagrangian particle trajectories as discussed in section 3.1, but they use highly empirical models based on the local turbulence categorization of section 5.3.2. The Gaussian puff model benchmark study in section 6.3.3 showed that there are disagreements between the Pasquill-Gifford parameterization of turbulence and those used by FLEXPART.

Both the Fukushima Daiichi simulations with the WRF meteorological data ensemble presented in section 6.3.1 and our simulation of the DPRK nuclear weapon test in 2017 in section 6.1.3 demonstrated that there are considerable uncertainties associated with the meteorological data on a grid-scale. In particular, the meteorological data can significantly affect simulated RN concentrations even at detectors near the emission source and thus on estimated emission intensities. Sections 5.2 and 6.3 discussed the empirical mesoscale model used by FLEXPART, altogether demonstrating that there are uncertainties at the micro-, meso-, and grid-scale of the FLEXPART ATM. Ultimately, combining the uncertainties of the ATM model with the uncertainties and complexities of the available RN data, it can be difficult to make conclusive statements about sensitive topics such as clandestine nuclear activities, as shown in section 6.1.4 regarding unusual measurements near the Korean peninsula in May 2010. This is especially complicated when dealing with particulate matter and the empirical deposition models as discussed in section 6.2.1 with simulations of volcanic ash following the eruptions in Iceland in 2010.

7.2   Future Work and Recommendations

Having clearly established the physical basis for the FLEXPART and HYSPLIT drift-diffusion Langevin models, we recommend additional effort for the direct solution of the turbulent Navier-Stokes equation that could provide the proper framework and accurate empirical

formulations with minimal assumptions for enhanced ATM studies. There can be large differences in expected dispersion of turbulent fluid flows depending on the characterization of the turbulence parameters chosen in both the drift-diffusion and advection-diffusion models. This can have significant impact in ATM studies for detection of clandestine nuclear activities but also for the safety analysis of nuclear power plants. Thus, it is important to use a turbulence model which is as accurate and physically based as possible for ATM. Such a microscale turbulence model could be derived using a small scale DNS model.

Given that the ATMs are highly dependent on the meteorological data not only for determining mean trajectory but also local turbulence closure models, it is thus essential that one use the most accurate and high resolution meteorological data possible. This requires a sophisticated physical model and data assimilation scheme such as those used by the ECMWF ERA5 or operational weather data sets. Future studies could thus minimize modeling errors by using sufficiently accurate meteorological data, possibly in an adaptive manner so as to also optimize computational cost.

Volcanic ash particulate simulations showed that large numbers of Lagrangian particles are necessary to minimize statistical errors in LPDMs. Furthermore, it showed that deposition processes can have a significant impact on estimated species concentrations, especially for larger particles. Thus, it is important to have reliable deposition models and an accurate species characterization. This is a non-trivial problem since these models are typically highly empirical, but it may be possible to produce more physically driven models provided sufficient computational resources. Coupling these physical deposition processes with chemical and radionuclide transmutation as well as a transport model closely based on the turbulent Navier-Stokes equation would then provide an advanced ATM.

References

1. A. Stohl, C. Forster, A. Frank, P. Seibert, and G. Wotawa, "Technical note: The Lagrangian particle dispersion model FLEXPART version 6.2," *Atmos. Chem. Phys.*, vol. 5, no. 9, p. 2461–2474, 2005. DOI: 10.5194/acp-5-2461-2005

2. A. Stohl, H. Sodemann, S. Eckhardt, A. Frank, P. Seibert, G. Wotawa, D. Morton, D. Arnold, and M. Harustak, "The Lagrangian particle dispersion model FLEXPART version 9.3," Tech. Rep., 2016.

3. K. Nishihara, H. Iwamoto, and K. Suyama, "Estimation of fuel compositions in Fukushima-Daiichi Nuclear Power Plant," Japan Atomic Energy Agency, Tech. Rep. JAEA-Data/Code 2012-018, Sep. 2012. URL: http://jolissrch-inter.tokai-sc.jaea.go.jp/pdfdata/JAEA-Data-Code-2012-018.pdf

4. L.-E. De Geer, "Radionuclide Evidence for Low-Yield Nuclear Testing in North Korea in April/May 2010," *Science & Global Security*, vol. 20, no. 1, p. 1–29, 2012. URL: http://scienceandglobalsecurity.org/archive/2012/03/radionuclide_evidence_for_low-.html

5. M. B. Kalinowski and C. Pistner, "Isotopic signature of atmospheric xenon released from light water reactors," *Journal of Environmental Radioactivity*, vol. 88, no. 3, p. 215–235, 2006. DOI: 10.1016/j.jenvrad.2006.02.003

6. M. B. Kalinowski, A. Axelsson, M. Bean, X. Blanchard, T. W. Bowyer, G. Brachet, S. Hebel, J. I. McIntyre, J. Peters, C. Pistner *et al.*, "Discrimination of nuclear explosions against civilian sources based on atmospheric xenon isotopic activity ratios," *Pure and applied geophysics*, vol. 167, no. 4-5, p. 517–539, 2010.

7. C. M. Wright, "Low-Yield Nuclear Testing by North Korea in May 2010: Assessing the Evidence with Atmospheric Transport Models and Xenon Activity Calculations," *Science & Global Security*, vol. 21, no. 1, p. 3–52, 2013. DOI: 10.1080/08929882.2013.754310

8. M. B. Kalinowski and M. P. Tuma, "Global radioxenon emission inventory based on nuclear power reactor reports." *J Environ Radioact*, vol. 100, no. 1, p. 58–70, Jan. 2009. DOI: 10.1016/j.jenvrad.2008.10.015

9. D. B. Turner, "Workbook of Atmospheric Dispersion Estimates," US Environmental Protection Agency, Tech. Rep. USEPA 999-AP-26, 1969.

10. J. H. Seinfeld and S. N. Pandis, *Atmospheric chemistry and physics: from air pollution to climate change*, 3rd ed. Wiley, 2016.

11. "NRC Regulatory Guide 1.23: Onsite Meteorological Programs," US Nuclear Regulatory Commission, Tech. Rep., Feb. 1972.

12. J. S. Irwin, "Dispersion Estimate Suggestion No. 8: Estimation of Pasquill Stability Categories," US Environmental Protection Agency, Tech. Rep., Jul. 1980.

13. A. Einstein, "Über die von der molekularkinetischen Theorie der Wärme geforderte Bewegung von in ruhenden Flüssigkeiten suspendierten Teilchen," *Annalen der Physik*, vol. 322, no. 8, p. 549–560, 1905.

14. P. Langevin, "Sur la théorie du mouvement brownien," *C. R. Acad. Sci.*, vol. 146, p. 530–533, 1908.

15. G. E. Uhlenbeck and L. S. Ornstein, "On the Theory of the Brownian Motion," *Phys. Rev.*, vol. 36, p. 823–841, Sep 1930.

16. A. Stohl, P. Seibert, G. Wotawa, D. Arnold, J. F. Burkhart, S. Eckhardt, C. Tapia, A. Vargas, and T. J. Yasunari, "Xenon-133 and caesium-137 releases into the atmosphere from the Fukushima Dai-ichi nuclear power plant: determination of the source term, atmospheric dispersion, and deposition," *Atmos. Chem. Phys.*, vol. 12, no. 5, p. 2313–2343, Mar. 2012. DOI: 10.5194/acp-12-2313-2012

17. P. W. Eslinger, S. Biegalski, T. W. Bowyer, M. W. Cooper, D. A. Haas, J. C. Hayes, I. Hoffman, E. Korpach, J. Yi, H. S. Miley *et al.*, "Source term estimation of radioxenon released from the Fukushima Dai-ichi nuclear reactors using measured air concentrations and atmospheric transport modeling," *Journal of environmental radioactivity*, vol. 127, p. 127–132, 2014.

18. M. Schöppner, W. Plastino, P. P. Povinec, G. Wotawa, F. Bella, A. Budano, M. De Vincenzi, and F. Ruggieri, "Estimation of the time-dependent radioactive source-term

from the Fukushima nuclear power plant accident using atmospheric transport modelling," *Journal of environmental radioactivity*, vol. 114, p. 10–14, 2012.

19. R. V. Arutyunyan, L. A. Bolshov, D. A. Pripachkin, V. N. Semyonov, O. S. Sorokovikova, A. L. Fokin, K. G. Rubinstein, R. Y. Ignatov, and M. M. Smirnova, "Estimation of radionuclide emission during the March 15, 2011 accident at the Fukushima-1 NPP (Japan)," *Atomic Energy*, vol. 112, no. 3, p. 188–193, Jul. 2012. DOI: 10.1007/s10512-012-9541-6

20. M. Chino, H. Nakayama, H. Nagai, H. Terada, G. Katata, and H. Yamazawa, "Preliminary estimation of release amounts of 131I and 137Cs accidentally discharged from the Fukushima Daiichi nuclear power plant into the atmosphere," *Journal of nuclear science and technology*, vol. 48, no. 7, p. 1129–1134, 2011.

21. G. R. Kumaresh, I. Fossan, M. M. Venkatraman, K. E. Giljarhus, Øystein Spangelo, and S. Jensen, "CFD-based transient ignition probability modeling of gas leaks in enclosures," *International Journal of Computational Methods*, vol. 13, no. 02, p. 1640006, 2016.

22. A. Stohl, A. Prata, S. Eckhardt, L. Clarisse, A. Durant, S. Henne, N. I. Kristiansen, A. Minikin, U. Schumann, P. Seibert *et al.*, "Determination of time-and height-resolved volcanic ash emissions and their use for quantitative ash dispersion modeling: the 2010 Eyjafjallajökull eruption," *Atmospheric Chemistry and Physics*, vol. 11, p. 4333–4351, 2011.

23. H. Webster, D. Thomson, B. Johnson, I. Heard, K. Turnbull, F. Marenco, N. Kristiansen, J. Dorsey, A. Minikin, B. Weinzierl *et al.*, "Operational prediction of ash concentrations in the distal volcanic cloud from the 2010 Eyjafjallajökull eruption," *Journal of Geophysical Research: Atmospheres*, vol. 117, no. D20, 2012.

24. N. Kristiansen, A. Stohl, A. Prata, N. Bukowiecki, H. Dacre, S. Eckhardt, S. Henne, M. Hort, B. Johnson, F. Marenco *et al.*, "Performance assessment of a volcanic ash transport model mini-ensemble used for inverse modeling of the 2010 Eyjafjallajökull eruption," *Journal of Geophysical Research: Atmospheres*, vol. 117, no. D20, 2012.

25. J. Fiates and S. S. Vianna, "Numerical modelling of gas dispersion using OpenFOAM," *Process Safety and Environmental Protection*, vol. 104, p. 277–293, 2016.

26. G. Wotawa, L.-E. De Geer, P. Denier, M. Kalinowski, H. Toivonen, R. D-Amours, F. Desiato, J.-P. Issartel, M. Langer, P. Seibert *et al.*, "Atmospheric transport modelling in

support of CTBT verification–Overview and basic concepts," *Atmospheric Environment*, vol. 37, no. 18, p. 2529–2537, 2003.

27. A. Ringbom, "Verifying the Comprehensive Nuclear-Test-Ban Treaty by Radioxenon Monitoring," in *AIP Conference Proceedings*, vol. 769, no. 1. American Institute of Physics, 2005, p. 1693–1697.

28. K. S. Rao, "Source estimation methods for atmospheric dispersion," *Atmospheric environment*, vol. 41, no. 33, p. 6964–6973, 2007.

29. S. Barrientos and F. Haslinger, "Seismological monitoring of the comprehensive nuclear-test-ban treaty," *Kerntechnik (1987)*, vol. 66, no. 3, p. 82–89, 2001.

30. M. Lawrence, M. Galindo, P. Grenard, and J. Newton, "Hydroacoustic monitoring system for the comprehensive nuclear-test-ban treaty," vol. 66, no. 3, p. 90–95, 2001. URL: http://inis.iaea.org/search/search.aspx?orig_q=RN:32036542

31. D. Christie, J. Vivas Veloso, P. Campus, M. Bell, T. Hoffmann, A. Langlois, P. Martysevich, E. Demirovic, and J. Carvalho, "Detection of atmospheric nuclear explosions: the infrasound component of the International Monitoring System," vol. 66, no. 3, p. 96–101, 2001. URL: http://inis.iaea.org/search/search.aspx?orig_q=RN: 32036541

32. M. Matthews and J. Schulze, "The radionuclide monitoring system of the Comprehensive Nuclear-Test-Ban Treaty Organisation: from sample to product," *Kerntechnik (1987)*, vol. 66, no. 3, p. 102–112, 2001.

33. J. Richelson, *Spying on the bomb: American nuclear intelligence from Nazi Germany to Iran and North Korea*. WW Norton & Company, 2007.

34. N. R. Council, *The Comprehensive Nuclear Test Ban Treaty: Technical Issues for the United States*. Washington, DC: The National Academies Press, 2012. DOI: 10.17226/12849

35. M. R. Koohkan, M. Bocquet, L. Wu, and M. Krysta, "Potential of the International Monitoring System radionuclide network for inverse modelling," *Atmospheric environment*, vol. 54, p. 557–567, 2012.

36. M. Nelkin, "In what sense is turbulence an unsolved problem?" *Science*, vol. 255, no. 5044, p. 566–570, 1992.

37. J. Lin, D. Brunner, C. Gerbig, A. Stohl, A. Luhar, and P. Webley, *Lagrangian modeling of the atmosphere*, ser. Geophysical Monograph Series. John Wiley & Sons, 2013, vol. 200.

38. R. R. Draxler and G. D. Hess, "Description of the HYSPLIT_4 Modeling System," Air Resources Laboratory, Tech. Rep., Dec. 1997.

39. S. B. Pope, *Turbulent Flows*. Cambridge University Press, 2000.

40. H. C. Rodean, *Stochastic Lagrangian models of turbulent diffusion*. Springer, 1996, vol. 45.

41. A. Bennett *et al.*, *Lagrangian fluid dynamics*. Cambridge University Press, 2006.

42. J.-P. Minier, S. Chibbaro, and S. B. Pope, "Guidelines for the formulation of Lagrangian stochastic models for particle simulations of single-phase and dispersed two-phase turbulent flows," *Physics of Fluids*, vol. 26, no. 11, p. 113303, 2014.

43. G. I. Taylor, "Diffusion by Continuous Movements," *Proceedings of the London Mathematical Society*, vol. s2-20, no. 1, p. 196–212, 1922.

44. B. J. Legg and M. R. Raupach, "Markov-chain simulation of particle dispersion in inhomogeneous flows: The mean drift velocity induced by a gradient in Eulerian velocity variance," *Boundary-Layer Meteorology*, vol. 24, no. 1, p. 3–13, 1982. DOI: 10.1007/BF00121796

45. S. B. Pope, "PDF methods for turbulent reactive flows," *Progress in energy and combustion science*, vol. 11, no. 2, p. 119–192, 1985.

46. V. Winiarek, M. Bocquet, O. Saunier, and A. Mathieu, "Estimation of errors in the inverse modeling of accidental release of atmospheric pollutant: Application to the reconstruction of the cesium-137 and iodine-131 source terms from the Fukushima Daiichi power plant," *Journal of Geophysical Research: Atmospheres*, vol. 117, no. D5, 2012.

47. K. S. Rao, "Uncertainty analysis in atmospheric dispersion modeling," *Pure and applied geophysics*, vol. 162, no. 10, p. 1893–1917, 2005.

48. S. R. Hanna, "A review of uncertainty and sensitivity analyses of atmospheric transport and dispersion models," *Developments in Environmental Science*, vol. 6, p. 331–351, 2007.

49. M. Astitha, J. Yang, H. Luo, and S. Rao, "Inherent Uncertainties in Atmospheric Models: Weather and Air Pollution," in *Air Pollution Modeling and its Application XXIV*. Springer, 2016, p. 513–518.

50. F. N. von Hippel and M. Schoeppner, "Reducing the danger from fires in spent fuel pools," *Science & Global Security*, vol. 24, no. 3, p. 141–173, 2016.

51. P. De Meutter, J. Camps, A. Delcloo, B. Deconninck, and P. Termonia, "On the capability to model the background and its uncertainty of CTBT-relevant radioxenon isotopes in Europe by using ensemble dispersion modeling," *Journal of environmental radioactivity*, vol. 164, p. 280–290, 2016.

52. S. A. Mekhaimr and M. A. Wahab, "Sources of uncertainty in atmospheric dispersion modeling in support of Comprehensive Nuclear–Test–Ban Treaty monitoring and verification system," *Atmospheric Pollution Research*, vol. 10, no. 5, p. 1383–1395, 2019.

53. R. B. Stull, *An introduction to boundary layer meteorology*. Springer Science & Business Media, 2012, vol. 13.

54. A. S. Monin and A. M. Yaglom, *Statistical Fluid Mechanics: Mechanics of Turbulence*, J. L. Lumley, Ed. MIT Press, Sep. 1971, vol. 1.

55. G. K. Batchelor, *An introduction to fluid dynamics*. Cambridge university press, 2000.

56. L. Landau and E. Lifshitz, *Fluid Mechanics: Volume 6*. Elsevier Science, 1987, no. v. 6.

57. P. K. Kundu and I. M. Cohen, *Fluid Mechanics*. Academic Press, Jan. 2010.

58. E. Özsoy, *Geophysical Fluid Dynamics I*. Springer, 2020.

59. G. K. Vallis, *Atmospheric and oceanic fluid dynamics*. Cambridge University Press, 2017.

60. J. Holton and G. Hakim, *An Introduction to Dynamic Meteorology*, ser. Academic Press. Elsevier Science, 2013.

61. A. E. Gill, *Atmosphere—ocean dynamics*. Elsevier, 2016.

62. R. A. Lindzen and R. S. Lindzen, *Dynamics in atmospheric physics*. Cambridge University Press, 2005.

63. A. Borovkov, *Probability Theory*, ser. Universitext. Springer London, 2013.

64. E. Çınlar, *Probability and stochastics*. Springer Science & Business Media, 2011, vol. 261.

65. L. C. Evans and R. F. Gariepy, *Measure theory and fine properties of functions*. CRC press, 2015.

66. V. Girardin and N. Limnios, *Applied probability*. Springer, 2018.

67. E. E. O'Brien, "The probability density function (pdf) approach to reacting turbulent flows," in *Turbulent reacting flows*. Springer, 1980, p. 185–218.

68. C. W. Gardiner, *Handbook of stochastic methods for physics, chemistry and the natural sciences*, 3rd ed., ser. Springer Series in Synergetics. Berlin: Springer-Verlag, 2004, vol. 13.

69. N. G. Van Kampen, *Stochastic processes in physics and chemistry*. Elsevier, 1992, vol. 1.

70. W. C. Welton and S. B. Pope, "PDF model calculations of compressible turbulent flows using smoothed particle hydrodynamics," *Journal of Computational Physics*, vol. 134, no. 1, p. 150–168, 1997.

71. H. Niederreiter, "Quasi-Monte Carlo methods and pseudo-random numbers," *Bulletin of the American Mathematical Society*, vol. 84, no. 6, p. 957–1041, 1978.

72. H. Wozniakowski, "Average case complexity of multivariate integration," 1989.

73. A. Z. Akcasu and A. Stolle, "Comments on the noise equivalent source in the Langevin technique," *Annals of Nuclear Energy*, vol. 16, no. 10, p. 493–508, Dec. 1989. DOI: 10.1016/0306-4549(89)90001-7

74. H. Risken, *The Fokker-Planck equation*, 2nd ed. Springer, 1996.

75. L. Arnold, *Stochastic differential equations*. John Wiley & Sons, 1974.

76. Z. A. Akcasu, "Fluctuations of macrovariables in nonlinear systems: Langevin equation approach," *Journal of Statistical Physics*, vol. 16, no. 1, p. 33–58, 1977.

77. S. Pope, "On the relationship between stochastic Lagrangian models of turbulence and second-moment closures," *Physics of Fluids*, vol. 6, no. 2, p. 973–985, 1994.

78. A. Stohl and D. J. Thomson, "A density correction for Lagrangian particle dispersion models," *Boundary-Layer Meteorology*, vol. 90, no. 1, p. 155–167, 1999.

79. S. R. Hanna, "Lagrangian and Eulerian time-scale relations in the daytime boundary layer," *Journal of Applied Meteorology*, vol. 20, no. 3, p. 242–249, 1981.

80. J. Wilson, B. Legg, and D. Thomson, "Calculation of particle trajectories in the presence of a gradient in turbulent-velocity variance," *Boundary-layer meteorology*, vol. 27, no. 2, p. 163–169, 1983.

81. D. Thomson, "Random walk modelling of diffusion in inhomogeneous turbulence," *Quarterly Journal of the Royal Meteorological Society*, vol. 110, no. 466, p. 1107–1120, 1984.

82. ——, "Criteria for the selection of stochastic models of particle trajectories in turbulent flows," *Journal of fluid mechanics*, vol. 180, p. 529–556, 1987.

83. D. Haworth and S. Pope, "A generalized Langevin model for turbulent flows," *The Physics of fluids*, vol. 29, no. 2, p. 387–405, 1986.

84. S. B. Pope, "A Lagrangian two-time probability density function equation for inhomogeneous turbulent flows," *The Physics of fluids*, vol. 26, no. 12, p. 3448–3450, 1983.

85. J. Rotta, "Statistische theorie nichthomogener turbulenz," *Zeitschrift für Physik*, vol. 129, no. 6, p. 547–572, 1951.

86. B. E. Launder, G. J. Reece, and W. Rodi, "Progress in the development of a Reynolds-stress turbulence closure," *Journal of fluid mechanics*, vol. 68, no. 3, p. 537–566, 1975.

87. J. Boussinesq, *Essai sur la théorie des eaux courantes*. Impr. nationale, 1877.

88. F. Greifzu, C. Kratzsch, T. Forgber, F. Lindner, and R. Schwarze, "Assessment of particle-tracking models for dispersed particle-laden flows implemented in OpenFOAM and ANSYS FLUENT," *Engineering Applications of Computational Fluid Mechanics*, vol. 10, no. 1, p. 30–43, 2016.

89. J. Boutahar, S. Lacour, V. Mallet, D. Quélo, Y. Roustan, and B. Sportisse, "Development and validation of a fully modular platform for numerical modelling of air pollution: POLAIR," *International Journal of Environment and Pollution*, vol. 22, no. 1-2, p. 17–28, 2004.

90. I. Korsakissok, B. Sportisse, V. Mallet, and D. Quélo, "Modeling of dispersion and scavenging in the Polyphemus platform. Applications to passive tracers." 2006.

91. D. Chanin and M. L. Young, "Code manual for MACCS2, User's guide," Sandia National Laboratories, Tech. Rep. SAND97-0594, May 1998, NUREG/CR-6613.

92. S. G. Homann and F. Aluzzi, "HotSpot Health Physics Codes Version 3.0 User's Guide," Lawrence Livermore National Laboratory, Tech. Rep., Aug. 2014.

93. F. Pasquill, "The estimation of the dispersion of windborne material," *Meteorol. Mag.*, vol. 90, no. 1063, p. 33–49, 1961.

94. F. A. Gifford, "Use of Routine Meteorological Observations for Estimating Atmospheric Dispersion," *Nuclear Safety*, vol. 2, no. 4, p. 47–51, 1961.

95. A. J. Simmons and D. M. Burridge, "An energy and angular-momentum conserving vertical finite-difference scheme and hybrid vertical coordinates," *Monthly Weather Review*, vol. 109, no. 4, p. 758–766, 1981.

96. R. Berkowicz and L. P. Prahm, "Evaluation of the profile method for estimation of surface fluxes of momentum and heat," *Atmospheric Environment (1967)*, vol. 16, no. 12, p. 2809–2819, 1982.

97. P. Zannetti, *Air pollution modeling: theories, computational methods and available software.* Springer Science & Business Media, 2013.

98. J. J. Monaghan, "Why particle methods work," *SIAM Journal on Scientific and Statistical Computing*, vol. 3, no. 4, p. 422–433, 1982.

99. ——, "Smoothed particle hydrodynamics," *Annual review of astronomy and astrophysics*, vol. 30, no. 1, p. 543–574, 1992.

100. W. Härdle, *Applied nonparametric regression.* Cambridge university press, 1990, no. 19.

101. R. L. Eubank, *Nonparametric regression and spline smoothing.* CRC press, 1999.

102. R. W. Hockney and J. W. Eastwood, *Computer simulation using particles.* crc Press, 1988.

103. M. Uliasz, "Lagrangian particle dispersion modeling in mesoscale applications," *SMR*, vol. 760, p. 23, 1994.

104. T. McMahon and P. Denison, "Empirical atmospheric deposition parameters—a survey," *Atmospheric Environment (1967)*, vol. 13, no. 5, p. 571–585, 1979.

105. M. Wesely and B. Hicks, "Some factors that affect the deposition rates of sulfur dioxide and similar gases on vegetation," *Journal of the Air Pollution Control Association*, vol. 27, no. 11, p. 1110–1116, 1977.

106. "SCALE Code System," Oak Ridge National Laboratory, Tech. Rep. ORNL/TM-2005/39, 2020.

107. J. C. Lee, *Nuclear Reactor Physics and Engineering*. John Wiley & Sons, 2020.

108. D. G. Cacuci, Ed., *Handbook of Nuclear Engineering*. Springer, 2010.

109. C. Demazière, *Modelling of Nuclear Reactor Multi-physics: From Local Balance Equations to Macroscopic Models in Neutronics and Thermal-hydraulics*. Academic Press, 2019.

110. G. Gorshkov, V. Zyabkin, and O. Tsvetkov, "The neutron background at the surface of the earth," *Soviet Atomic Energy*, vol. 17, no. 6, p. 1256–1260, 1964.

111. B. Kuzhevskij, O. Y. Nechaev, and E. Sigaeva, "Distribution of neutrons near the Earth's surface," 2003.

112. A. Gurevich, V. Antonova, A. Chubenko, A. Karashtin, G. Mitko, M. Ptitsyn, V. Ryabov, A. Shepetov, Y. V. Shlyugaev, L. Vildanova *et al.*, "Strong flux of low-energy neutrons produced by thunderstorms," *Physical review letters*, vol. 108, no. 12, p. 125001, 2012.

113. T. K. Flesch, J. D. Wilson, and E. Yee, "Backward-time Lagrangian stochastic dispersion models and their application to estimate gaseous emissions," *Journal of applied meteorology*, vol. 34, no. 6, p. 1320–1332, 1995.

114. P. Seibert and A. Frank, "Source-receptor matrix calculation with a Lagrangian particle dispersion model in backward mode," *Atmos. Chem. Phys.*, vol. 4, p. 51–63, 2004.

115. M. J. Krupcale, J. C. Lee, and T. W. Bowyer, "Radiological source term estimates of the Fukushima Daiichi nuclear accident," *Trans. Am. Nucl. Soc.*, vol. 116, no. 1, p. 741–743, Jun. 2017.

116. S. Saha, S. Moorthi, X. Wu, J. Wang, S. Nadiga, P. Tripp, D. Behringer, Y.-T. Hou, H. ya Chuang, M. Iredell, M. Ek, J. Meng, R. Yang, M. P. Mendez, H. van den Dool, Q. Zhang, W. Wang, M. Chen, and E. Becker, "NCEP Climate Forecast System Version 2 (CFSv2) 6-hourly Products." Research Data Archive at the National Center for Atmospheric Research, Computational and Information Systems Laboratory, 2011. URL: https://doi.org/10.5065/D61C1TXF

117. J. C. Lee and N. J. McCormick, *Risk and safety analysis of nuclear systems*. John Wiley & Sons, 2011.

118. D. Simon, *Optimal state estimation: Kalman, H infinity, and nonlinear approaches*. John Wiley & Sons, 2006.

119. J. L. Crassidis and J. L. Junkins, *Optimal estimation of dynamic systems*. CRC press, 2011.

120. E. Benhamou, "Kalman filter demystified: from intuition to probabilistic graphical model to real case in financial markets," Dec. 2018. URL: http://arxiv.org/abs/1811.11618v2;http://arxiv.org/pdf/1811.11618v2

121. D. P. Schaff, W.-Y. Kim, and P. G. Richards, "Seismological constraints on proposed low-yield nuclear testing in particular regions and time periods in the past, with comments on "Radionuclide Evidence for Low-Yield Nuclear Testing in North Korea in April/May 2010" by Lars-Erik De Geer," *Science & Global Security*, vol. 20, no. 2-3, p. 155–171, 2012.

122. W.-Y. Kim, P. G. Richards, D. P. Schaff, and K. Koch, "Evaluation of a seismic event, 12 May 2010, in North Korea," *Bulletin of the Seismological Society of America*, vol. 107, no. 1, p. 1–21, 2016.

123. T. J. Santner, B. J. Williams, and W. I. Notz, *The design and analysis of computer experiments*. Springer Science & Business Media, 2013.

124. A. Monin and A. Obukhov, "Basic laws of turbulent mixing in the surface layer of the atmosphere." *Contrib. Geophys. Inst. Acad. Sci. USSR*, vol. 151, p. 163–187, Sep. 1954.

125. E. Buckingham, "On Physically Similar Systems; Illustrations of the Use of Dimensional Equations," *Physical Review*, vol. 4, no. 4, p. 345–376, Oct. 1914. DOI: 10.1103/PhysRev.4.345

126. A. M. Obukhov, "Turbulence in an atmosphere with a non-uniform temperature," *Boundary-Layer Meteorology*, vol. 2, no. 1, p. 7–29, Mar. 1971. DOI: 10.1007/BF00718085

127. J. A. Businger, J. C. Wyngaard, Y. Izumi, and E. F. Bradley, "Flux-Profile Relationships in the Atmospheric Surface Layer," *Journal of the Atmospheric Sciences*, vol. 28, no. 2, p. 181–189, Mar. 1971. DOI: 10.1175/1520-0469(1971)028<0181:FPRITA>2.0.CO;2

128. D. Golder, "Relations among stability parameters in the surface layer," *Boundary-Layer Meteorology*, vol. 3, no. 1, p. 47–58, Sep. 1972. DOI: 10.1007/BF00769106

Appendix

Monin-Obukhov similarity theory

Air concentrations of atmospheric species are heavily dependent on the meteorological conditions of a given sampling site. Meteorology is the study of the atmosphere, including the interaction and temporal variation of its temperature, air pressure water vapor and mass flow. The Monin-Obukhov similarity theory [124] is an empirical method which describes the universal relationships between these non-dimensionalized variables of fluids based on the Buckingham π theorem [125]. In particular, it is a characterization of the turbulent mixing in the surface layer of the atmosphere.

A.1 Buckingham π theorem

The Buckingham π theorem is a method for computing sets of dimensionless parameters from a set of physical variables, even if the form of the equation is unknown. However, the choice of dimensionless parameters is not unique. The number of dimensionless terms that can be formed, p, is equal to the nullity of the dimensional matrix, and k is its rank. If there is a physical equation $f(q_1, q_2, \ldots, q_n) = 0$, where q_i are the n physical variables, and they are expressed in terms of k independent physical units, then the equation can be restated as $F(\pi_1, \pi_2, \ldots, \pi_p) = 0$, where π_i are the dimensionless parameters constructed from q_i by $p = n - k$ dimensionless equations of the form $\pi_i = q_1^{a_1} q_2^{a_2} \cdots q_n^{a_n}$. Here, the a_i are rational numbers, and they can be taken to be integers by redefining π_i to be raised to the power which clears all denominators.

A.2 Dimensionless parameters

We wish to characterize the turbulent mixing in the atmospheric surface layer using the following seven variables: $\partial \langle U_x \rangle / \partial z$, z, z_0, $U_\star$, ρ, g/T_0, and $\langle q_z \rangle = \rho c_{\mathrm{p}} \langle u_z \theta_{\mathrm{v}}' \rangle$. Here, $\partial \langle U_x \rangle / \partial z$ is the gradient of the horizontal velocity in the z direction, z is the vertical coordinate, z_0 is the surface roughness, $U_\star = \sqrt{\tau_0 / \rho}$ is the friction velocity, where τ_0 is the

surface shear stress, ρ is the air density, g is the gravitational constant, T_0 is the temperature of the air parcel brought adiabatically from (T, p) to the surface at pressure p_0 and is termed the *potential temperature*, and $\bar{q}_z$ is the vertical mean turbulent flux, where c_{p} is the specific heat capacity at constant pressure, and u_z and θ'_{v} are the perturbations of the vertical velocity and virtual potential temperature, respectively. Assuming that the roughness length does not affect the form of the physical equation but only its shape, we can neglect this parameter to reduce the set of physical variables to six. There are four independent physical units within the physical equation relating these variables: mass, length, time and temperature. Thus, the Buckingham π theorem predicts that there will be two dimensionless parameters in the physical equation.

The first parameter is called the flux Richardson number and is defined as

$$\mathrm{Rf} = -\frac{\kappa g z \langle q_z \rangle}{\rho c_{\mathrm{p}} T_0 U_\star^3},$$

where $\kappa \approx 0.40$ is the von Kármán constant. The flux Richardson number is equal to the ratio of the production of turbulent kinetic energy by buoyancy to its production by shear stresses. Depending on the sign of $\langle q_z \rangle$, Rf can be positive or negative. When $\langle q_z \rangle > 0 \Rightarrow \mathrm{Rf} < 0$, the atmosphere is unstable, and a positive fluctuation in velocity u_z coincides with a positive potential temperature fluctuation θ'_{v}; when $\langle q_z \rangle < 0 \Rightarrow \mathrm{Rf} > 0$, the atmosphere is stable; when $\langle q_z \rangle = 0 \Rightarrow \mathrm{Rf} = 0$, the atmosphere is adiabatic (neutral). Since the flux Richardson number is a dimensionless function of height above the ground, it can be written in terms of a length parameter [126]

$$\mathrm{Rf} = \frac{z}{L},$$

where

$$L = -\frac{\rho c_{\mathrm{p}} T_0 U_\star^3}{\kappa g \langle q_z \rangle} \tag{A.1}$$

is the Monin-Obukhov length. Similar to how the flux Richardson number indicates stability, L also indicates atmospheric stability, but the two parameters are inversely related, so smaller values of $|L|$ indicate larger deviations from neutral conditions. Physically, its magnitude is the height at which the production of turbulent kinetic energy due to mechanical shear stress and buoyancy are equal.

The second dimensionless parameter is the dimensionless velocity gradient,

$$\frac{\kappa z}{U_\star} \frac{\partial \langle U_x \rangle}{\partial z},$$

or alternately the temperature gradient,

$$\frac{\kappa z}{\theta_\star}\frac{\partial\langle\theta_v\rangle}{\partial z}.$$

A.3   Physical equations

Defining the flux Richardson number as the dimensionless length parameter $\zeta = \mathrm{Rf}$ (only in the surface layer), we use the Buckingham π theorem to derive a relationship between the two dimensionless parameters:

$$\frac{\partial\langle U_x\rangle}{\partial z} = \frac{U_\star}{\kappa z}\varphi_{\mathrm{M}}(\zeta),$$

where $\varphi_{\mathrm{M}}(\zeta)$ is the universal function for the mean velocity (i.e. momentum) profile in the nonadiabatic surface layer. If one instead uses the temperature gradient as the second dimensionless parameter, we obtain the relationship

$$\frac{\partial\langle\theta_v\rangle}{\partial z} = \frac{\theta_\star}{\kappa z}\varphi_{\mathrm{H}}(\zeta),$$

where $\theta_\star = -\langle u_z\theta_v'\rangle/U_\star$, and $\varphi_{\mathrm{H}}(\zeta)$ is the universal function for mean temperature (i.e. heat) profile in the surface layer.

A.4   Universal functions

Generally accepted forms of the universal functions functions are [10, 127]

$$\varphi_{\mathrm{M}}(\zeta) = \begin{cases} (1-15\zeta)^{-1/4} & \zeta < 0, \,(\text{unstable}) \\ 1 & \zeta = 0 \,(\text{neutral}) \\ 1+4.7\zeta & \zeta > 0 \,(\text{stable}) \end{cases},$$

and

$$\varphi_{\mathrm{H}}(\zeta) = \begin{cases} \varphi_{\mathrm{H}}(0)(1-9\zeta)^{-1/2} & \zeta < 0, \,(\text{unstable}) \\ \varphi_{\mathrm{H}}(0) & \zeta = 0 \,(\text{neutral}) \\ \varphi_{\mathrm{H}}(0)+4.7\zeta & \zeta > 0 \,(\text{stable}) \end{cases},$$

where $\varphi_{\mathrm{H}}(0) = 0.74$.

| $\bar{u}_x(10\,\text{m})$ (m s^{-1}) | Daytime | | | Nighttime | |
| | Incoming solar radiation | | | Cloudcover fraction | |
	Strong	Moderate	Slight	$\geq \frac{4}{8}$	$\leq \frac{3}{8}$
< 2	A	A-B	B		
2-3	A-B	B	C	E	F
3-5	B	B-C	C	D	E
5-6	C	C-D	D	D	D
> 6	C	D	D	D	D

Table A.1: Pasquill stability class based on the near-surface (10 m) wind, solar radiation, and cloudiness. *Source*: [9, 10]

Pasquill stability class	σ_θ at 10 m (degrees)	$\partial T/\partial z$ ($10^{-2}\,\text{K}\,\text{m}^{-1}$)
A (extremely unstable)	> 22.5	< -1.9
B (moderately stable)	17.5 to 22.5	-1.9 to -1.7
C (slightly unstable)	12.5 to 17.5	-1.7 to -1.5
D (neutral)	7.5 to 12.5	-1.5 to -0.5
E (slightly stable)	3.75 to 7.5	-0.5 to 1.5
F (moderately stable)	2.0 to 3.75	1.5 to 4.0
G (extremely stable)	< 2.0	> 4.0

Table A.2: Pasquill stability class based on the near-surface (10 m) wind direction standard deviation or surface layer temperature gradient. *Source*: [11, 12]

A.5   Pasquill stability classes

All of the results in the previous sections rely on the ability to estimate the Monin-Obukhov length L. There are a number of approaches available to do so, including using measurements. The simplest approach, however, is to use the Pasquill stability classes [93]. Tables A.1 and A.2 show two methods for estimating the Pasquill stability class based on different measured variables.

A.5.1   Estimation of L

The Monin-Obukhov length L is not typically measured but is instead estimated based on other atmospheric observations. The Monin-Obukhov length can then be parameterized in terms of the Pasquill stability class and the surface roughness length z_0 [128]:

$$\frac{1}{L} = a + b \log z_0, \tag{A.2}$$

Pasquill stability class	Coefficients	
	a	b
A (extremely unstable)	-0.096	0.029
B (moderately stable)	-0.037	0.029
C (slightly unstable)	-0.002	0.018
D (neutral)	0	0
E (slightly stable)	0.004	-0.018
F (moderately stable)	0.035	-0.036

Table A.3: Correlation parameters for the estimation of L using Eq. A.2.

with a and b given in Table A.3 for the different stability classes. Note that there are considerable uncertainties when estimating L using this scheme due to the variability in the meteorological variables which reside in a particular stability class.